



UNIVERSITÀ DI SIENA 1240

Dipartimento di Biotecnologie, Chimica e Farmacia

Dottorato in CHEMICAL AND PHARMACEUTICAL SCIENCES

XXXVI Ciclo

Coordinatore: Prof. Maurizio Taddei

POLYMERIC AND METAL-ORGANIC FRAMEWORKS FOR DRUG DELIVERY

Settore scientifico disciplinare: CHIM-03

Candidato

Simone Pepi

Dip. Biotecnologie, Chimica e Farmacia

Firma digitale del candidato

Supervisore

Prof.ssa AGNESE MAGNANI

Dip. Biotecnologie, Chimica e Farmacia

Co-supervisore

Prof.ssa GEMMA LEONE

Dip. Biotecnologie, Chimica e Farmacia

Anno accademico di conseguimento del titolo di Dottore di ricerca

2022/2023

Università di Siena
Dottorato in CHEMICAL AND PHAMACEUTICAL SCIENCES
XXXVI Ciclo

Data dell'esame finale

Commissione giudicatrice

Supplenti

INDEX

PREFACE

DRUG DELIVERY SYSTEMS (DDSs).....	i
-----------------------------------	---

CHAPTER I:

POLYMERIC MATRIX MEDIATED RELEASE AND ACTIVITY OF RED YEAST RICE AND ANNURCA APPLE EXTRACT	1
PART 1: INTRODUCTION	2
PART 2: MATERIALS AND METHODS.....	4
2.1 Materials	4
2.2 Polysaccharides matrix preparation	4
2.3 <i>In vitro</i> gastrointestinal digestion	4
2.4 HMG-CoA reductase inhibition test and lovastatin quantification	5
2.5 Differential Scanning Calorimetry (DSC)	5
2.6 Radical scavenging activity	5
2.7 Inhibition of HDL and LDL oxidation	6
2.8 Free cholesterol depletion.....	6
PART 3: RESULTS AND DISCUSSION	7
3.1 Polysaccharides matrix preparation	7
3.2 Anti HMG-CoA reductase activity	7
3.3 Differential Scanning Calorimetry (DSC)	10
3.4 Radical scavenging activity	12
3.5 Inhibition of HDL and LDL oxidation	13
3.6 Free cholesterol depletion.....	14
PART 4: CONCLUSIONS.....	15
BIBLIOGRAPHY	16

CHAPTER II:

CALCIUM IONS HYALURONAN/GELLAN GUM PROTECTIVE SHELL FOR DELIVERY OF OLEUROPEIN IN THE KNEE.....	20
PART 1: INTRODUCTION	21
PART 2: MATERIALS AND METHODS.....	22
2.1 Materials	22
2.2 Matrices preparation	22
2.3 Infrared Analysis (ATR-FTIR).....	23
2.4 Thermogravimetric Analysis (TGA)	23
2.5 Differential Scanning Calorimetry (DSC).....	23
2.6 Rheological Analysis	23
2.7 Assessment of <i>in vitro</i> oleuropein release	24
2.8 Free Radical Scavenging Activity (RSA).....	24
2.9 <i>In vitro</i> cell viability	25
2.10 Statistical analysis.....	25
PART 3: RESULTS AND DISCUSSION	26
3.1 Matrices preparation	26
3.2 Infrared analysis (ATR-FTIR).....	26
3.3 Thermogravimetric Analysis	29
3.4 Differential Scanning Calorimetry	30
3.5 Rheological analysis	32
3.6 Assessment of <i>in vitro</i> oleuropein release	34
3.7 Free Radical Scavenging Activity (RSA).....	34
3.8 <i>In vitro</i> cytotoxicity: cell viability	35
PART 4: CONCLUSIONS.....	37
BIBLIOGRAPHY	38

CHAPTER III:

POLYVINYL ALCOHOL FRAMEWORK FOR OLEUROPEIN EXTRACT DELIVERY: MATRIX CHARACTERIZATION AND RELEASE PROFILES	43
PART 1: INTRODUCTION	44
PART 2: MATERIALS AND METHODS	46
2.1 Materials.....	46
2.2 PVA frameworks syntheses.....	46
2.3 Swelling behavior	46
2.4 Thermogravimetric Analysis (TGA)	47
2.4.1 Total water content.....	47
2.4.2 Thermal stability.....	47
2.5 Differential Scanning Calorimetry (DSC).....	48
2.5.1 Types of water	48
2.5.2 Crystallinity and thermal behavior	49
2.6 Viscoelastic properties.....	49
2.6.1 Frequency sweep test (SAOS).....	49
2.6.2 Amplitude sweep test (SAOS and LAOS)	50
2.6.3 Creep-Recovery test	50
2.7 Tribological properties.....	50
2.8 Oleuropein extract release profiles	50
2.9 Statistical analysis.....	51
PART 3: RESULTS AND DISCUSSION.....	52
3.1 PVA frameworks syntheses.....	52
3.2 Swelling behavior	53
3.3 Thermogravimetric Analysis (TGA)	55
3.3.1 Total water content.....	55
3.3.2 Thermal stability.....	56
3.4 Differential Scanning Calorimetry (DSC).....	57

3.4.1	Types of water	58
3.4.2	Crystallinity and thermal behavior	59
3.5	Viscoelastic properties	60
3.5.1	Frequency sweep test (SAOS).....	60
3.5.2	Amplitude sweep test (SAOS and LAOS)	63
3.5.3	Creep-Recovery test	67
3.6	Tribological properties.....	68
3.7	Oleuropein extract release profiles	69
PART 4: CONCLUSIONS		71
BIBLIOGRAPHY		73
PART 5: SUPPORTING MATERIALS		75

CHAPTER IV:

VANADIUM BASED METAL-ORGANIC FRAMEWORK: SYNTHESIS AND CHARACTERIZATION		109
PART 1: INTRODUCTION		116
PART 2: MATERIALS AND METHODS		120
2.1	Materials.....	120
2.2	Metal-organic framework synthesis	120
2.3	Infrared analysis (ATR-IR).....	121
2.4	Dynamic light scattering analysis (DLS)	121
2.4.1	Average size determination	121
2.4.2	Particles stability (ζ - potential)	122
2.5	Vanadium determination via ICP-MS.....	123
2.6	Thermogravimetric analysis (TGA).....	123
2.7	Specific surface area and porosity	123
2.8	Transmission Electron Microscopy	125

PART 3: RESULTS AND DISCUSSION.....	127
3.1 Metal-organic framework synthesis.....	127
3.2 Infrared analysis (ATR-IR).....	128
3.3 Dynamic light scattering analysis (DLS).....	129
3.3.1 Average size determination.....	129
3.3.2 Particles stability (ζ - potential).....	131
3.4 Vanadium determination via ICP-MS.....	132
3.5 Thermogravimetric analysis (TGA).....	133
3.6 Specific surface area and porosity.....	135
3.7 Transmission Electron Microscope.....	137
PART 4: CONCLUSIONS	139
BIBLIOGRAPHY	141

CHAPTER V:

RELEASE AND ACTIVITY OF IRON COMPLEXES: EFFECT OF Fe OXIDATION STATES AND CHELATING AGENTS ON IRON BIO-ACCESSIBILITY FROM DIFFERENT SUPPLEMENTS.....	145
PART 1: INTRODUCTION	146
PART 2: MATERIALS AND METHODS	147
2.1 Materials.....	147
2.2 Infrared analysis	147
2.3 Differential scanning calorimetry (DSC).....	147
2.4 Thermogravimetric Analysis (TGA).....	147
2.5 Dynamic Light Scattering (DLS) measurements.....	148
2.6 Iron Bioavailability	148
2.6.1 Iron solubility.....	148
2.6.2 Iron Dialysability.....	148

2.6.3	Gastrointestinal method	149
2.7	Iron bioaccessability.....	149
2.8	Statistical Analysis.....	149
PART 3:	RESULTS AND DISCUSSIONS.....	150
3.1	Formulations.....	150
3.2	Infrared analysis	150
3.3	Differential Scanning Calorimetry (DSC)	152
3.4	Themogravimetric Analysis (TGA).....	153
3.5	Dynamic Light Scattering (DLS) measurements.....	154
3.6	Iron availability	155
3.7	Iron bio-accessibility: Caco-2 cells	157
PART 4:	CONCLUSIONS	158
	BIBLIOGRAPHY	159

CONCLUSIONS

	POLYMERIC AND METAL-ORGANIC FRAMEWORKS FOR DRUG DELIVERY SYSTEMS	164
--	--	-----

PREFACE

DRUG DELIVERY SYSTEMS (DDSs)

An important issue in therapeutic treatment of diseases is represented by the drug toxicity at high doses (adverse side effects) when, at the same time, it must be present in the systemic circulation for a time sufficient to achieve the desired therapeutic effects. Another critical aspect in drugs administration is that some of them have a very narrow therapeutic window and most of them are poorly soluble in aqueous media (physiological environments) showing a very low bioavailability. Targeted drug-delivery technology represents a valid solution to the problems connected with disease treatments, increasing the circulation stability of drugs (by protecting them within suitable vectors) and allowing them to reach and be active at the target cellular compartment at a suitable concentration, avoiding, at the same time, adverse side effects.

Suitable systems for drug-controlled delivery may be obtained, for example, by chemical modification of the drug by soluble polymers to increase the residence time in the diseased system, or to convey more favorable properties to this, such as the reduction of antigenicity or increased stability toward enzymes. In the polymer-drug conjugate the drug and the polymer are linked together by chemical bonds that can be either cleavable into the body to release the starting drug or stable to keep the drug-polymer conjugate as a new therapeutic product. For the latter, the polymer-drug binding must be designed to maintain the drug active moiety free for receptor binding. In such a way, not only desirable and constant drug levels are achieved, but also a delivery that may last longer. In developing drug delivery systems, by specific carriers, the drug is usually loaded during the process by which the matrix is produced or shaped, or it is absorbed into the preformed matrix from a concentrated drug solution. These systems require special designs, homogeneity of the components and purity.¹

Designing drug delivery systems is one of the most challenging issues in polymer science field.

¹ VERONESE, Francesco M.; CALICETI, Paolo. Drug delivery systems. In: Integrated Biomaterials Science. Boston, MA: Springer US, 2002. p. 833-873.

POLYSACCHARIDES

Despite the huge number of natural and synthetic polymers or lipidic vehicles used to realize drug carriers, polysaccharidic complexes remain as the simplest and the most economical way to realize an efficient drug delivery system. Polyelectrolyte complexes (PECs), formed by the electrostatic attractions between two oppositely charged polymers, have been used for the realization of controlled release formulations. Chitosan and xanthan gum are two of the most utilized and studied natural polysaccharides for the realization of PECs. Xanthan gum is an exopolysaccharide with a cellulosic backbone along which mannose and glucuronic acid moieties are found, and thanks to their presence, it can be considered an anionic polysaccharide able to form PEC with cationic polymers, such as chitosan, the only natural cationic polysaccharide. The large use of chitosan–xanthan gum PECs for the realization of controlled release systems for oral administration can be explained basing on several aspects. Firstly, nontoxic metabolites are produced during their degradation; secondly, chitosan–xanthan gum PEC shows a high enzymatic resistance; and finally, its swelling behavior is pH dependent. Moreover, the combination between a hydrophilic polymer (i.e., xanthan gum) and a structural polymer (i.e., chitosan) guarantees a balance between swelling ratio and elasticity and, therefore, a regulated drug release can be observed.²

Beside chitosan and xanthan gum, the most utilized polysaccharide in biomedical field is Hyaluronic acid.

Hyaluronic acid (HA) is a linear polysaccharide consisting of the repetition of a disaccharide composed of D-glucuronic acid (GLCA) and N-acetyl D-glucosamine (GlcNAc). HA belongs to the so called connective tissue polysaccharides, mucopolysaccharides or glycosaminoglycans. HA is ubiquitous among vertebrates and abundantly expressed in the extracellular matrix of all tissues, as well as on the cell surface. Despite its simple chemical structure, HA plays numerous molecular functions that contribute to the structure and physiology of the tissues, modulating cell behavior during morphogenesis, tissue remodeling and inflammation. The inherent biocompatibility and biodegradability together with the susceptibility to chemical modifications have made HA particularly attractive for the development of biomaterials with a broad clinical potential from ophthalmology to dermatology. Nevertheless, viscosupplementation still represents the main field of application for hyaluronic acid and its derivatives.³

² CONSUMI, Marco, et al. Xanthan Gum–Chitosan: Delayed, prolonged, and burst-release tablets using same components in different ratio. *Advances in Polymer Technology*, 2018, 37.8: 2936-2945.

³ LEONE, Gemma, et al. Sodium hyaluronate-g-2-((N-(6-aminohexyl)-4-methoxyphenyl) sulfonamido)-N-hydroxyacetamide with enhanced affinity towards MMP12 catalytic domain to be used as viscosupplement with increased degradation resistance. *Carbohydrate Polymers*, 2021, 271: 118452.

HA with molecular weight ranging from 500 kDa to 6000 kDa has been used for the development of viscosupplements. Despite the presence of several different HA-based commercial viscosupplements, the development of products with enhanced injectability and yet reasonable viscoelastic behavior for OA treatment is necessary. Indeed, if linear HA solutions have a lower viscosity, making injection easier, they are not as effective as crosslinked HA preparations because of their lower viscoelastic properties. Nevertheless, the higher the viscoelastic properties, the higher the force required to be injected. Moreover, if crosslinking HA significantly improves its viscoelastic properties and residence time, it only slows down HA physiological degradation by hyaluronidases with production of low molecular weight fragments, whose pro-inflammatory action is well known. This has directed research to find adequate hyaluronan substitutes for viscosupplementation, even if Hyaluronan still remains the gold standard. Very few studies on Gellan Gum, a linear, anionic extracellular polysaccharide with repeating tetrasaccharide units of d-glucose, d-glucuronic acid, d-glucose, and l-rhamnose, have been done for this application despite its wide use in biomedical engineering.⁴ So, an integration between those two polysaccharides could represent a good solution.

SYNTHETIC POLYMERS

Recently, a great deal of effort has focused on the design of optimal delivery systems for drugs and bioactive factors, such as magnetic nanoparticles, gold nanoparticles, liposomes, dendrimers, and aptamers. However, polymeric vehicles remain the most convenient and versatile way to deliver substances and, among polymers, one of the most utilized is polyvinyl alcohol (PVA). PVA is one of the largest produced polymers worldwide. It shows optimal properties such as high water affinity, wear resistance, biocompatibility and processability. For these characteristics, it has been used as tissue substitute, heavy metal ions absorbent, carrier for antimicrobial substances. Depending on its end use, PVA based material characteristics must be controlled and tailored to better respond. The main concern is about its stability and resistance. Nevertheless, it can be significantly improved by crosslinking it.⁵ For those reasons the PVA theta-gel formation will be performed and explored to evaluate the properties of those frameworks for the use as supplement and drug delivery system in osteoarthritis.

⁴ LEONE, Gemma, et al. Enriched Gellan Gum hydrogel as viscosupplement. *Carbohydrate Polymers*, 2020, 227: 115347.

⁵ LEONE, Gemma, et al. Poly-vinyl alcohol (PVA) crosslinked by trisodium trimetaphosphate (STMP) and sodium hexametaphosphate (SHMP): Effect of molecular weight, pH and phosphorylating agent on length of spacing arms, crosslinking density and water interaction. *Journal of Molecular Structure*, 2020, 1202: 127264.

METAL-ORGANIC FRAMEWORKS (MOFs)

Many carriers have been reported, but in the past decade MOFs have become a hotspot in the field of drug delivery devices for delivering loaded drug to desired sites. Metal-organic frameworks have the potential to be used as drug delivery systems, thanks to their specific characteristics, especially their exceptionally high surface area, large cavity size for drug encapsulation, and a controlled drug-release profile. Furthermore, the MOFs possess an intrinsic biodegradability due to the relative labile metal-ligand bonds and the tunable functionality for post-synthetic grafting of active molecules. A lot of active molecules of different nature (i.e. hydrophilic, hydrophobic, and amphiphilic) can be encapsulated in the MOFs' cavity and/or tethered with the framework structure. The active molecules loading can be performed either by covalent interaction or through noncovalent interactions.⁶

⁶ SINGH, Ram, et al. Metal organic frameworks for drug delivery. In: Applications of nanocomposite materials in drug delivery. Woodhead Publishing, 2018. p. 605-617.

**CHAPTER I:
POLYMERIC FRAMEWORKS
FOR DRUG DELIVERY**

**POLYMERIC MATRIX MEDIATED RELEASE AND
ACTIVITY OF RED YEAST RICE AND ANNURCA APPLE
EXTRACT**

PART 1: INTRODUCTION

Dyslipidemia, determining an abnormal amount of lipids in the blood, can be considered as one of the most relevant pathological conditions. Most dyslipidemia cases are due to wrong diet and lifestyle and statins are at the forefront strategy to manage them. Nevertheless, statins show several side-effects and are not always well tolerated. Consequently, in the last decades, the interest towards a nutraceutical approach has grown [1]. Red yeast rice (RZR) has been long studied for the cholesterol lowering ability of its component, monacolin K (lovastatin). Lovastatin can reduce blood cholesterol levels acting as inhibitor of the cholesterol biosynthesis rate-limiting enzyme, 3-hydroxy-3-methylglutaryl coenzyme A reductase (HMG-CoA). Lovastatin was the first anti-hypercholesterolemic drug approved by the United States Food and Drug Administration (FDA) [2]. Starting from 2002 European authorities warned on the use of high doses of red yeast rice and in 2011 determined in 10 mg of monacolins from fermented red yeast rice the amount to be consumed daily [1]. Our previous studies on the effect of different formulations on lovastatin release from RZR highlighted that 10 mg/day of monacolin k showed enhanced inhibitory activity against HMG-CoA reductase and lower cholesterol production compared with pravastatin and synthetic lovastatin [3-6]. Since the exact amount of monacolin K in RZR is highly variable, from 2022 June first, the European authorities imposed that individual portion of any product for daily consumption shall provide less than 3 mg of monacolins from red yeast rice. It is therefore necessary to find new formulations able to guarantee an effect on cholesterol levels close to that performed by 10 mg of monacolin K. Several approaches have been tested, and the best one appears to be the combination of different nutraceuticals. Evidence of synergetic effects of substances, that act with different mechanisms on lipid metabolism, were found [7]. Supplement products containing RZR and other bioactive compounds have been developed and tested for their anti-hyper cholesterol activity with very promising results [8]. A combination of RZR (providing 3 mg of monacolin K) and berberine (500 mg) have been developed (Armolid Plus®) to join the inhibition of HMG-CoA reductase enzyme by RZR to the enhancement of the hepatic uptake of cholesterol by berberine [7]. Several other combinations have been tested, such as RZR and soybean, RZR and lupin protein or pea protein, RZR and artichoke [9]. High interest in polyphenolic compounds from apple extracts is growing thanks to their ability to play a key role in cholesterol metabolism [10-12]. Comparing different apples varieties (Red Delicious, Pink Lady, Fuji and Golden Delicious), polyphenolic extracts from Annurca apple appeared more effective in decreasing cellular cholesterol accumulation and protecting cells against oxidative stress [13-14]. The polyphenolic profile of Annurca apple

variety, a typical cultivar of Campania region in Italy listed as a Protected Geographical Indication (IGP) product, has been obtained and it resulted one of the richest varieties [15].

Two different formulations containing 10 mg of lovastatin from RYR and a combination of lovastatin (3 mg) from RYR and Annurca apple extract respectively, were prepared and compared to verify their anti-hyper cholesterol action in terms of inhibition of HMG-CoA reductase enzyme, oxidation protection of HDL and LDL and total free cholesterol depletion, with the aim of evaluating if the combination of different nutraceuticals with different lipid-lowering activities can provide an alternative to high dose of monacolin K.

PART 2: MATERIALS AND METHODS

2.1 MATERIALS

Xanthan gum (XG: Mw: 1 MDa), Chitosan (C: Mw: 320 kDa, deacetylation degree $\geq 75\%$), Cholesterol Quantification Kit (MAK043), HMG-CoA reductase assay kit (CS10909) and solvents were purchased from Sigma Aldrich (Milan, Italy). All solvents were analytical or HPLC grade. Red yeast rice (RYR, titrated at 5%) and Annurca Apple Extract (Annurca Complex: AC) were provided by MediBase s.r.l. (Prato, Italy). Commercial products (Lesstat® and Lesstat forte®) were used as reference. Rosuvastatin was purchased in a local pharmacy.

2.2 POLYSACCHARIDES MATRIX PREPARATION

Cylindrical tablets (diameter: 0.5 cm; thickness: 1 cm, total weight: 1 g) were prepared mixing in proper proportion the two polymers (XG and C) and the two extracts (RYR and AC), by a vortex for 60 s (40 Hz). After that, the mixed polymers and extracts were pressed using a handpress with a loading weight of 5 tons, for 5 min.

2.3 *IN VITRO* GASTROINTESTINAL DIGESTION

Tablets dissolution was performed following a procedure already reported and slightly modified [3,14]. Briefly, each tablet was immersed in 250 mL of gastric simulating fluid containing 0.5 g of pepsin dissolved in HCl 0.1 N, the pH was adjusted to 2.0 with HCl 6 N, and then incubated at 37°C for 2 h. After the gastric digestion, the pH was raised to 6.5 with NaHCO₃ 0.5 N and then 5 mL of a mixture of pancreatin (8.0 mg/mL) and bile salts (50.0 mg/ mL) 1:1; v/v, were added and incubated at 37°C for 24 h. Samples were maintained under agitation (250 rpm). 5 aliquots (10 mL) for each sample were collected after 3h, 5h and 24 hours and lyophilized for following analyses.

2.4 HMG-CoA REDUCTASE INHIBITION TEST AND LOVASTATIN

QUANTIFICATION

Samples were prepared following the procedure previously reported [6]. Briefly, an aliquot of each sample was resuspended in 1 mL of PBS at pH 7.4 and 5 μ L were added to the assay kit following the supplier protocol. The rate of NADPH oxidation by HMG-CoA was monitored every 15 s at 340 nm for a period of 5 min using an Ultraspec 200 UV (Biotech, USA).

To quantify lovastatin, samples (injection volume 20 μ L) were analyzed using a HPLC-UV (Varian) equipped with a C18 column (250 mm \times 4.6 mm, 5 μ m, Varian). The mobile phase was a mixture of acetonitrile, water, and ethanol (5:3:1) and the flow rate was 1.0 mL/min. Lovastatin was quantified at 230 nm (LOD: 0.05 mg/L; LOQ: 0.10 mg/L). Calibration curve was obtained with the internal standard method using simvastatin: the method was linear in the range 0.1 mg/L–50 mg/L, the total run time of analysis was 30 min with the retention time of lovastatin being 19.52 min., [3].

2.5 DIFFERENTIAL SCANNING CALORIMETRY (DSC)

Thermographs of different formulations were recorded using Q1000 DSC (TA Instruments). A tablet of each sample was pulverized, and 15 mg were sealed in aluminum pans, equilibrated at -90°C and then heated to 400°C , using a heating ramp rate of $10^{\circ}\text{C}/\text{min}$ under nitrogen flow (50 mL/min).

2.6 RADICAL SCAVENGING ACTIVITY

The determination of DPPH \cdot radical scavenging capacity was evaluated following the steady state method as described by Mishra et al. [16] and Cheng et al. [17]. The method consists in monitoring the decrease in absorbance for different durations from 15 min to 6 h depending upon the antioxidant and its concentrations to obtain a steady state of decrease in absorbance of [DPPH \cdot]. The percentage of DPPH \cdot remaining at steady state was determined following Equation 1.

$$\% \text{ DPPH}_{\text{remaining}} = \left(\frac{A_f}{A_0} \right) \times 100$$

Equation 1

where A_0 and A_f correspond to the absorbance at 515 nm of DPPH \cdot alone and in presence of the scavenging species at steady state respectively. A_0 and A_f value was obtained at the steady state region where absorbance reaches the equilibrium and no further decrease in absorbance are observed. The effective concentration (EC50) value, defined as the concentration required to decrease the initial DPPH \cdot concentration by 50%, was determined.

2.7 INHIBITION OF HDL AND LDL OXIDATION

The antioxidant activity of formulations versus HDL and LDL was assessed following the procedure reported by Hillstrom et al. [18] with some modifications. Briefly, HDL (0.06 g of protein/L) and LDL (0.17 g of protein/L) were incubated at 37°C with Cu(II) (CuCl $_2$ 0.5 mmol/L) and 1 aliquot of each formulation or ascorbic acid (AA). Oxidation was assessed as the increase in absorbance at 245 nm during 3 h of incubation.

2.8 FREE CHOLESTEROL DEPLETION

An aliquot of each sample was redissolved in 1 mL of phosphate buffer (pH 6.8). 2 μ L of each sample were brought to a final volume of 50 μ L with cholesterol assay buffer, and then, 50 μ L of the provided Reaction Mix was added and incubated for 60 min at 37°C and then read at 570 nm by a Ultraspec 200 UV (Biotech, USA) [6].

PART 3: RESULTS AND DISCUSSION

3.1 POLYSACCHARIDES MATRIX PREPARATION

Changing the relative amount of chitosan and xanthan gum permits to modulate the release profile of monacolin K from RYR. Accordingly, two series of formulations were prepared as reported in Table 1.

Table 1: Composition of analyzed formulations.

Sample	Chitosan-Xanthan gum (%)	Monacolin K (mg)	AC (mg)
C1	20-80	10.01 ^(*)	0.00
C2	20-80	0.00	200
C3	20-80	2.992 ^(**)	200
C4	80-20	10.01 ^(*)	0.00
C5	80-20	0.00	200
C6	80-20	2.992 ^(**)	200
Rosuvastatin 5mg	/	/	/

^(*) corresponding to 200 mg of RYR; ^(**) corresponding to 59.8 mg of RYR

As reported in Table 1, formulations C1-C3 were obtained combining chitosan and xanthan gum in a ratio 1:4. This ratio guarantees a prolonged release of lovastatin from RYR and it was the ratio used in the commercial product Lesstat® (Medibase s.r.l., Prato Italy) [6]. Formulations C4-C6 were designed to guarantee a rapid release, obtainable combining chitosan and xanthan gum in a ratio 4:1. This is the ratio that have been used in the realization of the commercial product Lesstat Forte® (Medibase s.r.l., Prato Italy). Each polymer ratio was loaded with a single active component, i.e. RYR or AC, or a mixture of them.

3.2 ANTI HMG-COA REDUCTASE ACTIVITY

Monacolin K from RYR can reduce blood cholesterol thanks to its ability to inhibit HMG - CoA reductase, an enzyme that catalyzes the conversion of 3-hydroxyl-3-methylglutaryl CoA to mevalonate. When the enzyme is inhibited the production of cholesterol is inhibited. This activates a

family of transcription factors that induce the expression levels of proteins involved in the cholesterol biosynthesis and cholesterol uptake from extracellular environment such as low-density lipoprotein (LDL) receptor (LDLR). The elevation of hepatic LDLR expression levels facilitates the uptake of cholesterol from the blood circulation, which leads to the reduction of blood LDL cholesterol (LDL-C) level and disposal of cholesterol [8]. The effect of the presence of Annurca Complex (AC) on the RYR inhibiting action against HMG-CoA reductase was evaluated in both prolonged (C1 and C3) and rapid formulations (C4 and C6). After 3h of permanence in digestion fluid, formulations C3 and C6 resulted more active than the corresponding formulations C1 and C4. Indeed, we can see that either in formulations characterized by a prolonged release (C1-C3) or in formulations characterized by a delayed release (C4-C6) a significant higher activity against HMG-CoA reductase enzyme was observed in the presence of AC, i.e. C6 resulted more active than C4 and C3 resulted more active than C1, despite both formulations C3 and C6 contained a lovastatin amount of 3 mg against 10 mg loaded in formulation C1 and C4. The different polymer ratio (C3 vs C6 and C1 vs C4) did not affect the inhibition activity versus HMG-CoA reductase. Interestingly, after 5h in the digestion fluid, some effect of the polymer ratio can be observed recording a slightly higher activity for formulation C6 than for formulation C3, Figure 1. No significant difference was found after 24 hours. When only AC was present (formulations C2 and C5) no significant action was found against the enzyme.

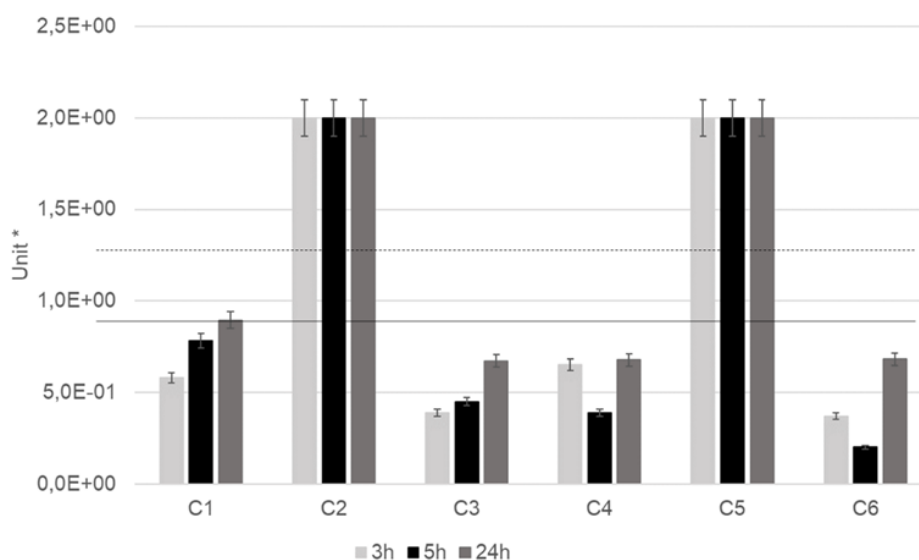
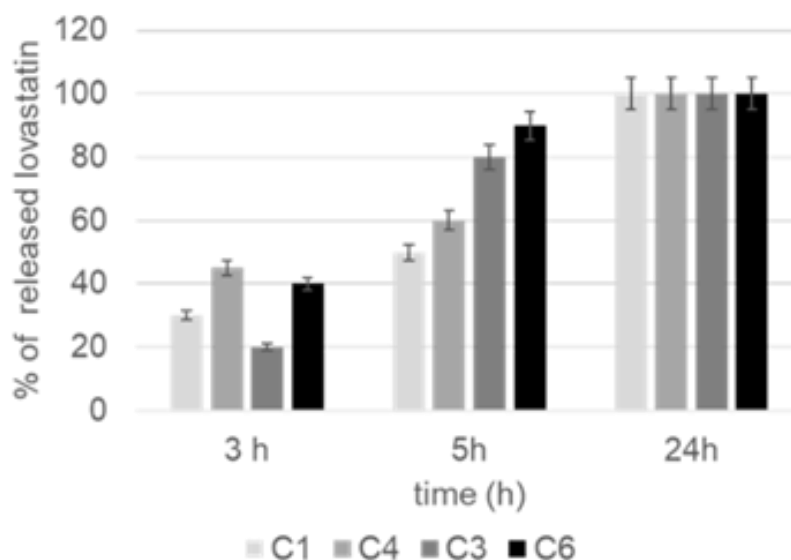
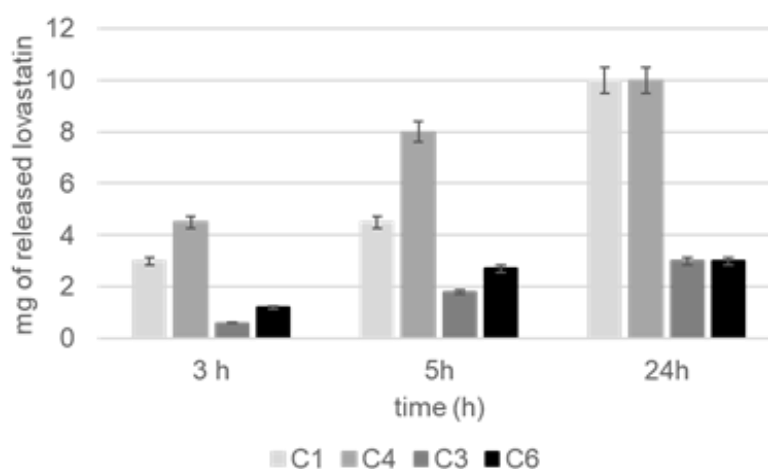


Figure 1: Inhibitory activity versus HMG-CoA reductase of all formulation as a function of kinetics release. One unit will convert 1.0 mmole of NADPH to NADP β per 1 minute at 37 °C. *The unit specific activity is defined as mmol/min/mg-protein (Units/mgP). The lower the value the higher the inhibiting action. Continuous line: aliquots obtained after digestion of two tablets of Rosuvastatin 5 mg; dotted line: aliquots obtained after digestion of one tablet of Rosuvastatin 5 mg).

The higher activity could be related to the capability of AC to enhance lovastatin release from RYR. The lovastatin profiles from tested formulations were superimposable but a significant different amount of lovastatin was registered.



A)



B)

Figure 2: Release profile of lovastatin from formulations as a function of digestion time expressed as percentage of loaded lovastatin (A) and expressed as mg of loaded lovastatin (B)

As shown in Figure 2A, either after 3h or 5h the polymer ratio affects the percentage of released lovastatin ($C4 > C1$ and $C6 > C3$) accordingly with a more rapid release when Xanthan gum and chitosan are combined in a ratio 1:4. The more rapid release can be related to the absence of interaction between RYR and xanthan gum when the polymer is present at a percentage lower than 70% [6]. Analyzing the absolute quantity of lovastatin released Figure 2B we can see that there is not

a linear correlation ($r = 0.53$) between lovastatin and HMG-CoA reductase inhibition. This arises two main conclusions. First it can be concluded that 3 mg of monacolin K is sufficient to significantly inhibit the enzyme, as also observed in other studies [19]. Second, the inhibition activity is related to different compounds or different monacolins from RYR [3,19]. Finally, as shown in Figure 2b in both series of formulations a higher release of lovastatin was recorded in the presence of AC at both after 3h and 5h.

3.3 DIFFERENTIAL SCANNING CALORIMETRY (DSC)

The capability of AC to affect lovastatin release from RYR was evaluated by DSC. Thermographs of RYR, AC and a combination of RYR and AC were recorded and depicted in Figure 3.

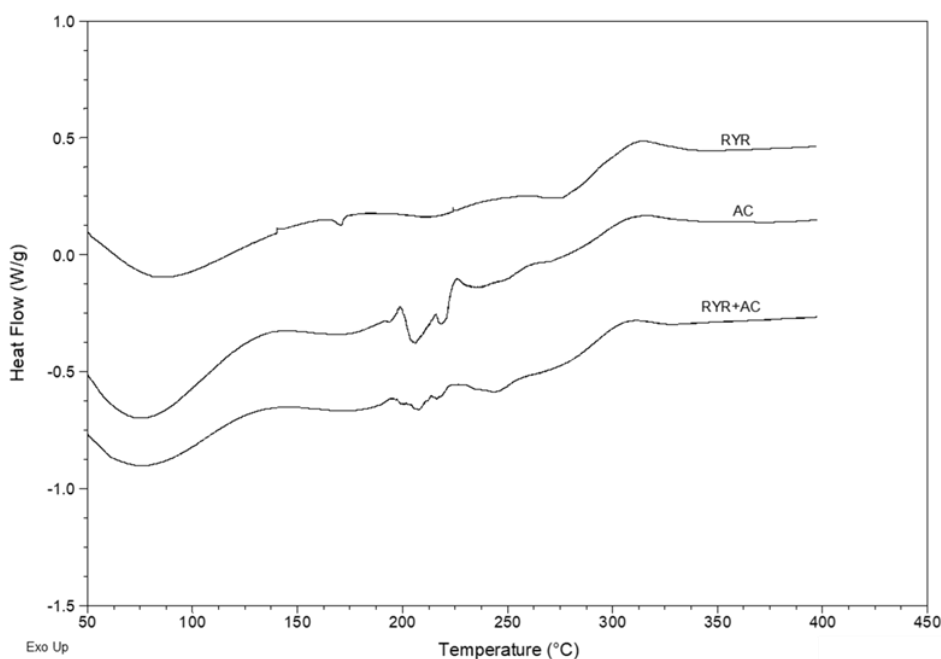
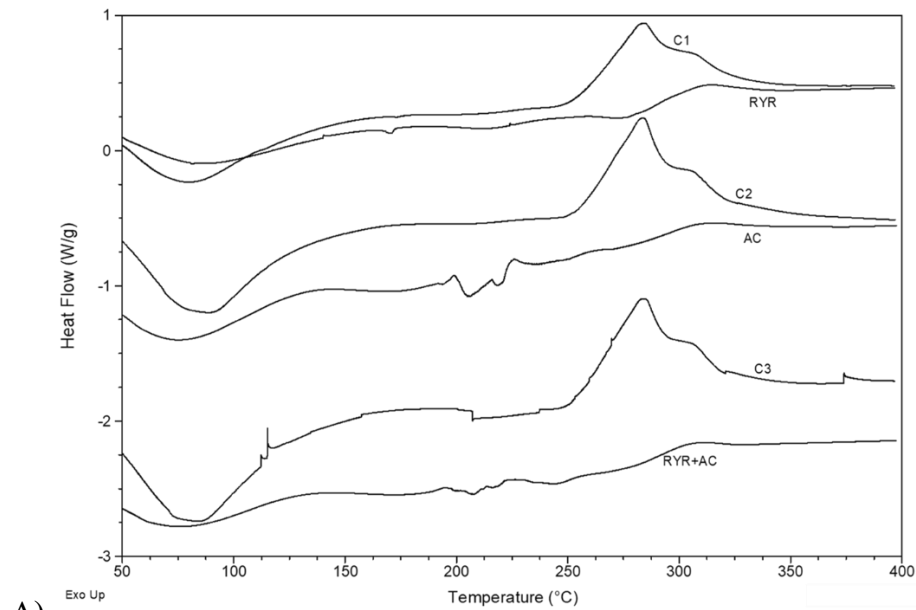
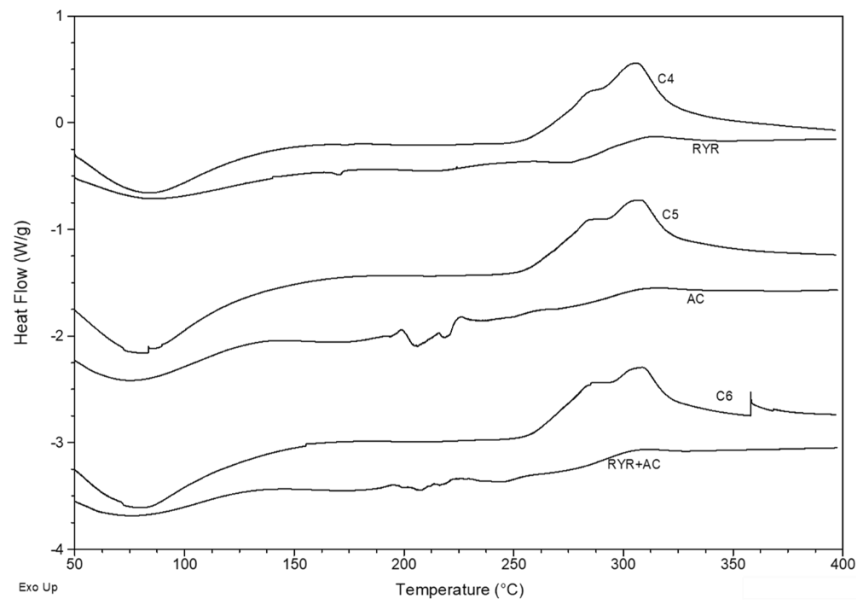


Figure 3: DSC thermographs of nutraceuticals, RYR, AC and AC + RYR.

No significant interactions can be derived between the two nutraceuticals even if the lovastatin melting point (171°C) is not evident in the thermograph of AC+RYR. AC decomposition, centered at 207°C, did not shift after combination with RYR. Thermographs of all the formulations were recorded and depicted in Figure 4.



A)



B)

Figure 4: (A) DSC thermographs of formulations C1-C3; (B) DSC thermographs of formulations C4-C6.

Comparing the first series of formulations, C1-C3 Figure 4A no significant interaction can be observed among any components. Differently, from what observed when only RYR in large amount was present [6] the presence of AC destabilizes RYR xanthan gum interactions thus favoring lovastatin release. A superimposable trend was observed for formulations C4-C6 Figure 4B. No interactions among components were found thus guaranteeing a complete release of free bioactive substances after complete digestion (24 h).

3.4 RADICAL SCAVENGING ACTIVITY

The role of oxidative stress in the development and progression of dyslipidemia is well-recognized. HDL oxidation has huge consequences on its capability to perform the reverse transport of cholesterol and on protect LDL from oxidation [20-22]. Indeed, it is well known that cholesterol accumulation is not primarily due to native LDL but instead due to the uptake of the oxidized form of LDL [23]. HDL and LDL are susceptible to lipid oxidation with consequent loss of their protective properties. Several studies have demonstrated that vitamins E and C can protect HDL from lipid oxidation with preservation of cardioprotective properties [24]. In this view, the antioxidant activity of all formulations was evaluated. The release kinetics were calculated and subsequently the antioxidant property was evaluated on the samples with respect to the DPPH[•] radical expressed in terms of EC50, i.e., the quantity of antioxidant or extract (in weight) necessary to break down 50% of the radical. Therefore, the lower the value of EC50 the higher the antiradical power. For the analyses, ascorbic acid was used as a control and the readings were carried out after 45' for all the samples. Rosuvastatin was also tested but it had no antioxidant action. EC50 values for ascorbic acid was found to be 0.08 and it resulted significantly higher than the value obtained for all the tested formulations. Among the formulations, C3 and C6 showed significantly lower values in comparison with the others, thus highlighting a very strong antioxidant activity of both RYR and AC, Figure 5. Results highlighted a synergistic effect of the two active compounds whose antioxidant activity increases when they are in combination.

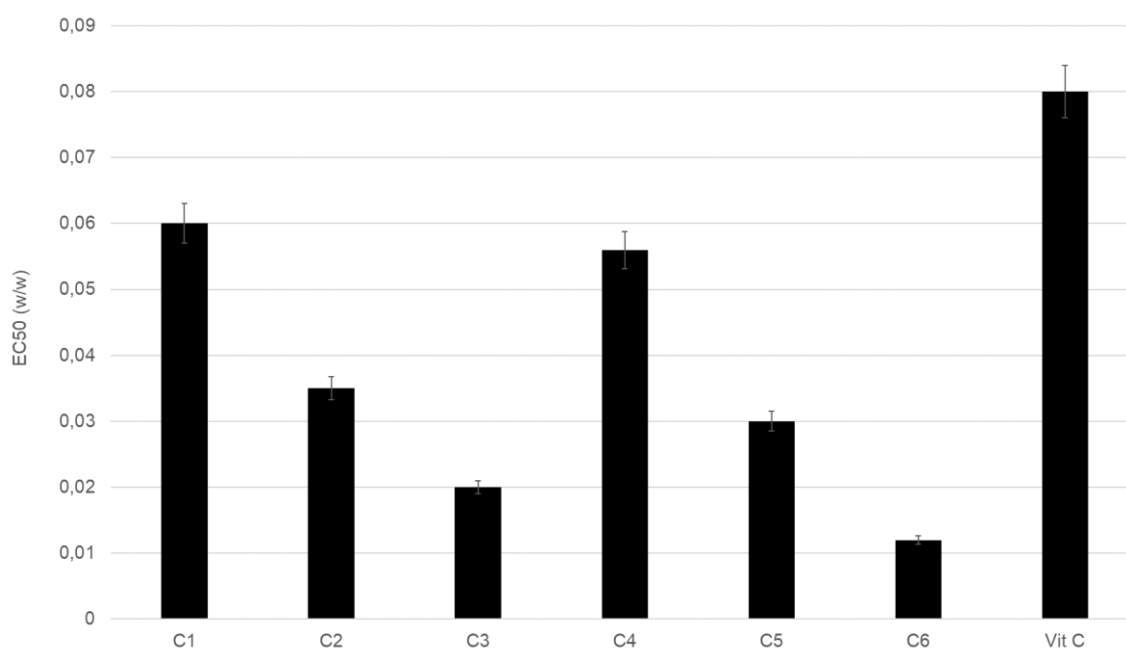


Figure 5: EC50 of all formulations for DPPH[•] free radical.

3.5 INHIBITION OF HDL AND LDL OXIDATION

Plasma lipoproteins oxidation is a key event in the development of atherosclerosis. It has been widely demonstrated that vitamins E and C reduce the oxidation of lipoproteins [24]. The ability of formulations to protect both HDL and LDL from the oxidizing action of copper ions (II) aliquots was evaluated. The results obtained, shown in Figure 6, highlighted that all formulations containing only RYR (C1 and C4), only AC (C2 and C5) and Rosuvastatin showed superimposable antioxidant activity than ascorbic acid versus LDL and HDL with a higher protecting activity to HDL. Contrarily, formulations C3 and C6, containing both RYR and AC, showed the same excellent antioxidant capacity towards both lipoproteins.

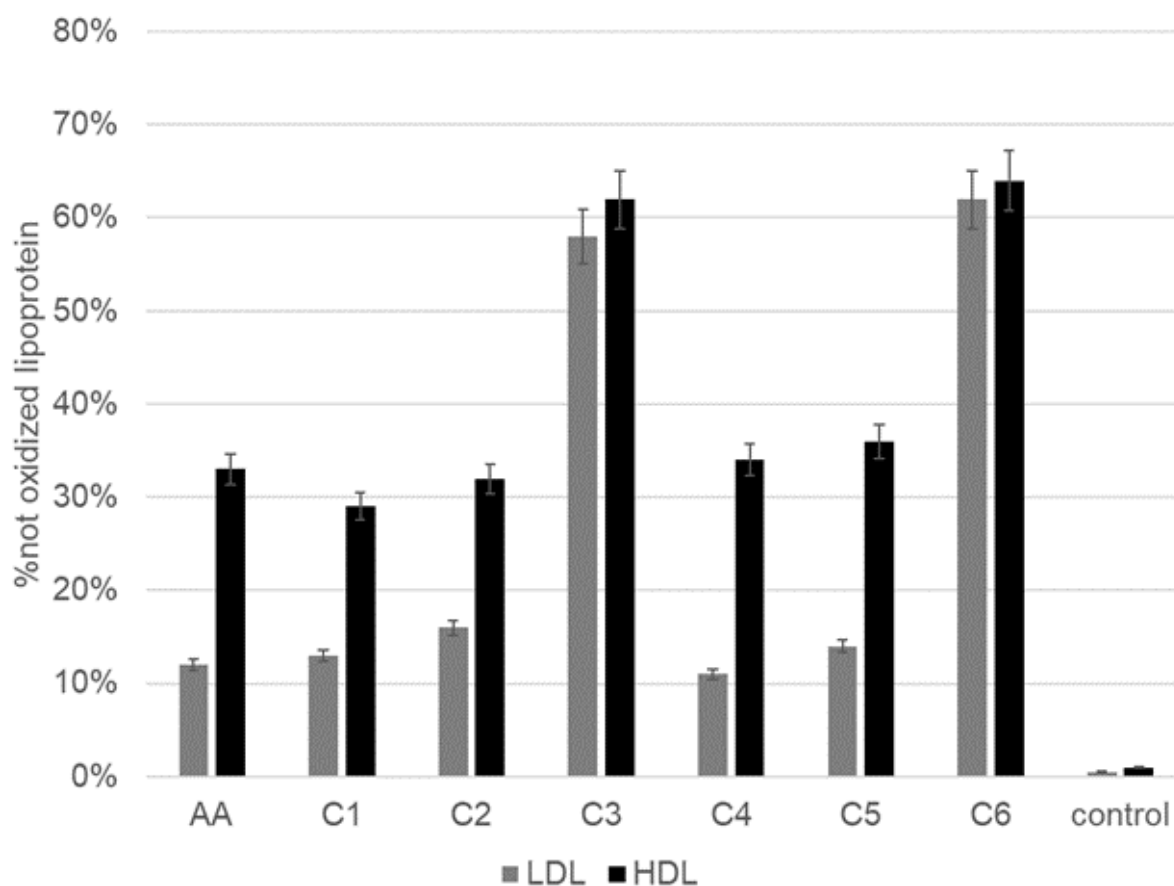


Figure 6: Percentage of not oxidized LDL (grey) and HDL (black). AA (ascorbic acid), control (absence of antioxidants).

3.6 FREE CHOLESTEROL DEPLETION

The capability of formulations to deplete free cholesterol was evaluated, Figure 7. Rosuvastatin (both 1 and 2 tablets) and formulations containing only RYR, i.e., C1 and C4, showed a superimposable low capability to bind free cholesterol reducing its concentration of about 15%. Contrarily, formulations containing only AC, thanks to the high content of procyanidins, are able to favor the stable complexation of free cholesterol [14]. Finally, formulations containing both RYR and AC showed the highest capability to deplete free circulating cholesterol, reducing its concentration of about 50%.

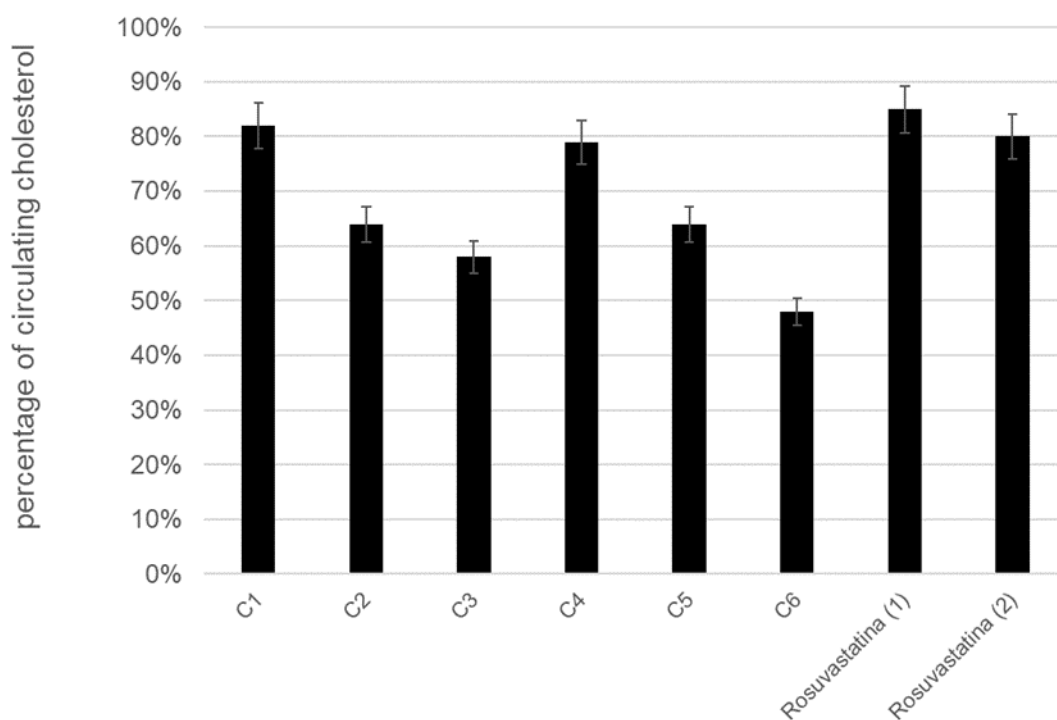


Figure 7: Percentage of free cholesterol after incubation with different formulations. Rosuvastatin (1): 1 tablet of Rosuvastatin 5mg; Rosuvastatin (2): 2 tablets of Rosuvastatin 5 mg

PART 4: CONCLUSIONS

Two series of formulations were obtained combining chitosan and xanthan gum in different percentages. The obtained formulations were loaded with RYR or AC or a combination of them to evaluate their efficacy in lowering cholesterol. The combination of Annurca apple extract and RYR showed a synergistic effect in terms of inhibition of HMG-CoA reductase, antioxidant activity towards both HDL and LDL and depleting free cholesterol. Thus, combination of phytochemical nutraceuticals with lipid lowering activity represents a valid alternative to the use of high dose of monacolin K.

BIBLIOGRAPHY

- [1] Santini A, Tenore GC, Novellino E. Nutraceuticals: A paradigm of proactive medicine. *Eur J Pharm Sci* 2017; 96: 53–61.
- [2] Monu M, Sehraw KD, Singh A, Chaudhary G, Bamal D, Sehrawat AR. An overview on the therapeutic potential and anticancer mechanism of Monacolin K / Lovastatin. *Pharmacol Res Mod Chinese Med* 2022; 5:10018.
- [3] Leone G, Consumi M, Pepi S, Lamponi S, Bonechi C, Tamasi G, Donati A, Rossi C, Magnani A. New formulations to enhance lovastatin release from red yeast rice (RYR). *J Drug Deliv Sci Technol* 2016; 36:110-9.
- [4] Leone G, Consumi M, Pepi S, Lamponi S, Bonechi C, Tamasi G, Donati A, Rossi C, Magnani A. Alginate-gelatin formulation to modify lovastatin release profile from red yeast rice for hypercholesterolemia therapy. *Ther Deliv* 2017; 8: 843-54.
- [5] Leone G, Consumi M, Franzi C, Tamasi G, Lamponi S, Donati A, Magnani A, Rossi C, Bonechi C. Development of liposomal formulations to potentiate natural lovastatin inhibitory activity towards 3-hydroxy-3-methyl-glutaryl coenzyme A (HMG-CoA) reductase. *J Drug Deliv Sci Technol* 2018; 43: 107-12.
- [6] Consumi M, Leone G, Pepi S, Tamasi G, Lamponi S, Donati A, Bonechi C, Rossi C, Magnani A. Xanthan Gum-Chitosan: Delayed, prolonged, and burst-release tablets using same components in different ratio. *Adv Polym Technol* 2018; 37: 2936-45.
- [7] Cicero AFG, Colletti A. Combinations of phytomedicines with different lipid lowering activity for dyslipidemia management: The available clinical data. *Phytomedicine* 2016; 23: 1113–8.
- [8] Chen G, Chen W, Xu J, Ma G, Hu X, Chen G. The current trend and challenges of developing red yeast rice-based food supplements for hypercholesterolemia. *J Future Foods* 2023; 3. 312-29.
- [9] Qiang Z, Lee SO, Ye Z, Wu X, Hendrich S. Artichoke extract lowered plasma cholesterol and increased fecal bile acids in Golden Syrian hamsters. *Phytother Res* 2012; 26: 1048–52.

- [10] Tenore GC, Calabrese G, Stiuso P, Ritieni A, Giannetti D, Novellino E. Effects of Annurca apple polyphenols on lipid metabolism in HepG2 cell lines: A source of nutraceuticals potentially indicated for the metabolic syndrome. *Food Res Int* 2014; 63: 252-7.
- [11] Tenore GC, Caruso D, Buonomo G, D'Urso E, D'Avino M, Campiglia P, Marinelli L, Novellino E. Annurca (*Malus pumila* Miller cv. Annurca) apple as a functional food for the contribution to a healthy balance of plasma cholesterol levels: Results of a randomized clinical trial. *J Sci Food Agric* 2017; 97: 2107-15.
- [12] Tenore GC, Caruso D, Buonomo G, D'Avino M, Ciampaglia R, Maisto M, Schisano C, Bocchino B, Novellino E. Lactofermented annurca apple puree as a functional food indicated for the control of plasma lipid and oxidative amine levels: Results from a randomised clinical trial. *Nutrients* 2019, 11, 122.
- [13] Tenore GC, Campiglia P, Stiuso P, Ritieni A, Novellino E. Nutraceutical potential of polyphenolic fractions from Annurca apple (*M. pumila* Miller cv Annurca). *Food Chem* 2012; 140: 614-22.
- [14] Tenore GC, Campiglia P, Ritieni A, Novellino E. In vitro bioaccessibility, bioavailability and plasma protein interaction of polyphenols from Annurca apple (*M. pumila* Miller cv Annurca). *Food Chem* 2013; 141: 3519–24.
- [15] Sommella E, Pepe G, Pagano F, Ostacolo C, Tenore GC, Russo MT, Novellino E, Manfra M, Campiglia P. Detailed polyphenolic profiling of Annurca apple (*M. pumila* Miller cv Annurca) by a combination of RP-UHPLC and HILIC, both hyphenated to IT-TOF mass spectrometry. *Food Res Int* 2015; 76: 466–77.
- [16] Mishra K, Ojha H, Chaudhury NK. Estimation of antiradical properties of antioxidants using DPPH assay: A critical review and results. *Food Chem* 2012; 130: 1036–43.
- [17] Cheng Z, Moore J, Yu LL. High-Throughput Relative DPPH Radical Scavenging Capacity Assay. *J Agric Food Chem* 2006; 54:7429–36.
- [18] Hillstrom RJ, Yacopin-Ammons AK, Lynch SM. Vitamin C Inhibits Lipid Oxidation in Human HDL. *J Nutr* 2003; 133: 3047–51.
- [19] Heinz T, Schuchardt JP, Möller K, Hadji P, Hahn A. Low daily dose of 3 mg monacolin K from RYR reduces the concentration of LDL-C in a randomized, placebo-controlled intervention. *Nutr Res* 2016; 36: 1162-70.

- [20] Zou J, Tian Z, Zhao Y, Qiu X, Mao Y, Li K, Shi Y, Zhao D, Liang Y, Ji Q, Ling W, Yang Y. Coenzyme Q10 supplementation improves cholesterol efflux capacity and antiinflammatory properties of high-density lipoprotein in Chinese adults with dyslipidemia. *Nutrition* 2022; 101: 111703.
- [21] Salamat S, Sharif SS, Nazary-Vanani A, Kord-Varkaneh H, Clark CCT, Mohammadshahi M. The effect of green coffee extract supplementation on serum oxidized LDL cholesterol and total antioxidant capacity in patients with dyslipidemia: A randomized, double-blind, placebo-controlled trial. *Eur J Integr Med* 2019; 28: 109-13.
- [22] Raveh O, Pinchuk I, Fainaru M, Lichtenberg D. Kinetics of lipid peroxidation in mixtures of HDL and LDL, mutual effects. *Free Radic Biol Med* 2001; 31: 1486–97.
- [23] Steinberg D. Low Density Lipoprotein Oxidation and Its Pathobiological Significance. *J Biol Chem* 1997; 272: 20963–6.
- [24] Nadeem N, Woodside JV, Kelly S, Allister R, Young IS, McEneny J. The two faces of α - and γ -tocopherols: an in vitro and ex vivo investigation into VLDL, LDL and HDL oxidation. *J Nutr Biochem* 2012; 23: 845–51.

**CHAPTER II:
POLYMERIC FRAMEWORKS
FOR DRUG DELIVERY**

**CALCIUM IONS HYALURONAN/GELLAN GUM
PROTECTIVE SHELL FOR DELIVERY OF OLEUROPEIN
IN THE KNEE**

PART 1: INTRODUCTION

Bioactive compounds, such as essential oils, polyphenols, or carotenoids, are substances derived from plant sources with the capability of exerting good effects on health [1]. Nevertheless, the maintenance of their activity is strictly bound to an efficient delivery to the action site. The encapsulation technology can be considered as the gold standard technology for achieving this goal. As reported by Canizales et al. [2], encapsulation permits to entrap bioactive principles within an immiscible vehicle able to protect and deliver the substance. Different vehicles, as liposomes [3–5] or polymeric complexes [1, 6, 7], can be used according to hydrophilicity, stability, and bioavailability of bioactive compounds.

One of the most studied bioactive substances is oleuropein, the most effective polyphenol in the olive leaves. It shows several nutritional and medicinal properties [8, 9]. Recently, it has been demonstrated that oleuropein protects against collagen II-induced arthritis in mice [10]. Mao et al. verified that oleuropein, causing a significant down-regulation of NO, COX-2, iNOS, cytokines IL-6 and TNF- α , has not only an anti-inflammatory action but is also able to exert analgesic and sedative effects both *in vitro* and *in vivo* [11]. Starting from that, we conjectured that entrapping oleuropein inside a compatible viscosupplement could permit its delivery inside the knee without losing its antioxidant activity and exploiting its analgesic effect against the strong pain associated with injection. Generally, a significant lack of bioavailability *in vivo* is found using the active principle instead of its original biocomplex, as already observed for other phytotherapeutics, [12, 13]. Consistently, the aim of this study is to encapsulate a vegetal bioactive matrix rich in oleuropein in a stable vehicle avoiding strong interactions between the vegetal complex and the polymeric shell to not affect the release or the activity of oleuropein.

The vegetal bioactive matrix rich in oleuropein was entrapped into calcium ions crosslinked gellan gum and hyaluronan formulations. Different polysaccharide ratios were tested, and the release kinetics and antioxidant activity of oleuropein were evaluated. Infrared spectroscopy and thermal analysis were performed to verify the absence of significant interactions between the polysaccharide shells and the bioactive matrix, thus guaranteeing a burst release of oleuropein. The adequate mechanical performance of the systems for the foreseen application as viscosupplement was also verified. Cytocompatibility of developed systems toward fibroblasts and human chondrocytes was assessed.

PART 2: MATERIALS AND METHODS

2.1 MATERIALS

Gellan Gum (Phytigel™, 1,000 kg/mol; low acylation degree) was purchased from Sigma-Aldrich (Milan, Italy). Hyaluronan sodium salt (HA) was kindly provided from SIFI S.p.A (MW: 2.0 MDa) (Italy). All chemicals and reagents used are of analytical grade.

2.2 MATRICES PREPARATION

Bioactive matrix (BM) containing oleuropein (60% w/w) was obtained by conventional maceration extraction from olive leaves and purification following the procedure reported by Tamasi et al. [14]. Briefly, samples of powdered olive leaves (1.0 g) were ultrasound assisted extracted by a hydro-alcoholic mixture (C₂H₅OH/H₂O, 80/20%, v/v): first extraction 5 mL, second and third extractions 2.5 mL, for 10 mL total volume of extraction. The extract was dried under nitrogen flow and then lyophilized, [14]. The procedure was repeated three times to achieve an adequate amount of BM.

A 0.1% w/v gellan gum (GG) solution was prepared in deionized water at 90°C. Once dissolved, the solution was cooled to room temperature under strong stirring to avoid gelation and BM added to the solution in an amount that was 50% w/w of the dried mass of the GG. HA 1% w/v solution was prepared by dissolving the polymer in bidistilled water. 0.5 M calcium chloride solution (10 mL) was added to HA solution. Then, GG solution containing BM were dropped into stirred HA solution using 10 mL syringe (needle G 20) at room temperature following the procedure reported by Das et al. [15]. Stirring was maintained to avoid the formation of beads. A semi-solid 3D matrix formed instantly. Then, it was filtered, washed, and freeze-dried. After lyophilization, sponge-like cylindrical matrices were obtained (5.0 cm ± 1.0 cm x 2.0 cm ± 0.5 cm). The remaining solution was dialyzed against water to quantify the unloaded oleuropein and to verify the absence of free HA. Different batches were prepared by changing the formulation composition.

2.3 INFRARED ANALYSIS (ATR-FTIR)

FTIR spectra of pristine polysaccharides and loaded and unloaded matrices in dry state were recorded using a FTIR spectrophotometer (NICOLET iS50FT-IR Thermo, USA), in the range $4,000\text{ cm}^{-1}$ – 750 cm^{-1} with a resolution of 2 cm^{-1} . Spectra were subjected to a spectral deconvolution process to improve the observability of the overlapping bands as reported in Bonechi et al.[16].

2.4 THERMOGRAVIMETRIC ANALYSIS (TGA)

TGA was used to test the thermal stability of polymeric systems, the analysis was performed using SDT-Q600 (TA Instruments, USA), following the procedure reported in Tamasi et al.[17]. Briefly, 10 mg of each sample (n=3) was put in a platinum crucible and heated from 30°C to 900°C , with a heating ramp of $10^{\circ}\text{C}/\text{min}$, under nitrogen flow.

2.5 DIFFERENTIAL SCANNING CALORIMETRY (DSC)

DSC was used to measure the thermal behavior of the polysaccharides' matrices; the thermographs were recorded using Q1000 calorimeter (TA instruments). 5mg of each sample (n=3) were sealed in an anodized aluminum hermetic pan and heated from 30°C to 300°C , with a heating rate $10^{\circ}\text{C}/\text{min}$. under nitrogen flow, [18].

2.6 RHEOLOGICAL ANALYSIS

All rheological analyses were performed at 37°C using a Discovery HR-2 Rheometer (TA Instruments), equipped with a plate-plate geometry ($\varnothing = 4\text{ cm}$): full swollen matrices in NaCl 0.9 % w/v were tested following a procedure already reported and finalized to characterize materials for the foreseen application as viscosupplement [19]. Briefly, Linear Viscoelasticity Region (LVR) was identified by strain-sweep tests varying material strain in the range 0.1 % – 10 % while maintaining fixed oscillation frequencies (i.e., 0.1 Hz, 1 Hz and 10 Hz). Elastic and viscous moduli in shear mode (G' and G'') of samples under a fixed oscillation strain of 0.2%, were measured as a

function of oscillation frequency in the range 0.1 Hz–10 Hz. A superimposable measure was done after the passage of swollen hydrogels through a syringe (G 16 needle) to verify their injectability. This property was also verified following the procedure described by Chen et al. [20] with slight modification. Briefly, strain sweep loop procedure was performed, starting from 0.2 % to 30 % at 1 Hz with a conditioning time of 5 s, and 10 points per decade were applied to materials. Then, the oscillation strain was decreased to the initial value, following the same procedure. All measurements were done in triplicate.

2.7 ASSESSMENT OF *IN VITRO* OLEUROPEIN RELEASE

The release profile of oleuropein from matrices was assessed following the procedure reported by Yang et al., [21]. Briefly, 50 mg of samples (n = 3) were dipped in 10 mL of physiological solution (0.9 % w/v in NaCl) and incubated at 37°C. The oleuropein released by the systems was quantified measuring the absorbance at 280 nm every 5 minutes until the release plateau, using a Lambda 25 (Perkin-Elmer) UV-Visible spectrophotometer.

2.8 FREE RADICAL SCAVENGING ACTIVITY (RSA)

The radical scavenging activity of released oleuropein was quantified following a previously reported method, [22], with some modifications [14]. Briefly, a stock solution of DPPH[•] (0.10 mM in CH₃OH) was prepared. A known volume of DPPH[•] solution was treated with Trolox standard solutions or a known amount of extract (diluted, if necessary). After 15 min of incubation, the absorbance at 517 nm was recorded by a dual-beam (against physiological solution) UV-Perkin Elmer Lambda 25 (optical pathway, 10 mm; cuvettes, PMMA/UV grade). The quenching percentage was calculated using Equation 2.

$$\Delta\text{Abs}_{517} \% = \left(1 - \frac{\text{Abs}_{\text{sample}}}{\text{Abs}_{\text{blank}}} \right) \times 100$$

Equation 2

Ab_{sample} corresponds to the absorbance of the radical solution treated with standards or samples, Ab_{blank} corresponds to absorbance of the not treated radical solution. All measurements were performed in triplicate.

2.9 *IN VITRO* CELL VIABILITY

Cytotoxicity of selected hydrogels against NIH3T3 mouse fibroblasts was evaluated applying the direct contact tests (ISO 10995-5: Biological evaluation of medical devices—Part 5: Tests for cytotoxicity: in vitro methods) which are adequate for testing any kind of sample. Fibroblasts viability was quantified by Neutral Red uptake (NRU) test after 24 h of incubation, reading the absorbance at 540 nm (UV/visible spectrophotometer, Lambda 25, Perkin Elmer).

Human chondrocytes were propagated following the standardized procedure previously reported [19]. Human chondrocytes viability and proliferation after 1, 3 and 5 days of incubation was quantified by NRU test after 24 h of incubation, reading the absorbance at 540 nm (UV/visible spectrophotometer, Lambda 25, Perkin Elmer).

2.10 STATISTICAL ANALYSIS

One-way ANOVA was used for multiple comparisons. Individual differences were tested by Fisher's test after the demonstration of significant intergroup differences by ANOVA and considered significant with $p < 0.05$.

PART 3: RESULTS AND DISCUSSION

3.1 MATRICES PREPARATION

GG and HA were combined in three different ratio and loaded with a fixed amount of the BM (Table 2).

Table 2: Polymeric matrices' composition.

SAMPLE ID	COMPOSITION (mM)			
	GG	HA	Ca	OL ⁽¹⁾
GGHA11CaBM	1	1	5	6×10^{-2}
GGHA12CaBM	1	2	5	6×10^{-2}
GGHA21CaBM	2	1	5	6×10^{-2}
GGHA11Ca	1	1	5	-
GGHA12Ca	1	2	5	-
GGHA21Ca	2	1	5	-
GGHA	1	1	-	-

⁽¹⁾Quantified starting from 50 mg of BM containing 60% of OL

GG: gellan gum; **HA:** hyaluronan; **Ca:** calcium ions; **OL:** oleuropein .

3.2 INFRARED ANALYSIS (ATR-FTIR)

IR spectra of native polysaccharides were recorded and compared with calcium ions crosslinked systems. Being HA and GG made of similar functional groups, both their IR spectra show a broad band due to intermolecular bonded OH stretching (3340 cm^{-1}) as well as a double band related to asymmetric and symmetric stretching of C–H groups (2920 cm^{-1} – 2850 cm^{-1}). Also, the bands centered at 1610 cm^{-1} and 1404 cm^{-1} , due to asymmetric and symmetric stretching of anionic carboxyl group, and the bands centered at 1145 cm^{-1} , 1077 cm^{-1} and 1044 cm^{-1} , due to hemiacetalic system C – O – C of saccharidic unit, are evident in both spectra. HA spectrum differs from that of GG for the presence of a shoulder centered at 1562 cm^{-1} , due to amidic NH bending. The corresponding amidic C = O band is present ($1,650 \text{ cm}^{-1}$), [23]. IR spectrum of calcium ions crosslinked system is superimposable to bare polysaccharides spectra as no new functional groups are added. Nevertheless,

anionic carboxyl group symmetric stretching band shifted from 1404 cm^{-1} to about 1420 cm^{-1} confirming an involvement of carboxylate groups in calcium ions coordination, as already verified for other bivalent ions, [24], Figure 1A. The broad band centered at 1630 cm^{-1} was deconvolved and compared with that of a mixture of the two polysaccharides without calcium ions. Deconvolution indicated that the large band in GGHA + Ca spectrum derives by the combination of two bands, one centered at 1650 cm^{-1} due to OH bending and a band centered at 1602 cm^{-1} due to asymmetric anionic carboxyl groups, Figure 1B. On the contrary, GG and HA mixture without calcium ions shows asymmetric anionic carboxyl groups band centered at 1608 cm^{-1} , Figure 1C. The slight shift toward lower wavenumbers (from 1608 cm^{-1} to 1602 cm^{-1}) confirmed the involvement of the functional group in calcium ions coordination, [24]. Finally, both mixture and crosslinked systems were acidified by HCl 0.1 M and IR spectra recorded. No significant increase of carboxylic acid C = O group band (1731 cm^{-1}) was observed in the presence of calcium ions, whereas a significant increase of that band was observed in IR spectrum of polymer mixture, Figure 1D.

IR spectra of BM loaded and unloaded matrix are depicted in Figure 1E. The presence of BM was confirmed by the shoulder at 1711 cm^{-1} [8] that is present in BM and loaded matrix spectra. Nevertheless, the presence of BM and the effective crosslinking of HA and GG were further analyzed by thermal analysis.

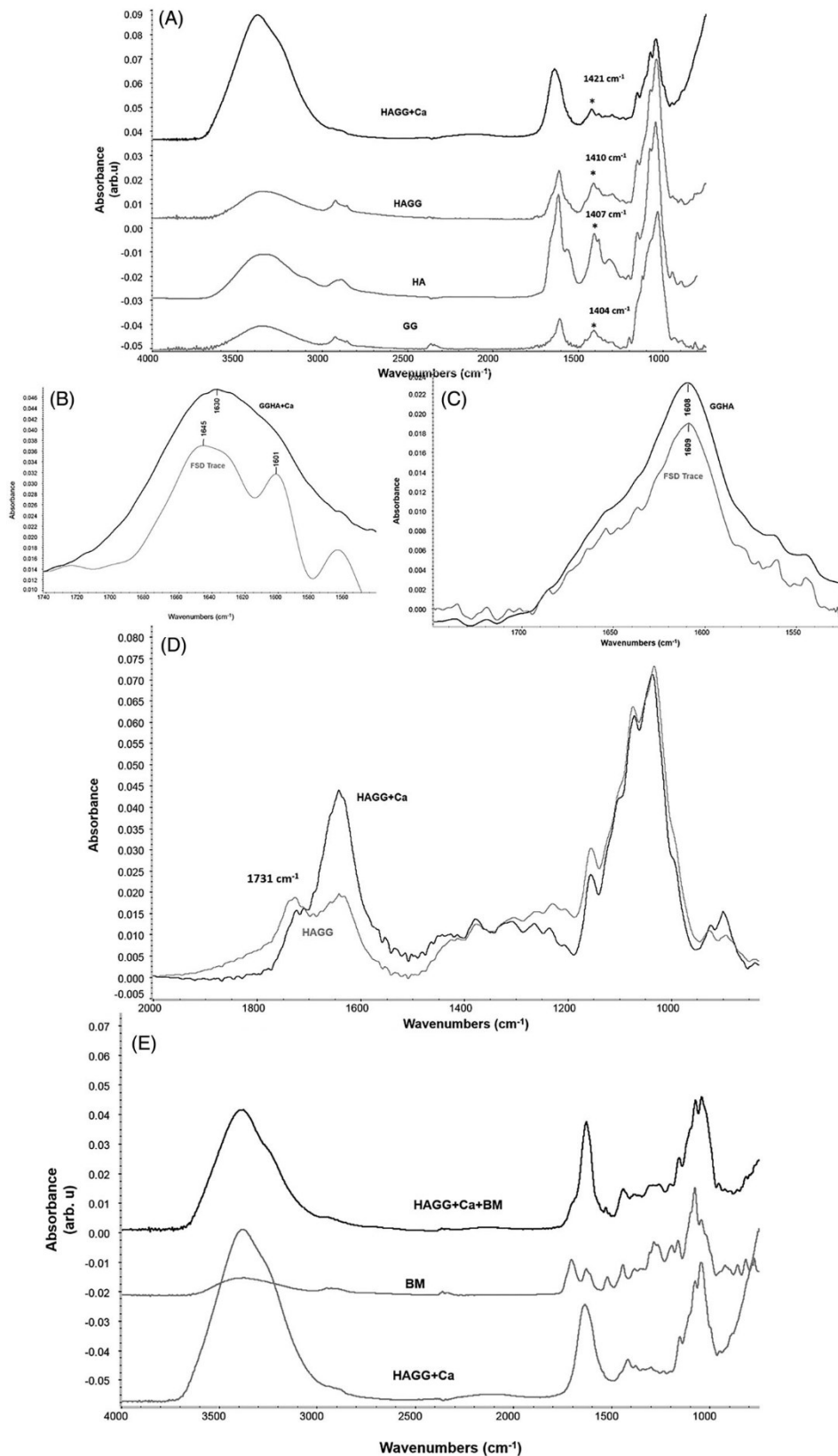


Figure 8: Infrared spectra of (A) comparison among pristine HA and GG polysaccharides spectra and physical and calcium ions added mixtures of them; (B) GGHA + Ca matrix deconvoluted 1630 cm^{-1} band; (C) GGHA physical mixture deconvoluted 1630 cm^{-1} band; (D) IR spectra of GGHA with and without Ca^{2+} ions after acid treatment; (E) Comparison between unloaded and BM loaded GGHA11Ca matrices. Spectrum of BM is also depicted.

3.3 THERMOGRAVIMETRIC ANALYSIS

Thermogravimetric analysis confirmed the crosslinking reaction. All matrices and native polysaccharides were heated from room temperature to 900°C, to completely degrade the organic compounds and obtain the remaining calcium oxide. A significant difference ($p < 0.05$) was found comparing the weight loss of native and crosslinked polysaccharides. Indeed, a lower weight loss was found for crosslinking systems that showed a mean total loss of about 70% against 85% – 90% weight loss for bare components, Table 3. A further confirmation of the crosslinking process can be obtained calculating R that is the ratio between the weight loss in the 200°C – 400°C temperature range and the weight loss in 400°C – 600°C range, [25]. In the former, we obtain the loss of free chains whereas in the latter the loss of condensed matter is mainly observed. R can be used as a measure of the structuring of a material after any treatment. Indeed, the lower R, the higher the compaction of the analyzed matrix. After crosslinking, R decreases of about 40% as shown by values reported in Table 3. A significant difference ($p < 0.05$) was found in the first temperature range weight loss (30°C – 120°C) that is related to water loss. Starting from bare polysaccharides a quite high weight loss is found, with HA showing 9.1% of weight loss against GG that shows only 6.8% loss. When they are mixed together without calcium ions a slight increase in the water absorption is found with an increase up to 12%, Figure 9A. When a stable 3D network is formed, it absorbs a significant higher amount of water ($p < 0.05$) that remains strictly bound to the structure also after drying the matrix by lyophilization. All 3D networks show a mean weight loss in the 30°C – 120°C range of about 25%.

The presence of calcium ions does not significantly affect the temperature at which the highest weight loss is observed ($p > 0.05$). Contrarily, the presence of BM provokes a shift in the region 200°C – 400°C as shown by the thermographs depicted in Figure 9B.

Table 3: TGA of the prepared matrices and of the native polysaccharides and bare leaves extract.

Sample ID	Weight Loss (%)								Tot. Weight Loss (%)	
	30°C – 120°C		120°C – 200°C		200°C – 400°C		400°C – 600°C		R	30°C – 900°C
GG	6.7	± 0.2	1	± 0.2	56	± 1	14	± 2	4	92 ± 2
HA	9.1	± 0.2	0.7	± 0.2	50	± 1	6.5	± 0.2	8	83 ± 2
GGHA	12	± 1	0.7	± 0.1	56	± 1	16	± 1	4	99 ± 1
BM	2.3	± 0.4	1.4	± 0.2	50	± 2	14	± 2	-	81 ± 2
GGHA11CaBM	27	± 1	6.4	± 0.3	17	± 2	6.6	± 0.3	3	67 ± 4
GGHA12CaBM	25	± 1	5.3	± 0.1	22	± 3	7.4	± 0.4	3	70 ± 2
GGHA21CaBM	24	± 1	4.2	± 0.5	20	± 1	7	± 0.3	3	68 ± 4
GGHA11Ca	24	± 1	6.8	± 0.2	20	± 1	5.1	± 0.2	4	64 ± 3
GGHA12Ca	28	± 1	5.3	± 0.4	19	± 1	6.5	± 0.1	3	68 ± 2
GGHA21Ca	27	± 1	4	± 0.5	21	± 1	8.1	± 0.3	3	74 ± 2

Data were reported as % mean value (n = 3); R is the ratio between the weight loss in the 200°C – 400°C and 400°C – 600°C range.

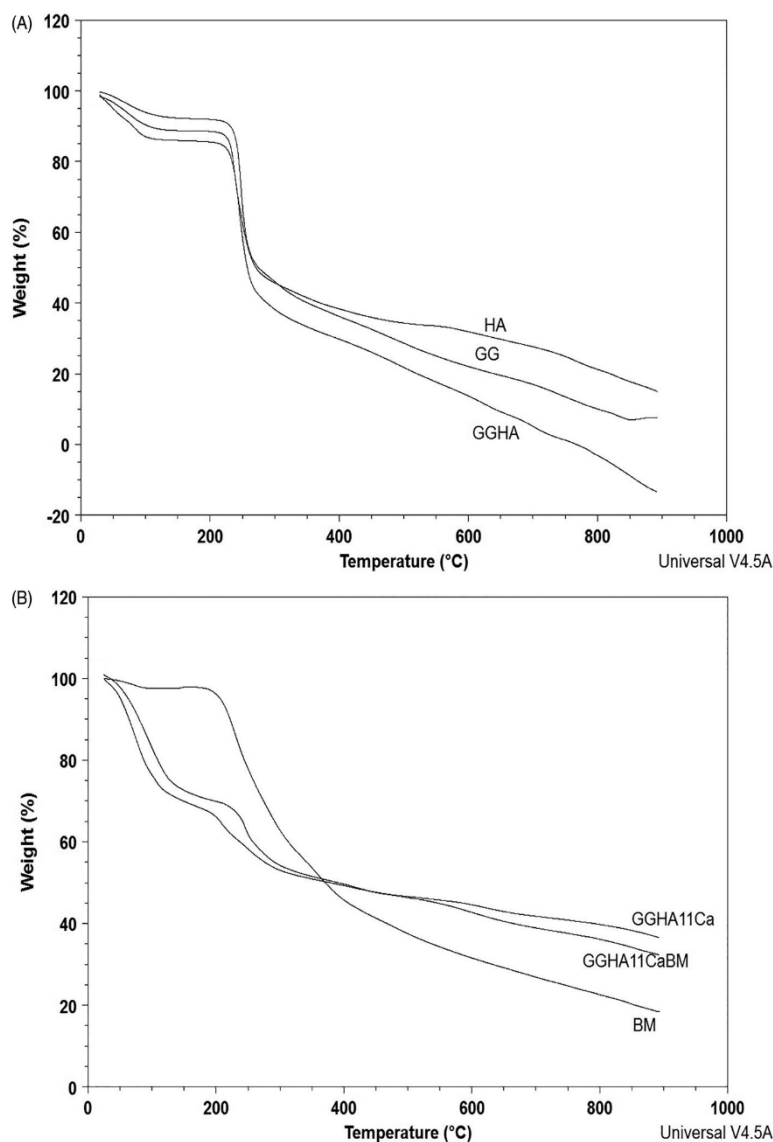


Figure 9: (A) Thermographs obtained plotting the weight (%) versus temperature of native polysaccharides HA and GG and a physical mixture of them (GGHA); (B) Thermographs obtained plotting the weight (%) versus temperature of unloaded and BM loaded GGHA11Ca matrices. A Thermograph of BM is also depicted.

3.4 DIFFERENTIAL SCANNING CALORIMETRY

DSC has been largely used to determine the interaction between mixture components [26], and the thermal behavior of the matrices. When a homogeneous phase is present, a single transition can be observed, [27]. The DSC curves of GGHA, GGHA11Ca, GGHA11CaBM and BM samples are shown in Figure 10A. The presence of calcium ions significantly affects the melting/decomposition temperature of the mixtures as shown by the shifting of the wide endothermic peak assigned to thermal transition of polysaccharidic systems toward higher temperatures. Moreover, the presence of

a single band confirms the obtainment of a single material with both polysaccharide components strictly joined, as also observed by Hezma et al. for other polymers [27]. Indeed, the broad asymmetric endothermic curve suggests the presence of different substances whereas pure polysaccharides are characterized by sharp melting endotherms, Figure 10B. Similarly, the presence of BM, that despite the presence of oleuropein cannot be detected as also observed by Nassir et al. [28] in their formulations, increased the melting temperature of the system of 8°C.

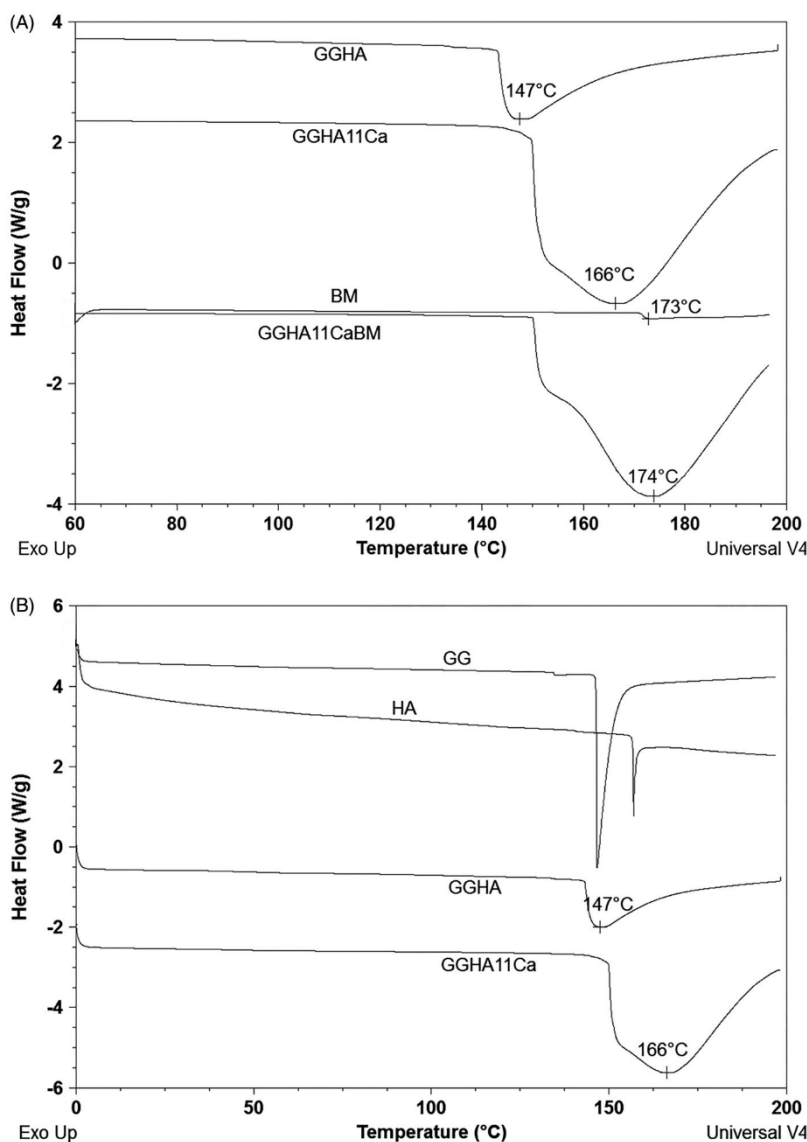


Figure 10: (A) DSC curves of physical mixture of polysaccharides (GGHA) and unloaded and BM loaded GGHA11Ca matrices. DSC curve of BM is also depicted as comparison; (B) Comparison of DSC curve of pristine polysaccharides (GG and HA) and their physical and calcium ions added mixtures.

3.5 RHEOLOGICAL ANALYSIS

Rheological properties were measured to examine mechanical stability of the developed formulations. Parameters were set to verify their performance as viscosupplement. The mechanical response of formulations, in terms of elastic and viscous components, as a function of oscillation frequency was analyzed, and the relative mechanical spectra depicted in Figure 11A. All formulations exhibit an elastic modulus higher than the viscous one ($G' > G''$), thus confirming their mechanical stability. G' and G'' values are strictly related to polysaccharides ratio. This can be explained with the different interaction between GG and HA with calcium ions. Indeed, HA can strongly self-associate and bind water molecules giving a stiff viscous system, like gelatin, [29]. This strong self-healing capability hinders the interaction with calcium ions in comparison with GG. So, when HA is present in a double amount in respect to GG the obtained hydrogel has significantly lower mechanical properties, that are strongly related to the capacity of different polysaccharides to bind calcium ions as also verified by Nickerson and Paulson in their study on gellan, k-carrageenan and alginate, [30]. However, all formulations show higher mechanical properties than natural synovial fluid. As reported by Fakhari and Berklund, [29], G' of human synovial fluid decreases from 23 Pa to 7 Pa in the presence of osteoarthritis or because of ageing. To counteract this irreversible process, when viscosupplementation is necessary, it appears preferable to use systems with increased rheological performance in terms of both G' and G'' to reduce the number of injections. Both GGHA12CaBM and GGHA21CaBM show a compatible rheological stiffness. Complex modulus of developed systems was monitored as a function of increasing and decreasing oscillation strain following the procedure described by Chen et al., [20], to confirm the injectability of the systems. The dependence of G^* by oscillation strain is depicted in Figure 11B.

Table 4: Elastic and viscous moduli values in shear mode at 2.5 Hz.

Sample ID	G' (Pa)			G'' (Pa)		
Healthy synovial fluid [29]	23			7		
Orthovisc TM [29]	60			46		
Synvisc TM [29]	111	±	13	25	±	2
GGHA11CaBM	1298	±	33	163	±	16
GGHA11CaBM_post injection	1264	±	29	158	±	14
GGHA21CaBM	723	±	22	128	±	12
GGHA21CaBM_post injection	643	±	32	126	±	8
GGHA12CaBM	284	±	9	35	±	4
GGHA12CaBM_post injection	275	±	10	37	±	2

All systems show the ability to reduce their viscosity by applying shear and immediately resume their consistency when the mechanical load is taken off, behaving as self-healing gels. Nevertheless, the high G^* value of GGHA11CaBM could provoke a painful injection, thus limiting its applicability. Swollen samples were injected through a syringe (16 G needle) and their G' and G'' moduli were recorded, to confirm the injectability. G' and G'' values at 2.5 Hz before and after the injection are summarized in Table 4.

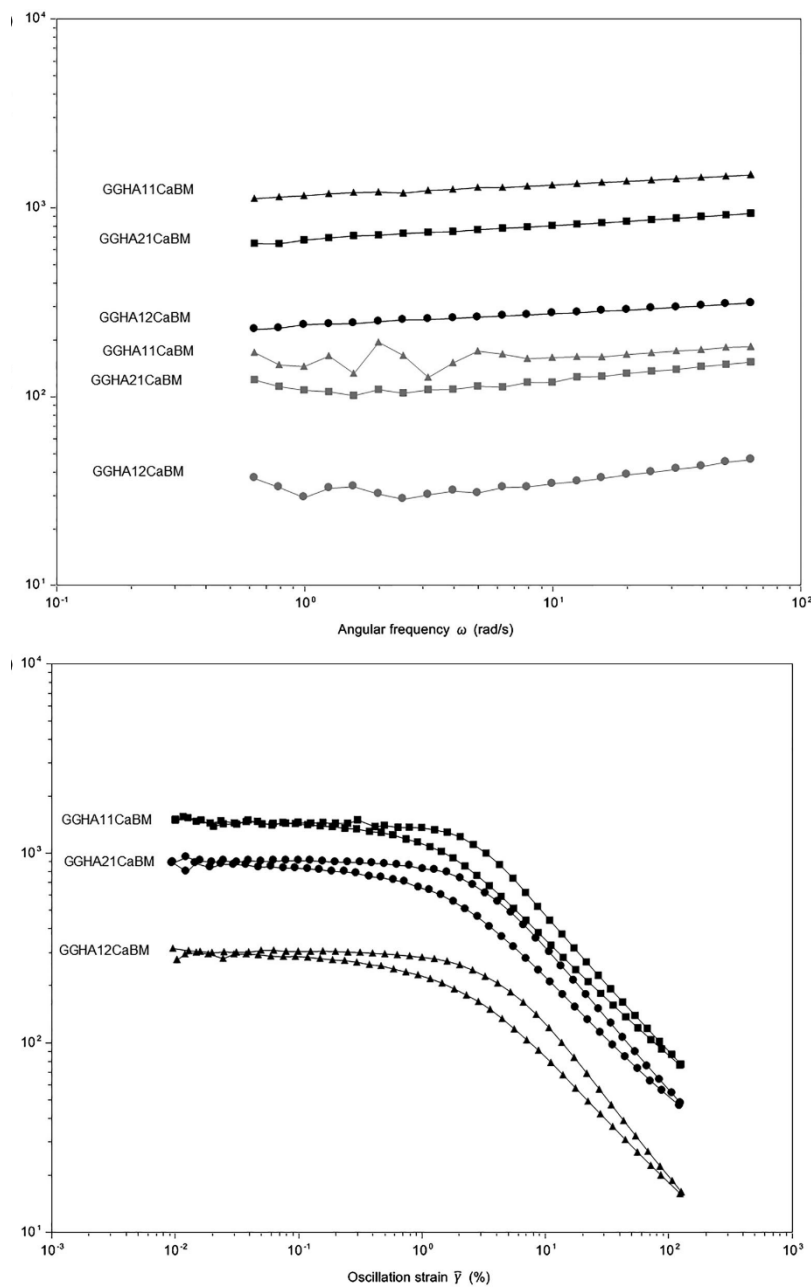


Figure 11: (A) Elastic Shear Modulus (G' - black) and Viscous Shear Modulus (G'' - grey) curves of loaded matrices hydrogels in the frequency range 0.1–10 Hz; (B) Complex modulus G^* ($G^* = |G' + iG''|$) as a function of increasing and decreasing oscillation strain.

3.6 ASSESSMENT OF *IN VITRO* OLEUROPEIN RELEASE

Kinetics release of oleuropein from matrices was assessed in pseudo-static condition since the knee compartment is characterized by very slow flow. Initial oleuropein content was determined by difference as reported before. GGHA21CaBM contained $0.33 \text{ mg} \pm 0.02 \text{ mg}$ of oleuropein for mg of dry matrix which decreased to $0.25 \text{ mg} \pm 0.03 \text{ mg}$ for mg of dry matrix in GGHA12CaBM and GGHA11CaBM matrices. We found a burst release of oleuropein in the first 30 minutes, regardless of the polysaccharides ratio, Figure 12, differently from results of Czapoet al. for their hyaluronan-based formulations [31]. This quick release could be useful for the foreseen application since being promptly released can counteract the pain associated with the injection. The release kinetics from GGHA12CaBM was not quantified for the immediate disaggregation of the matrix so a complete release was obtained at $t = 0$. Consequently, it was discarded for subsequent analyses.

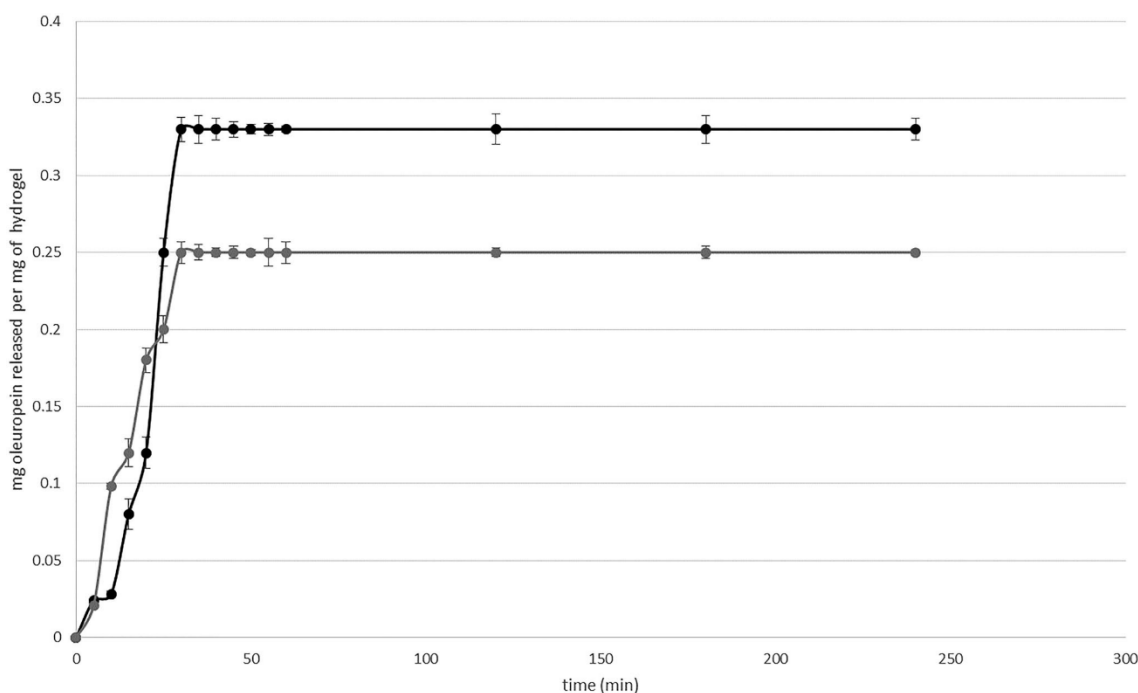


Figure 12: Release profiles of oleuropein from GGHA11CaBM (grey) and GGHA21CaBM (black).

3.7 FREE RADICAL SCAVENGING ACTIVITY (RSA)

The antioxidant activity of oleuropein released from polysaccharidic shells containing BM, namely GGHA11CaBM and GGHA21CaBM, against DPPH[•] radical was evaluated and compared with pure

oleuropein and Trolox, an analogous of vitamin E, commonly used in several assay as standard compound, [14]. GGHA21CaBM exhibited higher antioxidant activity than GGHA11CaBM as depicted in Figure 13. In comparison to standard oleuropein, all the oleuropein aliquots released by loaded shells exhibited higher levels of antioxidant activity. This further confirms the higher activity of natural complexes rather than single pure bioactive substances [32].

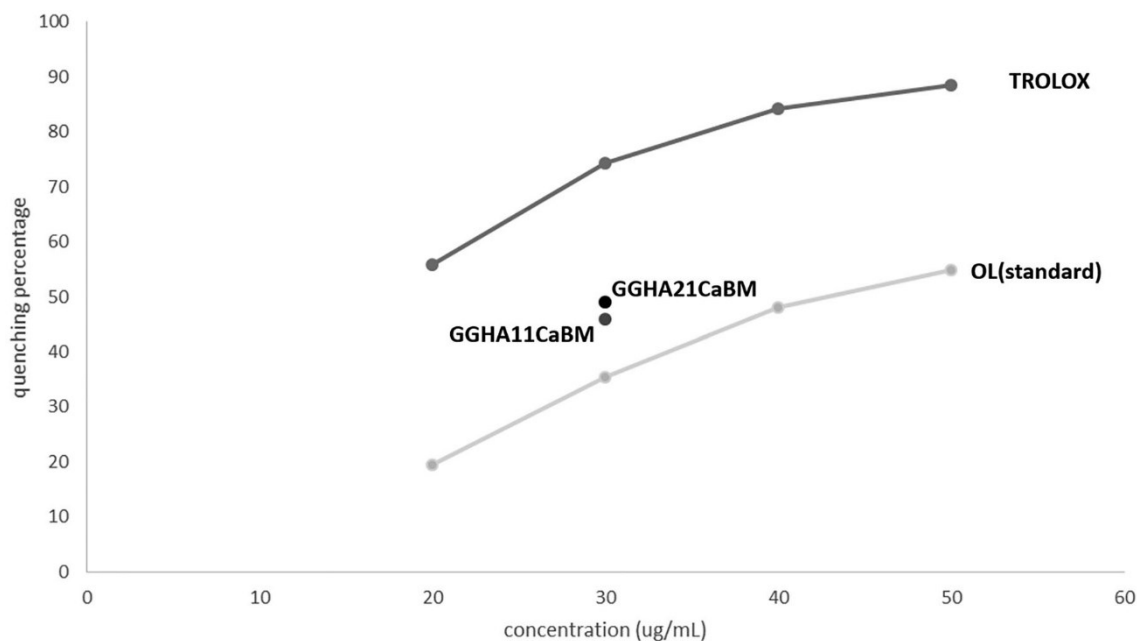


Figure 13: Antioxidant activity against DPPH of Trolox, standard oleuropein and BM released from matrices as a function of concentration.

3.8 *IN VITRO* CYTOTOXICITY: CELL VIABILITY

Cell viability test on calcium ions crosslinked shells was executed according to the ISO/FDIS 10993-5 standards. Polysaccharidic matrices were placed in contact with a monolayer of immortalized mouse fibroblasts (line NIH3T3) for 24 h. The NRU was quantified to exclude both the direct toxic effect (contact) and the indirect toxic effect on cellular vitality due to the release of toxic substances. No cytotoxic effect toward fibroblasts is found. No significant difference ($p > 0.05$) in NRU was found comparing cells in contact with samples or control (HDPE), Figure 14A.

GGHA11CaBM and GGHA21CaBM cytocompatibility toward HC was also assessed by NRU test as a function of incubation time, and results are depicted in Figure 14B. A time-dependent cell

proliferation is observed for both the samples. Cell proliferation percentage was not statistically different from medium ($p > 0.05$) and positive control (HDPE) at each time step.

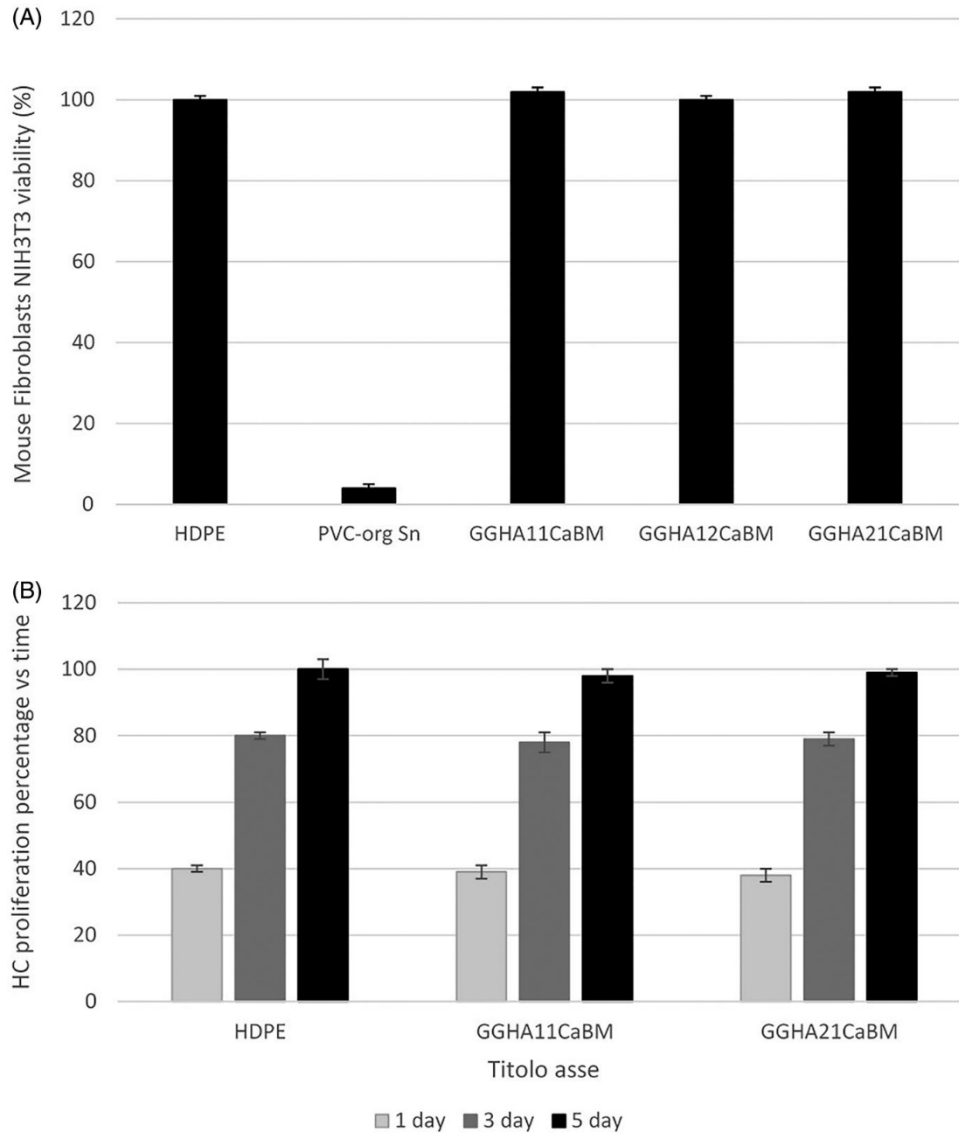


Figure 14: (A) Cell viability was measured by NRU test. Data are expressed as AVERAGE \pm SD of three experiment repeated in six replicates. No value is statistically different versus negative control, $p > 0.05$. HDPE: High Density Polyethylene; PVC-org. Sn: Polyvinyl chloride organotin-stabilized; (B) Percentage of chondrocytes proliferation as a function of incubation time (1, 3 and 5 days) evaluated by the NRU assay. Cell proliferation percentage represents the per cent increase with respect to starting cells number which represents 0% ($t=0$). Error bars represent standard deviation ($n=3$). No statistically difference ($p > 0.05$) for all the samples in comparison with medium or positive control (HDPE).

PART 4: CONCLUSIONS

Three different matrices were obtained combining Gellan Gum and Hyaluronan, in different ratios, crosslinked with calcium ions with the aim of creating a protective shell for the delivery of a natural bioactive matrix rich in oleuropein. The developed formulations did not show any significant interaction with the bioactive substance as highlighted by the burst release in 30 minutes. The burst release was necessary to permit oleuropein to quickly exert its anti-inflammatory and analgesic effect after it is injected in the knee. Its activity once released was verified and the used BM seems to have higher antioxidant activity than free oleuropein. Among the three developed matrices the most promising one is the formulation obtained combining GG and HA in a ratio 2:1, both in terms of rheological properties and antioxidant activity. Even if the cytocompatibility of the components is well known and verified, shells cytocompatibility has been analyzed and no cytotoxic effects were found.

BIBLIOGRAPHY

- [1] Rehman, A.; Ahmad, T.; Aadil, R. M.; Spotti, M. J.; Bakry, A. M.; Khan, I. M.; Zhao, L. L.; Riaz, T.; Tong, Q. Pectin Polymers as Wall Materials for the Nano-Encapsulation of Bioactive Compounds. *Trends Food Sci. Technol.* 2019, 90, 35–46. DOI: 10.1016/j.tifs.2019.05.015.
- [2] Canizales, J. R.; Rodriguez, G. R. V.; Avila, J. A. D.; Saldana, A. M. P.; Parrilla, E. A.; Ochoa, M. A. V.; Gonzalez Aguilar, G. A. Encapsulation to Protect Different Bioactives to Be Used as Nutraceuticals and Food Ingredients. In *Bioactive Molecules in Food. Reference Series in Phytochemistry*; Merillon, J. M.; Ramawat, K., Eds.; Springer: Cham. 2019
- [3] Della Giovampaola, C.; Capone, A.; Ermini, L.; Lupetti, P.; Vannuccini, E.; Finetti, F.; Donnini, S.; Ziche, M.; Magnani, A.; Leone, G.; et al. Formulation of Liposomes Functionalized with Lotus Lectin and Effective in Targeting Highly Proliferative Cells. *Biochim. Biophys. Acta. Gen. Subj.* 2017, 1861, 860–870., DOI: 10.1016/j.bbagen.2017.01.015.
- [4] Bonechi, C.; Donati, A.; Tamasi, G.; Pardini, A.; Rostom, H.; Leone, G.; Lamponi, S.; Consumi, M.; Magnani, A.; Rossi, C. Chemical Characterization of Liposomes Containing Nutraceutical Compounds: Tyrosol, Hydroxytyrosol and Oleuropein. *Biophys. Chem.* 2019, 246, 25–34. DOI: 10.1016/j.bpc.2019.01.002.
- [5] Leone, G.; Consumi, M.; Franzini, C.; Tamasi, G.; Lamponi, S.; Donati, A.; Magnani, A.; Rossi, C.; Bonechi, C. Development of Liposomal Formulations to Potentiate Natural Lovastatin Inhibitory Activity towards 3-Hydroxy-3-Methyl-Glutaryl Coenzyme A (HMG-CoA) Reductase. *J. Drug Deliv. Sci. Technol.* 2018, 43, 107–112. DOI: 10.1016/j.jddst.2017.09.019.
- [6] Gonzalez, E.; Gomez-Caravaca, A. M.; Gimenez, B.; Cebrian, R.; Maqueda, M.; Parada, J.; Martinez-Ferez, A.; Segura-Carretero, A.; Robert, P. Role of Maltodextrin and Inulin as Encapsulating Agents on the Protection of Oleuropein during in Vitro Gastrointestinal Digestion. *Food Chem.* 2020, 310, 125976. DOI: 10.1016/j.foodchem.2019.125976.
- [7] Leone, G.; Consumi, M.; Pepi, S.; Lamponi, S.; Bonechi, C.; Tamasi, G.; Donati, A.; Rossi, C.; Magnani, A. Alginate-Gelatin Formulation to Modify Lovastatin Release Profile from Red Yeast Rice for Hypercholesterolemia Therapy. *Ther. Deliv.* 2017, 8, 843–854. DOI: 10.4155/tde-2017-0025.

- [8] Aouidi, F.; Dupuy, N.; Artaud, J.; Roussos, S.; sallem, M.; Perrau Gaime, I.; Hamdi, M. Rapid Quantitative Determination of Oleuropein in Olive Leaves (*Olea europaea*) Using Mid- Infrared Spectroscopy Combined with Chemometric Analyses. *Ind. Crops Prod.* 2012, 37, 292–297. DOI: 10.1016/j.indcrop. 2011.12.024.
- [9] Hamdi, K. H.; Castellon, R. Oleuropein, a Non-Toxic Olive Iridoid, is an anti-Tumor Agent and Cytoskeleton Disruptor. *Biochem. Biophys. Res. Commun.* 2005, 334, 769–778. DOI: 10.1016/j.bbrc.2005.06.161.
- [10] Horcajada, M. N.; Sanchez, C.; Membrez Scalfo, F.; Drion, P.; Comblain, F.; Taralla, S.; Donneau, A. F.; Offord, E. A.; Henrotin, Y. Oleuropein or Rutin Consumption Decreases the Spontaneous Development of Osteoarthritis in the Hartley Guinea Pig. *Osteoarthr. Cartil.* 2015, 23, 94–102. DOI: 10.1016/ j.joca.2014.08.016.
- [11] Mao, X.; Xia, B.; Zheng, M.; Zhou, Z. Assessment of the Anti- Inflammatory, Analgesic and Sedative Effects of Oleuropein from *Olea europaea* L. *Cell. Mol. Biol.* 2019, 65, 52–55. DOI: 10.14715/cmb/2019.65.1.9.
- [12] Friedman, M. Tomato Glycoalkaloids: Role in the Plant and in the Diet. *J. Agric. Food Chem.* 2002, 50, 5751–5780. DOI: 10.1021/jf020560c.
- [13] Othman, N. B.; Roblain, D.; Chammen, N.; Thonart, P.; Hamdi, M. Antioxidant Phenolic Compounds Loss during the Fermentation of Chetoui Olives. *Food Chem.* 2009, 116, 662–669. DOI: 10.1016/j.foodchem.2009.02.084.
- [14] Tamasi, G.; Baratto, M. C.; Bonechi, C.; Byelyakova, A.; Pardini, A.; Donati, A.; Leone, G.; Consumi, M.; Lamponi, S.; Magnani, A.; Rossi, C. Chemical Characterization and Antioxidant Properties of Products and By-products from *Olea europaea* L. *Food Sci. Nutr.* 2019, 7, 2907–2920. DOI: 10.1002/ fsn3.1142.
- [15] Das, S.; Chaudhury, A.; Ng, K. A. Preparation and Evaluation of Zinc-Pectin-Chitosan Composite Particles for Drug Delivery to the Colon: Role of Chitosan in Modifying In Vitro and In Vivo Drug Release. *Int. J. Pharm.* 2011, 406, 11–20. DOI: 10.1016/j.ijpharm.2010.12.015.
- [16] Bonechi, C.; Lamponi, S.; Donati, A.; Tamasi, G.; Consumi, M.; Leone, G.; Rossi, C.; Magnani, A. Effect of Resveratrol on Platelet Aggregation by Fibrinogen Protection. *Biophys. Chem.* 2017, 222, 41–48. DOI: 10.1016/j.bpc.2016.12.004.

- [17] Tamasi, G.; Bonechi, C.; Donati, A.; Leone, G.; Rossi, C.; Cini, R.; Magnani, A. Analytical and Structural Investigation via Infrared Spectroscopy and Density Functional Methods of Cuprous Complexes of the Antioxidant Tripeptide Glutathione (GSH). Synthesis and Characterization of a Novel CuI-GSH Compound. *Inorganica Chim. Acta*. 2018, 470, 158–171. DOI: 10.1016/j.ica.2017.07.047.
- [18] Cappelli, A.; Paolino, M.; Anzini, P.; Giuliani, G.; Valenti, S.; Aggravi, M.; Donati, A.; Mendichi, R.; Zetta, L.; Boccia, A. C.; et al. Structure-Property Relationships in Densely Grafted p- Stacked Polymers. *J. Polym. Sci. A Polym. Chem.* 2010, 48, 2446–2461., DOI: 10.1002/pola.24016.
- [19] Leone, G.; Consumi, M.; Pepi, S.; Pardini, A.; Bonechi, C.; Tamasi, G.; Donati, A.; Lamponi, S.; Rossi, C.; Magnani, A. Enriched Gellan Gum Hydrogel as Visco-Supplement. *Carbohydr. Polym.* 2020, 227, 115347 DOI: 10.1016/j.carbpol.2019.115347.
- [20] Chen, M. H.; Wang, L. L.; Chung, J. J.; Young-Hun Kim, Y.-H.; Atluri, P.; Burdick, J. A. Methods to Assess Shear-Thinning Hydrogels for Application as Injectable Biomaterials. *ACS Biomater. Sci. Eng.* 2017, 3, 3146–3160. DOI: 10.1021/acsbiomaterials.7b00734.
- [21] Yang, F.; Xia, S.; Tan, C.; Zhang, X. Preparation and Evaluation of Chitosan-Calcium-Gellan Gum Beads for Controlled Release of Protein. *Eur. Food Res. Technol.* 2013, 237, 467–479. DOI: 10.1007/s00217-013-2021-y.
- [22] Brand-Williams, W.; Cuvelier, M. E.; Berset, C. Use of a Free Radical Method to Evaluate Antioxidant Activity. *LW T - Food Sci. Technol.* 1995, 28, 23–30. DOI: 10.1016/S0023-6438(95)80008-5.
- [23] Leone, G.; Consumi, M.; Lamponi, S.; Magnani, A. Combination of Static Time of Flight Secondary Ion Mass Spectrometry and Infrared Reflection-Adsorption Spectroscopy for the Characterisation of a Four Steps Built-up Carbohydrate Array. *Appl. Surf. Sci.* 2012, 258, 6302–6315. DOI: 10.1016/j.apsusc.2012.03.027.
- [24] Barbucci, R.; Leone, G.; Magnani, A.; Montanaro, L.; Arciola, C. R.; Peluso, G.; Petillo, O. Cu²⁺- and Ag⁺-Complexes with a Hyaluronane-Based Hydrogel. *J. Mater. Chem.* 2002, 12, 3084–3092. DOI: 10.1039/b205320a.
- [25] Leone, G.; Consumi, M.; Lamponi, S.; Bonechi, C.; Tamasi, G.; Donati, A.; Rossi, C.; Magnani, A. Thixotropic PVA Hydrogel Enclosing a Hydrophilic PVP Core as Nucleus Pulposus

- Substitute. *Mater. Sci. Eng. C Mater. Biol. Appl.* 2019, 98, 696–704. DOI: 10.1016/j.msec.2019.01.039.
- [26] Cappelli, A.; Razzano, V.; Paolino, M.; Grisci, G.; Giuliani, G.; Donati, A.; Mendichi, R.; Samperi, F.; Battiato, S.; Boccia, A. C.; et al. Bithiophene-Based Polybenzofulvene Derivatives with High Stacking and Hole Mobility. *Polym. Chem.* 2015, 6, 7377–7388. DOI: 10.1039/C5PY00904A.
- [27] Hezma, A. M.; Elashmawi, I. S.; Rajeh, A.; Kamal, M. Change Spectroscopic, Thermal and Mechanical Studies of PU/PVC Blends. *Physica B Condens. Matter.* 2016, 495, 4–10. DOI: 10.1016/j.physb.2016.04.043.
- [28] A. M.; Nassir, I. A. A.; Ibrahim, S. M.; M. W.; Tanuj, M. R.; Ain, I.; Ahmad, N. Shahzad, Surface Functionalized Folate Targeted Oleuropein Nano-Liposomes for Prostate Tumor Targeting: In Vitro and In Vivo Activity. *Life Sci.* 2019, 220, 136–146. DOI: 10.1016/j.lfs.2019.01.053.
- [29] Fakhari, A.; Berkland, C. Applications and Emerging Trends of Hyaluronic Acid in Tissue Engineering, as a Dermal Filler and in Osteoarthritis Treatment. *Acta Biomater.* 2013, 9, 7081–7092. DOI: 10.1016/j.actbio.2013.03.005.
- [30] Nickerson, M. T.; Paulson, A. T. Rheological Properties of Gellan, k-Carrageenan and Alginate Polysaccharides: Effect of Potassium and Calcium Ions on Macrostructure Assemblages. *Carbohydr. Polym.* 2004, 58, 15–24. DOI: 10.1016/j.carbpol.2004.06.016.
- [31] Csapo, E.; Szokolai, H.; Juhasz, A.; Varga, N.; Janovak, L.; Dekany, I. Cross-Linked and Hydrophobized Hyaluronic Acid- Based Controlled Drug Release Systems. *Carbohydr. Polym.* 2018, 195, 99–106. DOI: 10.1016/j.carbpol.2018.04.073.
- [32] Leone, G.; Consumi, M.; Pepi, S.; Lamponi, S.; Bonechi, C.; Tamasi, G.; Donati, A.; Rossi, C.; Magnani, A. New Formulations to Enhance Lovastatin Release from Red Yeast Rice (RYR). *J. Drug Delivery Sci. Technol.* 2016, 36, 110–119. DOI: 10.1016/j.jddst.2016.10.001.

**CHAPTER III:
POLYMERIC FRAMEWORKS
FOR DRUG DELIVERY SYSTEMS**

**POLYVINYL ALCOHOL FRAMEWORK FOR
OLEUROPEIN EXTRACT DELIVERY: MATRIX
CHARACTERIZATION AND RELEASE PROFILES**

PART 1: INTRODUCTION

Poly vinyl alcohol (PVA) is a synthetic thermoplastic polymer, soluble in water and in organic solvents depending on molecular weight [1]. It is usually prepared by polymerization of vinyl acetate (VAc), followed by partial or complete hydrolysis with ethanol in the presence of anhydrous sodium methylate or aqueous sodium hydroxide. The acetate group removal reaction can be controlled and the physical characteristics of PVA based materials depend on the degree of both polymerization and hydrolysis of the starting poly (vinyl acetate) (PVAc) [2]. As a hydrophilic polymer, PVA exhibits excellent water retention properties. The length of the polymeric chain, the degrees of hydrolysis and polymerization affect the solubility and the properties of PVA in water [1, 3]. Conditions for dissolution are primarily governed by the degree of hydrolysis, molecular weight, particle size distribution, and particle crystallinity. Optimum water solubility occurs at 87% – 89% hydrolysis [2], whereas at higher hydrolysis degree, PVA shows a high tendency to form gels through hydrogen bonding interactions. Hydrogen bonding interactions have an important effect on the rheological and mechanical properties of the polymer. Thanks to its mechanical properties, high ability to form films, nontoxicity, water-solubility, no carcinogenicity, hydrophilicity, good compatibility and biodegradability in human tissues and fluids, PVA is a polymer of great interest for various pharmaceutical and biomedical applications. Depending on the type of additives they contain, PVA hydrogels can be considered biocompatible in nature and being non-irritating to soft tissues when in contact with them, are suitable for many biomedical applications, such as contact lenses, wound dressing, coatings for sutures and catheters [4]. PVA is also used as polymeric drug delivery system to overcome all the limitations and disadvantages related to conventional therapeutic agents.

Polyethylene glycol (PEG) is a unique polyether diol, usually manufactured by the aqueous anionic polymerization of ethylene oxide, although other polymerization initiators can be employed. A variety of molecular weights (1'000 Da–50'000 Da) can be obtained with low polydispersity. At room temperature the water soluble and hygroscopic polymer is a colorless viscous liquid at molecular weight < 600 Da, and a waxy white solid at molecular weights > 800 Da [5].

PEG is widely used in biomedical field for drug delivery, tissue engineering, bioconjugation and surface functionalization applications. It is even an amphiphilic polymer; it dissolves in organic solvents as well as in water. FDA has approved PEG for use in pharmaceutical, food and cosmetics formulations, since it is non-toxic and can be excreted by a combination of renal and hepatic pathways.

Both PVA and PEG can be used to obtain hydrogels. Hydrogels are three-dimensional, hydrophilic, polymeric networks that exhibit the ability to swell in water and retain a significant fraction of the

latter within their structure. Moreover, they can respond to the fluctuations of environmental stimuli. As a kind of smart biomaterial, hydrogels find widespread applications in medical and pharmaceutical sectors. This is due to their high hydrophilicity and soft consistency, which make them close to human soft tissues [6]. There is a wide variety of natural and synthetic polymer-based hydrogels, which can be physically or chemically crosslinked. Physically crosslinked hydrogels have gained significance due to their relative ease of production and the use of crosslinking agents is generally avoided during their synthesis protocol. Dissolution of physically cross-linked gels is prevented by physical interactions, which exist between different polymer chains [7]. The formation of three-dimensional matrices is obtained by adjusting some parameters such as temperature, pressure, ionic strength, and pH. They may show inhomogeneities or network defects and poor stability. In chemically crosslinked hydrogels covalent bonds exist between different polymer chains. Therefore, they are stable and cannot be dissolved in any solvents unless the covalent crosslink points are cleaved [8]. The main difference between the two types of hydrogels lies in the different behavior they show in aqueous solutions: chemical hydrogels, thanks to the presence of covalent bonds, are insoluble and stable; physical hydrogels become unstable and may degrade quicker, due to the absence of strong bonds between the chains [3]. PVA-PEG chemically crosslinked hydrogels can be prepared adding some other crosslinking agents, [9, 10], or with drastic irradiation procedures, such as γ -ray or electron beams, [11].

In this work, 42 different physical PVA-PEG based hydrogels, in the form of theta-gels, were prepared at room temperature, testing the crystallization occurrence at basic pH (10 or 12). In this work, PVA-PEG theta-gels were synthesized to overcome the water instability of physically crosslinked matrices, gain better mechanical properties and not using a long multistep synthesis process, even common to other theta-gel synthesis, [12]. The influence of both polymers molecular weight and pH of crystallization on the swelling and rheological properties of the synthesized theta-gels was evaluated.

PART 2: MATERIALS AND METHODS

2.1 MATERIALS

PVA (27kDa, 47kDa, 61kDa, 125kDa, 195kDa: 99% hydrolysis degree; 31kDa, 205kDa: 88% hydrolysis degree), PEG (4kDa, 8kDa and 20kDa), NaOH, and NaCl were purchased by Merck.

2.2 PVA FRAMEWORKS SYNTHESSES

Polymeric frameworks were synthesized starting from 10% w/w PVA solution and 10% w/w PEG solution in ultrapure water (UPW). Both solutions were basified with 1 M NaOH till the chosen pH (pH =10 or pH=12) and let them rest for 30 minutes. After that, the two solutions were mixed vigorously and let them rest for 24 hours, to permit the re-crystallization of PVA. After 24 hours, the solution was removed, and the samples freeze-dried. The dry samples were washed with UPW to eliminate the unreacted PEG and NaOH. 42 frameworks, changing PVA and PEG molecular weight and pH value were obtained.

2.3 SWELLING BEHAVIOR

The swelling behavior of all the frameworks were measured in physiological solution at 37 °C. About 20 mg of each gel in dry state was put in an excess of 154 mM NaCl and the weight change was monitored every 30 minutes for 8 hours, and then after 24, 48 and 72 hours. The swelling behavior was expressed in terms of swelling ratio (SR %) and uptake ratio (UR %), [9, 12]. The SR % is the percentage of swelling in the selected media, in comparison with the dry gel, and it is defined in Equation 3.

$$\text{SR \%} = \left(\frac{w_s - w_d}{w_s} \right) \times 100$$

Equation 3

The UR% is the amount of solution that the framework can uptake in comparison to its dry weight, this variable is defined in Equation 4.

$$\text{UR \%} = \left(\frac{w_s - w_d}{w_d} \right) \times 100$$

Equation 4

Where for both equations the terms w_s and w_d corresponds to the weight of the swollen and dried matrix, respectively.

2.4 THERMOGRAVIMETRIC ANALYSIS (TGA)

TGA technique was used to quantify the total water content and the thermal stability of the frameworks. The analyses were performed with an SDT-Q600 (TA Instruments). Thermal Advantage Release 5.5.22 was used for instrument control and TA Instruments Universal Analysis 2000 v. 4.5.4. was used for data analysis.

2.4.1 TOTAL WATER CONTENT

The total water content (W_H %) was measured using the following thermal program: 10 mg of the full swollen gel in UPW were put in a Pt crucible and heated from 30 °C to 300 °C at 10 °C/min., in inert atmosphere (N_2 , 100 mL/min.). The total water for a swollen polymeric matrix can be derived by the weight loss in the 30 °C – 200 °C temperature range.

2.4.2 THERMAL STABILITY

The thermal stability was quantified heating 10 mg of each polymeric matrix at dry state from 30 °C to 600 °C at 10 °C/min., in inert atmosphere (N_2 , 100mL/min.), [13].

2.5 DIFFERENTIAL SCANNING CALORIMETRY (DSC)

DSC analyses were conducted on both swollen and dried hydrogels. DSC of full swollen frameworks in water permitted to measure the enthalpy of fusion of water and to calculate, combining the TGA total water content, the freezable and non-freezable water and the free and bound freezable water. On the dry state materials was performed a calorimetric analysis to evaluate the crystallization behavior. For the analysis was used a DSC Q1000 (TA Instruments Leatherhead, United Kingdom). Thermal Advantage Release 5.5.22 was used for instrument control and TA Instruments Universal Analysis 2000 v. 4.5.4 for data analysis.

2.5.1 TYPES OF WATER

5 mg of each swollen gel in UPW were sealed in an aluminum hermetic anodized pan. The thermal program consisted in cooling the sample to $-40\text{ }^{\circ}\text{C}$ ($0.2\text{ }^{\circ}\text{C}/\text{min.}$), keeping for 5 minutes at $-40\text{ }^{\circ}\text{C}$, and finally heating from $-40\text{ }^{\circ}\text{C}$ to $40\text{ }^{\circ}\text{C}$ at $0.2\text{ }^{\circ}\text{C}/\text{min.}$ All the steps of the method were performed under N_2 flow at $50\text{ mL}/\text{min.}$. The total water content is expressed in Equation 5.

$$W_{\text{H}} = W_{\text{fH}} + W_{\text{nfH}}$$

Equation 5

Where W_{H} , W_{fH} and W_{nfH} are the weight of the total water in the sample, the weight of freezable and the weight of non-freezable water, respectively. The freezable H_2O can be obtained integrating the endothermic peak corresponding to melting of the frozen H_2O in the hydrogel sample (ΔH_{m}) and quantifying the latent heat of melting of pure free H_2O (ΔH). Not considering the minimal differences in enthalpy of melting of frozen H_2O in different crystalline structures, the ratio $\Delta H_{\text{m}}/\Delta H$ corresponds to the weight of freezable H_2O per gram of full swollen hydrogel (WSG), Equation 6, [14].

$$\frac{W_{\text{fH}}}{W_{\text{SG}}} = \frac{\Delta H_{\text{m}}}{\Delta H}$$

Equation 6

Applying the Equation 6 is possible to calculate the W_{fH} and from the Equation 5 the W_{nfH} . It can be even possible to distinguish the free freezable water (ffH) from the bound freezable water (bfH). It is possible using the signal of the heating rate (HR) in the thermograms: from the maximum within the melting peak of water, and using the point to point integral of the peak, it was possible to attribute the amount of the two types of freezable water, [9].

2.5.2 CRYSTALLINITY AND THERMAL BEHAVIOR

1 mg – 5 mg of the dry state framework were sealed in a hermetic anodized aluminum pan and subjected to a heating ramp from 10 °C to 250 °C at a heating rate of 10 °C/min. in a N₂ flux of 50 mL/min..

2.6 VISCOELASTIC PROPERTIES

The mechanical behavior of the frameworks in the Small Amplitude Oscillation Shear (SAOS) and in the Large Amplitude Oscillation Shear (LAOS) regimes was analyzed by rheology. For all the analyses the samples were analyzed in the full swollen state in 154 mM NaCl at 37 °C. The tests were performed using a Discovery Hybrid Rheometer-2 (DHR-2) (TA Instruments), mounting a plate-plate stainless steel geometry (diameter 40 mm) equipped with Peltier steel plate environmental system. For the instrument control and data analysis was used TA Instruments software TRIOS v.4.1.1.33073.

2.6.1 FREQUENCY SWEEP TEST (SAOS)

Samples were subjected to a strain sweep test in a range of strain from $1 \times 10^{-2}\%$ to $5 \times 10^{-0}\%$ at three different frequencies (0.1 Hz, 1 Hz and 10 Hz) to find the LVR, that represents the range of strain the material properties do not depend on the stress, strain or strain rate. The Frequency sweep test was performed in a frequency range from 0.1 Hz to 10 Hz at a constant strain of 5×10^{-4} , as deducted by the strain sweep test.

2.6.2 AMPLITUDE SWEEP TEST (SAOS AND LAOS)

The Strain sweep test was performed at a constant frequency of 1 Hz, and the test consists in two consecutive strain ramps: the first one from $10^{-2}\%$ to $10^2\%$, followed by the back return ramp from $10^2\%$ to $10^{-2}\%$.

2.6.3 CREEP-RECOVERY TEST

The Creep step was performed for 90 s at 50 Pa, followed by a Recovery step at 0 Pa for 180 s, so when all the samples were relaxed and had reached a plateau.

2.7 TRIBOLOGICAL PROPERTIES

The Tribological test was performed on swollen matrices in 154 mM NaCl at 25 °C using a Discovery Hybrid Rheometer-2 (DHR-2) (TA Instruments) equipped with a three 5/16” stainless steel truncated balls upper geometry. For the instrument control and data analysis was used TA Instruments software TRIOS v. 4.1.1.33073. The test was conducted as a Flow sweep, from 0.01 rad/s to 10 rad/s, with a load force of 3 N to obtain the coefficient of friction (COF) curve.

2.8 OLEUROPEIN EXTRACT RELEASE PROFILES

The polymeric frameworks were loaded with Oleuropein 60% extract, and the *in vitro* release was evaluated using a previous method slightly modified, [15]: the absorbance was measured at 325 nm every 60 minutes for 6 hours and after 24 hours, using a spectrophotometer Specord 210.

The loaded samples were prepared dipping about 50 mg of dry state frameworks in a water 10 mg/L of the Oleuropein extract. After the matrix was fully swollen it was removed from the solution and put in UPW. The remaining solution was dialyzed against water to quantify the unloaded oleuropein, then from the withdrawals it was evaluated the sample release behavior.

2.9 STATISTICAL ANALYSIS

3 replicates were used for each analysis. The effect of pH was tested with a One-Way ANOVA test: if no significant difference ($p > 0.05$) is found for the same sample, the two results were mediated, increasing the replicates number (from $n = 3$ to $n = 6$). The influence on the analyzed properties of the polymers (PVA and PEG) molecular weight was tested with a Two-Way ANOVA test.

PART 3: RESULTS AND DISCUSSION

3.1 PVA FRAMEWORKS SYNTHESSES

The synthesized frameworks were summarized in Table 5 and Table S 1, where the final form of the products was highlighted. The matrices based on 31 kDa PVA did not form any gel system, whereas PVA 205 kDa molecular weight-based matrices gave unstable gel product that underwent disruption during the washing process.

Table 5: Nomenclature, reaction parameters and state of synthesized frameworks.

PVA MW	PEG MW	pH	Sample Name	Form (*)	PVA MW	PEG MW	pH	Sample Name	Form (*)
27kDa	4kDa	12	270412	SG (All)	27kDa	4kDa	10	270410	SG (All)
	8kDa		270812			8kDa		270810	
	20kDa		272012			20kDa		272010	
31kDa	4kDa	12	310412	NN (All)	31kDa	4kDa	10	310410	NN (All)
	8kDa		310812			8kDa		310810	
	20kDa		312012			20kDa		312010	
47kDa	4kDa	12	470412	SG (All)	47kDa	4kDa	10	470410	SG (All)
	8kDa		470812			8kDa		470810	
	20kDa		472012			20kDa		472010	
61kDa	4kDa	12	610412	SG (All)	61kDa	4kDa	10	610410	SG (All)
	8kDa		610812			8kDa		610810	
	20kDa		612012			20kDa		612010	
125kDa	4kDa	12	1250412	SG (All)	125kDa	4kDa	10	1250410	SG (All)
	8kDa		1250812			8kDa		1250810	
	20kDa		1252012			20kDa		1252010	
195kDa	4kDa	12	1950412	SG (All)	195kDa	4kDa	10	1950410	SG (All)
	8kDa		1950812			8kDa		1950810	
	20kDa		1952012			20kDa		1952010	
205kDa	4kDa	12	2050412	NG (All)	205kDa	4kDa	10	2050410	NG (All)
	8kDa		2050812			8kDa		2050810	
	20kDa		2052012			20kDa		2052010	

(*) SG = Stable Gel Form; NG = Not stable Gel Form; NN = No gel formed.

This can be due to the lower hydrolysis degree: 88 % instead of 99 % of all the other PVA molecular weight. The not complete hydrolyzation of the acetate groups may cause an encumbrance and a not proper alignment of the PVA chains, that cannot reorganize them and generate a stable framework.

In fact, the presence of medium concentration (10 % w/w) of the two polymers in molar ratio 1:1, causes a phase incompatibility, that raises a contraction of the PVA phase, and so a proximity of the polymer's groups that can in this way interact and form the polymeric framework as theta-gels, [16].

3.2 SWELLING BEHAVIOR

The swelling behavior was evaluated using SR % and SU % parameters. The One-Way ANOVA test highlighted that pH does not affect the swelling behavior of the frameworks ($p > 0.05$), so the results reported and discussed represent the average values of the samples obtained using the same PVA and PEG. The SR % and UR % results were summarized in Figure S 1a-e and in Figure S 2a-e, respectively. All the samples reached the equilibrium state after 6 hours, so the results were reported till the 7 hours of swelling. The equilibrium SR % for all the 15 samples are reported in a radar plot, dividing each PVAs with the three PEG MW (Figure 15) to evaluate the influence of the PVA and PEG MW on the SR %. The influence of the length of the two polymers on SR% is almost the same ($p = 3 \times 10^{-7}$ for PVA MW and $p = 6 \times 10^{-7}$ for PEG MW) in the entire series of samples. In general, an increase of the PVA and PEG MW corresponds to a SR % increase for all the frameworks. Besides this similarity, it is possible to split hydrogels into low - medium MW (L/M-MW) and high MW (H-MW). The L/M-MW matrices show enhanced SR % with respect to the H-MW samples, for all the used PEG. Moreover, L/M-MW hydrogels have different behavior from one PEG to another and from one PVA to another ($p = 3 \times 10^{-6}$ and $p = 9 \times 10^{-5}$, respectively), the H-MW ones have not significant influence of the PVA and PEG ($p > 0.05$), as is possible to notice from Figure 15.

Figure 16 summarizes in a radar plot the equilibrium $1 / SU$ % for all the 15 samples, dividing each PVAs with the three PEG MW: the results in the radar plot are expressed in terms of $1 / SU$ %, because in this way the normal distribution is granted. The data highlight that both the PVA and PEG MW affect the swelling uptake. In fact, increasing both the PVA and the PEG length a significant increase of the $1 / SU$ % can be observed (with respectively $p = 4 \times 10^{-6}$ and $p = 6 \times 10^{-6}$). Dividing the PVA molecular weight in two subgroups (L/M-MW and H-MW), is possible to examine the dependence of this swelling property on PVA and PEG MW. For the L/M-MW series the dependence on the PVA and PEG MW remain the same, even if the PVA length loses some influence ($p = 1 \times 10^{-4}$), whereas PEG length conserves its influence ($p = 5 \times 10^{-6}$) in respect to the entire series. For the H-MW PVA the influence of the two polymers loss the significance that they have in the entire series, and so the values flattered on the same average values, showing the same swelling behavior, as for SR %.

Cahrron et al. experienced that an increase in the PEG concentration promotes an increase in the SR% and UR%, but on the other hand, an increase in the PVA concentration does not affect in a significant way the swelling behavior, [12]. From those results is even possible to hypothesize an increasing porogenic effect of the PEG increasing its concentration.

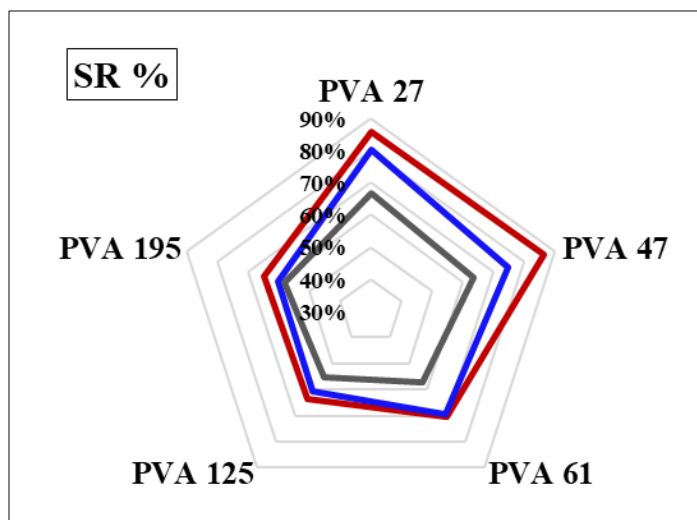


Figure 15: Radar graph of the equilibrium SR % of the PVA in comparison with the different PEG MW (4 kDa in red, 8 kDa in blue, 20 kDa in dark grey).

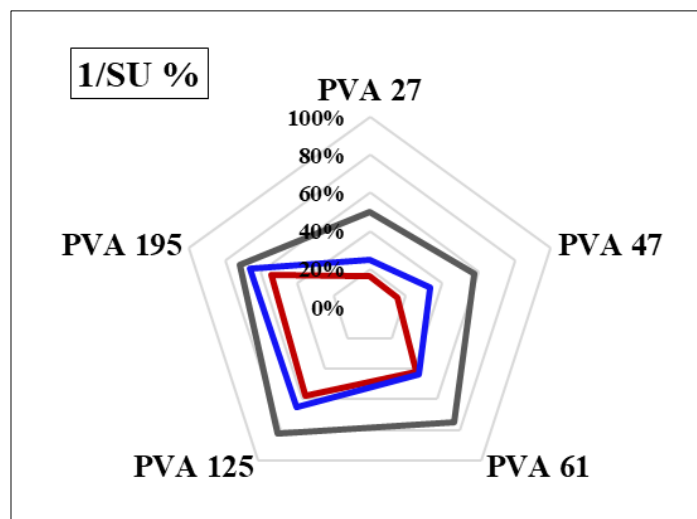


Figure 16: Radar graph of the equilibrium SU % of the PVA in comparison with the different PEG MW (4 kDa in red, 8 kDa in blue, 20 kDa in dark grey).

3.3 THERMOGRAVIMETRIC ANALYSIS (TGA)

TGA is commonly used to measure the change in weight due to a precise thermal program, which either the sample or the reference (generally an empty crucible) is subjected at, in a defined atmosphere. Here, thermal analysis was used to measure the total water content in a full swollen sample, and the thermal stability in a dry state material.

The effect of the pH was not significant ($p > 0.05$) for both the total water content and thermal stability, so the data were merged for the same PVA-PEG products.

3.3.1 TOTAL WATER CONTENT

The W_H % was derived by the weight loss in the region between 30 °C and 200 °C, [14]. The obtained values are reported in Figure 17. From the graph is possible to notice that only PEG MW have influence in the W_H % ($p = 7 \times 10^{-3}$) whereas no effect is played by PVAs ($p > 0.05$). Nevertheless, the synergic use of the two polymers together produces a combined influence on the final properties of the frameworks ($p = 8 \times 10^{-3}$).

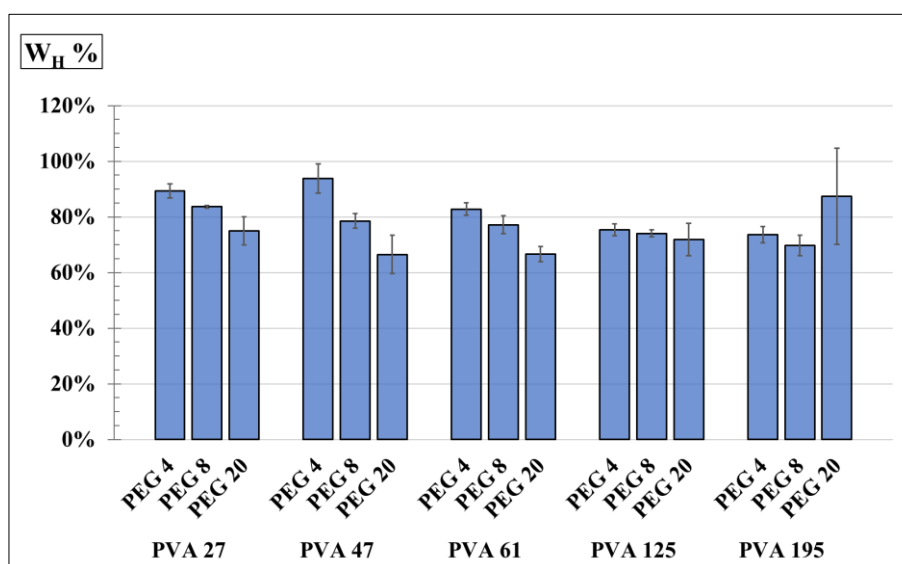


Figure 17: Total water content frameworks from TGA.

Dividing the frameworks in two different subgroups, as in the previous discussions, it is possible to notice that the PVA based L/M-MW are influenced by both the PVA ($p = 3 \times 10^{-2}$) and PEG ($p = 5 \times 10^{-5}$) MW, even if the most important contribution is still given by the second one. As

already observed for the PVA based H-MW frameworks, not statistically difference ($p > 0.05$) was found within the series.

3.3.2 THERMAL STABILITY

The TGA thermograms and its first derivative as a function of temperature (DTG, weight loss / °C) are reported in Figure S 3, Figure S 5, Figure S 7, Figure S 9, Figure S 11: the average TGA and SDT divided by PVA MW are depicted in Figure S 13. Three ranges of temperature are generally examined in polymeric materials: 30 - 200°C, 200 - 400 °C, and 400 - 600 °C (Table 6). The first range is associated to the evaporation of the bulk and hydration water, being no other volatiles in the sample. The second range is associated with the degradation of the aliphatic carbon chains and the third one corresponds to the carbonation process, i.e., the degradation of the condensed chains of the polymeric material, [14]. From the weight losses in the second and third ranges of temperature is possible to calculate the R-value that is the ratio between the weight loss in the third range and that in the second one. This parameter corresponds to the material degree of complexity, and so, much more thermally stable is the material, higher are the organization of the material and the R-value.

Table 6: Weight losses in the characteristic temperature ranges for polymers.

Temperature Ranges	Weight Loss (%)			R
	30 °C – 200 °C	200 °C – 400 °C	400 °C – 600 °C	
PVA 27 PEG 4	6.0 ± 0.2	73.9 ± 0.4	15.4 ± 1.3	0.21 ± 0.02
	5.6 ± 0.3	65.6 ± 5.6	24.1 ± 7.3	0.37 ± 0.14
	5.9 ± 0.2	68.3 ± 1.5	22.1 ± 2.5	0.32 ± 0.04
PVA 47 PEG 4	5.3 ± 0.0	72.9 ± 0.3	17.7 ± 0.3	0.24 ± 0.00
	5.1 ± 0.9	66.2 ± 0.3	24.4 ± 0.4	0.37 ± 0.00
	5.3 ± 0.7	67.4 ± 2.3	23.9 ± 2.4	0.36 ± 0.05
PVA 61 PEG 4	5.1 ± 0.4	67.9 ± 1.2	22.1 ± 0.0	0.32 ± 0.01
	4.4 ± 0.5	65.5 ± 4.1	26.6 ± 4.8	0.41 ± 0.10
	4.4 ± 0.3	67.0 ± 0.4	24.7 ± 1.5	0.37 ± 0.02
PVA 125 PEG 4	4.2 ± 0.1	66.1 ± 3.1	26.0 ± 2.0	0.40 ± 0.04
	4.5 ± 0.2	67.3 ± 1.0	25.4 ± 0.8	0.38 ± 0.01
	3.9 ± 0.2	65.8 ± 4.7	25.3 ± 0.8	0.39 ± 0.04
PVA 195 PEG 4	4.2 ± 0.5	66.4 ± 1.1	27.0 ± 1.0	0.40 ± 0.03
	4.6 ± 0.5	66.0 ± 0.6	27.0 ± 1.0	0.41 ± 0.02
	4.1 ± 0.3	67.8 ± 0.2	25.2 ± 0.7	0.37 ± 0.01

The weight loss in the range 30 – 200 °C and the R-values are shown in Figure 18a and Figure 18b, respectively. The weight loss in 30°C- 200°C range can be associated to the hydrophilicity of the polymeric matrices. It is possible to notice that the weight loss in this region is influenced only by the PVA MW (3×10^{-5}), and not from the PEG MW ($p > 0.05$): so, increasing the PVA MW the hydrophilicity decreases. As already observed for the swelling behavior, in PVA L/M-MW series PVA MW maintains its influence, whereas for the H-MW PVA series no statistical difference is observed.

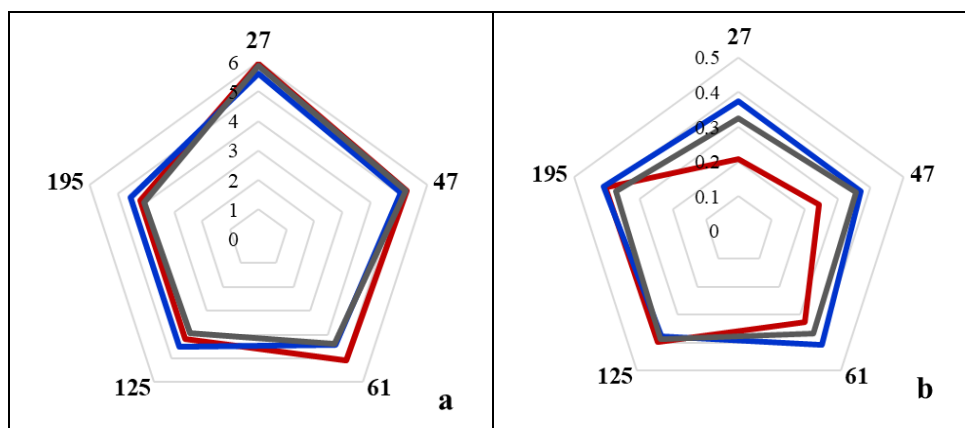


Figure 18: The TGA results for (a) weight loss in the first range of temperature, and (b) the R-values. In red, blu and grey the 4 kDa, 8 kDa and 20kDa, respectively.

The R-values results show that the stability of the system is slightly affected by both PVA ($p = 0.03$) and PEG ($p = 0.02$) MWs. As in the case of the first range of temperature weight loss, dividing the frameworks in L/M-MW and H-MW PVAs, the only that are statistically different are those who are prepared from the first group of PVAs (0.02). Furthermore, it can be seen that only the use of PEG 4 kDa can ensure a statistically different R-value.

3.4 DIFFERENTIAL SCANNING CALORIMETRY (DSC)

Differential scanning calorimetry is commonly used to measure thermal transitions in a sample, in comparison to a reference (generally an empty pan), subjected to the same thermal program and the same environment. The DSC was used in this work to measure on the full swollen in UPW

frameworks the types of water within them (using also the total water content from TGA analysis), and on the dry state ones the crystallinity and in general their thermal behavior.

Preliminary statistical tests on DSC analysis highlighted that the pH of reaction does not affect the properties of the final framework. Consequently, data for the same sample at different pHs were merged.

3.4.1 TYPES OF WATER

DSC was performed on full UPW swollen samples, and both the freezable (W_{fH} %) and non-freezable water (W_{nfH} %) were calculated from the endothermic melting peak in thermograms. The free (W_{ffH} %) and bound freezable water (W_{bfH} %), [9], were also calculated. All data are reported in the Table S 2. The relative values of W_H , W_{fH} and W_{bfH} for all the UPW full swollen frameworks are depicted in Figure 19. The influence of the MW of the two polymers is not statistically relevant for freezable water. (for both PVA and PEG, $p > 0.05$). The bound-freezable water values did not show a normal distribution; thus, ANOVA analyses were not performed. However, it is possible to observe for this variable a trend similar to that of W_{fH} .

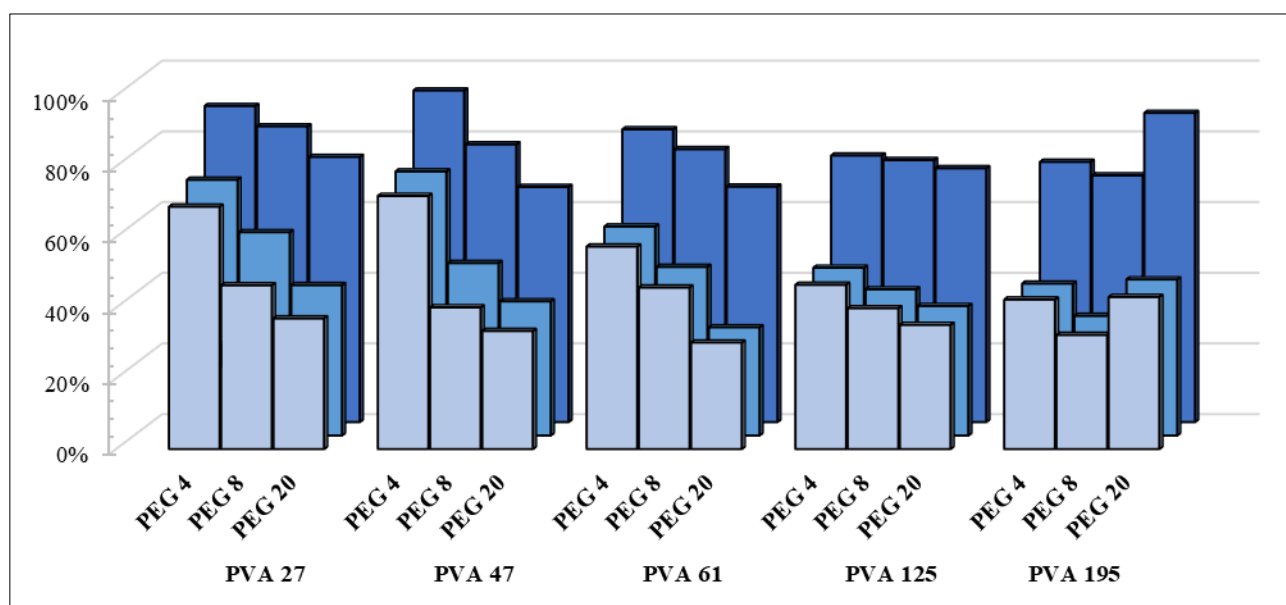


Figure 19: Relative amount of W_{fH} (■) and W_{bfH} (■), and absolute amount of total water content, W_H (■).

3.4.2 CRYSTALLINITY AND THERMAL BEHAVIOR

The enthalpy of fusion (ΔH_m) and the temperature of fusion (T_m) of the polymeric matrices were obtained by DSC : All the DSC thermograms are reported in Figure S 4, Figure S 6, Figure S 8, Figure S 10 and Figure S 12. Statistically analyzed results are summarized in Figure S 14.

PVA, PEG MW and neither their interaction influences the enthalpy of fusion values, the ΔH_m for all samples are not statistically different in the whole series of framework. Regarding the melting temperature, the data can't be processed as obtained, because they are not gaussian and no transformation of data results effective to let the data be processed as gaussian. For this reason, the data were treated as temperature difference (ΔT_m) of one of the frameworks ($T_{m,f}$) with respect to the native PVA ($T_{m,n}$), used for the matrix preparation. The results for the two melting temperatures are reported in Figure 20a, and the difference between these two parameters in Figure 20b.

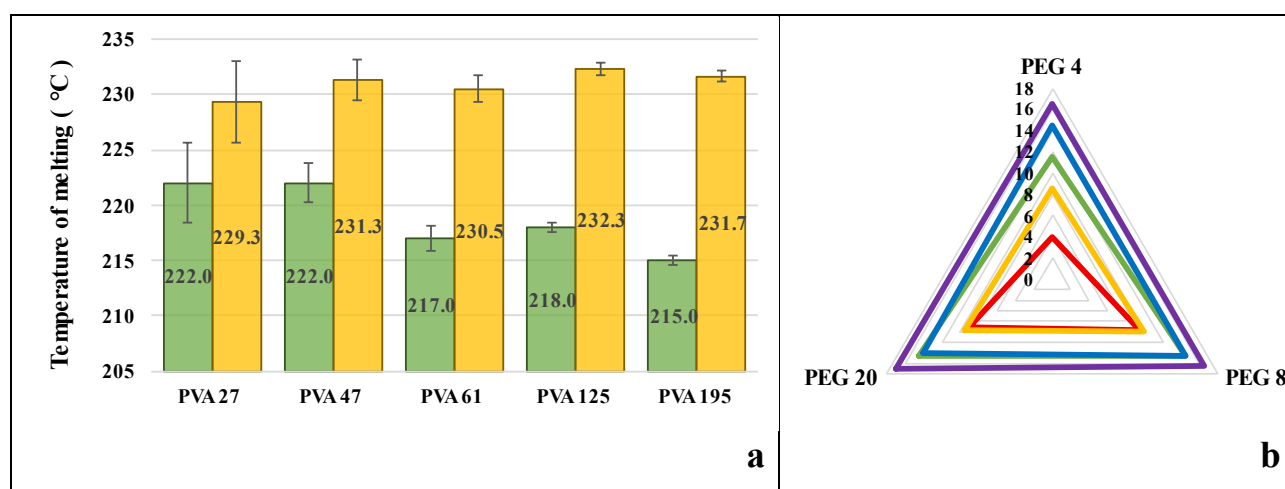


Figure 20: (a) T_m of the native PVA (green) and of the corresponding theta-gel (yellow); (b) ΔT_m between the theta-gel and the corresponding PVA: 27 kDa in red, 47 kDa in yellow, 61 kDa in green, 125 kDa in blue and 195 kDa in purple.

The obtained parameters are mainly affected by PVA MW ($p = 7 \times 10^{-8}$) and slightly by PEG ($p = 1 \times 10^{-2}$). An increase of the ΔT_m can be observed increasing PVA MW. For the PEG 4 kDa the difference in the melting temperature is different for all the PVA MW, whereas for the PEG 8 kDa and 20 kDa, the PVA 27 kDa and 47 kDa, and the PVA 61 kDa and 125 kDa groups together with similar values of ΔT_m . Another important aspect rises by the comparison of the frameworks and the

native PVAs about the melting behavior: the matrices values for the samples produced starting from the same PVA were averaged and compared with the ones of the native PVA. Finally, it can be highlighted the difference between the frameworks and the native polymers: ΔH_m is not statistically different between the two series, but the $T_{m, f}$ is statistically different from $T_{m, n}$ ($p = 4 \times 10^{-5}$): so from the statistical analysis performed is possible to observe that the frameworks have an increased T_m ($231^\circ\text{C} \pm 1.0^\circ\text{C}$ versus $219^\circ\text{C} \pm 3^\circ\text{C}$), and so an increase in melting stability, but a conservation of their crystallinity.

3.5 VISCOELASTIC PROPERTIES

The frameworks were tested for the viscoelastic properties, in terms of viscoelastic moduli in and outside the linear viscoelastic region, and in terms of compliance and recoverable compliance. For these issues, three different tests were run: frequency sweep test and amplitude sweep test for the moduli, and creep-recovery test for the compliance. All tests were performed with samples in the full swollen form, in 154 mM NaCl, at 37°C . For all tests a preliminary One-Way ANOVA was performed, and for all the rheological results no influence of the reaction pH was found ($p > 0.05$), so the results for the frameworks with the same PVA/PEG combination were mediated.

3.5.1 FREQUENCY SWEEP TEST (SAOS)

The viscoelastic moduli of the frameworks were measured in a range of frequency at a constant strain, that was within the LVR. The detailed results for the test are reported in Figure S 15, Figure S 16, Figure S 17, Figure S 18, Figure S 19: they are divided in terms of PVA, PEG and reaction pH. The results for the PVA matrices are discussed in terms of their overall viscoelastic properties ($G^* = |G' + iG''|$), and the ratio of the two moduli ($\tan \delta = G'' / G'$), [17],

From the Two-Way ANOVA, the $\tan \delta$ values for the frameworks show no significant difference within the whole series ($p > 0.05$), for both PVA and PEG, with an average value of 0.08 ± 0.02 . Consequently, it is possible to assess that all the samples are strong gels, being the $\tan \delta$ for all matrices less than 0.1 (Table 7), [18]. G^* did not change in the whole range of tested frequency, Figure 21. Moreover, the Two-Way ANOVA test pointed out that this parameter is influenced by both PVA ($p = 5 \times 10^{-5}$) and PEG ($p = 9 \times 10^{-7}$) MW: in general, increasing the PEG MW, the G^*

increases. This trend is clearly evident in the case of the PEG 4 kDa, less evident for the 8 kDa polymer, and no changes were found when 20 kDa PEG was used.

Table 7: Frequency sweep results for the G^* and $\tan \delta$.

Frequency Sweep Test		
SAMPLE ID	G^* (Pa)	$\tan \delta$ (-)
274	3243 ± 3508	6.7E-02 ± 4.4E-03
278	16452 ± 5589	9.8E-02 ± 4.4E-02
2720	29869 ± 3962	7.6E-02 ± 1.7E-02
474	5383 ± 482	6.9E-02 ± 7.0E-03
478	15677 ± 4793	6.2E-02 ± 1.5E-02
4720	21588 ± 2915	7.8E-02 ± 1.5E-02
614	7227 ± 3899	5.7E-02 ± 1.4E-03
618	22221 ± 10124	6.5E-02 ± 1.1E-02
6120	53202 ± 3817	8.8E-02 ± 1.2E-02
1254	23079 ± 7747	4.8E-02 ± 4.4E-03
1258	27394 ± 5473	8.4E-02 ± 5.3E-03
12520	44305 ± 1932	9.5E-02 ± 6.1E-03
1954	35314 ± 12235	8.1E-02 ± 2.6E-03
1958	27432 ± 2341	8.6E-02 ± 2.0E-02
19520	36906 ± 3142	8.5E-02 ± 1.7E-02

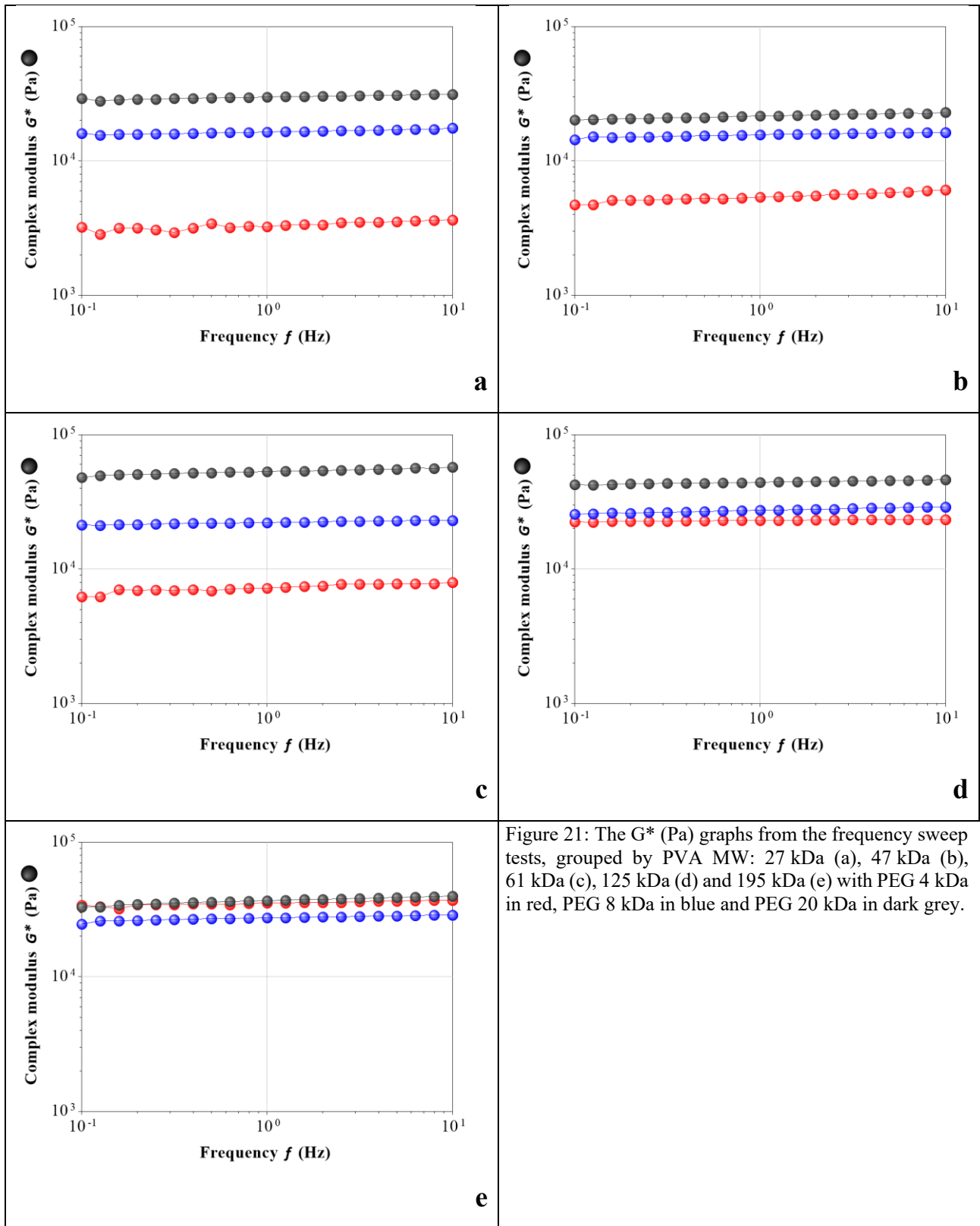


Figure 21: The G^* (Pa) graphs from the frequency sweep tests, grouped by PVA MW: 27 kDa (a), 47 kDa (b), 61 kDa (c), 125 kDa (d) and 195 kDa (e) with PEG 4 kDa in red, PEG 8 kDa in blue and PEG 20 kDa in dark grey.

3.5.2 AMPLITUDE SWEEP TEST (SAOS AND LAOS)

The amplitude loop test in SAOS and LAOS regimes was performed to test how the frameworks respond to a 100% strain and if there are changes in the mechanical properties after that process. The test was performed in continuous way, using an increasing amplitude strain ramp, followed by a decreasing one. In Figure 22 a is depicted the amplitude sweep loop test results for the 2782 framework: during this test, the sine stain-stress curves was collected for each point, and at the point (1), (2) and (3) they were mathematically elaborated with TRIOS software. The Lissajous plot was the results of that procedure, and the normalized ones for the SAOS in the first ramp (SAOS 1), in the second one (SAOS 2) and in the LAOS were reported in Figure 22 b. Those plots shows graphically if alteration in the mechanical properties occurs, and from the integral of the SAOS ellipsoidal curves is possible to calculate the Dissipated Energy Density (DED, in J/m^3), that is the deformation energy related to the sheared volume of the sample, [17]. All the curves of the amplitude sweep loop tests and Lissajous Plots for all the frameworks are reported in the SUPPORTING MATERIALS, Figure S 20 -Figure S 24 and Figure S 25 - Figure S 29. From those graphs is possible to observe that all the frameworks possess a crossover point before to reach the 100% strain and all of them possess a very different viscoelastic behavior in the SAOS and LAOS analyzed regions.

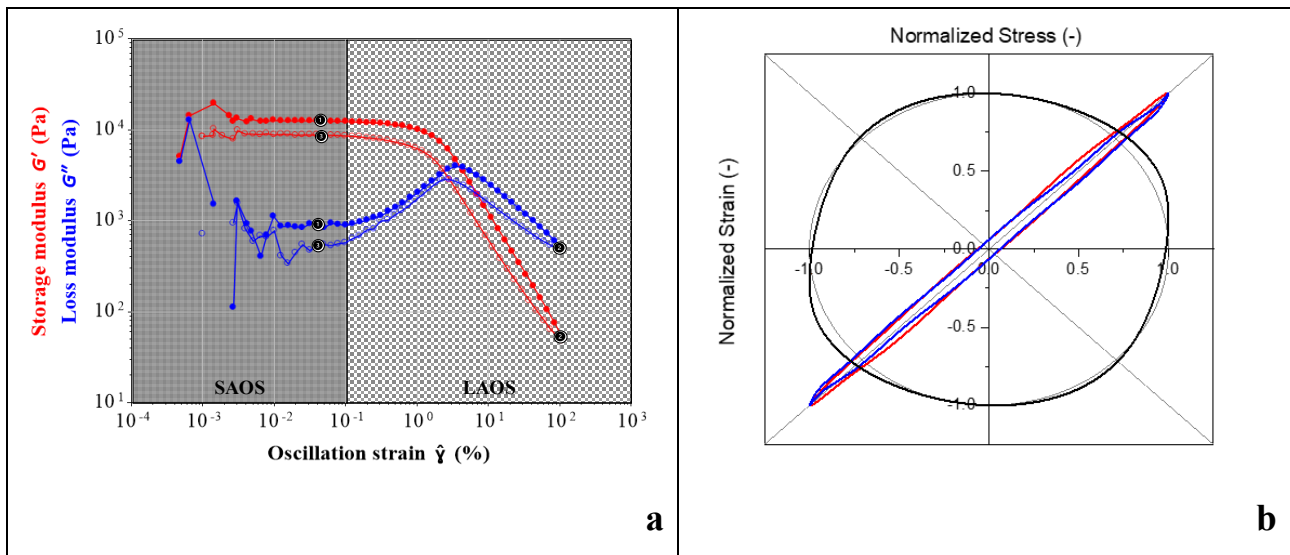


Figure 22: Results of the 2782 framework: **(a)** Amplitude Sweep test results: the full symbols refer to the increasing strain step and the empty ones to the decreasing one. **(b)** The Lissajous plot of the normalized stress/strain values in the SAOS 1 ($\gamma=5 \times 10^{-2} \%$, $\delta=4^\circ$, in the increasing step), SAOS 2 ($\gamma=5 \times 10^{-2} \%$, $\delta=4^\circ$, in the decreasing step) and LAOS ($\gamma=1 \times 10^{-2} \%$).

From the amplitude sweep tests and the Lissajous Plots, the elastic (G') and viscous (G'') moduli, the crossover points in the first (CO 1) and second (CO 2) amplitude sweep step, and the DED in SAOS 1 and SAOS 2 were derived and used to discuss the mechanical behavior of the frameworks. All parameters are reported in Table 8.

The moduli are subjected to a crossover, so the mechanical behavior of polymeric frameworks switches from a strong elastic gel to a viscous one and go back to a strong elastic one in the second amplitude sweep step. Statistical analysis was performed on the moduli in the three selected conditions: SAOS 1 and SAOS 2 that correspond to the 5×10^{-2} % strain in LVR, of the first and second amplitude sweeps tests, respectively and LAOS that corresponds to the 100% strain. From the One-way ANOVA test is evident that no statistical differences are detected from the same moduli, G' and G'' , of the SAOS 1 and 2 ($p > 0,05$). For this reason, the values of the SAOS 1 and 2 were averaged. From this analysis raises that the influence on these parameters can be addressed to both PEG MW ($p = 4 \times 10^{-15}$ and $p = 2 \times 10^{-14}$, for G' and G'' respectively) and PVA MW ($p = 8 \times 10^{-14}$ and $p = 1 \times 10^{-9}$, for G' and G'' respectively). Increasing the PEG MW the elastic modulus increases for L/M MW PVA. For PVA 195 kDa base frameworks no significant differences in moduli value was found for all PEGs. Similarly, increasing PVA MW the storage modulus increases. Starting from PVA 61 kDa, elastic modulus does not change in the M/H-MW PVA series. It is possible to observe the same behavior, but with different absolute values, for the viscous modulus, in terms of PEG and PVA influence. About the moduli in LAOS condition, results highlighted that only PVA maintain its influence, but with less significance: passing from $p = 8 \times 10^{-14}$ to $p = 3 \times 10^{-2}$ and $p = 1 \times 10^{-9}$ to $p = 2 \times 10^{-3}$, for G' and G'' respectively. PEG MW lost every influence ($p > 0.05$) on the moduli in that strain region.

The crossover point (CO) of the frameworks is the limit of the analyzed samples, where the $\tan \delta$ is equal to 1, and so where the $G' = G''$: this point depends on the material mechanical properties and on its behavior when subjected to specific stresses or strains. The CO 1 and CO 2 were not normally distributed, so a transformation must be done: the $1/x$ was selected to let the statistical analysis occurs. A preliminary One-Way ANOVA test shows no significant difference between the CO 1 and CO 2 values for all the frameworks: so the two variables were merged. All data are summarized in Table 8 and Figure 23. It is possible to deduce that for the $1/CO$ the overall behavior for all the frameworks is the same of the G' in SAOS conditions. For this transformed parameter, as for the G' value, the most influent parameter is the PEG MW with $p = 4 \times 10^{-11}$, whereas for PVA MW $p = 7 \times 10^{-4}$ was found.

DED permits to determine if a material has been damaged or has lost some of its mechanical properties. DED values are not normally distributed. So, the data were analyzed as the DED 2

normalized for the corresponding DED 1 (DED 2 / DED 1): performing this ration of the two DEDs, the values of that parameter become normally distributed. A Two-Way ANOVA test was performed to evaluate the PVA and PEG influence on this parameter: PVA MW is the only parameter that has a slight effect on the DED ratio ($p = 0.02$), PEG MW has no effect ($p > 0.05$). From the Figure 24 is possible to note that for PEG 4 kDa the values of the DED ratio are quite constant in the entire series of PVA, for the PEG 8 kDa a marked difference can be appreciated between the L-MW and M/H-MW PVAs, with the latter ones showing a high value of the parameter. In the end, for the 20 kDa PEG the results show that all the PVAs have quite the same value, the only difference is the 27 kDa PVA, that in the entire PEG series keep almost constant its DED ratio value.

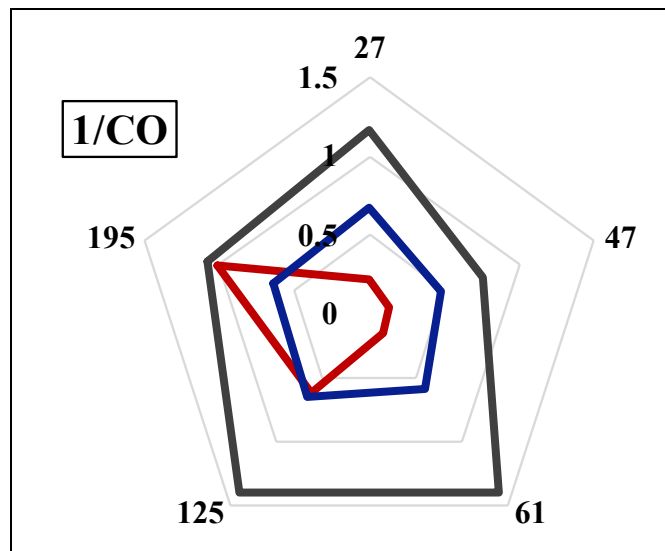


Figure 23: 1/CO of the polymeric frameworks with PEG 4 kDa in red, 8 kDa in blue and 20 kDa in dark grey.

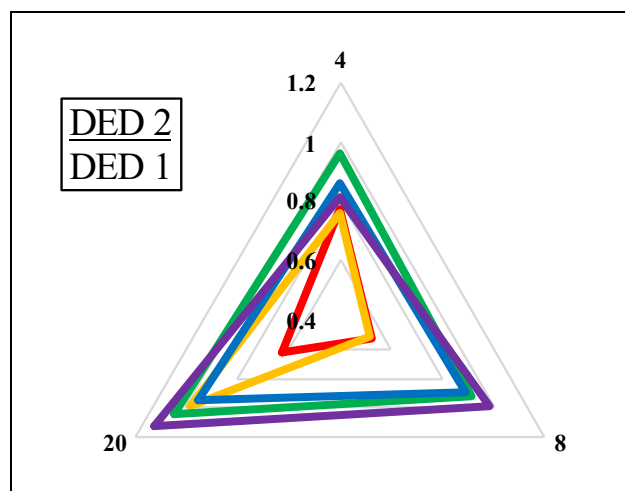


Figure 24: Ratio of the DED in the SAOS 2 in respect to the SAOS 1; with the PVA 27 kDa in red, 47 kDa in yellow, 61 kDa in green, 125 kDa in blue and 195 kDa in purple.

Table 8: Data from the amplitude sweep analyses in LAOS and SAOS.

SAMPLE	Amplitude Sweep Test									
	G' (Pa)			G'' (Pa)			Cross-Over Strain (%)		Dissipated Energy Density (N/m ²)	
	SAOS 1	LAOS	SAOS 2	SAOS 1	LAOS	SAOS 2	CO 1	CO 2	SAOS 1	SAOS 2
274	3237 ± 3501	47 ± 0	2843 ± 2776	209 ± 220	254 ± 180	220 ± 216	8.5 ± 6.6	5.9 ± 5.2	1.9E-04 ± 1.3E-04	1.6E-04 ± 1.4E-04
278	16353 ± 5489	36 ± 26	10091 ± 1878	1729 ± 1264	419 ± 137	865 ± 450	2.7 ± 1.9	1.8 ± 1.5	1.4E-03 ± 9.8E-04	6.7E-04 ± 3.7E-04
2720	29778 ± 3912	21 ± 7	20024 ± 13105	2303 ± 792	483 ± 180	1679 ± 1384	1.0 ± 0.0	0.8 ± 0.3	1.1E-01 ± 1.6E-01	1.0E-01 ± 1.4E-01
474	5370 ± 483	138 ± 19	3845 ± 1408	367 ± 4	559 ± 162	245 ± 135	7.7 ± 0.3	8.2 ± 0.9	2.4E-04 ± 6.9E-05	1.9E-04 ± 1.0E-04
478	15643 ± 4769	53 ± 30	10390 ± 1906	1005 ± 536	607 ± 146	511 ± 226	3.3 ± 1.5	2.0 ± 1.2	7.9E-04 ± 4.3E-04	4.0E-04 ± 1.8E-04
4720	21524 ± 2930	54 ± 36	19302 ± 4795	1651 ± 87	623 ± 145	1701 ± 45	1.7 ± 0.6	1.2 ± 0.4	1.3E-03 ± 7.8E-05	1.3E-03 ± 2.1E-05
614	7215 ± 3892	135 ± 18	7343 ± 3758	417 ± 234	692 ± 313	433 ± 306	7.0 ± 2.1	6.9 ± 2.3	3.4E-04 ± 2.2E-04	3.4E-04 ± 2.3E-04
618	22177 ± 10118	173 ± 162	23496 ± 14249	1392 ± 415	1289 ± 880	1353 ± 894	1.9 ± 0.1	1.5 ± 0.1	6.6E-02 ± 9.2E-02	7.7E-02 ± 1.1E-01
6120	52991 ± 3745	103 ± 10	47588 ± 1881	4703 ± 979	1101 ± 18	5295 ± 1953	0.9 ± 0.0	0.6 ± 0.0	2.2E-01 ± 3.0E-01	2.5E-01 ± 3.5E-01
1254	23051 ± 7733	141 ± 20	21557 ± 6610	1133 ± 476	1100 ± 37	1025 ± 451	1.9 ± 0.4	1.5 ± 0.5	9.2E-04 ± 4.0E-04	7.9E-04 ± 3.3E-04
1258	27300 ± 5465	230 ± 163	27030 ± 3651	2270 ± 313	1431 ± 547	2128 ± 489	1.9 ± 1.1	1.6 ± 0.7	1.8E-03 ± 2.8E-04	1.6E-03 ± 3.7E-04
12520	44107 ± 1898	105 ± 7	43424 ± 1171	4174 ± 450	1135 ± 32	4087 ± 242	0.8 ± 0.0	0.7 ± 0.0	3.3E-03 ± 4.0E-04	3.1E-03 ± 1.5E-04
1954	35199 ± 12188	122 ± 18	35055 ± 11615	2853 ± 1074	960 ± 94	2408 ± 837	1.3 ± 0.6	1.0 ± 0.5	2.3E-03 ± 8.6E-04	1.8E-03 ± 5.7E-04
1958	27326 ± 2285	122 ± 15	27949 ± 2142	2371 ± 753	1038 ± 88	2388 ± 742	1.7 ± 0.3	1.5 ± 0.2	1.9E-03 ± 6.0E-04	1.8E-03 ± 5.4E-04
19520	36773 ± 3183	47 ± 17	34876 ± 3244	3103 ± 350	697 ± 207	3738 ± 1209	1.0 ± 0.1	0.9 ± 0.1	1.4E-01 ± 1.9E-01	1.7E-01 ± 2.4E-01

3.5.3 CREEP-RECOVERY TEST

The creep-recovery test was performed to evaluate the behavior of the frameworks, in terms of compliance (J), if subjected to a constant stress within the LVR, and their subsequent recoverable compliance (J_R). The recovered compliance as the percentage of the recoverable compliance in respect to the corresponding compliance was also calculated. The results at steady state are reported in Table 9, the complete creep-recovery curves of each framework are reported in Figure S 30 - Figure S 34. The compliance and the recoverable compliance resulted to be not normally distributed, so they were transformed in their reciprocal values ($1/x$): in this way the frameworks were statistically analyzed by a Two-Way ANOVA. The compliance of those materials resulted to be affected by the PVA and PEG MW, with $p = 3 \times 10^{-3}$ and $p = 4 \times 10^{-2}$, respectively. The compliance followed two different behaviors along the PVA series. In general, the L/M-MW show a decrease of the parameters increasing PEG MW. The H-MW PVA series maintain quite constant compliance values along the whole PEGs series. The recoverable compliance is not normally distributed, so it was analyzed as transformed ($1/x$): PEG has an influence on this parameter greater than PVA, with respectively $p = 4 \times 10^{-3}$ and $p = 2 \times 10^{-2}$. Instead of analyzing the recoverable compliance, it appears to be more important to analyze the recovered compliance, i.e. the recoverable compliance in respect to the corresponding compliance. No statistical differences were found for this variable ($p > 0.05$), so the recovered compliances for all the prepared materials are almost the same and they can be averaged to $56 \% \pm 22 \%$.

Table 9: Creep-Recovery test results as Compliance, Recoverable Compliance and Recovered Compliance.

Creep-Recovery test								
SAMPLE ID	Compliance (1/Pa)		Recoverable Compliance (1/Pa)			Recovered Compliance (%)		
274	1156	± 776	3118	± 1'242		35%	± 11%	
278	3328	± 3599	6392	± 81		52%	± 56%	
2720	5813	± 1410	10757	± 4058		56%	± 8%	
474	1548	± 1911	2952	± 1'421		42%	± 45%	
478	7008	± 4834	12445	± 5'356		53%	± 16%	
4720	5542	± 712	14688	± 4'769		39%	± 8%	
614	4141	± 2678	5411	± 2'954		74%	± 9%	
618	6400	± 1890	10348	± 4'463		64%	± 9%	
6120	11088	± 3557	25136	± 2'401		44%	± 10%	
1254	13882	± 4802	16212	± 5'323		85%	± 2%	
1258	11827	± 1086	15358	± 2'306		77%	± 5%	
12520	10016	± 5773	15747	± 8'329		63%	± 4%	
1954	6369	± 2264	14059	± 9'213		51%	± 17%	
1958	4078	± 913	14249	± 10'622		43%	± 38%	
19520	13789	± 4009	23045	± 3'482		59%	± 8%	

3.6 TRIBOLOGICAL PROPERTIES

Tribological properties were tested with a flow sweep test, measuring the coefficient of friction dependence on the sliding speed. All the COF overlaid curves are reported in Figure S 35. The coefficient of friction values at 75000 $\mu\text{m/s}$ was used for statistical analysis, Figure 25. The framework 2740 was not stable at the selected condition of tribological test, so its COF curve is not reported in Figure S 35a. Nevertheless, a value for the 2740 framework was selected to perform the statistical analysis on this series of data: the value for the COF of this material was fixed to 1, a value that is much greater of the average ones resulted from the test for all samples. The obtained values are not normally distributed, even without the fixed value for the 2740, so the reciprocal ($1/x$) transformation was done. A One-Way ANOVA was performed to test if the pH has any influence in the final framework: the pH of the reaction has no effect on the matrix for the COF ($p > 0.05$). So as in previous cases the values were averaged, and a Two-Way ANOVA was performed to evaluate the influence of the other parameters of synthesis on the final materials. This statistical analysis shows that the PVAs has less influence on the final behavior about the $1/\text{COF}$, in comparison with the PEGs, with respectively $p = 2 \times 10^{-3}$ and $p = 5 \times 10^{-5}$. From Figure 25 is possible to notice that the COFs for all PVAs and PEGs 8 kDa and 20 kDa are constant in the entire series of data, but for the 4 kDa PEG is possible to observe an evident decrease increasing the PVA MW.

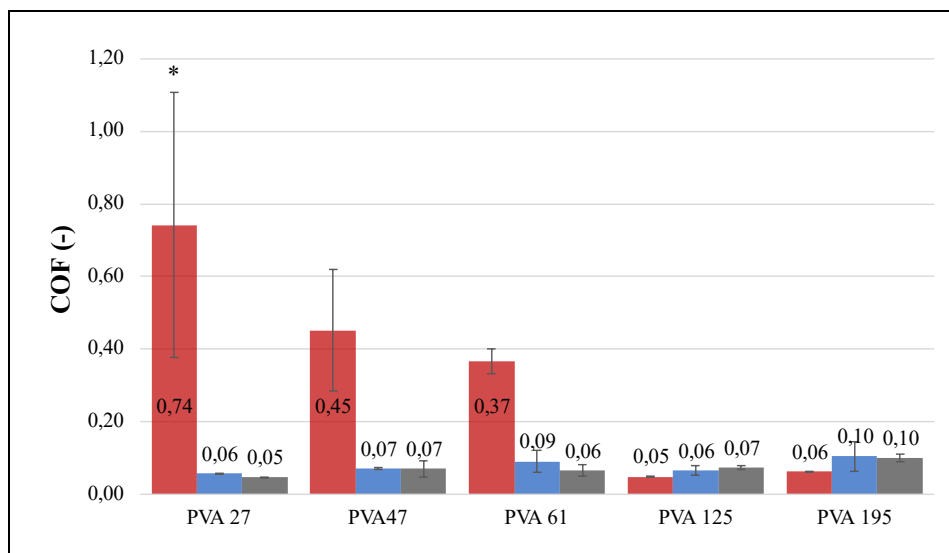


Figure 25: COF for the divided for the PVA MW with the PEG 4 kDa in red, 8 kDa in blue and 20 kDa in dark grey.

3.7 OLEUROPEIN EXTRACT RELEASE PROFILES

Oleuropein extract release was evaluated measuring the absorbance of the UPW release solution at 325 nm: further calculations were performed, and the percentage of the released extract was then plotted as a function of time, Figure S 36. Some additional statistical analysis was performed on those results, in particular on those obtained at 24 h: the influence on the last point of the release profile shows that both PVA and PEG MW have almost the same influence on this parameter, with $p = 1 \times 10^{-4}$ and 2×10^{-4} respectively. The PVA 195 kDa has for all PEGs the higher value in terms of 24 h release. The 2740 has even a high release at this condition: it may be caused by its much span morphology, see Table S 1.

A Three-Way ANOVA test on the release percentage in the entire series of results, processing in addition to the PVA and PEG MW the time of release, and their combination was done. The frameworks release of the extract is influenced by all the tested parameters, Table 10. The statistical analysis indicates that the maximum release is not reached during 24 h: for this reason, those systems can be used as slow-release systems. This may be caused by the high fraction of the bound-freezable water present in all the frameworks.

Table 10: Three-Way ANOVA results for the entire series of frameworks for the release profiles.

TESTED VARIABLES	p - VALUES
PVA MW	3E-23
PEG MW	2E-25
Time (h)	3E-25
PVA MW x PEG MW	2E-17
PVA MW x Time (h)	3E-04
PEG MW x Time (h)	9E-03
PVA MW x PEG MW x Time (h)	2E-01

PART 4: CONCLUSIONS

The work focused on the production and characterization of PVA-based frameworks. The frameworks were prepared as theta-gels, using the principle of the contraction of the allowed volume caused by the mixing of the immiscible solutions of PVAs and PEGs. PVA-PEG theta-gels were synthesized to overcome the water instability of physically crosslinked matrices, gain better mechanical properties and not using a long multistep synthesis process. Different PVA and PEG MW were used to test their influence on the properties of the final framework. The reaction was performed at basic pH (i.e. 10 and 12) to test the influence of this parameter on the prepared materials and to evaluate the possibility to integrate those materials in previous PVA crosslinking reactions, as structure enhancer.




The frameworks were then characterized in terms of their thermal, hydrophilic, mechanical, tribological properties and to their release of a loaded vegetable extract. During the characterization process, it resulted that the pH parameters do not affect the final properties, in all the material series for all the analyzed properties: so it emerges that the frameworks can be prepared in basic environment, without any change on the final characteristics of the framework.

This full characterization, especially in terms of rheological properties, was performed to evaluate the influence of the synthesis parameters on the final gel characteristics. This allows to evaluate the proper MW of the two polymers to be used to have a determinate property of the final framework. This approach can be a starting point to develop new polymeric matrices that can be integrated from the ones reported in this work or even to use the matrices here reported as drug delivery systems, with the final properties tuned, using the adequate PVA-PEG combination.

A table summarizing the PVA and PEG synthesis parameters that influence the frameworks properties was reported, Table 11.

Table 11: Summarizing table for the PVA-PEG influence on the framework's properties.

Property	Variable	PVA MW	PEG MW	PVA vs PEG
Swelling	SR %			≈
	I/UR %			≈
TGA	WH%			<<
	WL 30°C - 200°C			>>
	R			≈
DSC	WfH %			=
	WbfH%			NA
	ΔHm			=
	ΔTm			>>
Viscoelastic	G* (1Hz)			<
	tan δ (1Hz)			=
	G' (SAOS 1-2)			<
	G'' (SAOS 1-2)			<<
	G' (LAOS, 100%)			>
	G'' (LAOS, 100%)			>>
	1/CO			>>
	DED 2/DED 1			>
	J (Steady state, 90s)			>
	JR (Steady state, 180s)			<
	J (Steady state)/JR (Steady state)			=
	1/COF			<
	Extract release	% 24h		
Profile (1h-24h)				<<

Legend:	
Colors	
	p > 0.05
	0.05 > p > 0.005
	p < 0.005

PVA vs PEG	
=	=
≈	less then 1 order of magnitude
>	1-2 orders of magnitude
>>	more then 2 order of magnitude
<	1-2 orders of magnitude
<<	less then 2 order of magnitude

BIBLIOGRAPHY

- [1] E. Marin, J. Rojas and C. Yhors, "A review of polyvinyl alcohol derivatives: Promising materials for pharmaceutical and biomedical applications," *African Journal of Pharmacy and Pharmacology*, vol. 8, no. 24, pp. 674-684, 2014.
- [2] E. Chiellini, A. Corti and R. Solaro, "Biodegradation of poly(vinyl alcohol) based blown films under different environmental condition," *Polym. Deg. Stab.*, vol. 64, p. 305, 1999.
- [3] C. Hassan and N. Peppas, "Structure and applications of poly(vinyl alcohol) hydrogels produced by conventional crosslinking or by freezing/thawing methods," *Adv. Polym. Sci.*, vol. 37, p. 153, 2000.
- [4] S. H. Yang, Y. S. Lee, F. H. Lin, J. M. Yang and K. S. Chen, "Chitosan/poly (vinyl alcohol) blending hydrogel coating improves the surface characteristics of segmented polyurethane urethral catheters.," *J. Biomed. Mater. Res*, vol. 2, no. 83, pp. 304-313, 2007.
- [5] F. E. Bailey Jr and J. Koleske, "Poly (ethylene oxide) Academic Press.," *New York, NY, USA.*, 1976.
- [6] A. S. Hoffman, "Hydrogels for biomedical applications," *Advanced drug delivery reviews*, no. 64, pp. 18-23, 2012.
- [7] B. Slaughter, S. S. Khurshid, O. Z. Fisher, A. Khademhosseini and N. A. Peppas, "Hydrogels in regenerative medicine," *Advanced materials*, Vols. (32-33), no. 21, pp. 3307-3329, 2009.
- [8] H. J. Chung and T. G. Park, "Self-assembled and nanostructured hydrogels for drug delivery and tissue engineering.," *Nano Today*, vol. 5, no. 4, pp. 429-437, 2009.
- [9] G. Leone, M. Consumi, S. Pepi, A. Pardini, C. Bonechi, G. Tamasi, A. Donati, C. Rossi and A. Magnani, "Poly-vinyl alcohol (PVA) crosslinked by trisodium trimetaphosphate (STMP) and sodium hexametaphosphate (SHMP): Effect of molecular weight, pH and phosphorylating agent on length of spacing arms, crosslinking density and water interaction," *Journal of Molecular Structure*, vol. 1202, p. 127264, 2020.
- [10] S. Das and U. Subuddhi, "Controlled delivery of ibuprofen from poly (vinyl alcohol)– poly (ethylene glycol) interpenetrating polymeric network hydrogels," *Journal of pharmaceutical analysis*, vol. 9, no. 2, pp. 108-116, 2019.

- [11] W. Li, F. Xue and R. Cheng, "States of water in partially swollen poly (vinyl alcohol) hydrogels," *Polym.*, no. 46, pp. 12026-12031, 2005.
- [12] P. N. Charron, S. E. Blatt, C. McKenzie and R. A. Oldinski, "Dynamic mechanical response of polyvinyl alcohol-gelatin theta-gels for nucleus pulposus tissue replacement. *Biointerphases*, 12(2).," vol. 12, no. 2, 2017.
- [13] C. M. Hassan and N. A. Peppas, "Cellular PVA hydrogels produced by freeze/thawing," *Journal of Applied Polymer Science*, no. 76, pp. 2075-2079, 2000.
- [14] G. Leone, A. Bidini, S. Lamponi and A. Magnani, "States of water, surface and rheological characterisation of a new biohydrogel as articular cartilage substitute," *Polym. Adv. Technol.*, no. 24, pp. 824-833, 2013.
- [15] M. Consumi, G. Leone, S. Pepi, A. Pardini, S. Lamponi, C. Bonechi, G. Tamasi, C. Rossi and A. Magnani, "Calcium ions hyaluronan/gellan gum protective shell for delivery of oleuropein in the knee," *International Journal of Polymeric Materials and Polymeric Biomaterials*, vol. 71, no. 6, pp. 414-424, 2022.
- [16] Y. Chen, J. Song, S. Wang and W. Liu, "PVA-Based Hydrogels: Promising Candidates for Articular Cartilage Repair," *Macromolecular Bioscience*, vol. 21, no. 10, p. 2100147, 2021.
- [17] T. G. Mezger, *The Rheology Handbook*, Hanover: Vincentz Network, European Coating Library, 2014.
- [18] A. Borzacchiello, F. Della Sala and L. A. Ambrosio, " Rheometry of polymeric biomaterials," in *Characterization of Polymeric Biomaterials*, Woodhead Publishing, 2017, pp. 233-253.

PART 5: SUPPORTING MATERIALS

S 1: TABLES

Table S 1: PVA samples after the reaction and purification process.















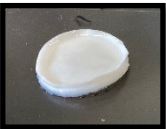




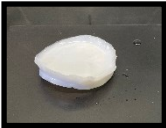


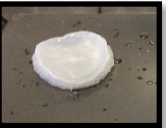


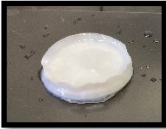




PEG	4 kDa		8 kDa		20 kDa	
PVA \ pH	12	10	12	10	12	10
27 kDa						
	270412	270410	270812	270810	272012	272010
47 kDa						
	470412	470410	470812	470810	472012	472010
61 kDa						
	610412	610410	610812	610810	612012	612010
125 kDa						
	1250412	1250410	1250812	1250810	1252012	1252010
195 kDa						
	1950412	1950410	1950812	1950810	1952012	1952010

Table S 2: Different types of water in the UPW full swollen samples.

	■WH %	■W _{ff} %	■W _{bff} %*
PVA 27 PEG 4	89% ± 3%	81% ± 6%	95% ± 3%
PEG 8	84% ± 0%	69% ± 5%	81% ± 26%
PEG 20	75% ± 5%	57% ± 6%	87% ± 16%
PVA 47 PEG 4	94% ± 5%	80% ± 3%	96% ± 1%
PEG 8	79% ± 3%	62% ± 17%	82% ± 24%
PEG 20	67% ± 7%	57% ± 4%	88% ± 15%
PVA 61 PEG 4	83% ± 2%	71% ± 17%	97% ± 3%
PEG 8	77% ± 3%	62% ± 2%	96% ± 4%
PEG 20	67% ± 3%	46% ± 6%	98% ± 1%
PVA 125 PEG 4	75% ± 2%	63% ± 9%	98% ± 0%
PEG 8	74% ± 1%	56% ± 3%	96% ± 1%
PEG 20	72% ± 6%	51% ± 10%	96% ± 1%
PVA 195 PEG 4	74% ± 3%	58% ± 7%	98% ± 1%
PEG 8	70% ± 4%	49% ± 4%	95% ± 4%
PEG 20	87% ± 17%	50% ± 7%	97% ± 1%

* Data are not statistically different $p > 0.05$.

S 2: FIGURES

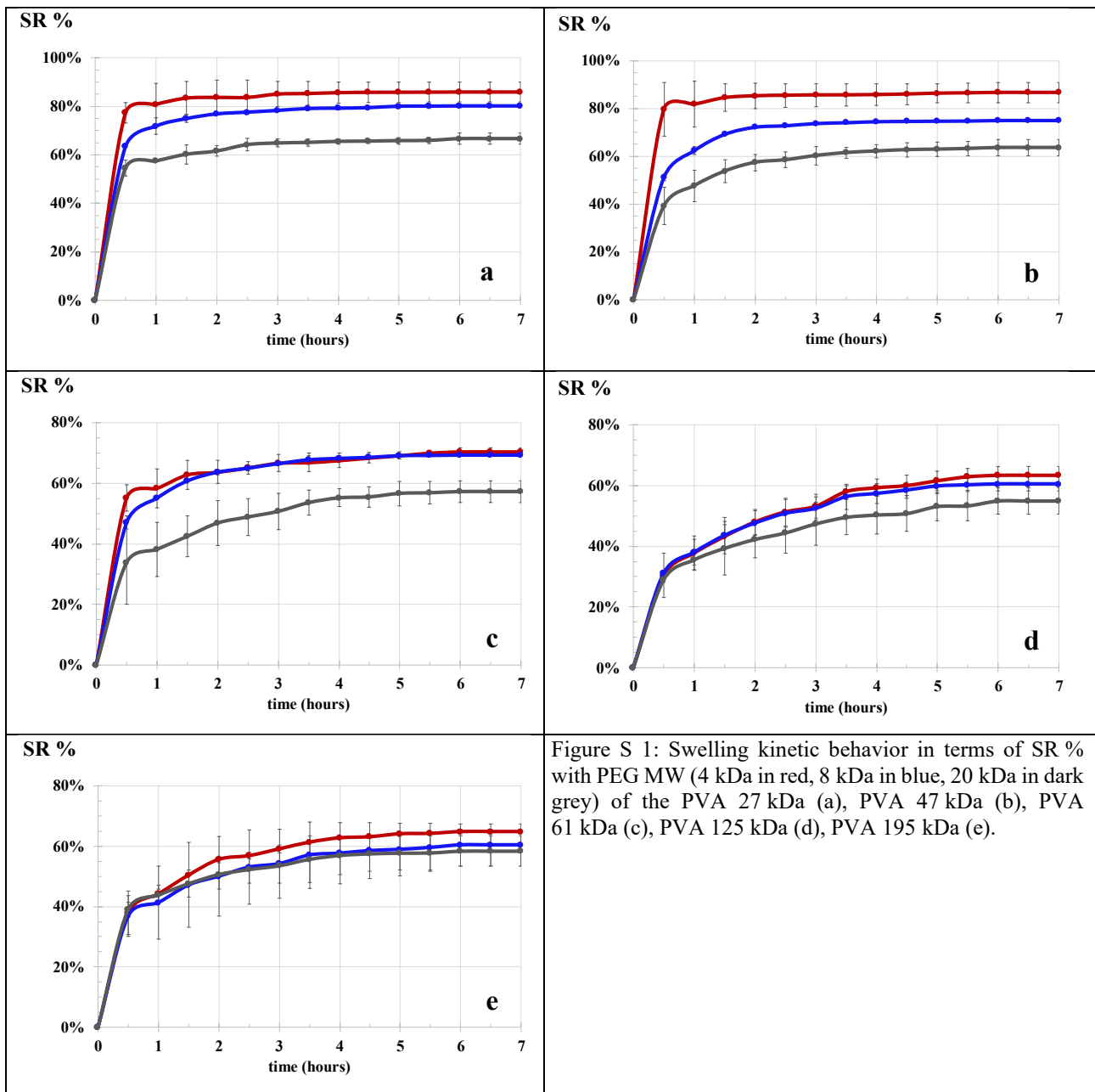


Figure S 1: Swelling kinetic behavior in terms of SR % with PEG MW (4 kDa in red, 8 kDa in blue, 20 kDa in dark grey) of the PVA 27 kDa (a), PVA 47 kDa (b), PVA 61 kDa (c), PVA 125 kDa (d), PVA 195 kDa (e).

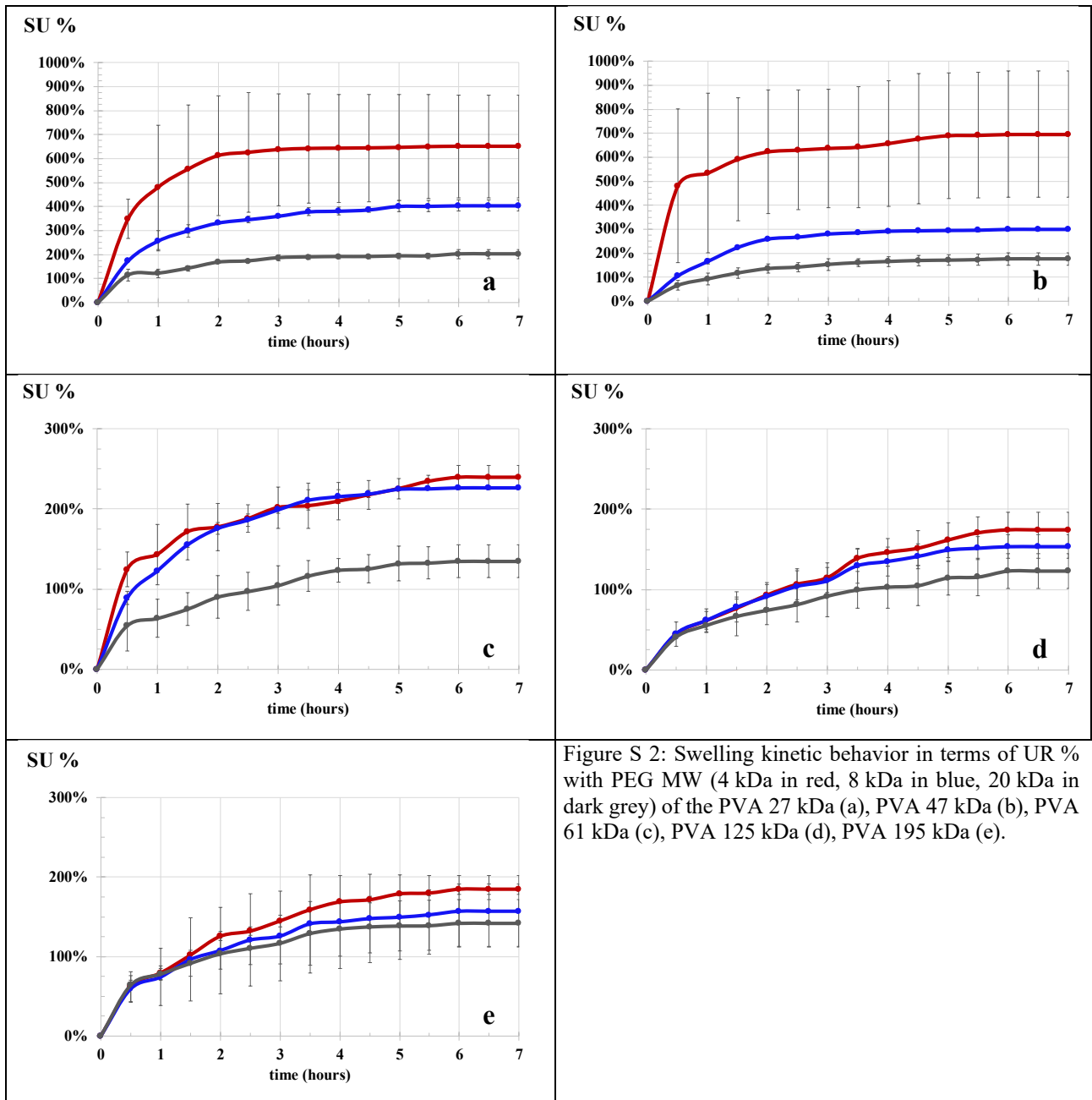
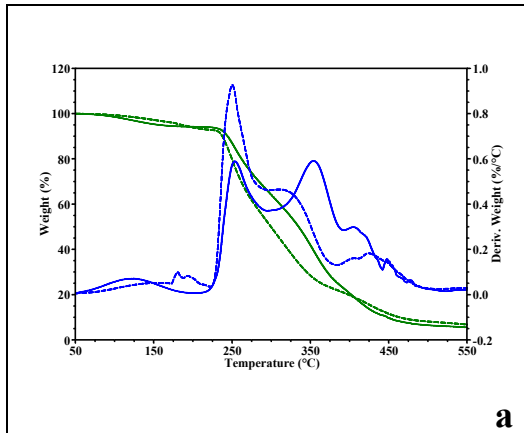
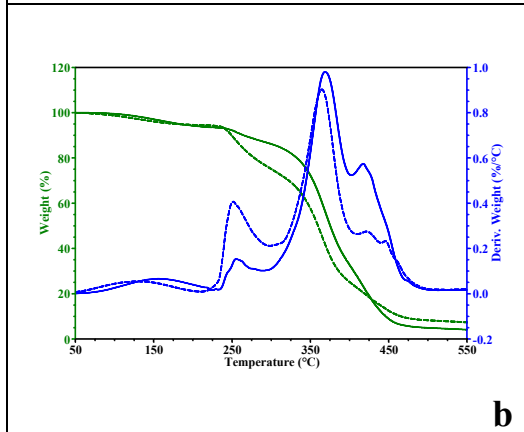


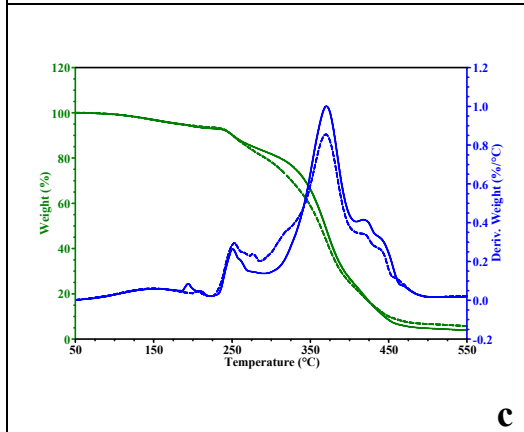
Figure S 2: Swelling kinetic behavior in terms of UR % with PEG MW (4 kDa in red, 8 kDa in blue, 20 kDa in dark grey) of the PVA 27 kDa (a), PVA 47 kDa (b), PVA 61 kDa (c), PVA 125 kDa (d), PVA 195 kDa (e).



a

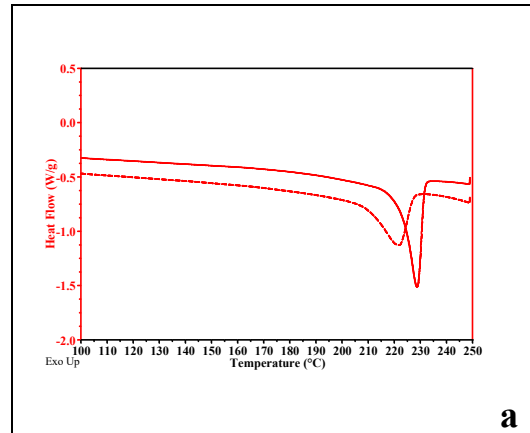


b

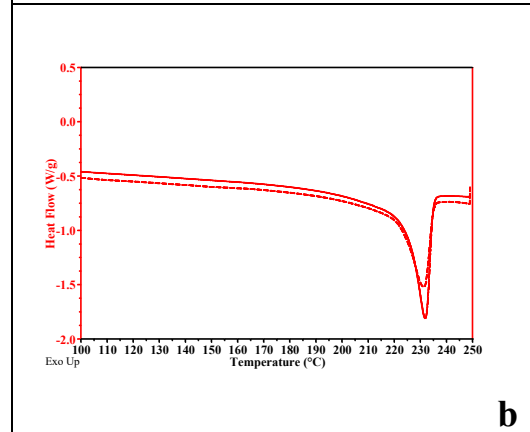


c

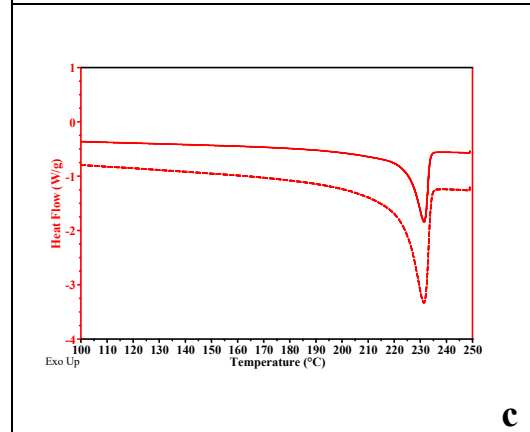
Figure S 3: TGA and SDT of the 27 kDa PVA pH 10 (solid line) and pH 12 (dash line), with the PEG: 4 kDa in the first row, 8 kDa in the second one, 20 kDa in the last one.



a



b



c

Figure S 4: DSC of the 27 kDa PVA pH 10 (solid line) and pH 12 (dash line), with the PEG: 4 kDa in the first row, 8 kDa in the second one, 20 kDa in the last one.

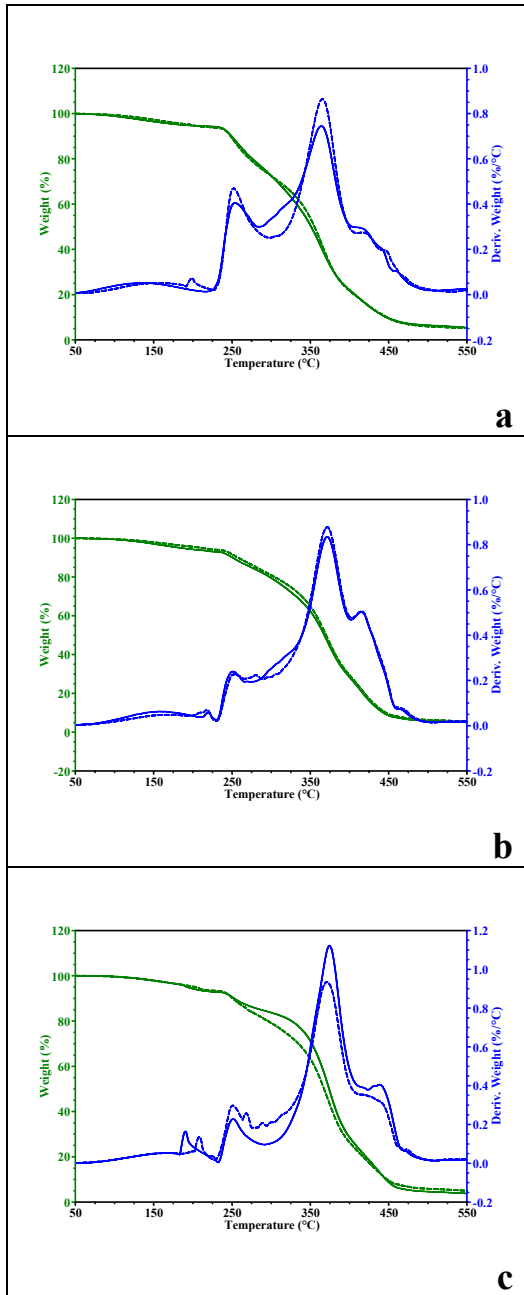


Figure S 5: TGA and SDT of the 47 kDa PVA pH 10 (solid line) and pH 12 (dash line), with the PEG: 4 kDa in the first row, 8 kDa in the second one, 20 kDa in the last one.

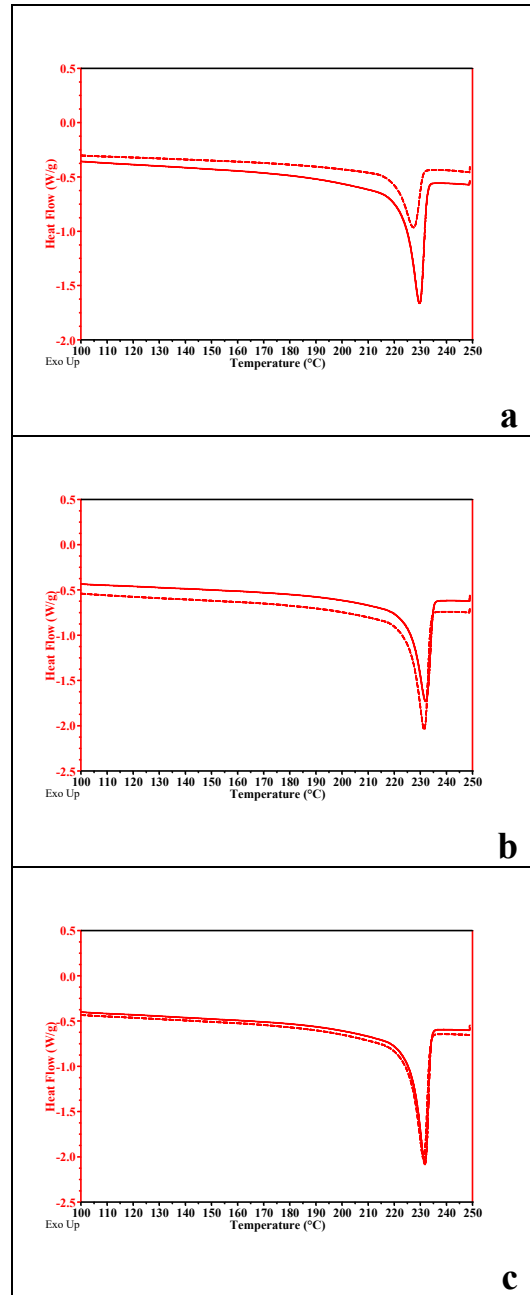


Figure S 6: DSC of the 47 kDa pH 10 (solid line) and pH 12 (dash line), with the PEG: 4 kDa in the first row, 8 kDa in the second one, 20 kDa in the last one.

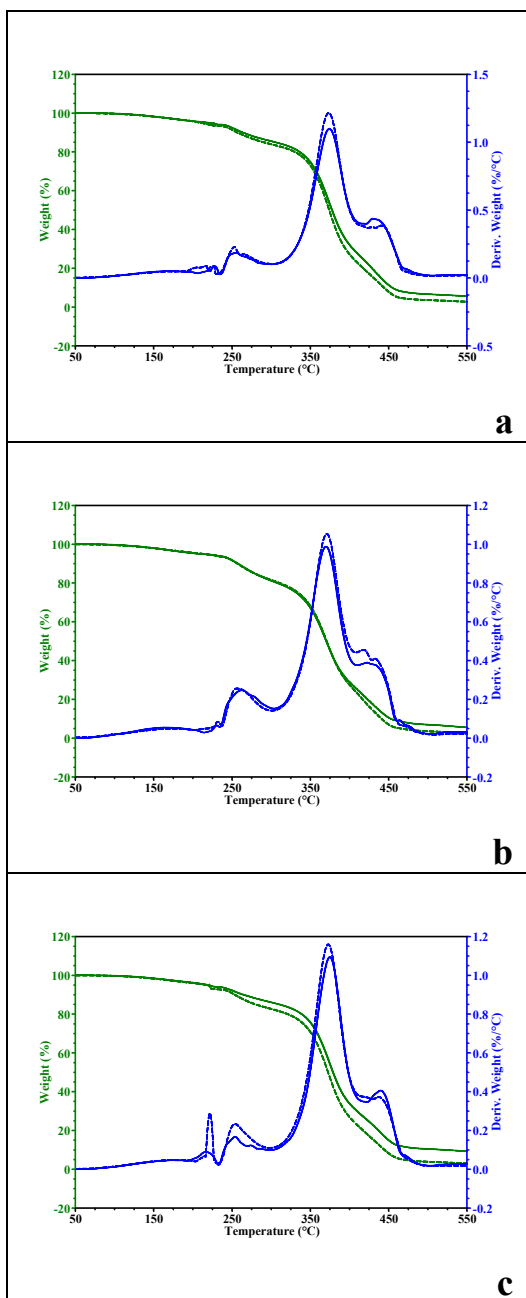


Figure S 7: TGA and SDT of the 61 kDa pH 10 (solid line) and pH 12 (dash line), with the PEG: 4 kDa in the first row, 8 kDa in the second one, 20 kDa in the last one.

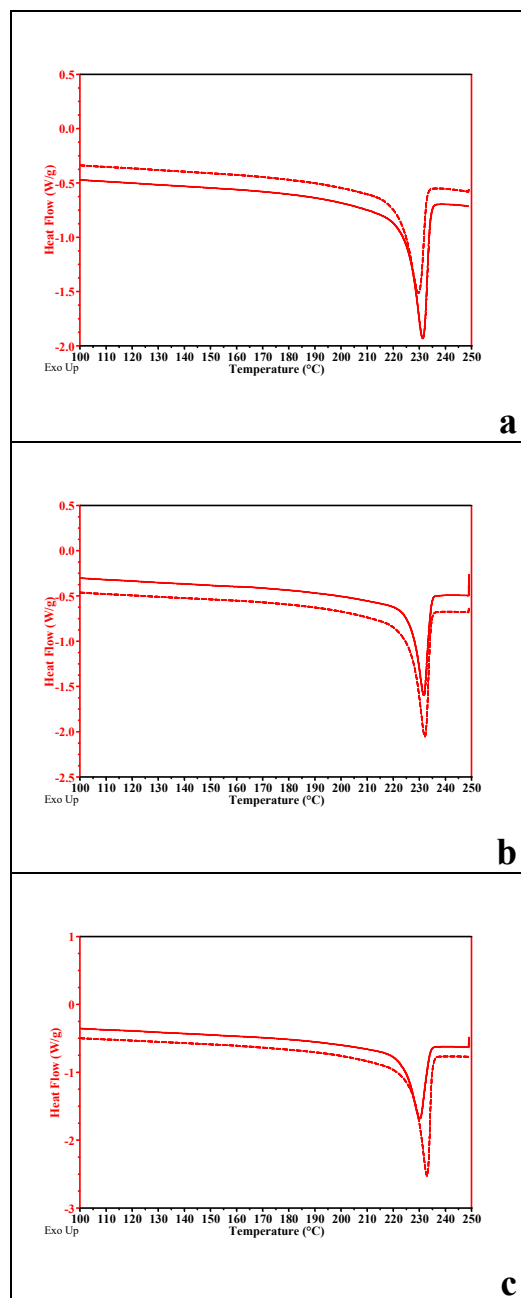
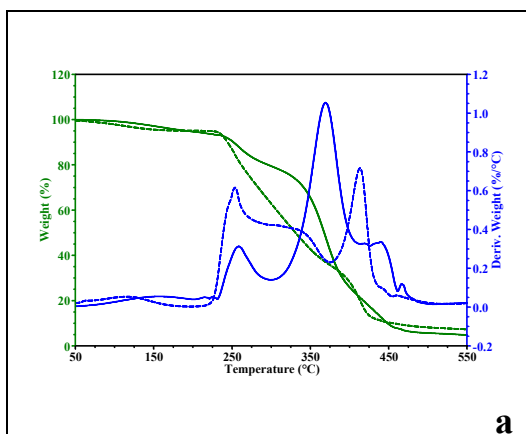
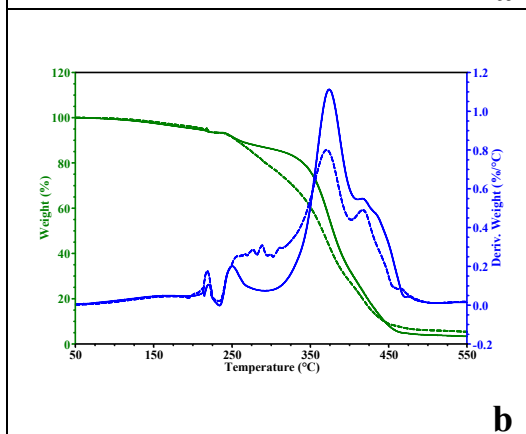


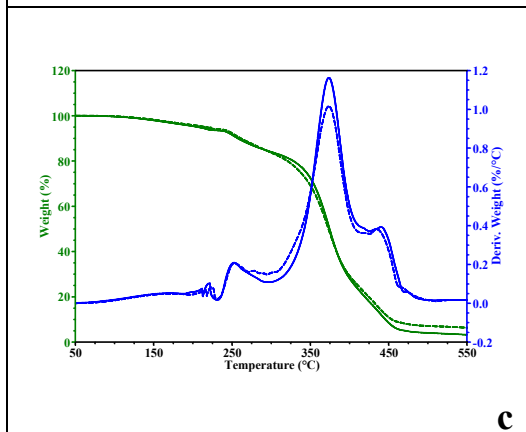
Figure S 8: DSC of the 61 kDa pH 10 (solid line) and pH 12 (dash line), with the PEG: 4 kDa in the first row, 8 kDa in the second one, 20 kDa in the last one.



a

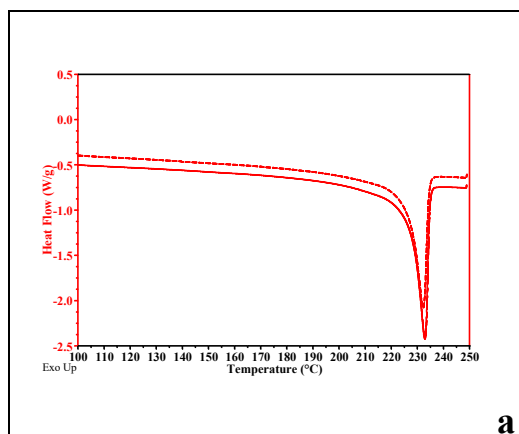


b

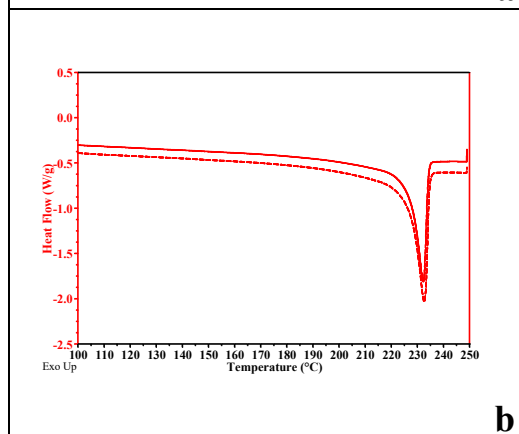


c

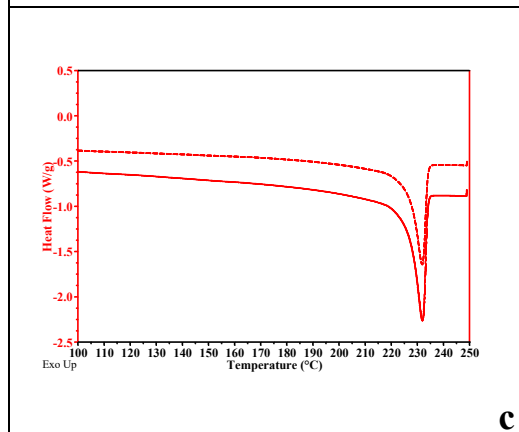
Figure S 9: TGA and SDT of the 125 kDa pH 10 (solid line) and pH 12 (dash line), with the PEG: 4 kDa in the first row, 8 kDa in the second one, 20 kDa in the last one.



a

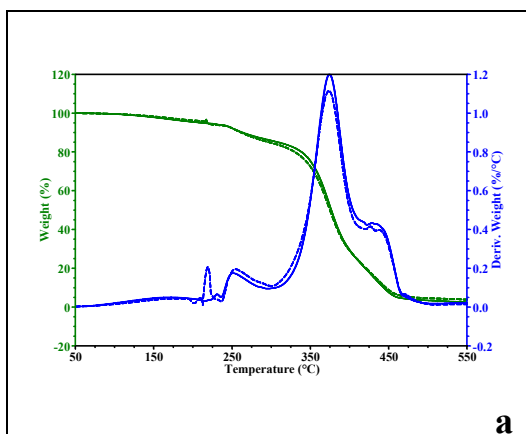


b

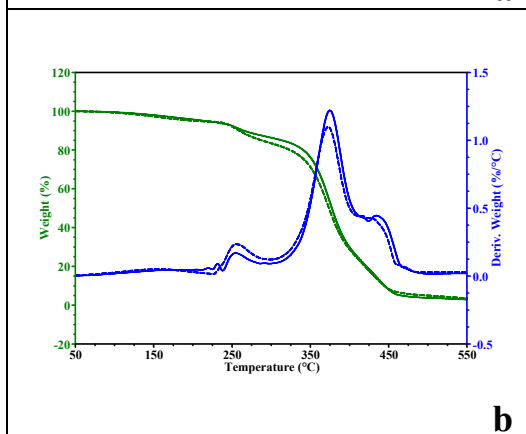


c

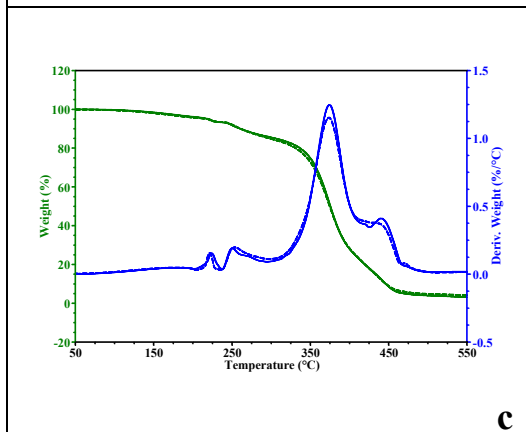
Figure S 10: DSC of the 125 kDa pH 10 (solid line) and pH 12 (dash line), with the PEG: 4 kDa in the first row, 8 kDa in the second one, 20 kDa in the last one.



a

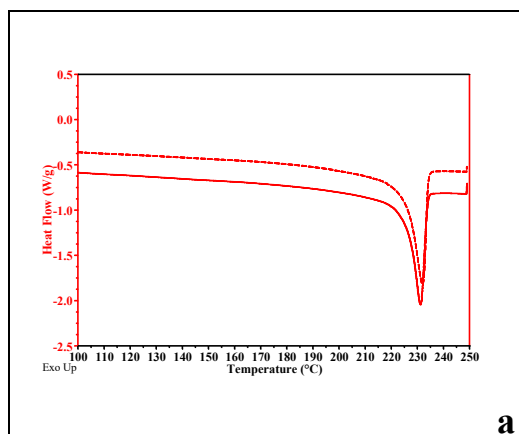


b

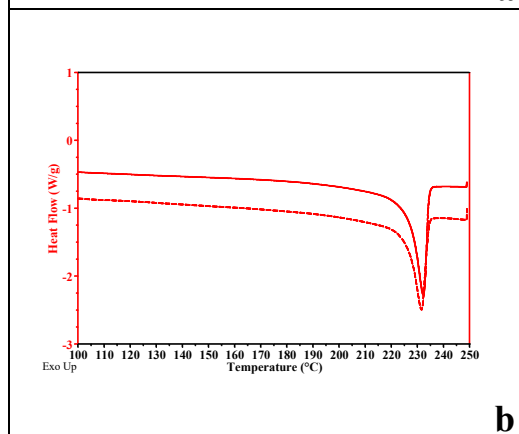


c

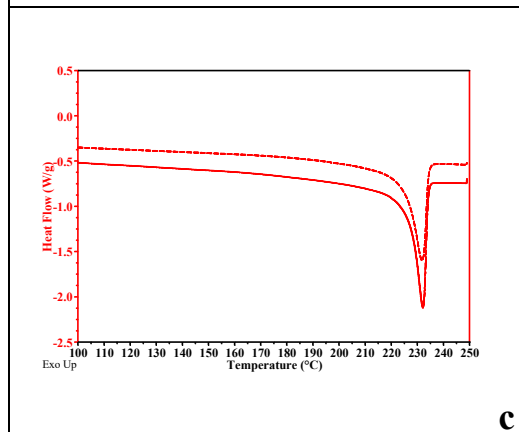
Figure S 11: TGA and SDT of the 195 kDa pH 10 (solid line) and pH 12 (dash line), with the PEG: 4 kDa in the first row, 8 kDa in the second one, 20 kDa in the last one.



a



b



c

Figure S 12: DSC of the 195 kDa pH 10 (solid line) and pH 12 (dash line), with the PEG: 4 kDa in the first row, 8 kDa in the second one, 20 kDa in the last one.

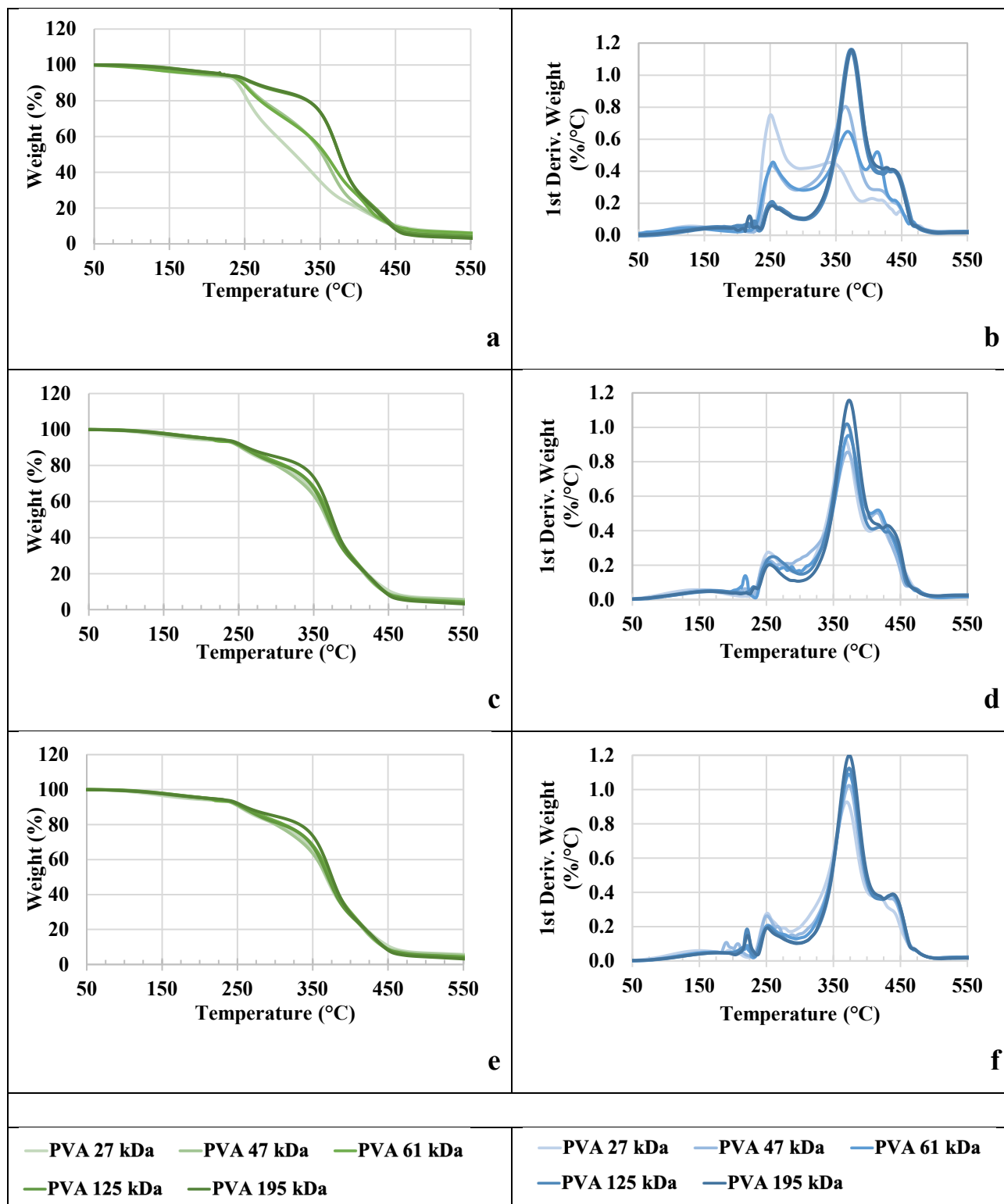


Figure S 13: Averaged TGA (a, c, e) and SDT (b, d, f), grouped by PEG: 4 kDa in the first row, 8 kDa in the second one, 20 kDa in the last one.

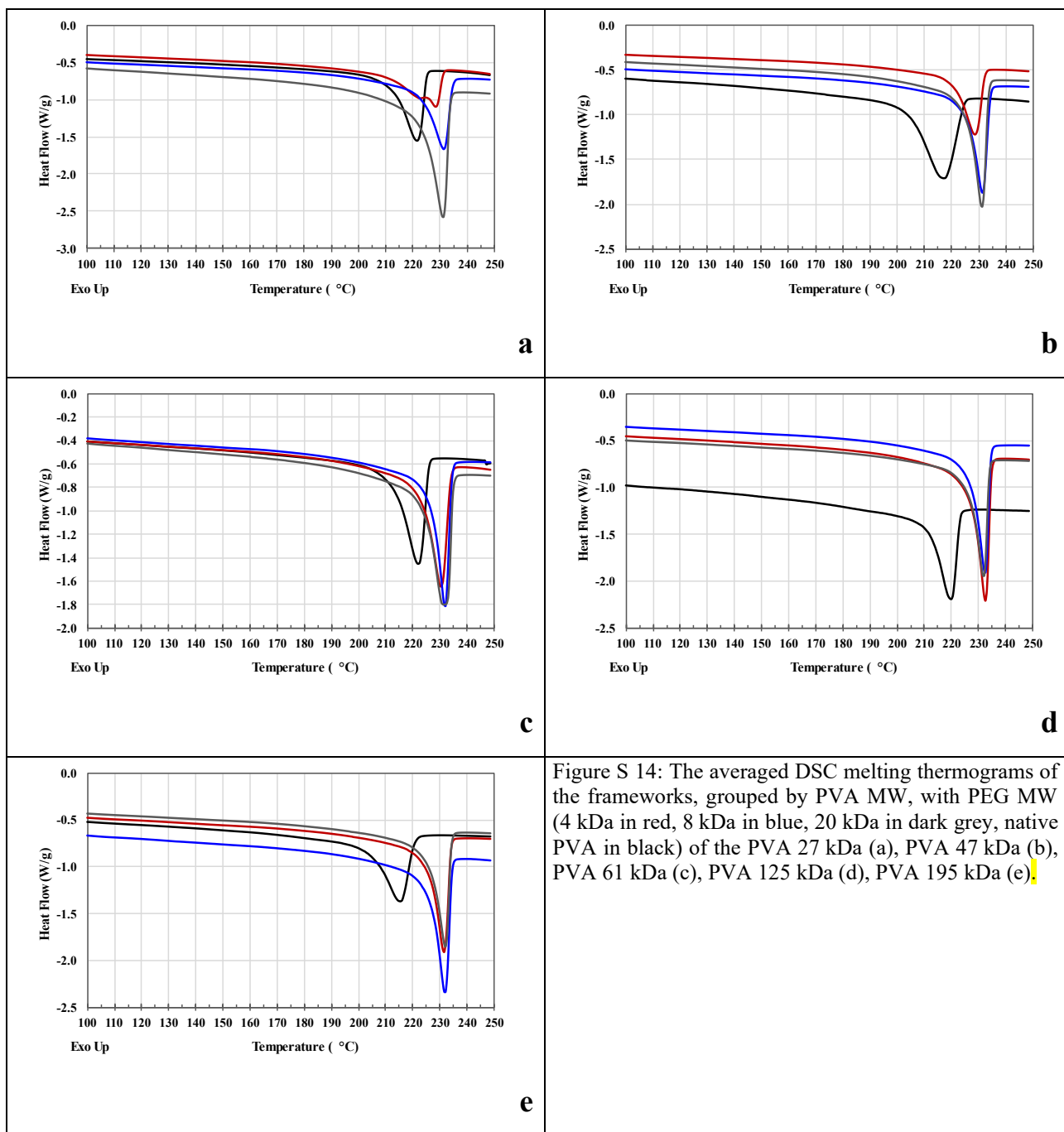


Figure S 14: The averaged DSC melting thermograms of the frameworks, grouped by PVA MW, with PEG MW (4 kDa in red, 8 kDa in blue, 20 kDa in dark grey, native PVA in black) of the PVA 27 kDa (a), PVA 47 kDa (b), PVA 61 kDa (c), PVA 125 kDa (d), PVA 195 kDa (e).

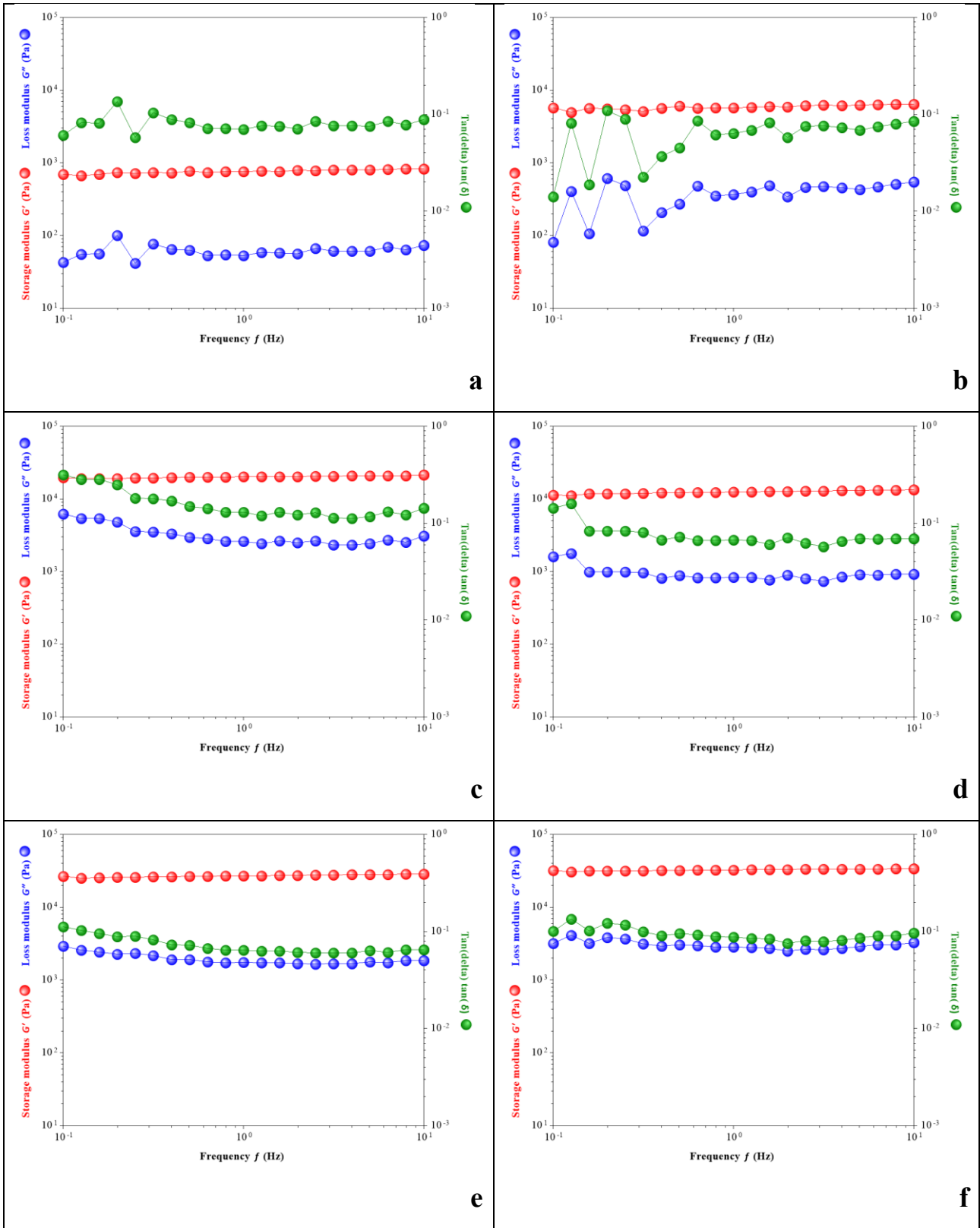


Figure S 15: Shear moduli of PVA 27 kDa based frameworks in frequency sweep test at pH 10 (a, c, e) and pH 12 (b, d, f) and PEG 4 kDa (a, b) PEG 8 kDa (c, d) and PEG 20 kDa (e, f).

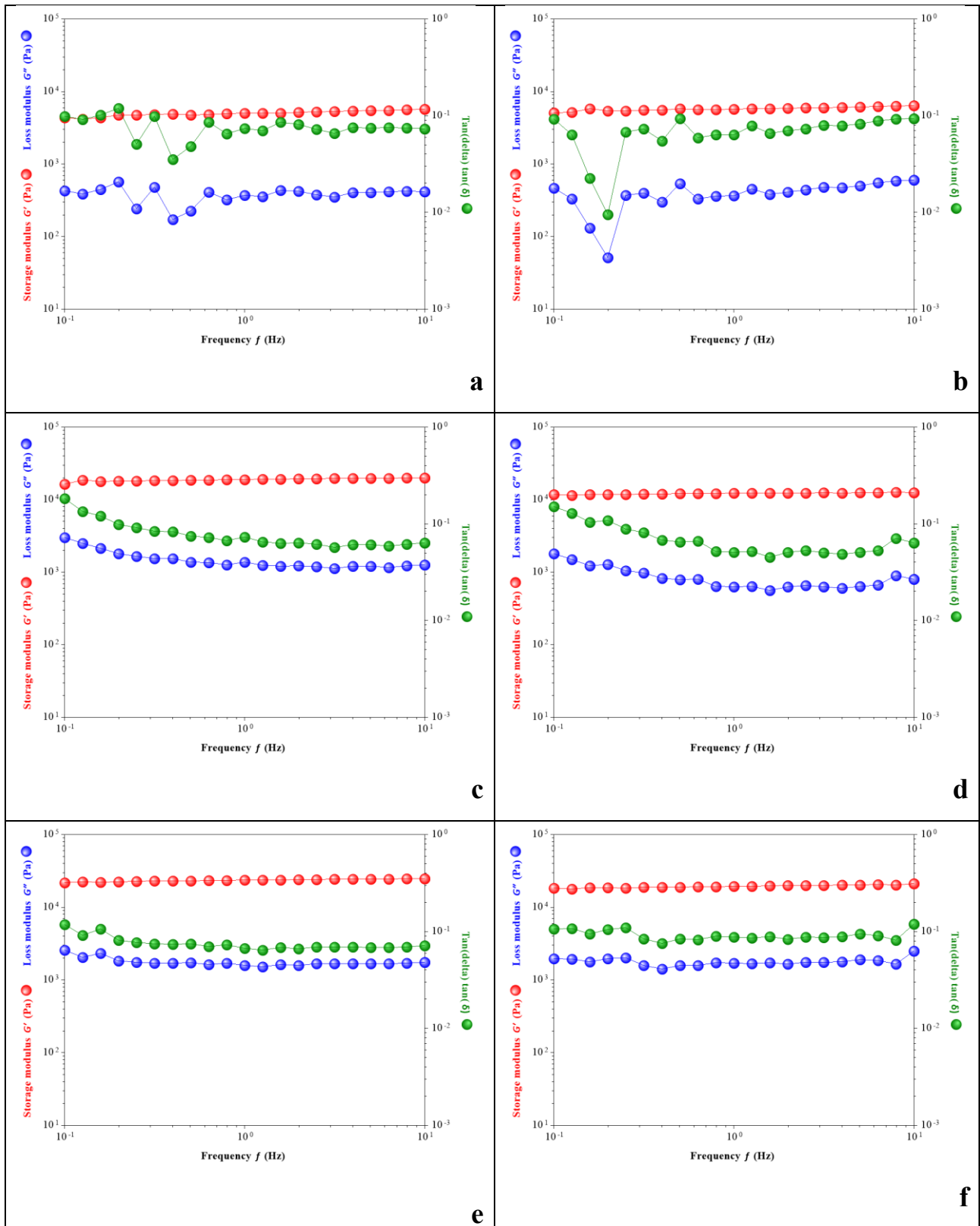


Figure S 16: Shear moduli of PVA 47 kDa based frameworks in frequency sweep test at pH 10 (a, c, e) and pH 12 (b, d, f) and PEG 4 kDa (a, b) PEG 8 kDa (c, d) and PEG 20 kDa (e, f).

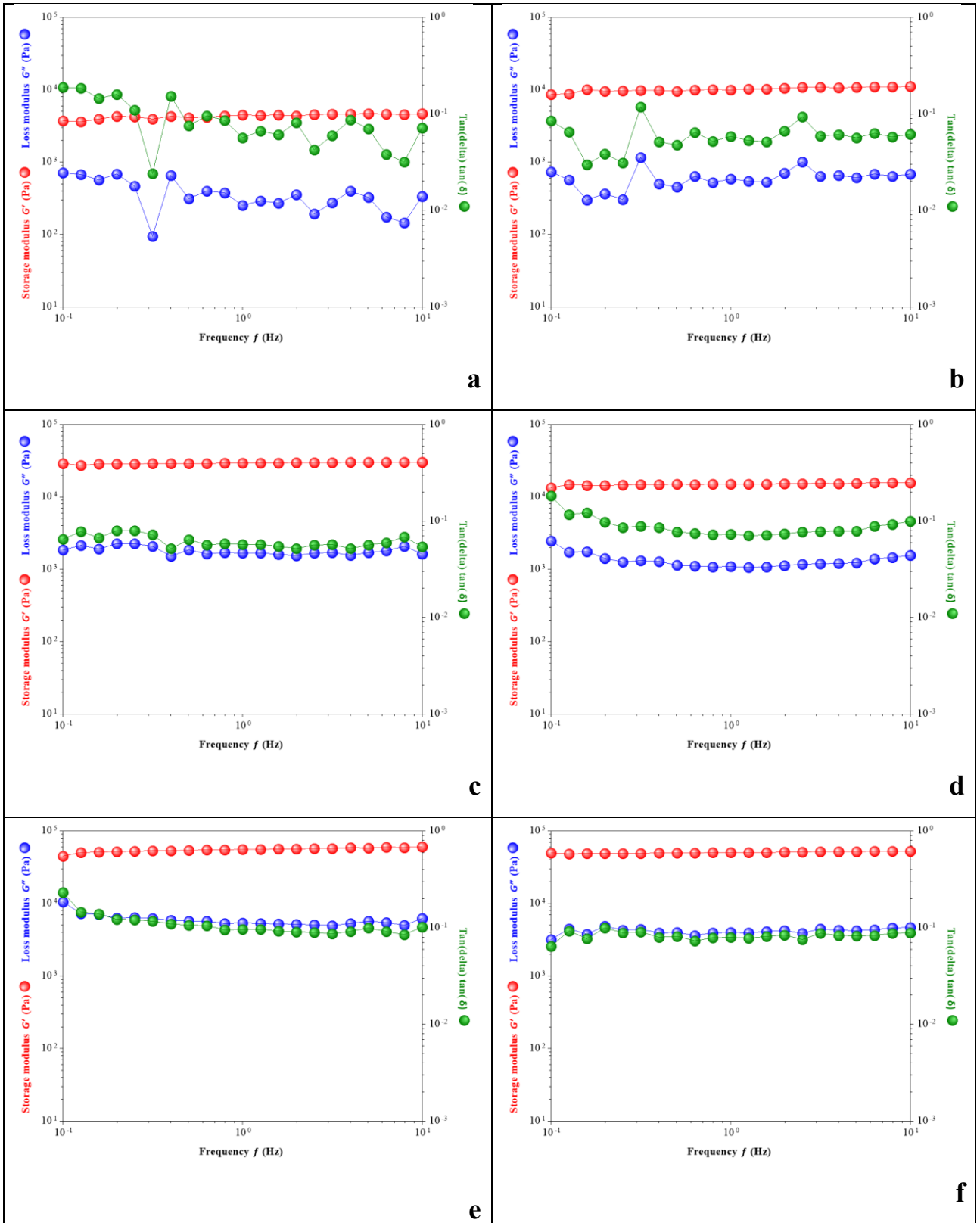


Figure S 17: Shear moduli of PVA 61 kDa based frameworks in frequency sweep test at pH 10 (a, c, e) and pH 12 (b, d, f) and PEG 4 kDa (a, b) PEG 8 kDa (c, d) and PEG 20 kDa (e, f).

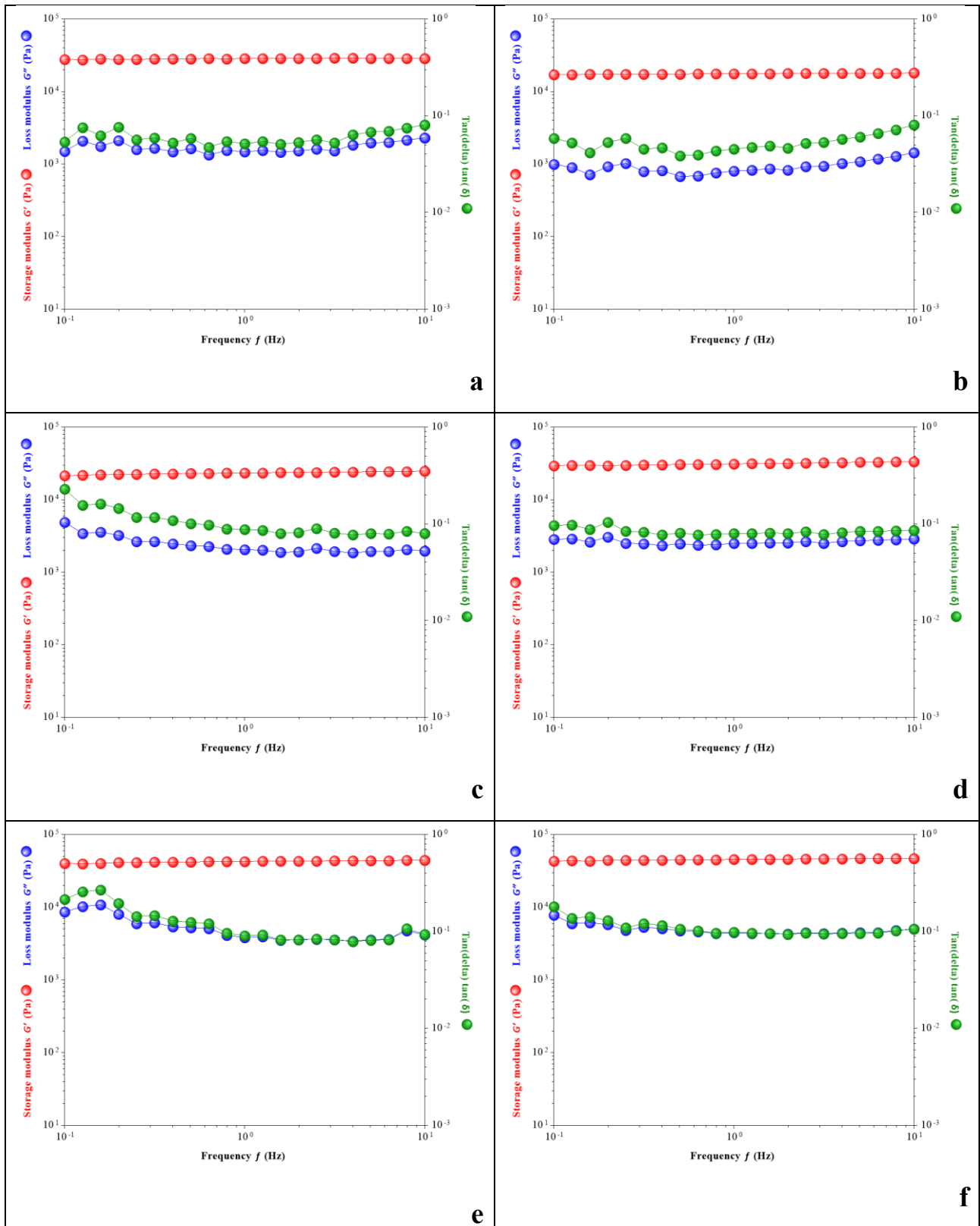


Figure S 18: Shear moduli of PVA 125 kDa based frameworks in frequency sweep test at pH 10 (a, c, e) and pH 12 (b, d, f) and PEG 4 kDa (a, b) PEG 8 kDa (c, d) and PEG 20 kDa (e, f).

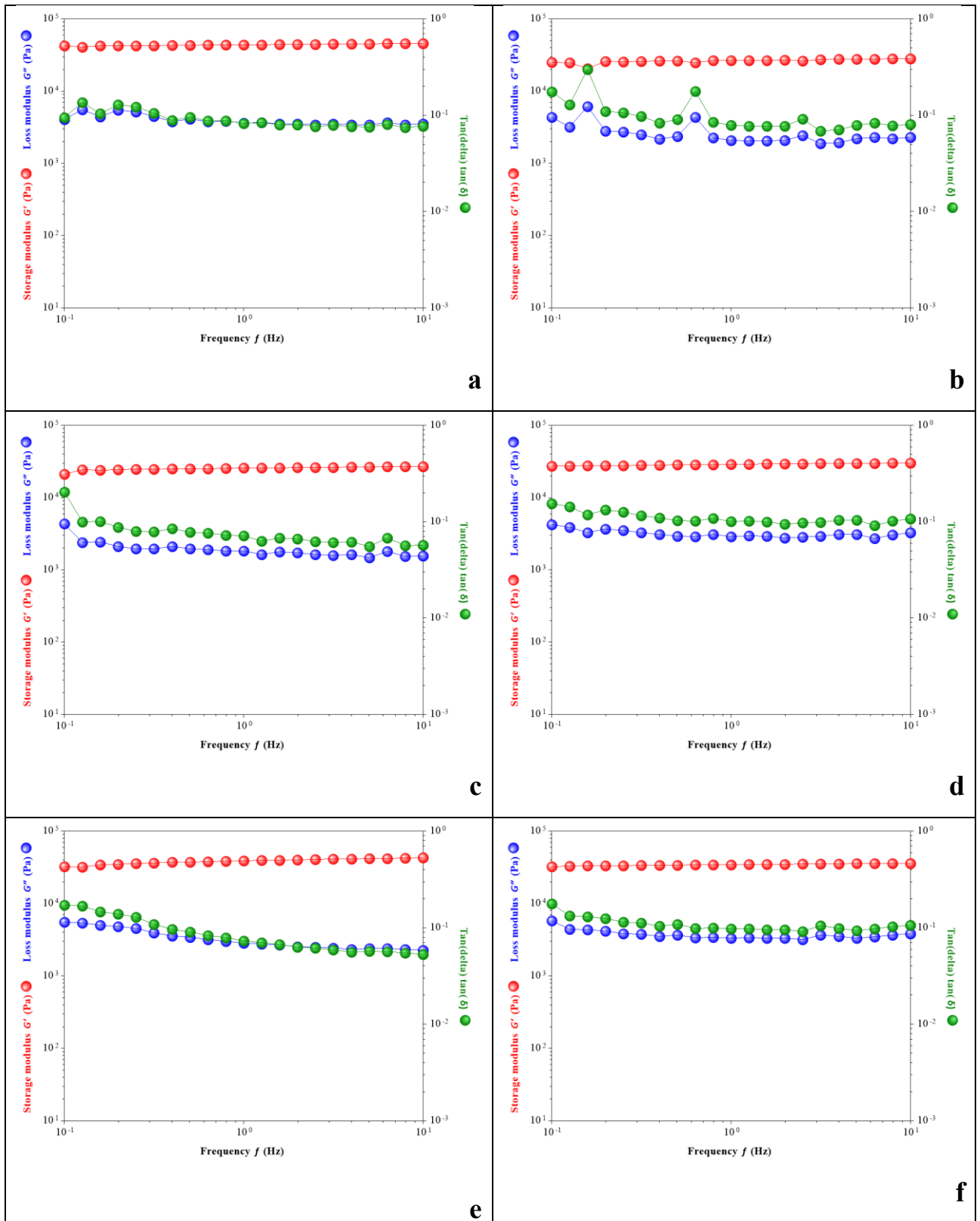


Figure S 19: Shear moduli of PVA 195 kDa based frameworks in frequency sweep test at pH 10 (a, c, e) and pH 12 (b, d, f) and PEG 4 kDa (a, b) PEG 8 kDa (c, d) and PEG 20 kDa (e, f).

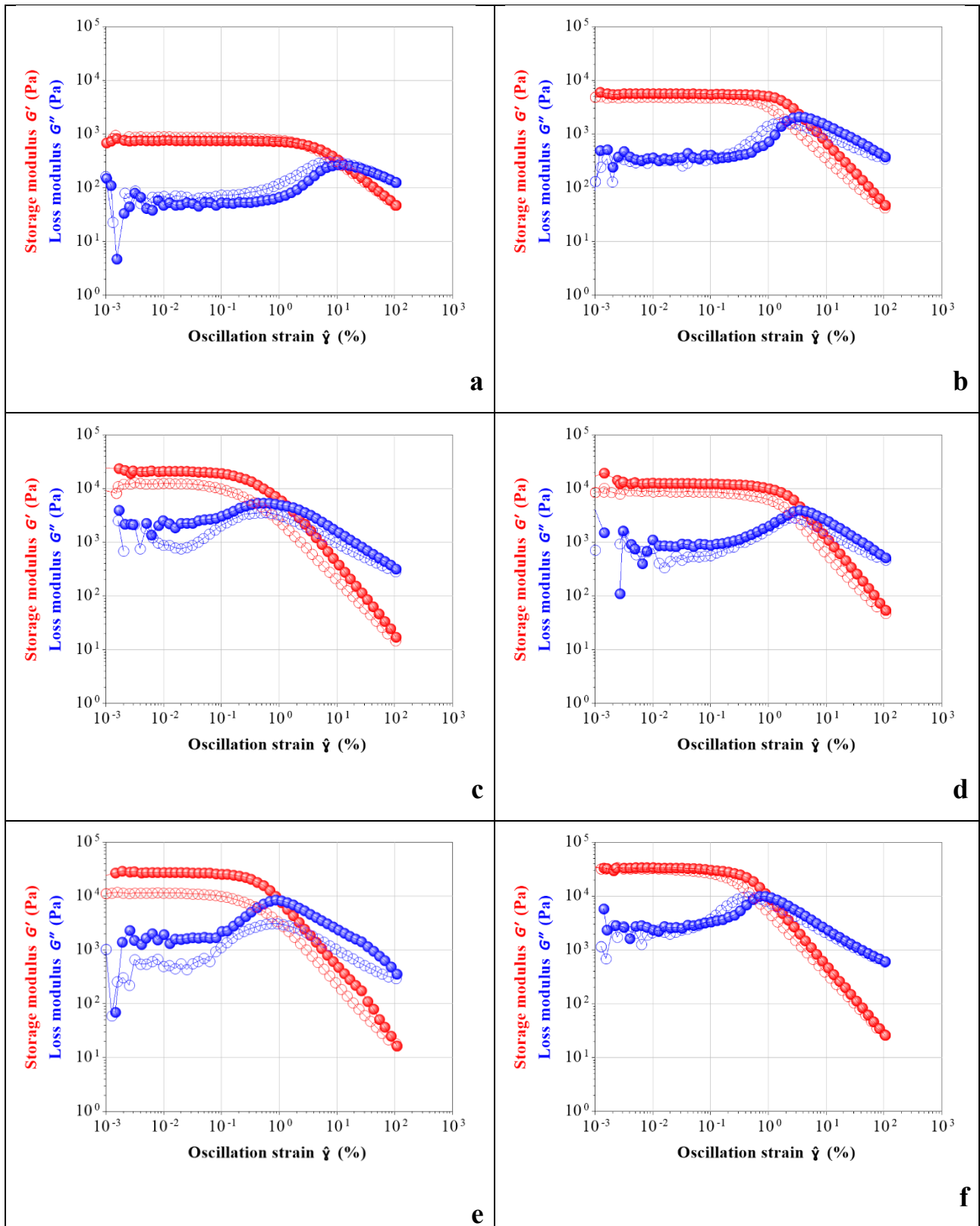


Figure S 20: Shear moduli of PVA 27 kDa based frameworks in loop amplitude sweep test at pH 10 (a, c, e) and pH 12 (b, d, f) and PEG 4 kDa (a, b) PEG 8 kDa (c, d) and PEG 20 kDa (e, f).

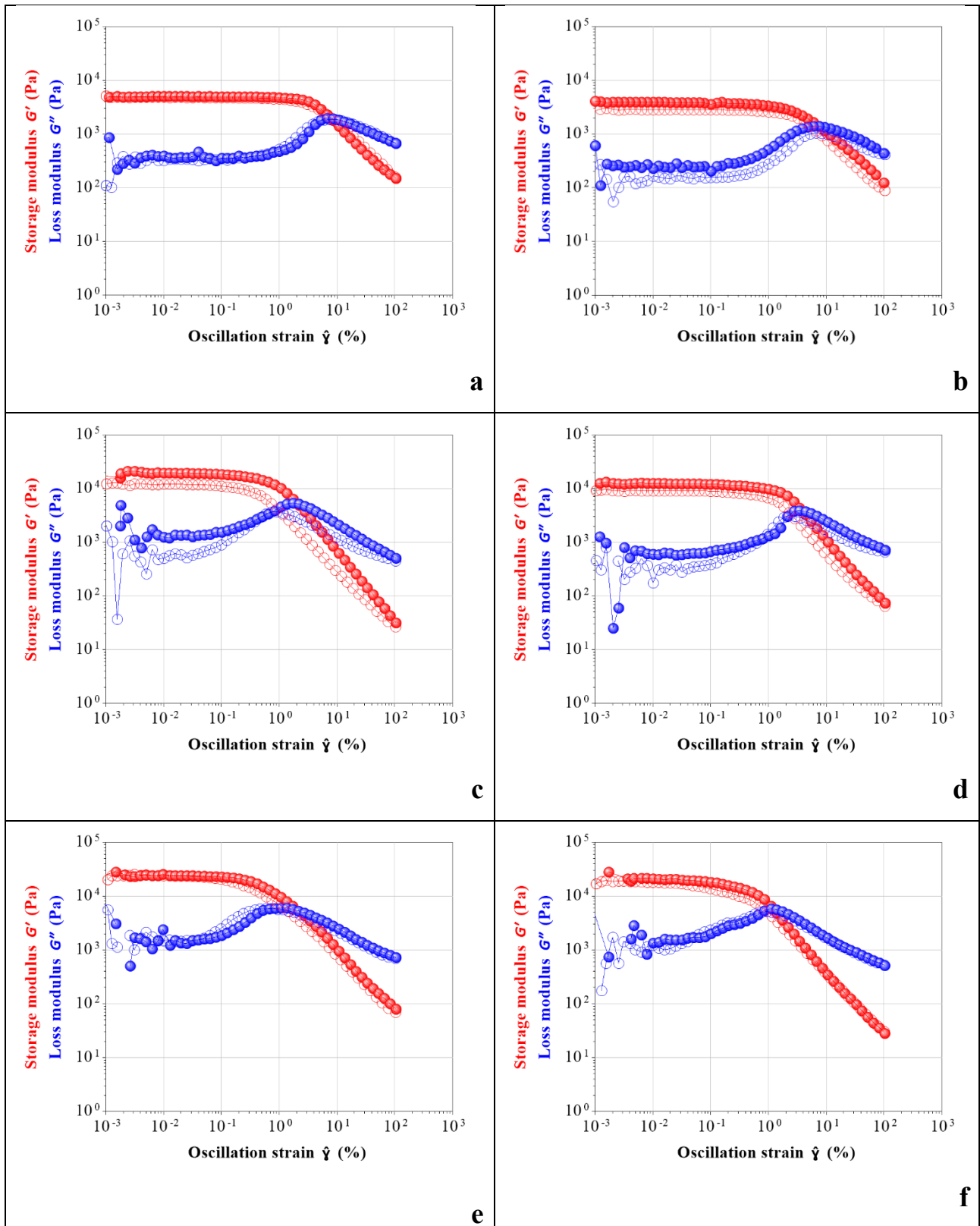


Figure S 21: Shear moduli of PVA 47 kDa based frameworks in loop amplitude sweep test at pH 10 (a, c, e) and pH 12 (b, d, f) and PEG 4 kDa (a, b) PEG 8 kDa (c, d) and PEG 20 kDa (e, f).

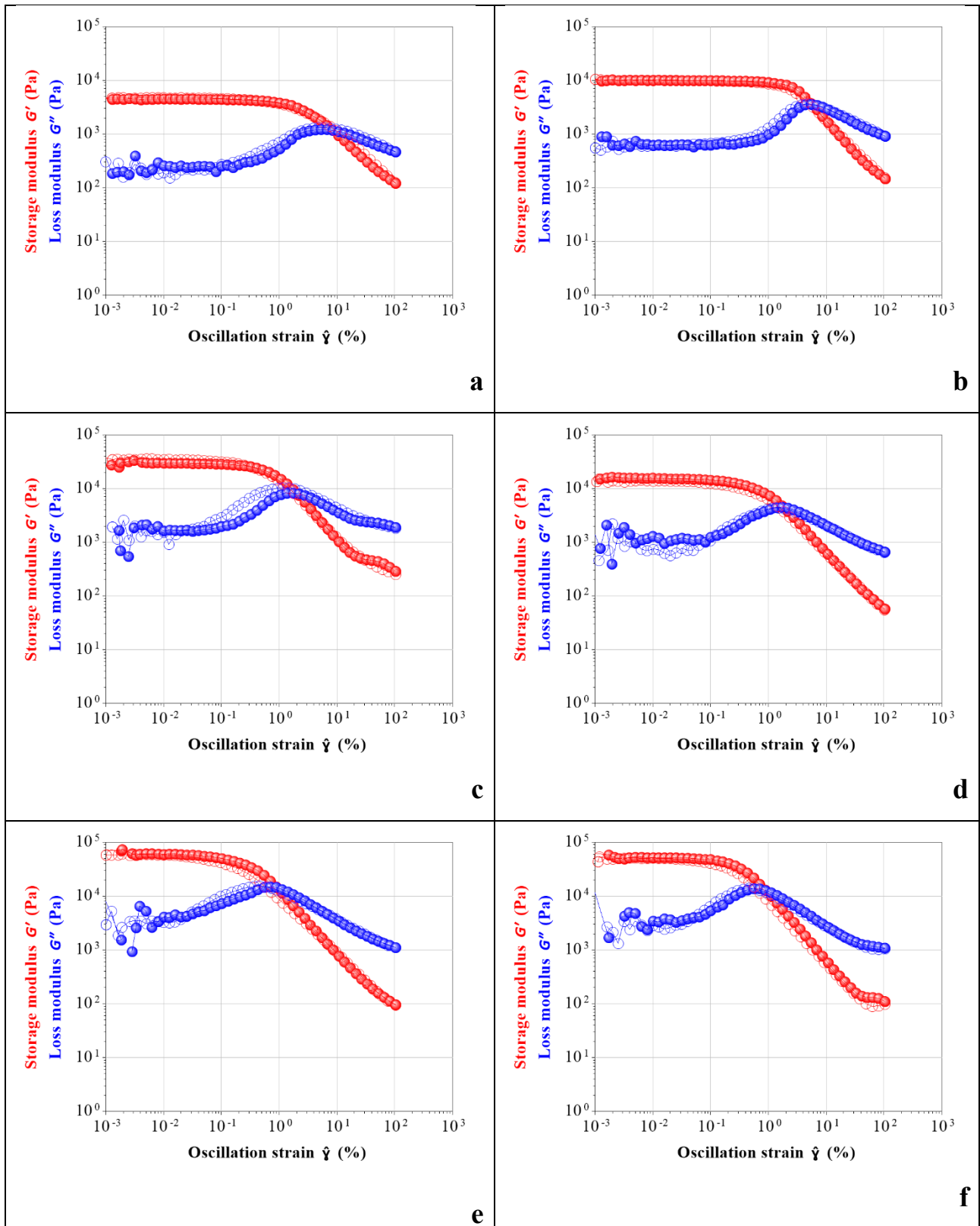


Figure S 22: Shear moduli of PVA 61 kDa based frameworks in loop amplitude sweep test at pH 10 (a, c, e) and pH 12 (b, d, f) and PEG 4 kDa (a, b) PEG 8 kDa (c, d) and PEG 20 kDa (e, f).

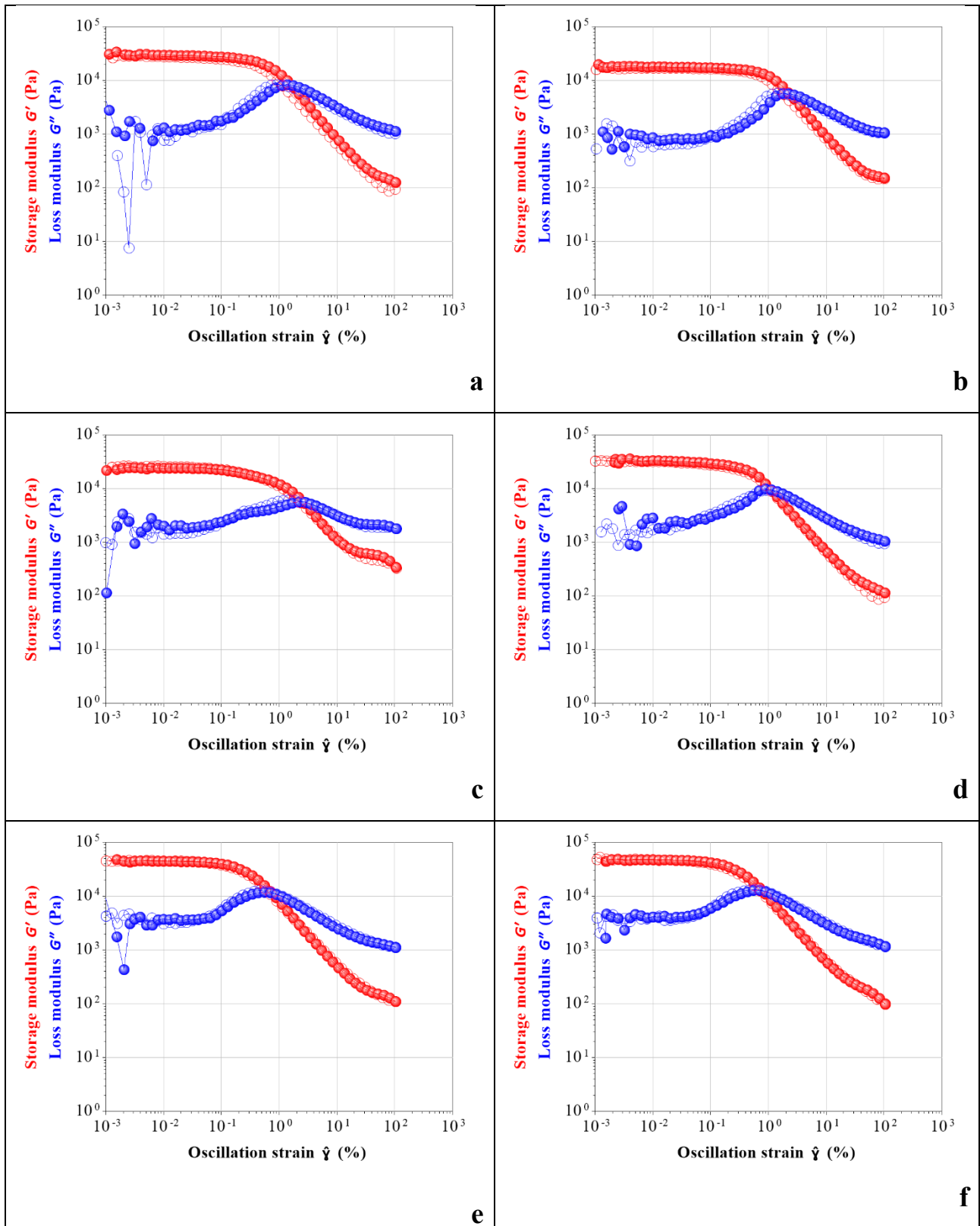


Figure S 23: Shear moduli of PVA 125 kDa based frameworks in loop amplitude sweep test at pH 10 (a, c, e) and pH 12 (b, d, f) and PEG 4 kDa (a, b) PEG 8 kDa (c, d) and PEG 20 kDa (e, f).

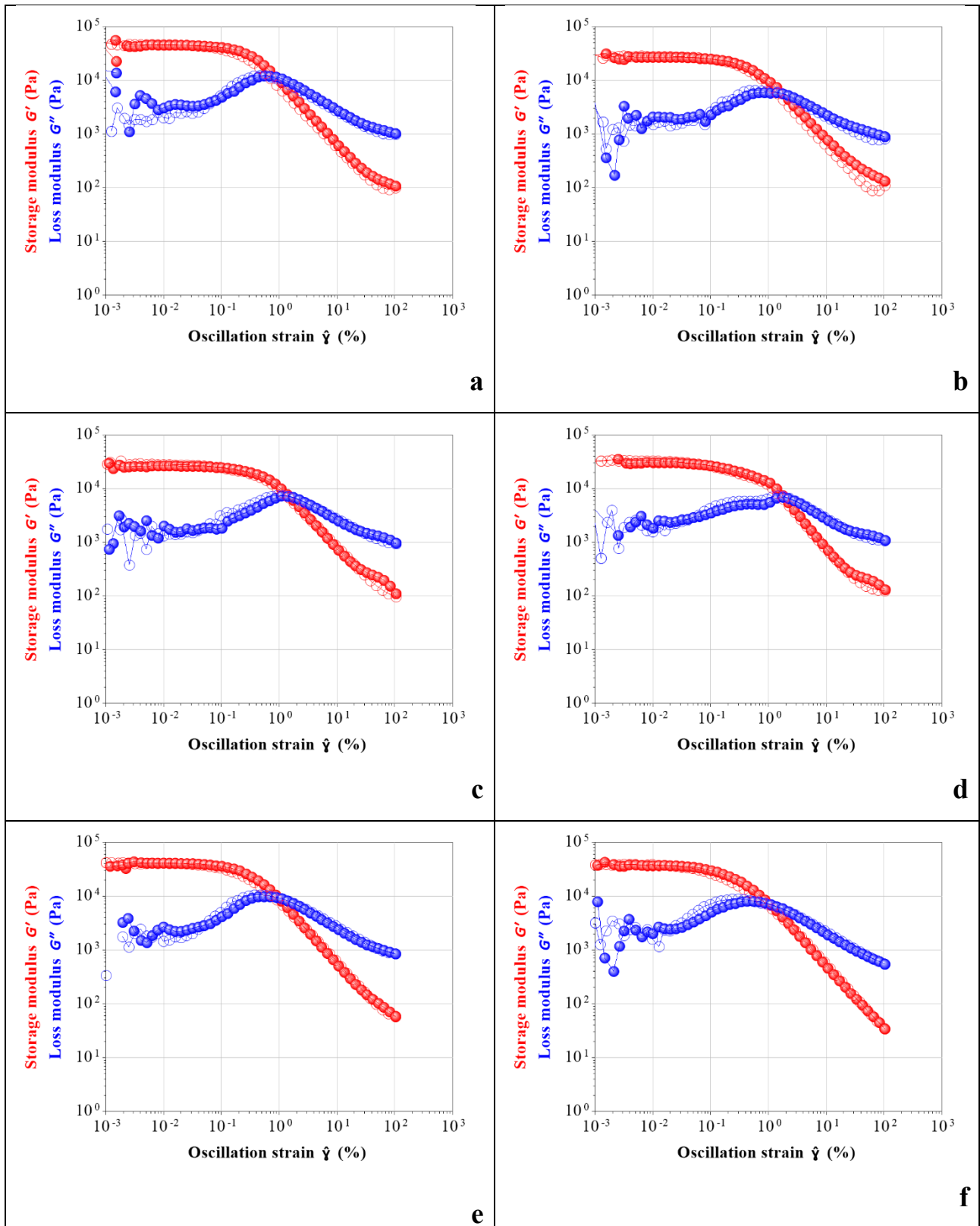


Figure S 24: Shear moduli of PVA 195 kDa based frameworks in loop amplitude sweep test at pH 10 (a, c, e) and pH 12 (b, d, f) and PEG 4 kDa (a, b) PEG 8 kDa (c, d) and PEG 20 kDa (e, f).

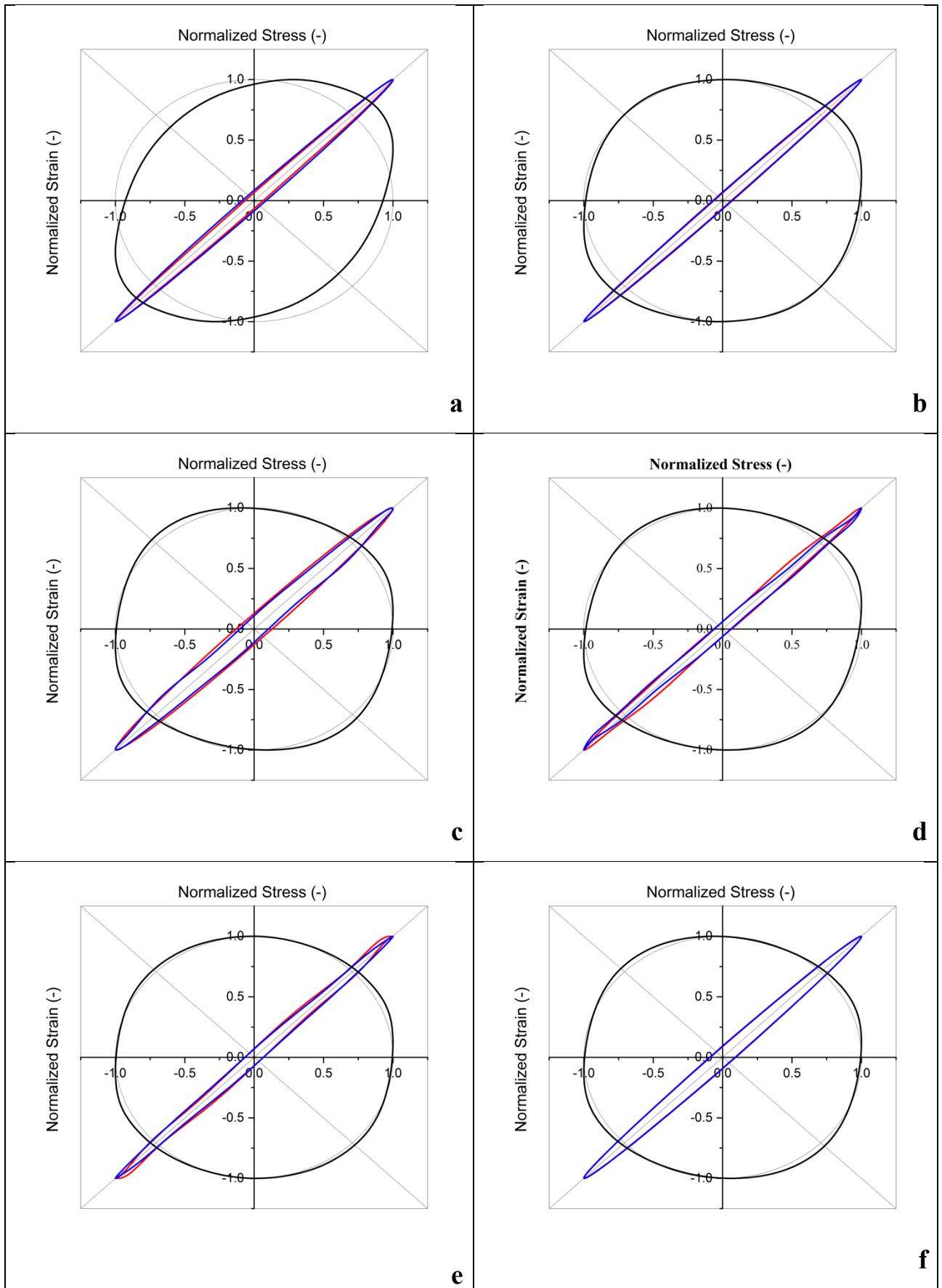


Figure S 25: Normalized Lissajous plot in SAOS and LAOS regime, of PVA 27 kDa based frameworks from loop amplitude sweep test at pH 10 (a, c, e) and pH 12 (b, d, f) and PEG 4 kDa (a, b) PEG 8 kDa (c, d) and PEG 20 kDa (e, f).

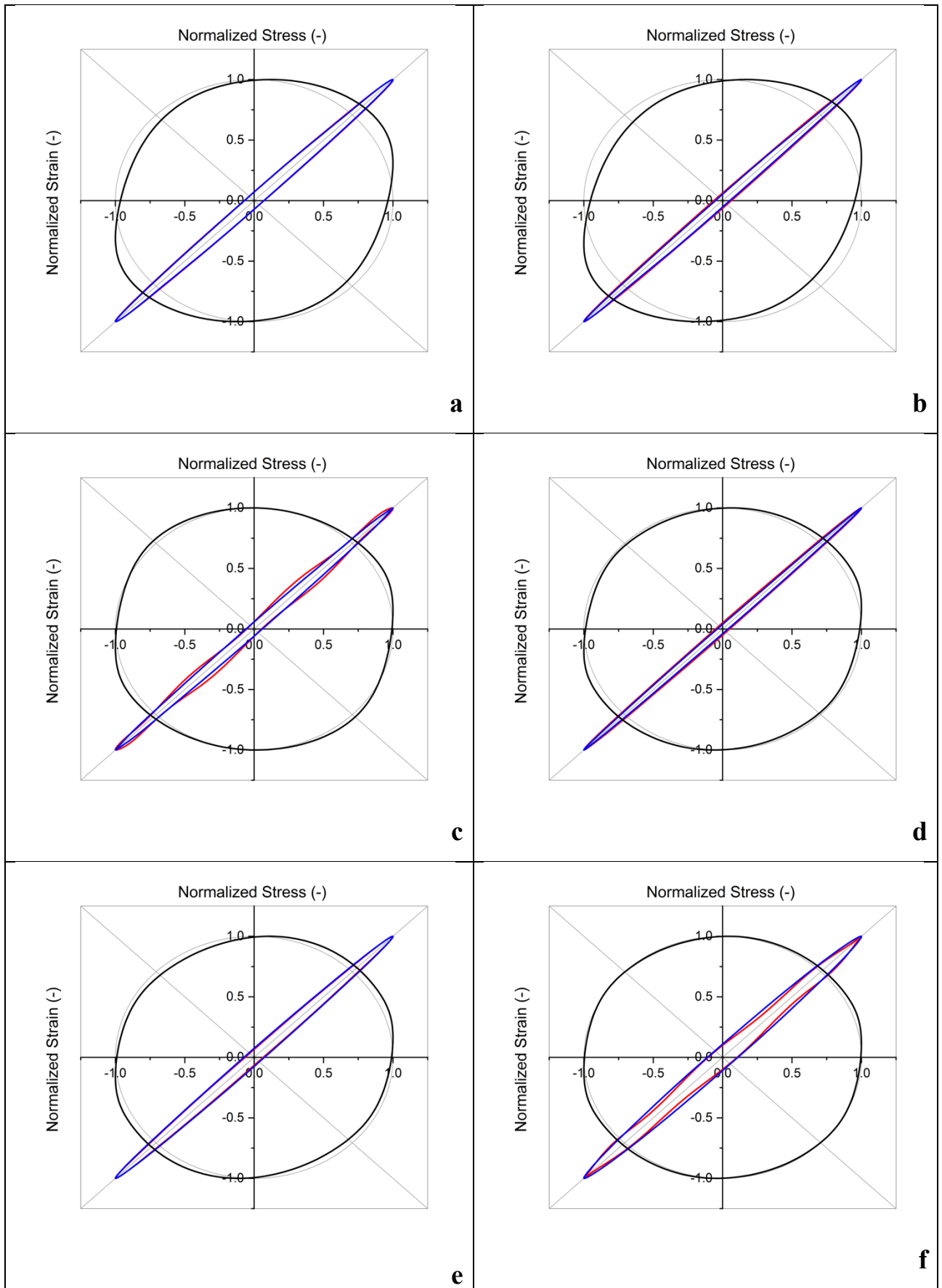


Figure S 26: Normalized Lissajous plot in SAOS and LAOS regime, of PVA 47 kDa based frameworks from loop amplitude sweep test at pH 10 (a, c, e) and pH 12 (b, d, f) and PEG 4 kDa (a, b) PEG 8 kDa (c, d) and PEG 20 kDa (e, f).

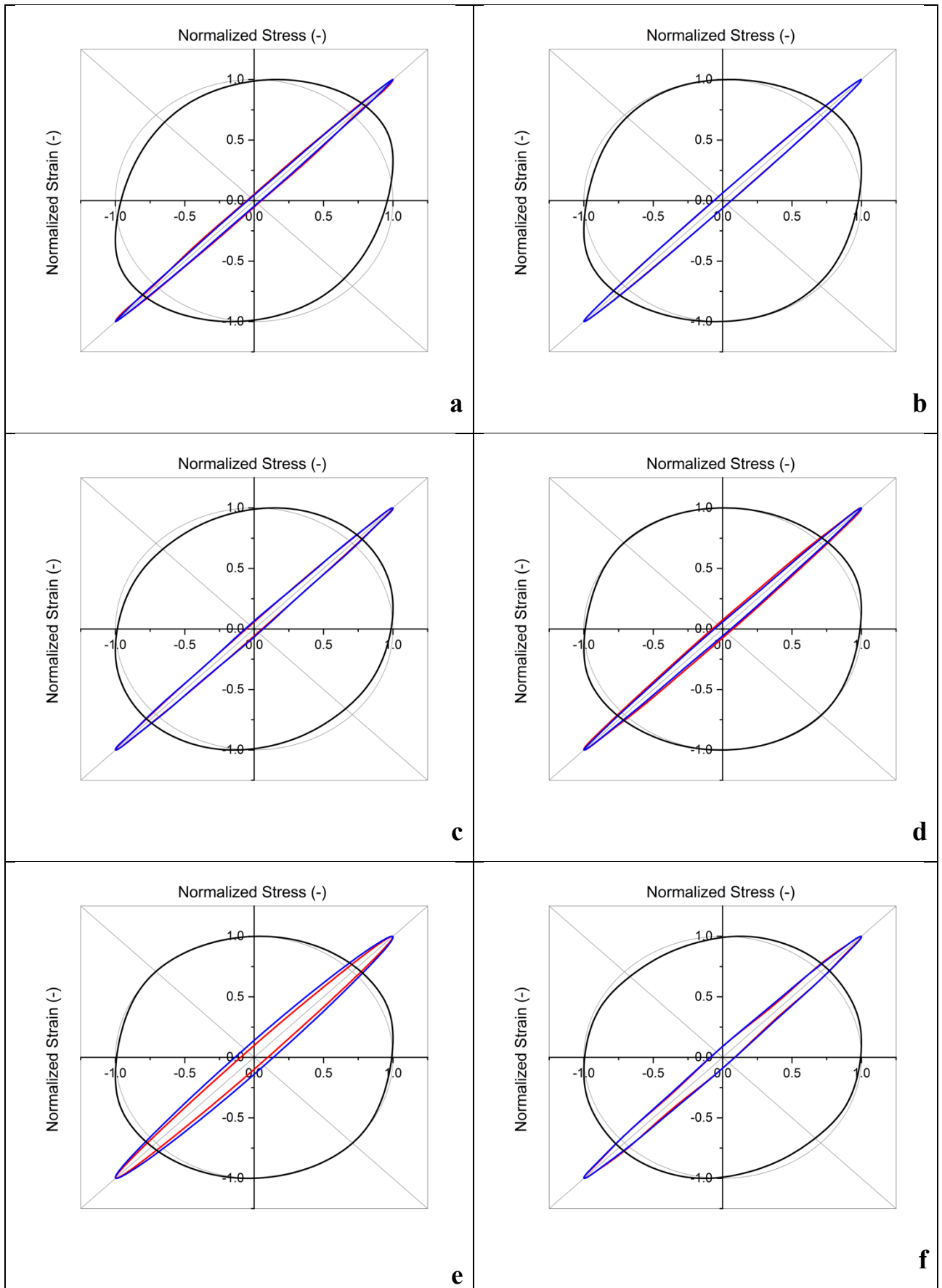


Figure S 27: Normalized Lissajous plot in SAOS and LAOS regime, of PVA 61 kDa based frameworks from loop amplitude sweep test at pH 10 (a, c, e) and pH 12 (b, d, f) and PEG 4 kDa (a, b) PEG 8 kDa (c, d) and PEG 20 kDa (e, f).

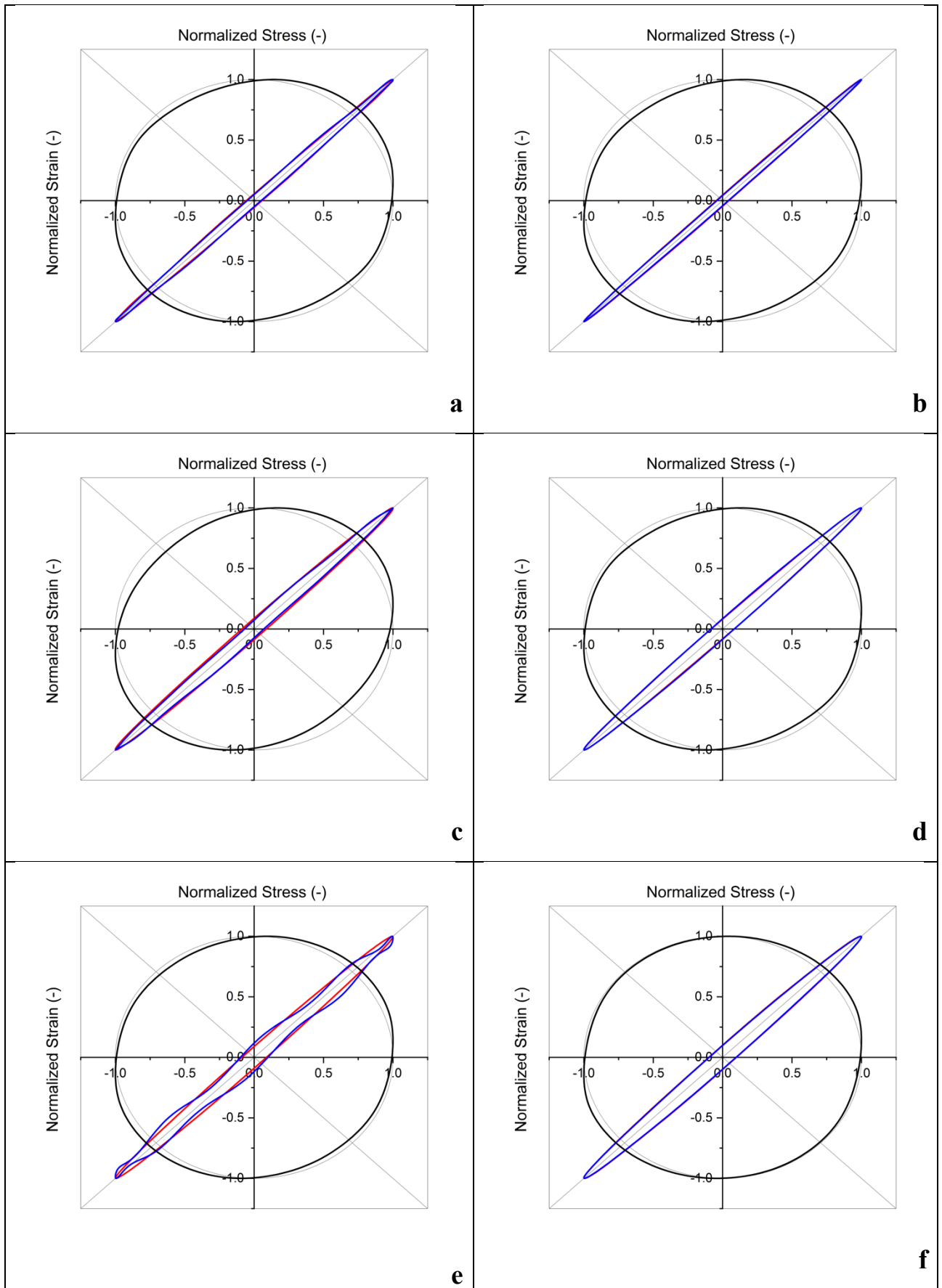


Figure S 28: Normalized Lissajous plot in SAOS and LAOS regime, of PVA 125 kDa based frameworks from loop amplitude sweep test at pH 10 (a, c, e) and pH 12 (b, d, f) and PEG 4 kDa (a, b) PEG 8 kDa (c, d) and PEG 20 kDa (e, f).

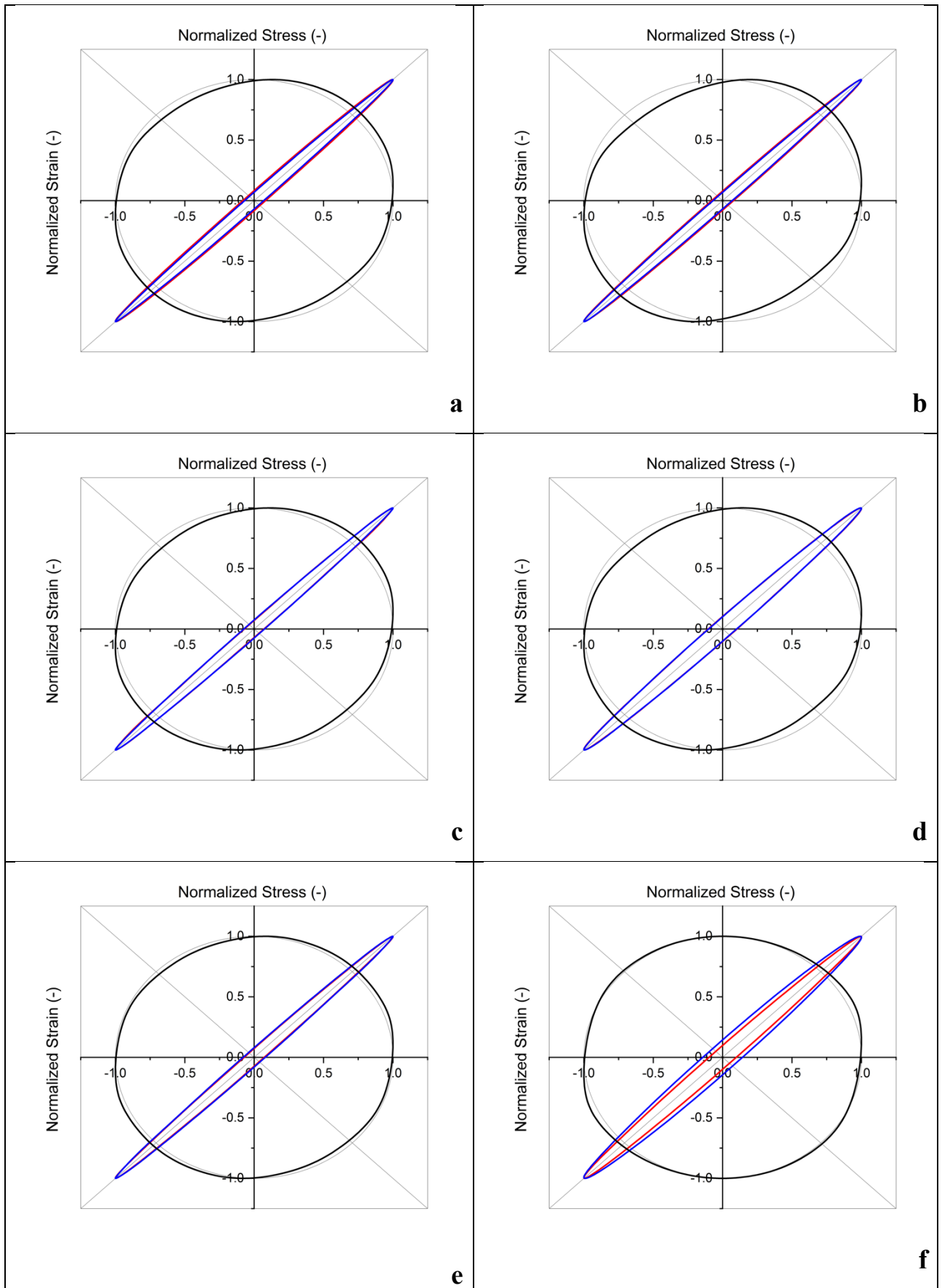


Figure S 29: Normalized Lissajous plot in SAOS and LAOS regime, of PVA 195 kDa based frameworks from loop amplitude sweep test at pH 10 (a, c, e) and pH 12 (b, d, f) and PEG 4 kDa (a, b) PEG 8 kDa (c, d) and PEG 20 kDa (e, f).

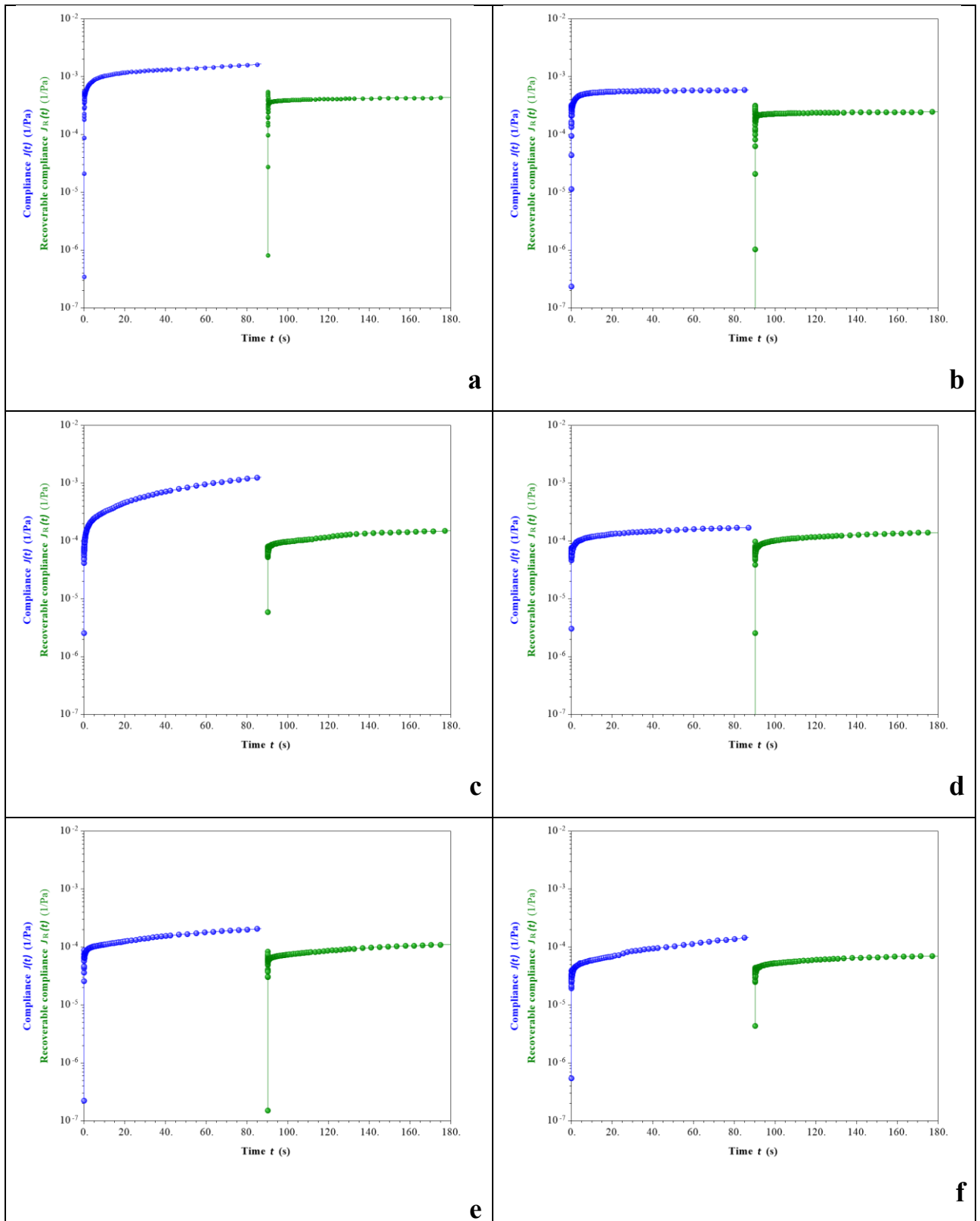


Figure S 30: Compliance $J(t)$, the blue curve) and Recoverable compliance ($J_R(t)$, the green curve) of PVA 27 kDa based frameworks in creep-recovery test at pH 10 (a, c, e) and pH 12 (b, d, f) and PEG 4 kDa (a, b) PEG 8 kDa (c, d) and PEG 20 kDa (e, f).

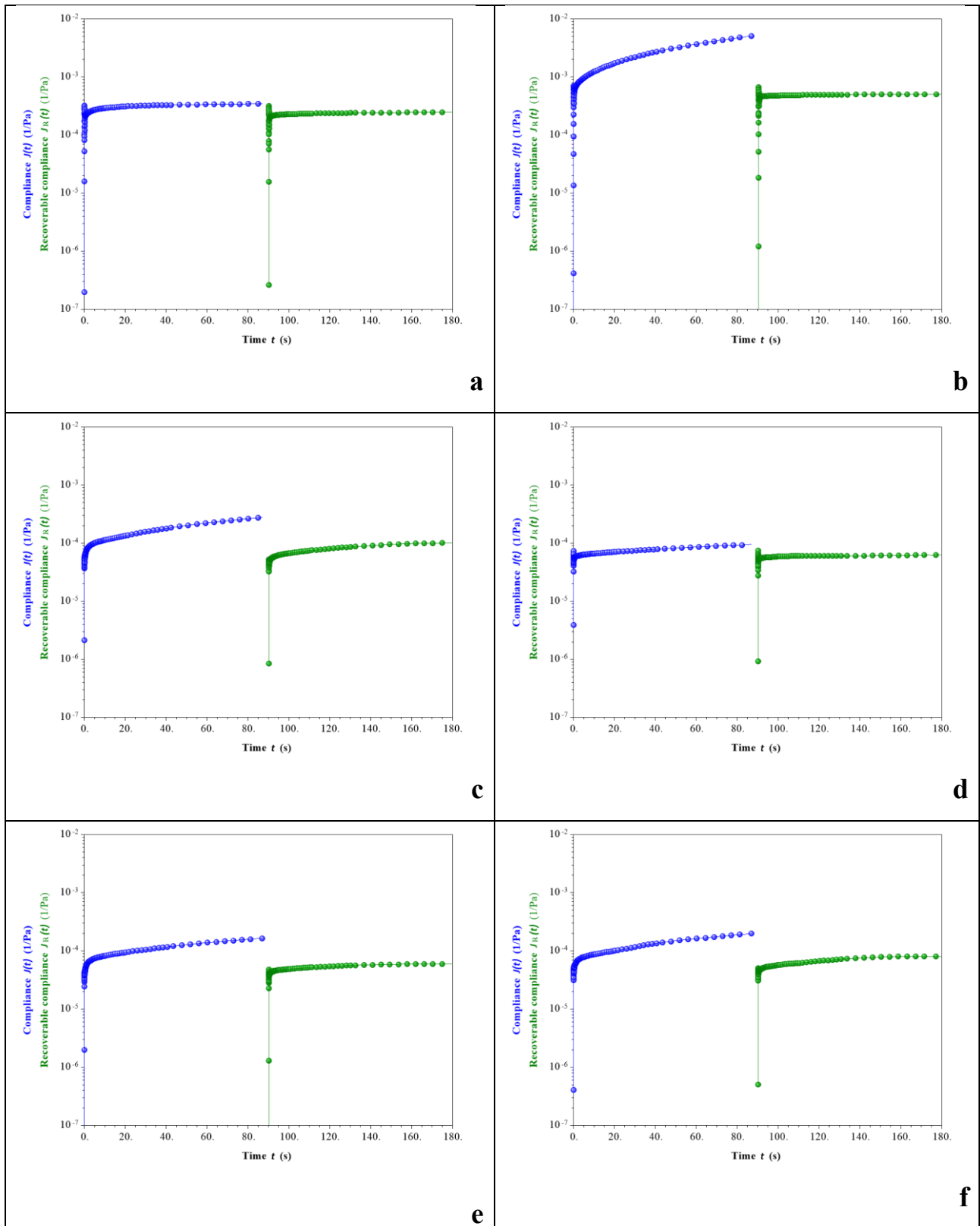


Figure S 31: Compliance $J(t)$, the blue curve) and Recoverable compliance ($J_R(t)$, the green curve) of PVA 47 kDa based frameworks in creep-recovery test at pH 10 (a, c, e) and pH 12 (b, d, f) and PEG 4 kDa (a, b) PEG 8 kDa (c, d) and PEG 20 kDa (e, f).

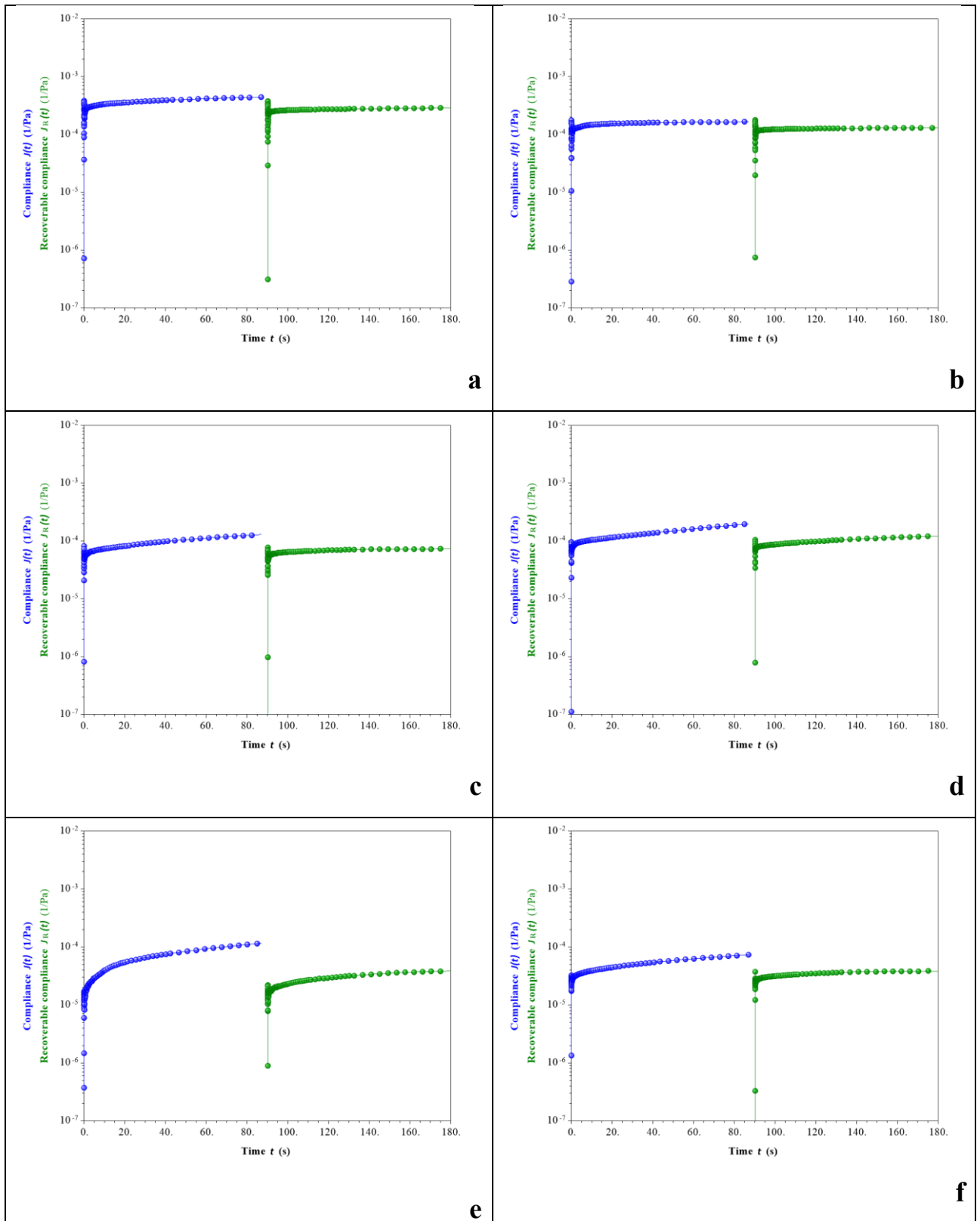


Figure S 32: Compliance $J(t)$, the blue curve) and Recoverable compliance ($J_R(t)$, the green curve) of PVA 61 kDa based frameworks in creep-recovery test at pH 10 (a, c, e) and pH 12 (b, d, f) and PEG 4 kDa (a, b) PEG 8 kDa (c, d) and PEG 20 kDa (e, f).

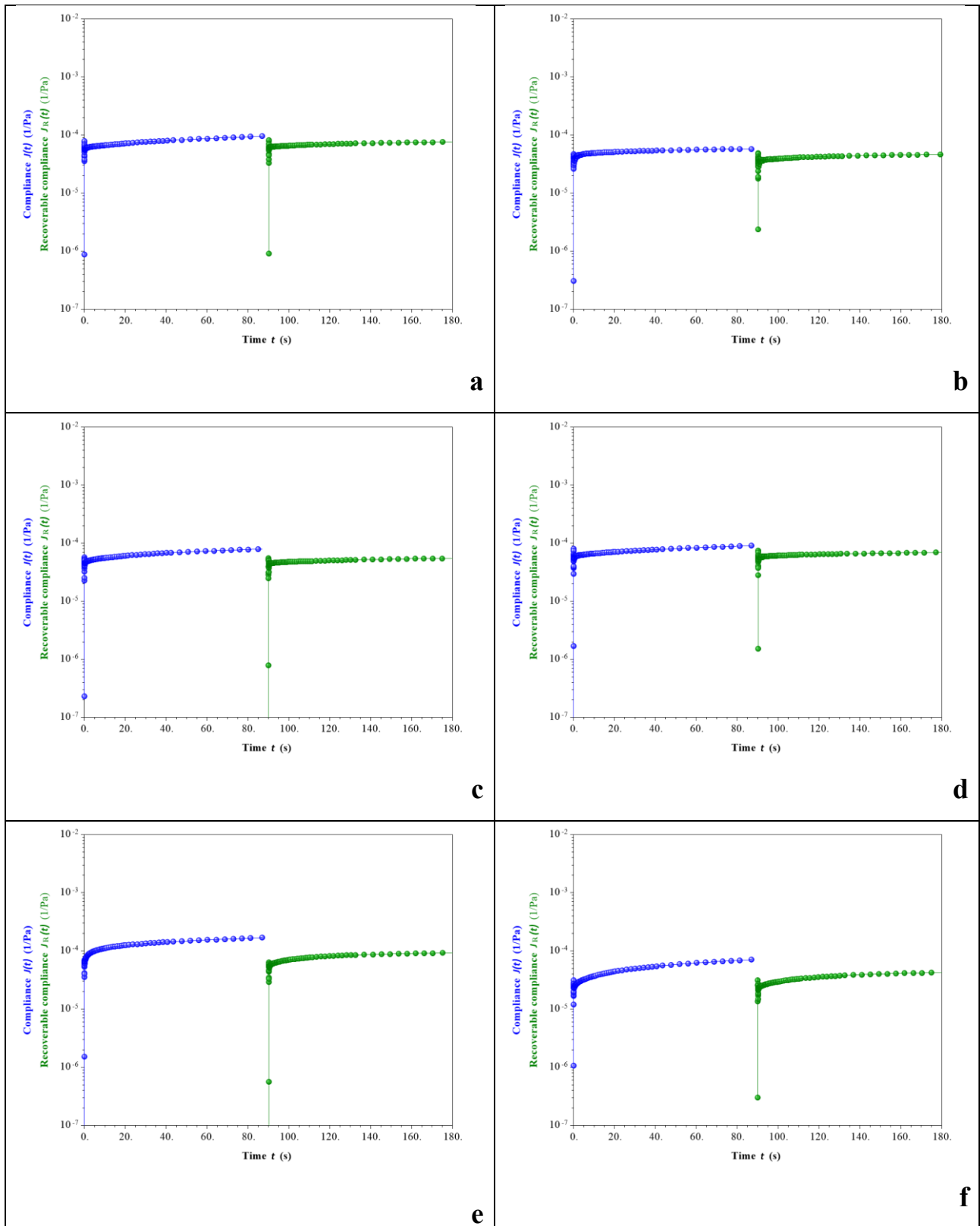


Figure S 33: Compliance $J(t)$, the blue curve) and Recoverable compliance ($J_R(t)$, the green curve) of PVA 125 kDa based frameworks in creep-recovery test at pH 10 (a, c, e) and pH 12 (b, d, f) and PEG 4 kDa (a, b) PEG 8 kDa (c, d) and PEG 20 kDa (e, f).

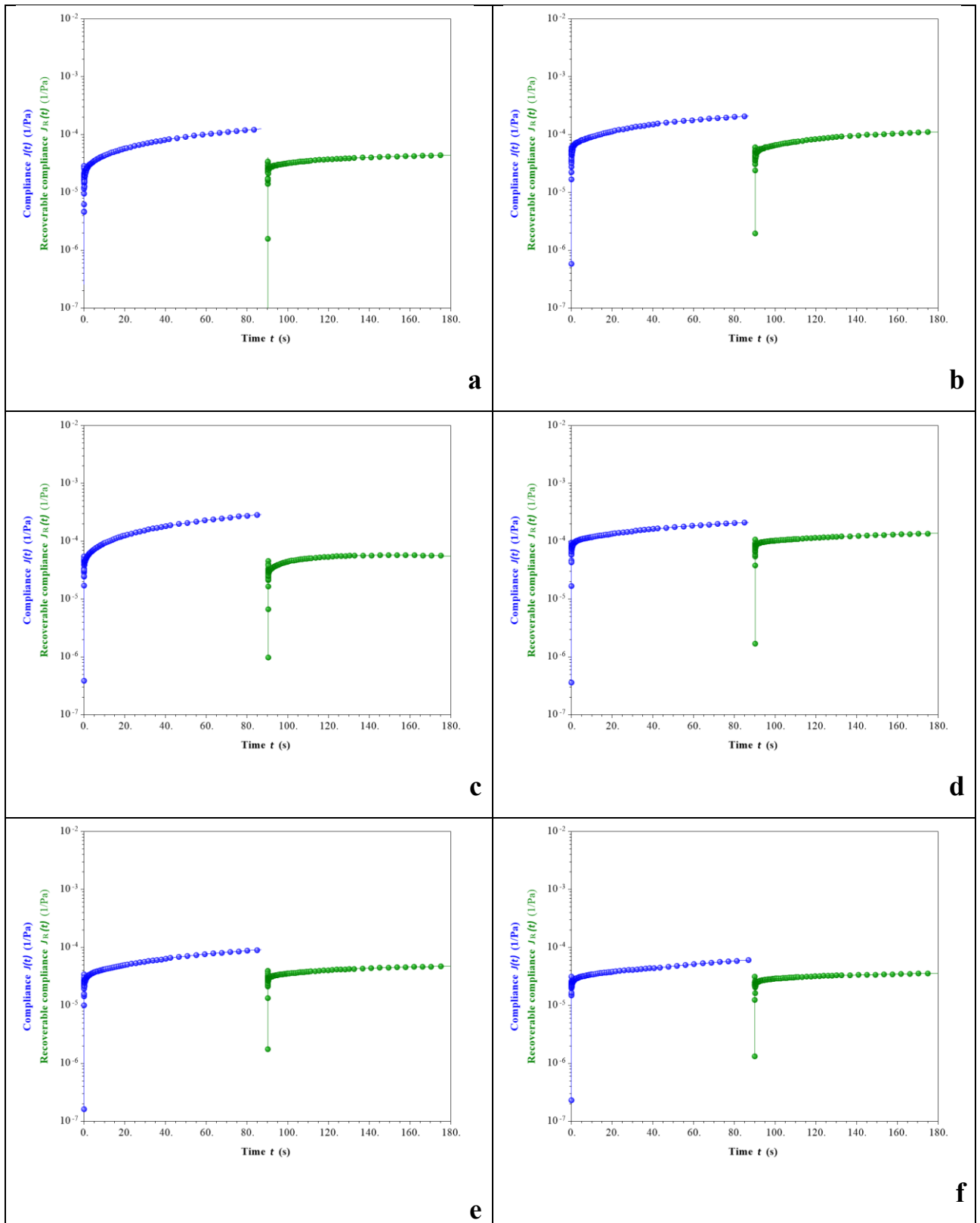
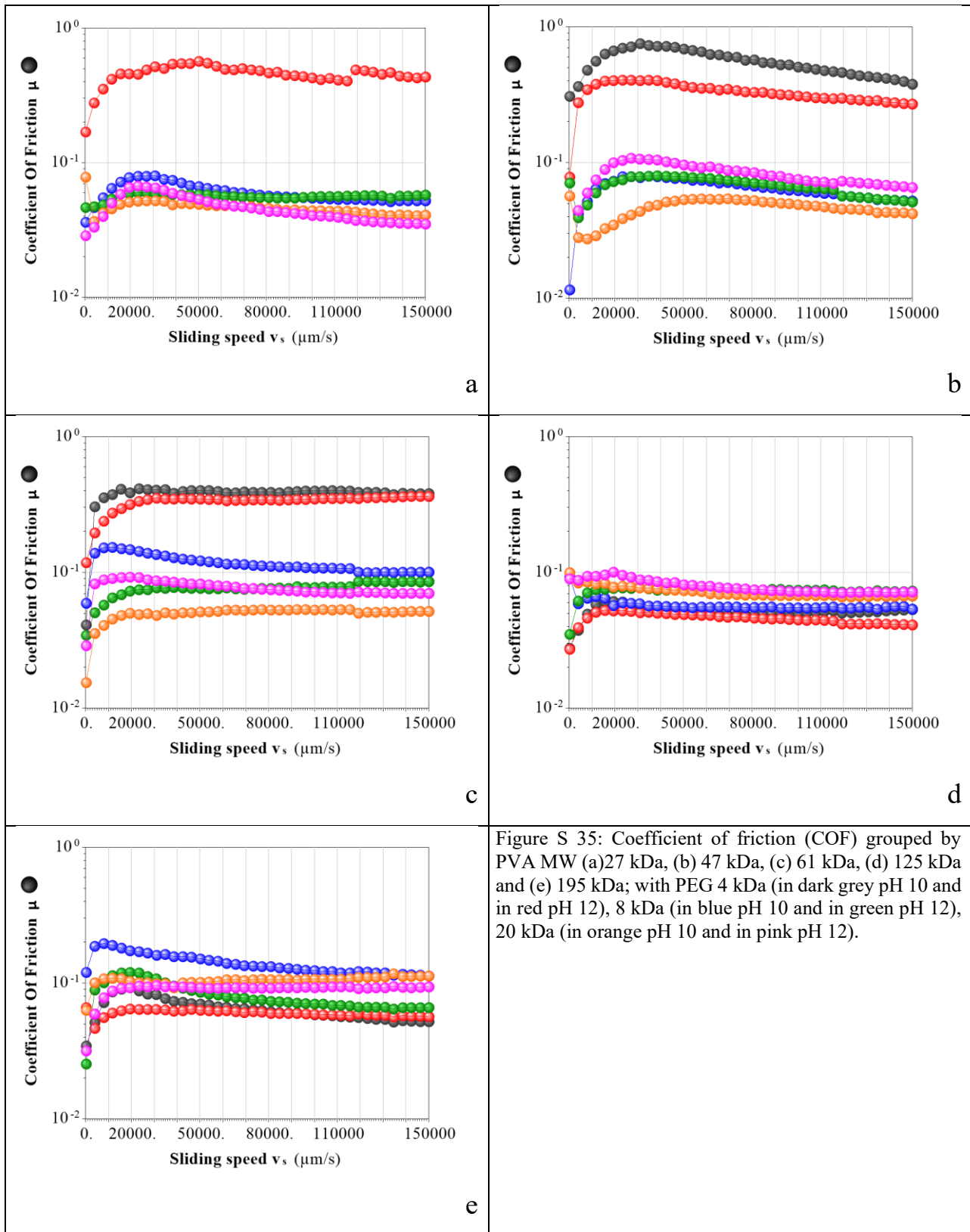


Figure S 34: Compliance $J(t)$, the blue curve) and Recoverable compliance ($J_R(t)$, the green curve) of PVA 195 kDa based frameworks in creep-recovery test at pH 10 (a, c, e) and pH 12 (b, d, f) and PEG 4 kDa (a, b) PEG 8 kDa (c, d) and PEG 20 kDa (e, f).



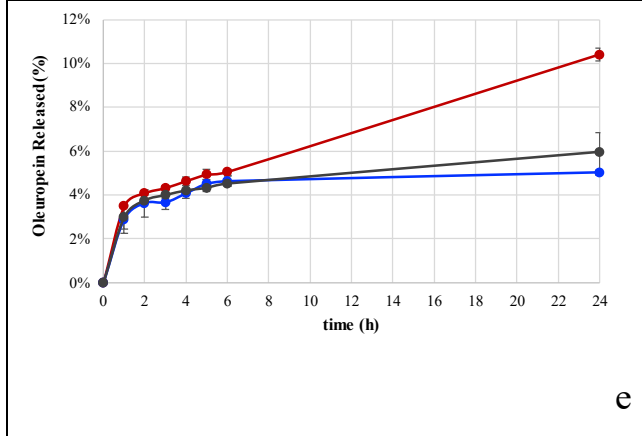
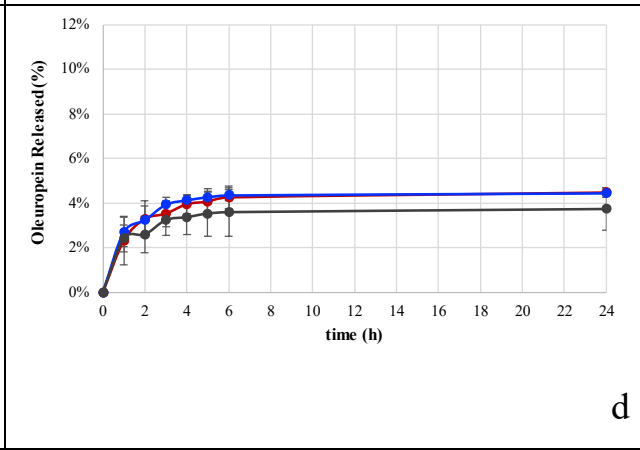
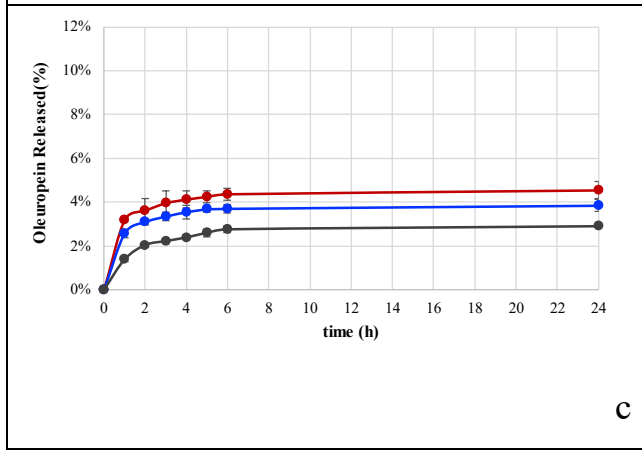
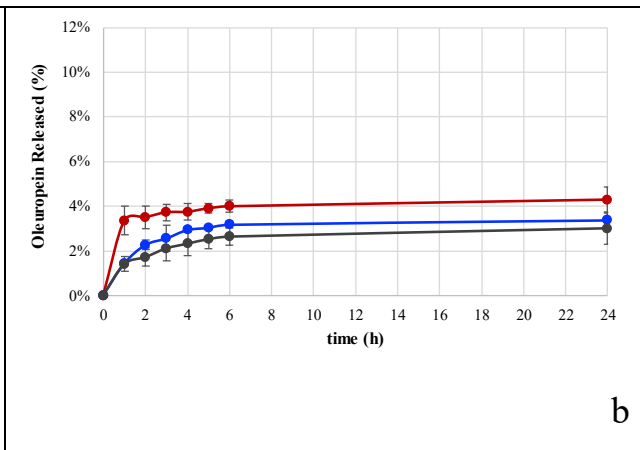
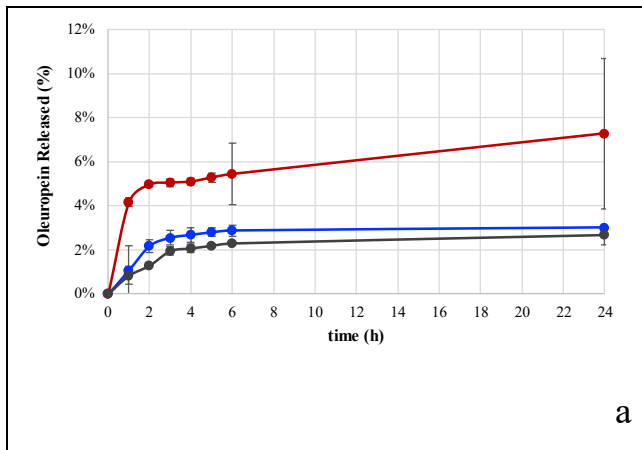


Figure S 36: Oleuropein extract release, grouped by PVA MW (a)27 kDa, (b) 47 kDa, (c) 61 kDa, (d) 125 kDa and (e) 195 kDa, with PEG MW (4 kDa in red, 8 kDa in blue, 20 kDa in dark grey).

**CHAPTER IV:
METAL-ORGANIC FRAMEWORKS
FOR DRUG DELIVERY**

**VANADIUM BASED METAL-ORGANIC FRAMEWORK:
SYNTHESIS AND CHARACTERIZATION**

PART 1: INTRODUCTION

Metal-organic frameworks (MOFs) are hybrid materials made by an organic and an inorganic component, behaving like a single entity with peculiar physico-chemical properties, high surface area and wide range of pore sizes (up to 90% free volume of porosity), functionalization abilities, environment designation possibility, that may be used in wide variety of fields [1], Figure 26.

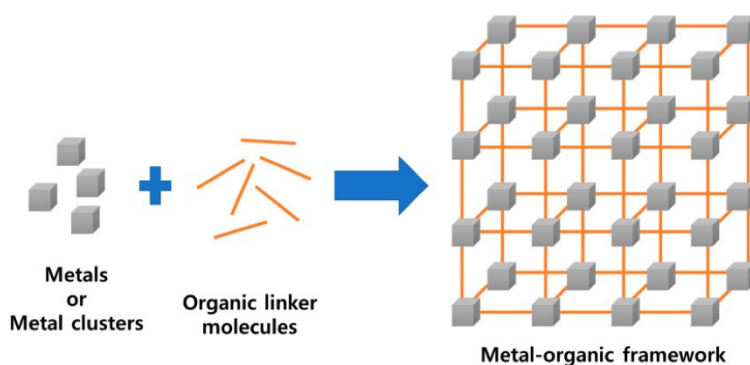


Figure 26: Schematic composition of a generic MOF [2].

Because of their exceptionally high surface area, large cavity size for drug encapsulation, and a controlled drug-release profile, they have already been reported for their applications in strategic domains including drug delivery systems (DDSs). Due to the relatively labile metal-ligand bonds, MOFs show intrinsic biodegradability and versatile functionality for post-synthetic grafting of drug molecules. They can be designed to reach suitable drug-loading capability and long-time release process to achieve the best therapeutic effects with the lowest side effects for active pharmaceutical ingredients. In physiological environments, the efficiency of drug delivery mostly depends on both the pore characteristics and structural stability of materials.

MOFs are synthesized by self-assembly of a connector (a metal) and a linker (organic molecule), where connectors and organic linkers are bound together through a strong covalent bond to form porous crystalline structures, [3]. There are many methods of syntheses and the most used are the solvothermal and non-solvothermal ones. The first method is performed in sealed reactors at high temperature and pressures, the second one is performed in standard open synthetic systems, using ambient pressure and temperatures below the melting point of the used solvents. These two methods are not widely used, because of their lower yield and products quality as compared to the unconventional synthetic methods. One of the most promising unconventional synthetic methods is that assisted by ultrasounds (US). This method is based on the acoustic cavitation generated by US.

The US generate pressure fluctuations in the liquid medium leading to bubbles formation, growth and collapse: the solvent constantly expands and contracts, till it gains a critical dimension that depends on the used medium and the US frequency, Figure 27. The bubbles' collapse is quite an adiabatic process, resulting in a huge energy buildup in the bubbles. The cavitation bubbles may collapse near the solid surface of the substrate activating it or play a deagglomeration or splitter of larger particles and aggregates. The localized hotspots may lead to powerful shock waves and microjets, generated by cavitation phenomena, that may result in an effective stirring and/or mixing of the liquid layers [4, 5].

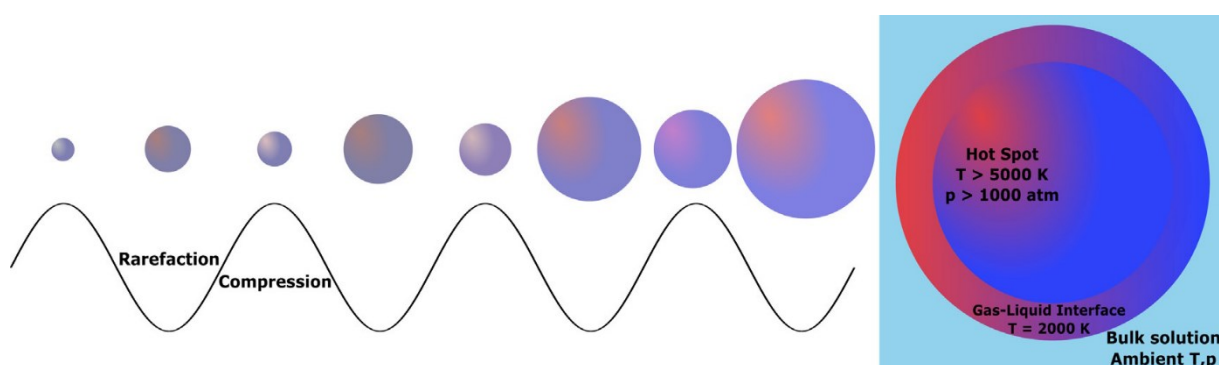


Figure 27: Bubble dynamic in the cavitation process [6].

The US assisted synthesis reaction may occur:

- inside the bubbles, that acts as micro or nano reactors with extreme temperatures ($T > 5000 \text{ K}$) and pressures ($P > 1000 \text{ atm}$),
- at the interface between the bubble and the solvent bulk: the efficiency of this process depends on the hydrophobicity of the reactants and their ability to accumulate at the liquid/gas interface, [7],
- near the bubble surface: the reactants are in the bulk solution, but they react with the radicals that are formed in the bubbles by the elevated temperature and pressure.

MOFs structure can be tuned and synthesized to let the controlled released of active molecules in the organism. The use of these frameworks as drug delivery systems focuses the attention on the utilization of non-toxic components and their affinity with both the target site of treatment and loaded active molecules. Consequently, particles must biodegrade without the production of toxic species for the organism. Some crucial properties of MOFs as DDSs reside on their extremely high porosity

and specific surface area that allow the drugs to be loaded in the pores and to be released efficiently. In fact, some nano-MOFs have been used for example in the anti-tumoral therapies, because of their extremely efficiency and selectivity in the cancer cell treatments [8].

The most important feature of MOFs is the possibility to design the pores with determined sizes selecting organic linkers with determined shapes, and specific environments through functionalization of the organic linkers. Other important features of these systems are their high loading capacities and great flexibility, that enables dynamic behavior in porous coordination networks. MOFs also facilitate the drug affinity to target cells. Some MOFs suffer from chemical instability: this feature can be at the same time a limitation but also an advantage because it allows the framework to easily biodegrade in the organism after drug release. MOFs can encapsulate and/or tether drugs of different nature, including hydrophilic, hydrophobic, and amphiphilic molecules. In the application of MOFs as DDSs, several factors must be considered, including the physio-chemical properties of both the matrix and drug. The versatility of this kind of matrices for drug delivery allows the realization of several kinds of formulations, including tablets, pills, films, patches, and nanoparticles providing the possibility to explore their specific drug delivery applications while enhancing patient's compliance. Drugs can be loaded in the DDS either in situ, during the synthesis of MOFs, or in post-synthetic phase. The drug can be encapsulated in the systems by either covalent binding (MOF functionalization with drug) or non-covalent interactions, [3]. In MOF-based DDSs, a crucial aspect is the design of a biocompatible and biodegradable system; thus, the choice of the metal is a fundamental issue: the metal must have minimal or non-toxic properties, [9], or even active positive action.

Vanadium is an essential metal in humans in low amounts (i.e. 0.05 μM) but gains toxicity in concentration that exceeds 25mM. The excess of V may cause pro-oxidant processes, increase the generation of ROS and oxidative stress, induce inflammatory and fibrotic changes in the lungs associated with its redox-active nature and ability to intensify lipid peroxidation (LPO), and generic toxicity [10]. In low amount the potential benefic effect of vanadium opens the possibility of a therapeutic use of this metal: for example, as anti-bacterial and anti-diabetic agent, it may play a cardioprotective and anti-hypercholesterolemic role, and also an antioxidant function, Figure 28.

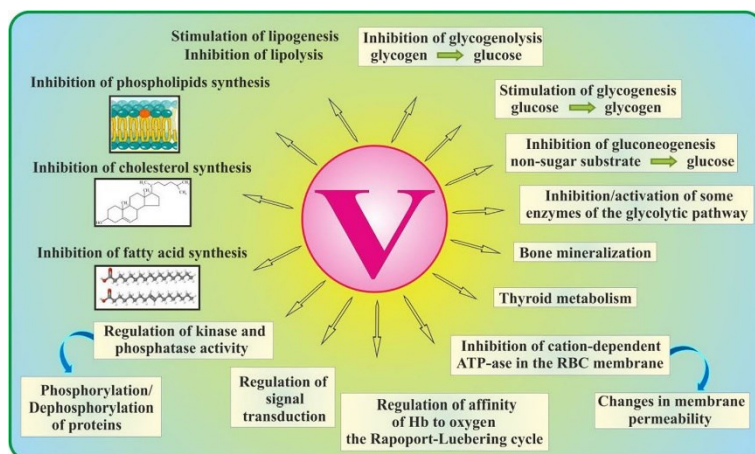


Figure 28: Role of vanadium in the mammalian organism [10].

Vanadium in general, and the V (V) in particular, may be used in bone regeneration therapies: in fact, vanadium is applied in tissue engineering to obtain biomaterials that allow regeneration of damaged tissues/organs and restoration of their lost functions [10]. Vanadium can be used for this purpose because it possesses an osteogenic effect enhancing differentiation, proliferation, and mineralization of osteoblasts and MSCs and suppressing osteoclast differentiation and bone resorption. V (IV) at low concentration ($< 25\text{mM}$) seems to play a stimulation role for the pathways of the mitogen-activated protein kinase (MAPK) and extracellular signal-regulated kinase (ERK), that are involved in the osteoblast function [11]. Vanadium was loaded into bone repair scaffolds and had success in helping to stimulate osteochondral development *in vitro* without increased cytotoxicity [12]. To mitigate the possible side effects of vanadium, Mg metal can be in association. Indeed, Mg mitigates the pro-oxidant activity of V and induces limitation of the increase in the hepatic LPO [10]. In addition, magnesium has angiogenic effects for bone regeneration therapies: it promotes differentiation, migration, and capillary network formation of endothelial cells, and induces secretion of proangiogenic factors [13].

Gallic acid, a small molecule with a high antioxidant potential, represents one of the best organic linkers for MOFs synthesis. Moreover, thanks to its antioxidant activity, it is an ideal molecule to be linked with vanadium for a bone regenerative therapy, to mitigate the side effects of the metal release during the MOFs' degradation.

PART 2: MATERIALS AND METHODS

2.1 MATERIALS

VOSO₄ x H₂O (VS), Gallic Acid (GA), NaOH, 0,2 μm filters made of cellulose acetate (CA), Vanadium standard solution 1000 mg/L (TraceCERT®), Indium standard solution 1000mg/L (TraceCERT®), HNO₃ 70% (≥99.999% trace metals basis) and all other reagents and solvents were purchased from Merck and used without any further purification.

2.2 METAL-ORGANIC FRAMEWORK SYNTHESIS

MOF synthesis was first performed using hydrothermal synthesis approach, using a standard apparatus of for organic synthesis. In a second phase, an ultrasound assisted reaction was performed, using a US bath or an US probe, [14]. A 20 mM gallic acid solution in 20 mM NaOH was prepared: after complete dissolution of GA, the solution was left to activate. Then an equimolar quantity of VO²⁺ was added to the solution and let to completely dissolve: once the solution was ready, the reaction media was treated following the two approaches listed before. GA and vanadyl were treated at the same condition of the product reaction.

In the case of the hydrothermal approach, the reaction was performed in a round glass flask, equipped with a condenser on-line with a vapor trap and under N₂. The reaction was carried on for 24 hours, after that reaction was left to reach room temperature and then filtered.

The ultrasound assisted synthesis was performed using two different apparatus. The first ultrasound synthesis method was performed using an ultrasound bath Bandelin 320W output power. The reaction solutions were completely immersed in the bath and the reaction was carried on for 1 hour. After the reaction time was over, the suspensions were filtered and the solid products were analyzed with DLS, to test the product quality and reproducibility. The second US method was performed using an Ultrasonic Processor VCX 750, output frequency 20 kHz, equipped with a 19" US probe (SONICS AND MATERIALS INC.), Figure 29. The reaction consisted in 20 minutes of active sonication, setting the pulsed-on phase at 1 second or 59 seconds. The amplitude of sonication probe was set at 20% or 90%. Once the 20 minutes were over the four different reactions were filtered immediately (hot filtering) and the precipitate was washed with 4 synthesis volumes of ultrapure water (UPW). After that, the CA filters were put under vacuum for 24 h, to let the excess of solvent to evaporate. The

filtered solution was then analyzed to verify that no smaller particles were passed throughout the filter.



Figure 29: US processor VCX 750 with 19" probe.

2.3 INFRARED ANALYSIS (ATR-IR)

IR spectra were acquired using a Nicolet iS50 FT-IR (Thermo), equipped with an ATR accessory with a Ge crystal [15].

The dry solid-state samples and background spectra were collected in the spectral range from 600 cm^{-1} – 4000 cm^{-1} , with 64 scans, with a resolution of 4 cm^{-1} . The spectra were acquired and processed with the software OMNIC v.9.8.372.

2.4 DYNAMIC LIGHT SCATTERING ANALYSIS (DLS)

The size distribution and its average value were measured by DLS tests. The stability of the particles in suspension was tested by ζ – potential. For the analysis was used a Zetasizer Pro Red (Malvern), and the software ZS XPLOER v.3.2.1.11 for data acquisition and analyses.

2.4.1 AVERAGE SIZE DETERMINATION

The size distribution of MOFs is measured homogeneously suspending the solid sample in UPW, and the average particle size is measured approximating to the hydrodynamic diameter of the spheres that have the same behavior in suspension of the real shaped particles: for this reason, this measure is an approximated one, generated by an extrapolation from the interpretation of the scattering data.

This technique can measure particle sized from 1 nm to 1 μm . Nano-sized suspended particles undergo to the Brownian motion, so is possible to measure their size using the Stokes-Einstein, Equation 7:

$$D_h = \frac{T K_B}{3\pi\eta D_t}$$

Equation 7

Where D_h corresponds to the hydrodynamic diameter, T to the thermodynamic temperature, K_B to the constant of Boltzmann, η to the dynamic viscosity, and D_t to the translational diffusion coefficient, [16].

The samples after proper dilutions, were analyzed with 10 mm four transparent faces PMMA cuvettes, with a scattering angle of 173° . The analyses were performed at 25°C in triplicates.

2.4.2 PARTICLES STABILITY (ζ - POTENTIAL)

Stability and surface charge play important roles for MOFs' application in biomedical field, thus the ζ – potential analysis of these systems is mandatory. Once a suspension occurs, a surface particles charge is generated, depending on the properties of the species that are suspended. In this condition, the particles move in the suspension media toward a certain direction with a specific rate, if an electrical potential is applied to the suspension. This is due to the interaction between the applied electric field and the surface charge of the particles. The rate of charged particles is proportional to the potential charge of the shear plane of the particles: this is what it is commonly indicated as ζ – potential. This parameter is useful to evaluate the stability of colloidal suspensions. The ζ – potential is associated to the surface charge: for this reason, large values of this parameter (positive or negative) indicate that is present a massive repulsion between the charged particles, supporting the colloidal stability of the system [16].

The samples after proper dilutions, were analyzed in DTS1070 cuvettes. The analyses were performed at 25°C in triplicates.

2.5 VANADIUM DETERMINATION VIA ICP-MS

Samples at dry state were weighted, $21 \text{ mg} \pm 1 \text{ mg}$, and then digested with a mix of acids (3 mL HCl (37% v/v) and ???) using a microwave (MW) digester ETHOS D Microwave Labstation (Milestone). The MW digestion procedure was performed at different power, following the present procedure: the first step was set at 250 W for 2 minutes, then 2 minutes at 0 W, 6 minutes at 250 W, 5 minutes at 400 W and finally at 550 W for 8 minutes, [17]. After that, the sample was recovered from the PTFE wells with a 0.2 % v/v HNO₃ and diluted to 50 mL with the same solvent; before the samples analysis a D200 dilution was also performed.

The digested and diluted samples were analyzed with an 8900 ICP-MS Triple Quad (Agilent), for the content of vanadium in the metal-organic frameworks. The calibration curve was performed by subsequent dilution, starting from a 1000 mg/L of V (O2SI, USA, solution in 5% HNO₃ and Tr HF) standard stock solution. The 115 In line was used as internal standard (TraceCERT®, stock solution 1 g/L in 2% v/v HNO₃), added on-line using an ISTD G3280-60590 kit from Agilent. The necessary dilution for the analyses were performed by volumetric way, using a dilute HNO₃: 70 % v/v HNO₃ ($\geq 99.999 \%$, for trace metals analysis), diluted with 1 % UPW (18.2 M Ω ·cm at 25°C).

2.6 THERMOGRAVIMETRIC ANALYSIS (TGA)

TGA was used to measure the thermal stability of the MOFs. The analyses were performed with an SDT-Q600 (TA Instruments). Thermal Advantage Release 5.5.22 was used for instrument control and TA Instruments Universal Analysis 2000 v. 4.5.4. was used for data analysis.

The thermal stability was performed on 5 mg of the frameworks at dry state: the sample was put in a Pt crucible and heated from 30 °C to 700 °C at 10 °C/min., in inert atmosphere (N₂, 1000 mL/min.).

2.7 SPECIFIC SURFACE AREA AND POROSITY

The MOFs have generally a high surface area and a high porosity, so they have a high loading capacity, [16]. These two characteristics can be measured by gas absorption-desorption isotherms, using the theory by Brunauer-Emmett-Teller (BET) for the specific surface area, and the Barrett-Joyner-Halenda (BJH) method for the porosity and pore distribution determination. Calculating the physically adsorbed gas on the MOF surface, the specific surface area can be calculated. In fact, the

gas, that is adsorbed, forms a monolayer on the analyzed particles thanks to weak van der Waals forces. Data were treated with the BET adsorption isotherm Equation 8, to calculate the V_m :

$$\frac{1}{\left[V_{\alpha} \left(\frac{P_0}{P} - 1\right)\right]} = \frac{C - 1}{V_m C} \times \frac{P}{P_0} + \frac{1}{V_m C}$$

Equation 8: BET adsorption isotherm.

Where P and P_0 are partial vapor pressure of adsorbate gas in equilibrium with the surface at 77.4 K and saturated pressure of adsorbate gas in pascals, respectively. V_{α} is the volume of gas adsorbed at standard temperature and pressure (STP) [273.15 K and atmospheric pressure (1.013×10^5 Pa)], in milliliters, V_m is the volume of gas adsorbed at STP to produce an apparent monolayer on the sample surface, in milliliters. C is a dimensionless constant which is associated with the enthalpy of adsorption of the adsorbate gas on the powder sample.

Plotting the adsorption-desorption isotherm and calculating the V_m , it can be calculated the effective surface area (m^2/g), using Equation 9:

$$S_{BET} = \frac{V_m N_{\alpha}}{m \times 22.400}$$

Equation 9

Where N is the Avogadro constant, α is the effective cross-sectional area of one adsorbate molecule, in square meters, m is the mass of the solid powder, and 22,400 is the molar volume of adsorbate gas (in this case N_2) at STP [16].

A high specific surface area is not sufficient to ensure that the system can be a good drug delivery system, because the loading molecules has to reach the loading site and that site has to be of the proper dimensions to let the desired molecules enter the pores: for this reason, is useful to determine the pores volume and their distribution. For this characterization is used the BJH method, that is based on the Kelvin Equation 10, that correlates the pore radius with the relative pressure (P/P^0), that corresponds to that of the capillary nitrogen condensation, [18].

$$\ln \frac{P}{P^0} = \frac{2\gamma V_M}{rRT}$$

Equation 10

Where the r is the Kelvin radius.

The BJH method assumes that the pores are cylindrical and that within a pore there is a liquid layer adsorbed on the wall of the pore with a thickness t and a liquid capillary with a radius r , that follow the Kelvin principle. The dimension of each pore is determined using the Equation 11.

$$r_p = r + t$$

Equation 11

For the analyses, 150 mg-200 mg of dry state frameworks were pre-treated with the FlowPrep apparatus: the samples were insufflated by N_2 and kept at elevated temperature (120 °C), at which no sample degradation occurs, for 4 hours. After that, the samples were degassed keeping them at 120 °C under vacuum for 1 hour. Then the frameworks were analyzed using N_2 as adsorption gas, at the temperature of 77.4 K, using a gas porosimeter 3Flex (Micromeritics).

2.8 TRANSMISSION ELECTRON MICROSCOPY

TEM can be used to analyze the MOFs samples to evaluate their crystalline structure and study the guest nanoparticles loaded in the frameworks. The principle of electron microscopy is to use a focus electron beam to obtain a high magnification of the surface topology, that makes it possible to perform visual analysis of the morphology of the particle surface. The transmission electron microscopy (TEM), in particular, exploits the scattered electron beam that passes through the materials' thin section creating an interference image in the detector. Generally, MOFs have a particular morphology which depends on the metal ion, organic ligand, and/or solvent used in synthesis. By changing any of these precursors, the morphology may be changed. For the conventional TEM analyses was used a Tecnai G2 Spirit (FEI). The particles were suspended in UPW, then 2 μ L were deposited on a sample holder and then let dry for 2 minutes. Once the time was over, the sample holder was put into the TEM and the analyses were performed.

The samples were then analyzed by the cryo-TEM technique, using CM200FEG (Philips). The samples were prepared depositing the framework suspension in the sample holder and then using the Vitrobot Mark IV (FEI), that remove the excess of sample and suddenly froze it using liquid nitrogen, producing a water amorphous system within which the particles are suspended in the form they are in the heterogenous systems.

PART 3: RESULTS AND DISCUSSION

3.1 METAL-ORGANIC FRAMEWORK SYNTHESIS

The solution of GA and V were prepared using the procedure previously described: the solution turns its color from transparent to pink, and then to yellow, becoming green during the GA dissolution, and finally very dark blue when the vanadium was added, Figure 30a-e.

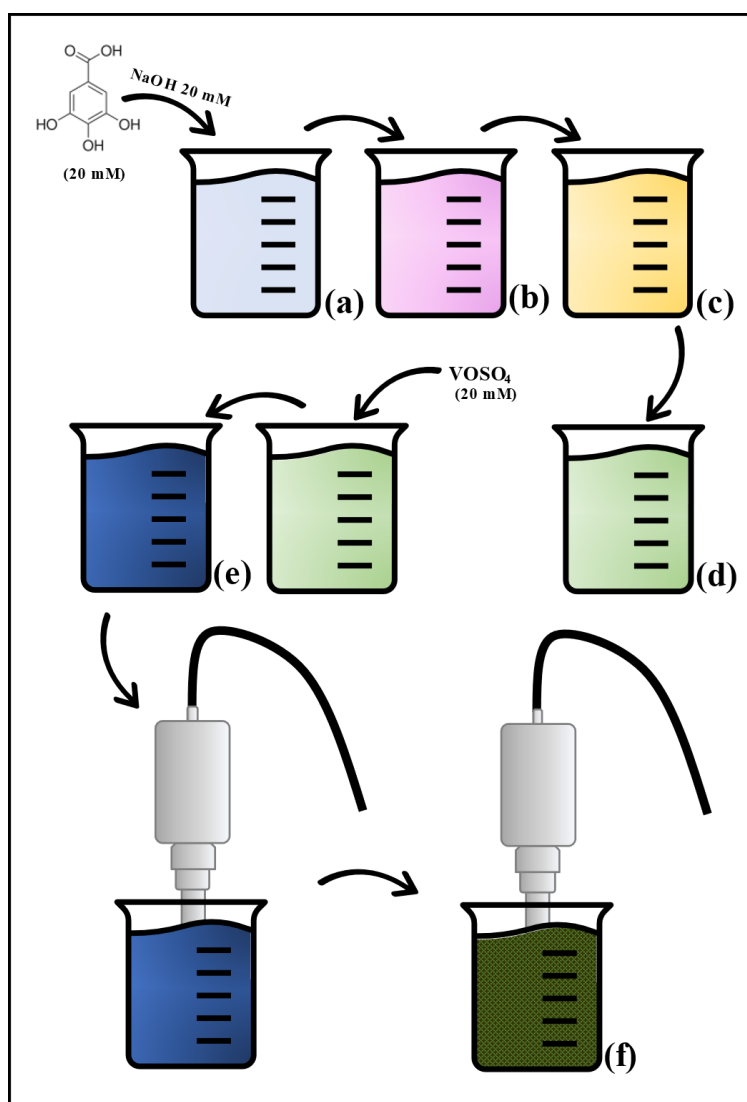


Figure 30: Solution appearance after GA in the NaOH 20mM, VOSO₄ additions, and after the synthetic US probe process.

The hydrothermal approach did not produce MOFs, no particles were found in the 0.2 μm filter. To confirm the particles' absence, the filtered liquid fraction was analyzed by DLS. No particles were detected either in the framework synthesis nor in the bare reactants.

The ultrasound bath approach did not give any sample in the reactant-only systems. In the case of the framework systems, the US bath produced some solid particles that were analyzed by DLS to test their reproducibility. No significant reproducibility was found.

The US probe synthesis was performed testing different reaction times. 20 minutes was chosen as the shorter time necessary to obtain MOFs. Indeed, shorter times did not produce any solid framework. The reaction media appears to be turbid and with a change in color from very dark blue to green-brown one, Figure 30f. The complete set of samples is reported in Table 12.

Table 12: Synthesized frameworks from the US probe approach.

Framework	Amplitude (%)	Pulse-on (s)	Purification
MVG_2001	20	1	hot filtration
MVG_2059	20	59	hot filtration
MVG_9001	90	1	hot filtration
MVG_9059	90	59	hot filtration

3.2 INFRARED ANALYSIS (ATR-IR)

Superimposable IR spectra for all the 8 frameworks were obtained. The overlaid IR spectra are reported in Figure 31a. For a clear graphical interpretation, only the spectra of MVG_2001c is reported in Figure 31b.

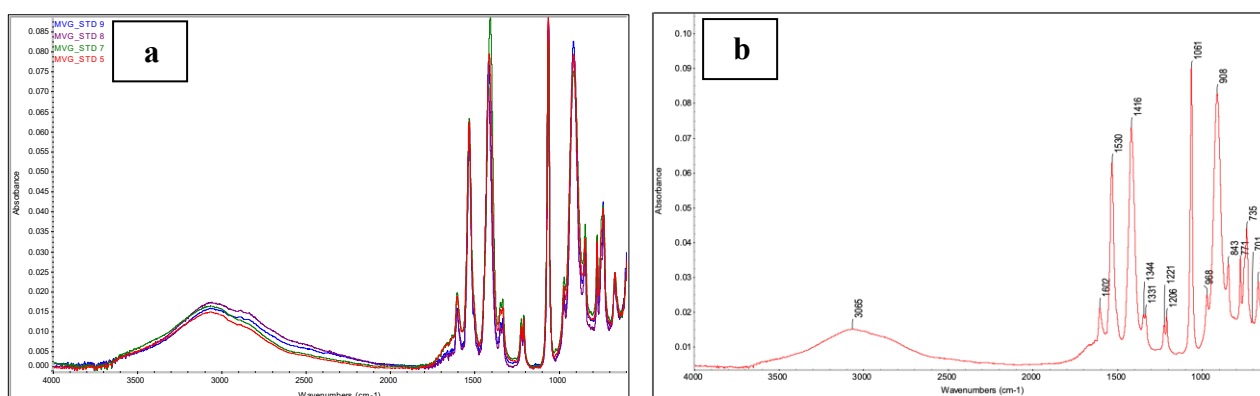


Figure 31: ATR FT-IR overlaid spectra of the 4 frameworks (a) and of the MVG_2001c (b).

The bands assignments are reported in Table 13. IR analysis confirms the presence of V-O species with the bands at:

- 1061 cm^{-1} , associated with the V-O stretching,
- 908 cm^{-1} , associated to the V=O symmetrical stretching,
- 735 cm^{-1} and 666 cm^{-1} associated to the symmetric and asymmetric O-V-O stretching, respectively, [19].

The presence of GA is confirmed by bands at 1530 cm^{-1} and the 1416 cm^{-1} , associated with the COO^- bending and stretching respectively [20], and that at 843 cm^{-1} associated with the 1,2,3,5-tetrasubstituite (C-H bending out of plane).

Table 13: IR bands assignment from the spectrum in Figure 31b.

Wavenumber (cm^{-1})	Structure
1530	COO^- asymmetric stretching
1416	COO^- symmetric stretching
1221	C-O stretching (Ar-O-R) C-O stretching (RCOOR')
1206	C-O stretching (Ar-O-R) C-O stretching (RCOOR')
1061	V-O stretching
908	V=O symmetric stretching
843	1,2,3,5-tetrasubstituite (C-H bending out of plane)
735	O – V – O symmetric stretching
666	O – V – O asymmetric stretching

3.3 DYNAMIC LIGHT SCATTERING ANALYSIS (DLS)

3.3.1 AVERAGE SIZE DETERMINATION

DLS was used to control that no products of synthesis pass throughout the filter membrane, and that no frameworks formation occurs in the cases of the two reactants only synthesis. For all the

synthesized frameworks, no products were found in the filtered liquid. Even for the single reactants' reaction, no product was found in the solution reaction.

The average particle size and its distribution is measured with DLS, as approximated to the hydrodynamic diameter of the sphere that has the same motion in the suspended media. The average size distributions are depicted in Figure 32.

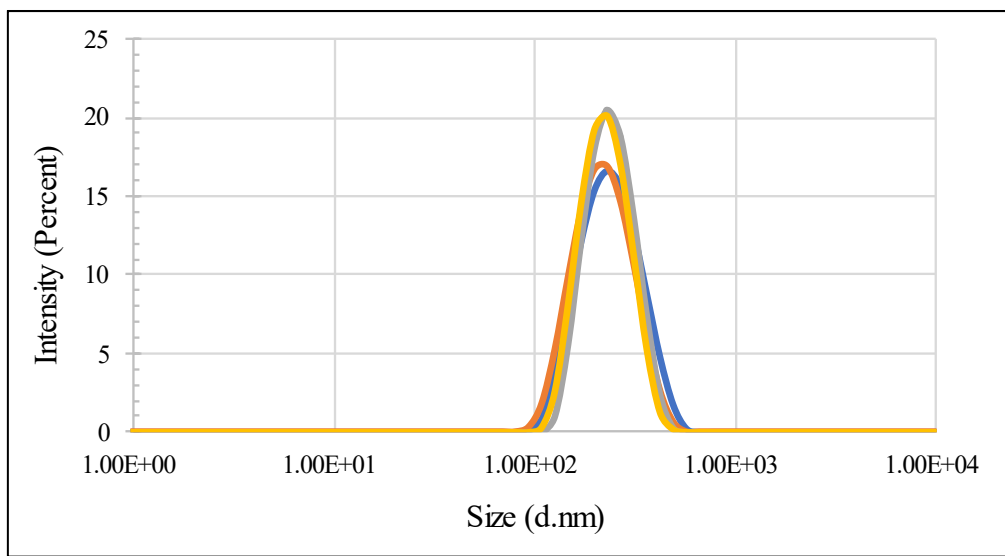


Figure 32: Size distribution averaged of MVG frameworks, for the MVG_2001 in blue, MVG_2059 in orange, MVG_9001 in grey and MVG_9059 in yellow.

All the tested frameworks possess the same behavior and the same type of distribution. They are composed of only one population and so they are monodispersed ($PDI = 0.071 \pm 0.034$) around the average particle size of $218 \text{ nm} \pm 9 \text{ nm}$. The single frameworks average size values are reported in Table 14. The obtained results were analyzed by a Two-Way ANOVA test, to evaluate the dependence of the particle size on the two synthetic parameters (i.e. amplitude of sonication and pulse-on time). The results of this analysis are depicted in Figure 33a-b: both the parameters affected the size of the frameworks, with the active pulse time that has a higher effect on this property than the sonication amplitude ($p = 3 \times 10^{-6}$ and $p = 1 \times 10^{-3}$ respectively). The graphs show how the average size of this series of frameworks is affected by the amplitude of sonication: for both 1 s and 59 s the increase in the percentage of amplitude generates a slight increase in the size. The slope of the two curves in Figure 33a differs only by minimal changes in their value (5.4 nm and 7.5 nm for 1 s and 59 s respectively). Contrarily, the pulse-on time has an opposite effect as compared to the % amplitude: increasing the time, the size decreases, Figure 33b. The change in time of the active sonication generates an effect that is the same for the two series of data. In fact, the two curves possess the same

slope, regardless of slight differences, and so the same effect of the amplitude is confirmed on the frameworks synthesized with the 1 s and 59 s pulse-on (-16.0 nm and -13.8 nm for 20% and 90% respectively).

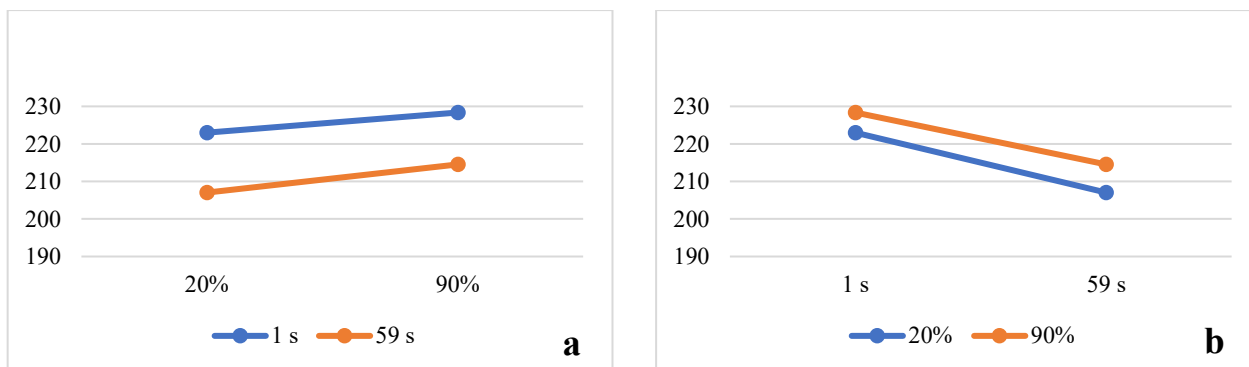


Figure 33: Two-Way ANOVA test results on average particle size from the analysis on the MVG frameworks (n = 3).

3.3.2 PARTICLES STABILITY (ζ - POTENTIAL)

The ζ – potential is the measure of the surface charge of the suspended particles: higher (either negative or positive) is the charge, higher are the repulsive forces between particles in the suspension, and so higher is the colloidal stability of the system in the media. Results, reported in Table 14, were subjected to a Two-Way ANOVA test. Statistical analysis shows that both the single parameters and their interaction affect the stability of the system. In particular, the sonication amplitude influences the stability of the particles less than both the active pulse time and interaction between the two synthetic parameters, ($p = 1 \times 10^{-6}$ for the amplitude, $p = 4 \times 10^{-10}$ for the active pulse time and $p = 1 \times 10^{-9}$ for the interaction of the two variables). How the two parameters affect the stability of the suspended particles is represented in Figure 34a-b. Analyzing the effect of amplitude of sonication is possible to notice that for the 1 s pulse-on frameworks, once the amplitude increases, the stability increases, whereas for the 59 s of active sonication time, once the amplitude increases, the stability decreases, Figure 34a. Analyzing the pulse-on time of sonication is possible to notice that for the lower amplitude the increase in the active time does not affect this parameter, but in the case of the higher amplitude, the increase in the amplitude is reflected in the decrease of the stability of the suspended particles, Figure 34b. Concluding, frameworks synthesized with the 90% amplitude and 1 s pulse-on sonication time (i.e. MVG_9001) revealed the highest colloidal stability.

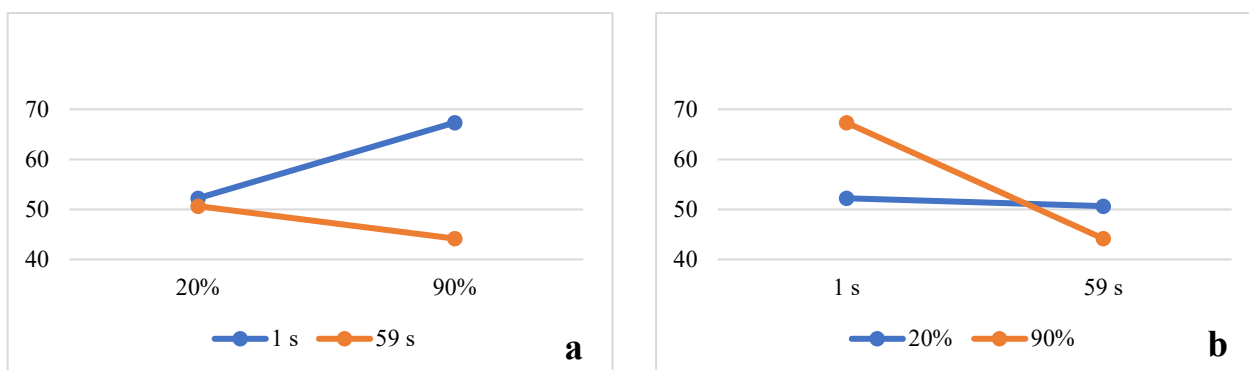


Figure 34: Two-Way ANOVA test results on ζ – potential from the analysis on the MVG frameworks (n = 3).

Table 14: Z-Average from the DLS test for all the single frameworks and for those grouped by hot filtered ones (MVG_h), and for all the synthesized MOFs.

Sample	Z-Average (nm)	Polydispersity index (PDI)	ζ – POTENTIAL (mV)
MVG_2001h ⁽¹⁾	223.0 ± 3.5	0.106 ± 0.010	-52.22 ± 0.38
MVG_2059h ⁽¹⁾	207.1 ± 2.0	0.087 ± 0.031	-50.65 ± 0.98
MVG_9001h ⁽¹⁾	228.4 ± 1.8	0.041 ± 0.015	-67.34 ± 0.07
MVG_9059h ⁽¹⁾	214.5 ± 0.7	0.051 ± 0.024	-44.16 ± 0.52
MVG_h ⁽²⁾	218.2 ± 8.7	0.071 ± 0.034	-53.59 ± 8.89
⁽¹⁾ n = 3; ⁽²⁾ n = 12			

3.4 VANADIUM DETERMINATION VIA ICP-MS

ICP-MS technique was used to evaluate the amount of vanadium in the frameworks. The tests and the calibration curve were performed using the line of the 115 In line as internal standard. The calibration curve, Figure 35, produce as result the calibration equation that is $y = 0.0463x + 0.005$ ($R^2 = 0.998$). From this equation, the vanadium concentration of the four MVG samples was calculated.

The amount of vanadium in the MOFs resulted to be $39\% \pm 9\%$ for the MVG_2001, $31\% \pm 10\%$ for the MVG_2059, $41\% \pm 2\%$ for the MVG_9001 and $34\% \pm 4\%$ for the MVG_9059. From a Two-Way ANOVA test performed on those results, it is possible to notice that the results are not statistically different one from each other: $p > 0.05$ for all the frameworks in this series. The vanadium amount in the MOFs permitted to obtain the molar ratio with GA, contained in the frameworks. The particles synthesized with 1 s of active time of sonication contain V, 1.5 times higher than those

obtained using 59 s pulse-on times. In particular, MVG_2001 and MVG_9001 possess a molar ratio V:GA of 3:1. The ratio decreases to 2:1 for the MVG_2059 and MVG_9059.

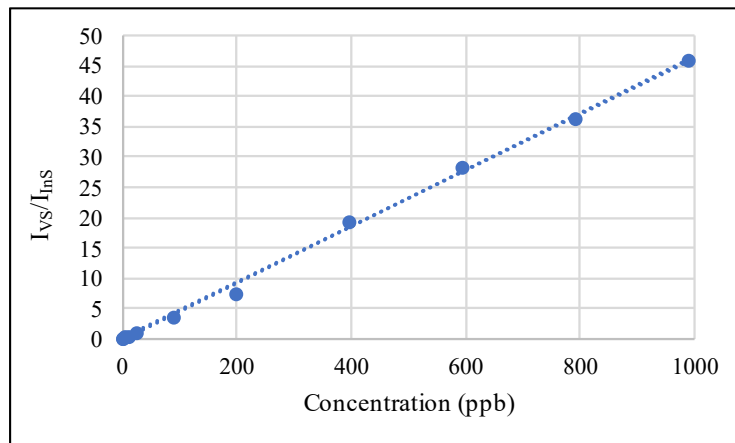


Figure 35: Calibration curve for vanadium as ratio of the intensities in respect to that of the internal standard (i.e. In).

3.5 THERMOGRAVIMETRIC ANALYSIS (TGA)

The thermogravimetric analysis was used to test the thermal stability of the MOFs. TGA thermograms are reported in Figure 36. The four frameworks possess the same behavior, that is different from that of the starting reactant. The major differences can be found in the temperature region 50°C – 500°C [21].

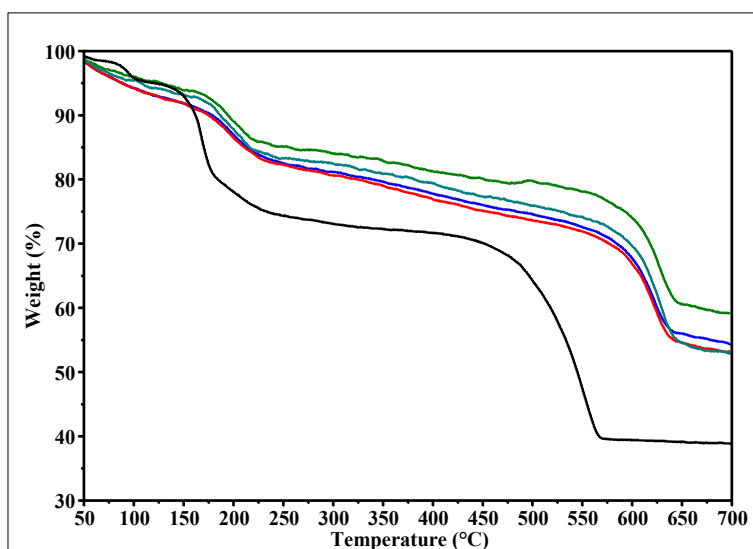


Figure 36: TGA of the $VOSO_4$ (black) and of the frameworks MVG_2001 (blue), MVG_2059 (red), MVG_9001 (green) and MVG_9059 (teal).

From thermographs reported in Figure 37, it is possible to notice that the synthesized MOFs have enhanced thermal stability in respect to the vanadium salt used for the reaction. The weight loss steps of this kind of samples can be associated to the evaporation of absorbed solvents or water till 120°C, from 120°C to 500°C the weight loss can be associated to the crystallization water, and finally, for weight losses over the 500°C the weight loss can be related to the degradation of the sample [22]. The VOSO₄ DTG thermogram shows three main weight loss temperatures: 93°C (absorbed water), 169°C (crystallization water), and 550°C (salt degradation). MVG samples thermographs do not present the peak associated with the loss of absorbed humidity, but only the peak due to the loss of the crystallization water. Moreover, MOFs lose their crystallization water at a significantly higher temperature (28°C) than vanadium salt, VOSO₄.

The frameworks' degradation temperatures are all comparable, but higher of about 70°C in comparison with vanadium salt. All TGA and DTG data are reported in Table 15. All values possess a good correlation ($r = 0.81$) with the amount of vanadium in the MOFs.

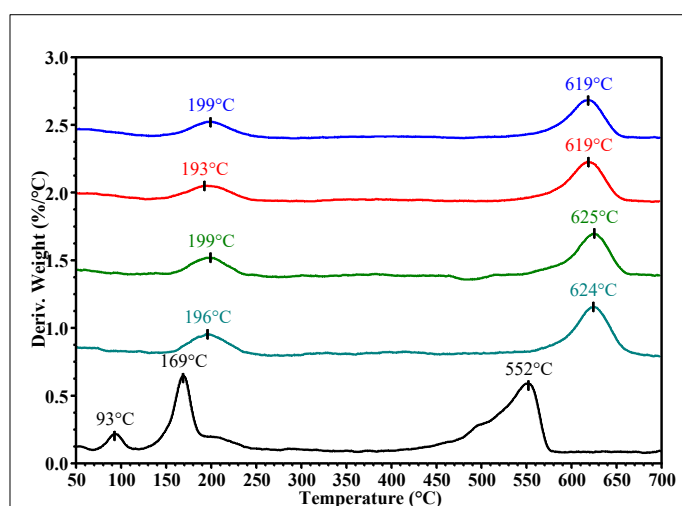


Figure 37: DTG of the VOSO₄ (black) and of the frameworks MVG_2001 (blue), MVG_2059 (red), MVG_9001 (green) and MVG_9059 (teal).

Table 15: TGA and DTG results for the VOSO₄ and the synthesized MOFs.

Sample	TGA Weight Loss (% w/w)			DTG T _{max} (°C)	
	30°C – 350°C	350°C – 700°C	Residue 700°C	30°C – 350°C	350°C – 700°C
MVG_2001	20.4% ± 0.3%	25.3% ± 0.4%	54.3% ± 0.4%	199°C	619°C
MVG_2059	21.0% ± 0.3%	25.8% ± 0.2%	53.2% ± 0.3%	193°C	619°C
MVG_9001	17.1% ± 0.1%	23.7% ± 0.2%	59.2% ± 0.2%	199°C	625°C
MVG_9059	19.1% ± 0.1%	28.0% ± 0.4%	52.9% ± 0.3%	196°C	624°C
VOSO ₄	27.7% ± 0.2%	33.4% ± 0.3%	38.9% ± 0.3%	93°C/169°C	552°C

3.6 SPECIFIC SURFACE AREA AND POROSITY

The specific surface area and pore volume of each obtained framework were measured with the isotherm gas absorption technique. Dried samples were preliminary treated to eliminate the residual humidity. The specific surface area was calculated using the BET method (S_{BET}), and the porosity and porous distribution was calculated with the BJH method.

Results are listed in Table 16. In general, 20% amplitude permits to obtain a greater surface area than 90% amplitude. Nevertheless, some differences can be seen for samples MVG_2001 and MVG_2059: MOF synthesized with the 1 s pulse-on has a 35% higher specific surface area. On the other hand, for the 90% amplitude of sonication, the 1 s pulse-on presents a decrease of the surface area of -12 %, in respect to the 59 s.

The pore volume follows the same trend as the specific surface area. The pore size distribution for the four samples is reported in Figure 38. Samples show same pore size behavior and are characterized by a pore multidimension size distribution. All the frameworks possess at low pore width the same values. At larger pore width some differences among the frameworks appear. MVG_9001 and MVG_9059 show the same values in the entire pore width range: so, there is no influence of the active pulse time on the 90% amplitude samples. MVG_2001 and MVG_2059 show different values from the 90% amplitude samples and between each other. The MVG_2001 possesses the highest pore values in the whole width range, the MVG_2059 till the 100 Å width shows the same values as the 90% amplitude samples, but from 100 Å to 400 Å the values increase, reaching the ones of other 20% based framework. Finally, the pores' shape of the frameworks can be classified according to the aspect and the type of the hysteresis in the adsorbing-desorbing diagrams, Figure 39e. All the MOFs present a graph that can be correlated to the H3 case (Figure 23e) so all the 4 frameworks possess wedged-shaped pores.

In respect to other gallic acid based MOFs, the four synthesized frameworks show lower surface area and higher pore volume. In fact, synthesized MOFs showed only 25 % of the surface area of Mg-gallate[23]. Contrarily, frameworks pore's volume is 3.5 times higher than Mg-gallate, [23].

Table 16: BET surface area and pore volumes of the MVG frameworks.

Sample	BET surface area (m ² /g)	Pore volume (cm ³ /g)
MVG_2001	115.3 ± 0.2	0.61
MVG_2059	85.4 ± 0.1	0.54
MVG_9001	71.6 ± 0.1	0.49
MVG_9059	80.2 ± 0.1	0.63

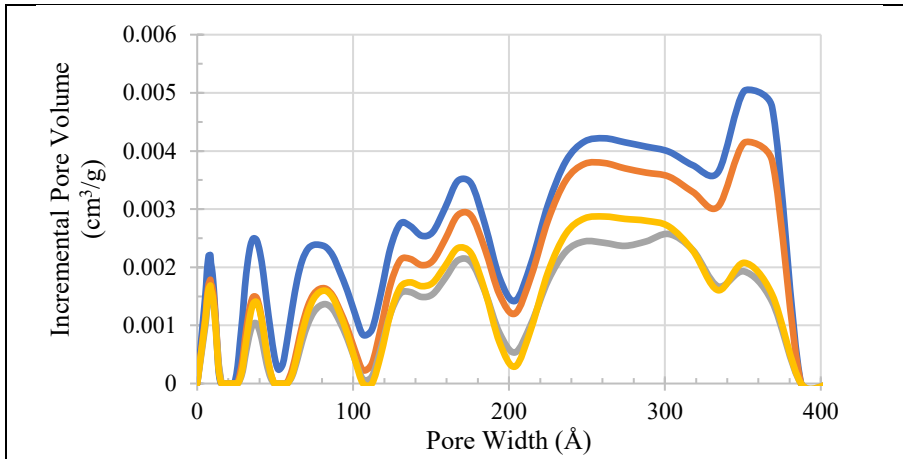


Figure 38: Pore size distribution (PSD) of the MVG_2001 (blue), MVG_2059 (orange), MVG_9001 (grey), MVG_9059 (yellow). Modeled by DFT model: N₂ – Tarezone NLDFT, Esf = 30.0K.

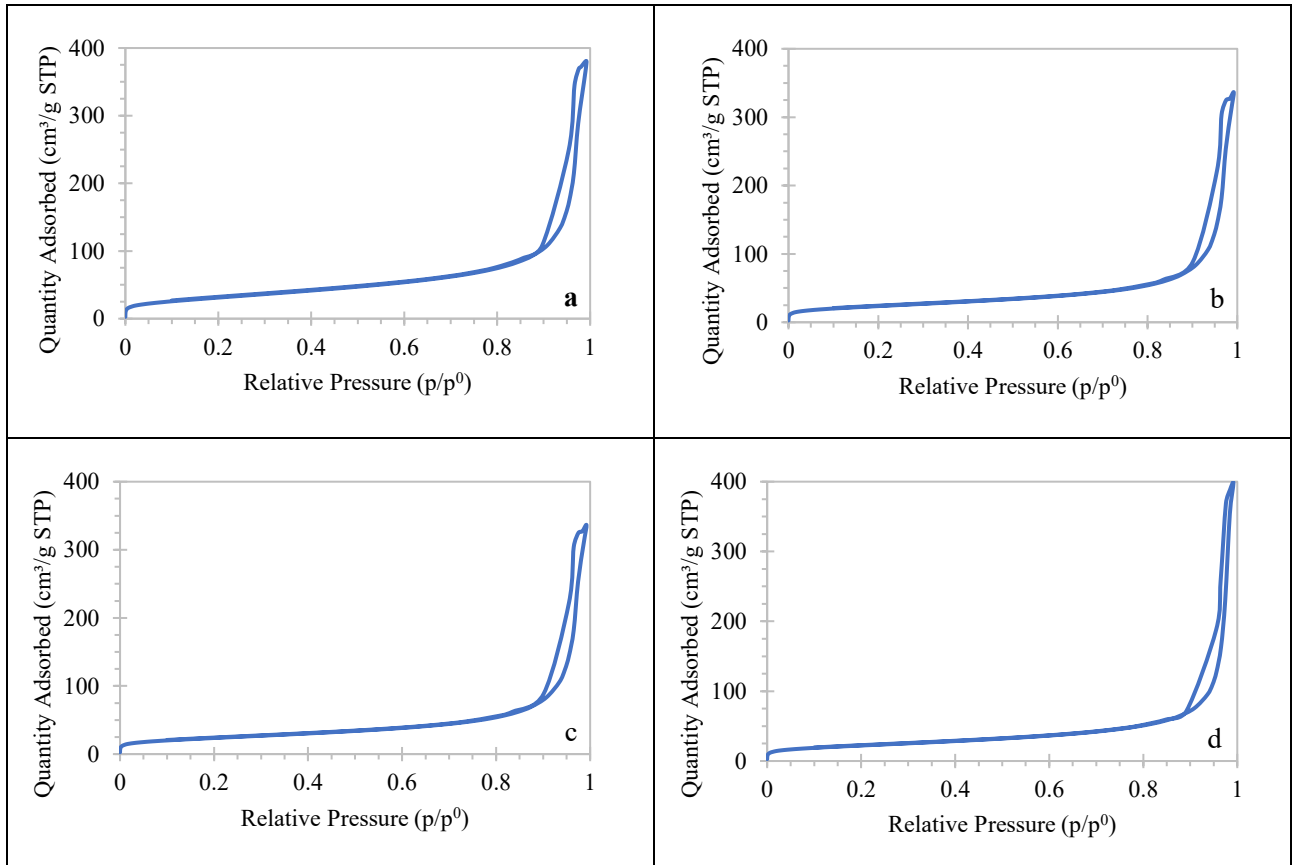
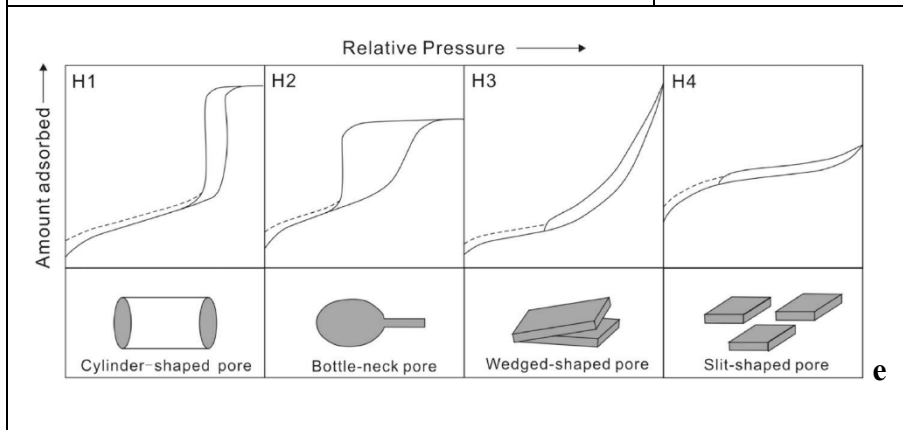


Figure 39: Curves of adsorbing-desorbing of MVG_2001 (a), MVG_2059 (b), MVG_9001 (c), MVG_9059 (d), and the classification of the curves of adsorbing-desorbing on the basis of the pore shape [24].



3.7 TRANSMISSION ELECTRON MICROSCOPE

The frameworks were characterized for their shape by transmission electron microscopy: the samples were first analyzed with the conventional TEM at the dry-state form, then they were tested with the cryo-TEM in water at frozen state. TEM images are reported in Figure 40a-d: from the pictures is possible to notice that all the frameworks possess the same overall shape when dried. The process consists in quite fast drying of the suspension, so the particles must organize and crystallize quickly. The particles of all the samples are needle-shaped and they are uniform in the dimensions within each sample, so the small needle-shaped aggregates are very rare. On the other hand, the sample in the cryo-TEM images result in a different state and form in respect to the conventional TEM. From the Figure 41 is possible to notice the particles shape that they assume in a suspension. All the analyzed frameworks assumed a round shape, with some small and big aggregates deriving from the aggregation of other small round-shaped particles.

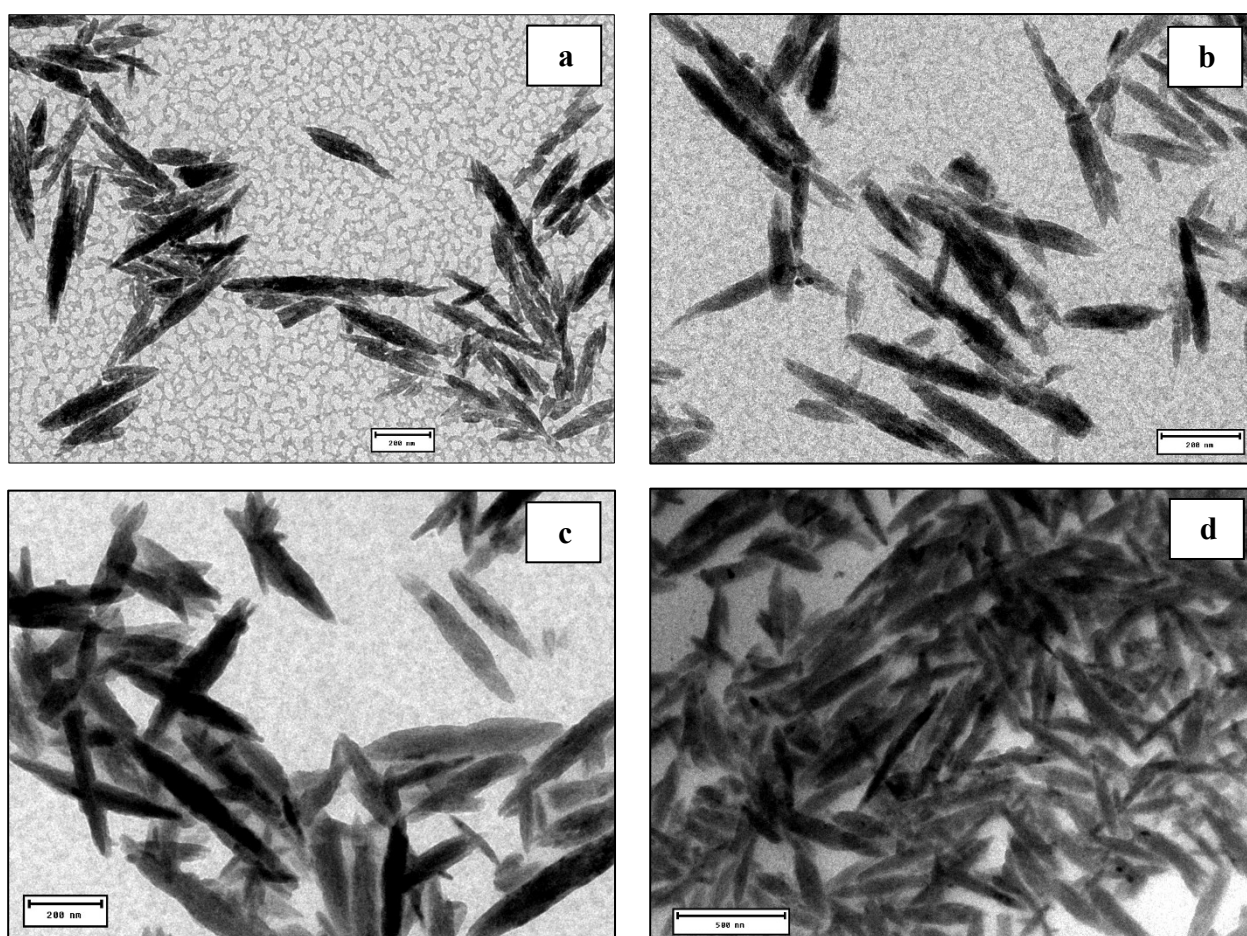


Figure 40: TEM images acquired at dry state of the MOFs MVG_2001 (a) with a scale bar of 200 nm, MVG_2059 (b) with a scale bar of 200 nm, MVG_9001 (c) with a scale bar of 200 nm and MVG_9059 (d) with a scale bar of 500 nm.

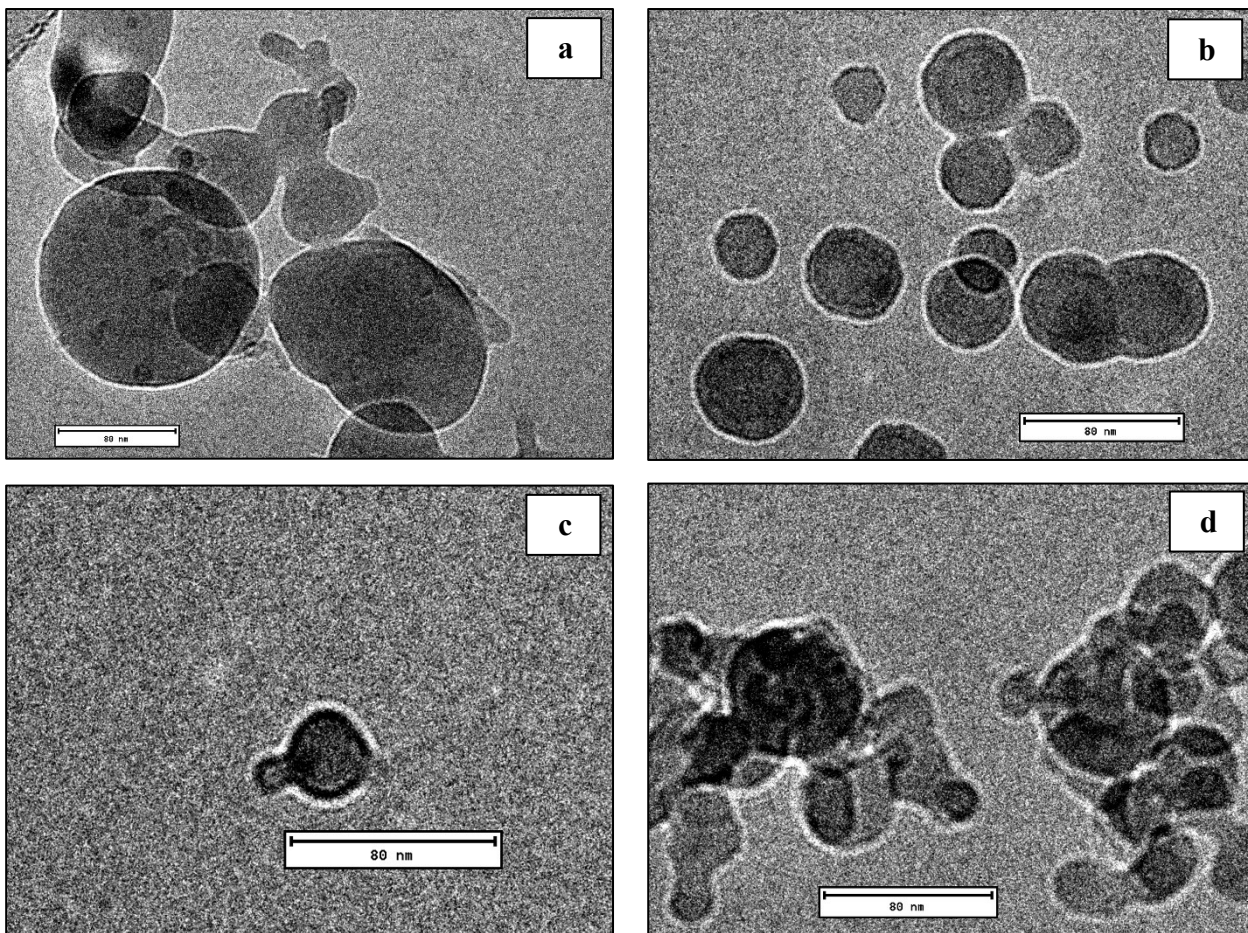


Figure 41: cryo - TEM images acquired in water at frozen state of the MOFs MVG_2001 (a), MVG_2059 (b), MVG_9001 (c) and MVG_9059 (d) all with a scale bar of 80 nm.

PART 4: CONCLUSIONS

Four different metal-organic frameworks based on vanadium (IV) and gallic acid were synthesized and characterized.

Different synthetic procedures were tested, i.e. hydrothermal configuration, ultrasound bath and ultrasound probe. Only the US probe procedure resulted effective to synthesize the frameworks, due to its tunability, reproducibility and more effective in the power supply to the reaction solution. The reaction was designed to test two important parameters that can affect the frameworks: the active sonication time and the amplitude of sonication.

The synthesized MOFs were characterized with the ATR-FTIR technique to confirm their composition: all the MVG frameworks resulted to be composed of vanadium oxygenated species and gallic acid derivative.

DLS analysis permitted to obtain their size distribution and their surface charge. The MVGs possess the same size distribution around $219\text{nm} \pm 9\text{nm}$, with a $\text{PDI} = 0.071 \pm 0.034$. From a Two-Way ANOVA statistical test the influence of the two synthesis parameters, i.e. the sonication amplitude and the active sonication time were tested. The size of the MOFs is affected by the active time of sonication and in lower amount by the sonication amplitude: an increase in the amplitude determines a slight increase in the particle size, whereas an increase in the pulse-on time determines an appreciable increase in the particle dimension.

The ζ – potential of the frameworks resulted -54 ± 9 , so the systems show a very high colloidal stability in UPW suspension. A Two-Way ANOVA highlighted that the active sonication time affects the surface charge more than the sonication amplitude. For the 1 s pulse-on frameworks increasing the amplitude of sonication an increase of stability resulted. Contrarily, for the 59 s of active sonication time samples, once the amplitude increases, the stability decreases. The pulse-on time of sonication for the lower amplitude does not affect the stability, but in the case of a higher amplitude, increasing the amplitude a decrease of the stability of the suspended particles is found. As highlighted by ζ – potential analysis, the frameworks with higher colloidal stability are those synthesized with the 90% amplitude and 1 s pulse-on sonication time (i.e. MVG_9001).

The vanadium content obtained by ICP-MS, was similar for the four MOFs, and no statistical differences were found for the parameters that were changed for the synthesis ($p > 0.05$). From these results, the molar ratio between the metal and the organic linker (V:GA) was calculated: MVG_2001 and MVG_9001 possess a molar ratio of 3:1 whereas MVG_2059 and MVG_9059 show a molar ratio of 2:1. This means that the 1 s based MOFs possess 1.5 times the vanadium that the 59 s ones and it may suggest a different organization or connectivity within the frameworks.

A TGA analysis was performed on the MOFs to test their thermal stability and their thermal behavior till 700 °C, in inert atmosphere. All the frameworks have the same thermal behavior, that is different from that of the vanadium salt used for the synthesis: the weight losses till 500 °C are less sudden (sharp?) than those of the vanadium salt. From the DTG signal is possible to notice that the MOFs sample possesses an enhanced thermal stability in respect of the vanadyl and a different crystallization water conformation.

Isothermal absorption-desorption tests allowed the specific surface area to be evaluated together with the pore size and pore size distribution. The 20 % based frameworks possess a greater S_{BET} , if compared to the 90 % based ones. For the 1 s based MOFs is observed a decrease in the S_{BET} of -12%, if compared to the 59 s based frameworks. The PSD of all the samples show that the systems possess a not unique value of pore dimension. The quantity (of ...what.. water?) absorbed in the absorption-desorption graphs suggests that for all the frameworks show wided-shaped pores.

The conventional transmission electron microscopy and cryo-TEM revealed the topology of the synthesized samples. Conventional TEM provided the form and the organization of the frameworks when rapidly dried: for all samples the organization corresponds to needle-shaped aggregates with the same overall dimensions. The cryo-TEM provided the form of the particles when they are suspended in UPW: all the MVGs possess round-shaped aggregates in suspension, and the bigger particles seem to be aggregates of smaller round-shaped ones.

This work represents a starting experimental step for the synthesis of vanadium-based frameworks. Future characterization of these systems is necessary and some evaluations are already in progress. One is the p-XRD analysis of the powdered MOFs, to evaluate their effective conformation and to study more deeply the effects of the two set parameters on MOFs structure. Another still in progress analysis is the evaluation of the cytotoxicity of these particles as a function of both the synthetic parameters and concentration of the suspension.

The obtained particles will be then supported by viscoelastic polymeric matrices and the new systems characterized also in terms of influence of the polymeric matrices on their structure and behavior.

The loading of active molecules or natural extracts into the frameworks will also be evaluated together with their release profiles.

Finally, some other synthetic parameters will be tested and evaluated with the same approach proposed in this work: the time of reaction and the molar ratio of the reactants will be evaluated.

BIBLIOGRAPHY

- [1] H. Furukawa, K. E. Cordova, M. O'Keefe and O. M. Yaghi, "The chemistry and applications of metal-organic frameworks," *Science*, vol. 341, no. 6149, p. 1230444, 2013.
- [2] S. Dutt, K. Ashwani and S. Shivendra, "Synthesis of Metal Organic Frameworks (MOF) and Their Derived Materials for Energy Storage Applications," *Clean Technology*, vol. fasc. 1, pp. 140-66, 2023.
- [3] R. Singh, "Metal organic frameworks for drug delivery," *Applications of Nanocomposite Materials in Drug Delivery*, pp. 605-617, 2018.
- [4] T. J. Mason and J. P. Lorimer, "The Uses of Power Ultrasound in Chemistry and Processing," *Applied Sonochemistry*, p. 303, 2002.
- [5] K. S. Suslick, "Sonochemistry," *Science*, vol. 247, no. 4949, pp. 1439-1445, 1990.
- [6] C. Vaitsis, G. Sourkouni and C. Argiris, "Sonochemical synthesis of MOFs," *Metal-Organic Frameworks for Biomedical Applications*, pp. 223-244, 2020.
- [7] A. Henglein, "Sonochemistry: historical developments and modern aspects," *Ultrasonics*, vol. 25, no. 1, pp. 6-16, 1987.
- [8] H. Kazemzadeh and M. Mozafari, "Adsorption, delivery, and controlled release of therapeutic molecules from MOFs," *Metal-Organic Frameworks for Biomedical Application*, pp. 297-320, 2020.
- [9] I. Christodoulou, C. Serre and R. Gref, "Metal-organic frameworks for drug delivery: Degradation mechanism and in vivo fate," *Metal-Organic Frameworks for Biomedical Applications*, pp. 467-489, 2020.
- [10] A. Ścibior, Ł. Pietrzyk, Z. Plewa and A. Skiba, "Vanadium: Risks and possible benefits in the light of a comprehensive overview of its pharmacotoxicological mechanisms and multi-applications with a summary of further research trends," *Journal of Trace Elements in Medicine and Biology*, vol. 61, p. 126508, 2020.
- [11] A. M. Cortizo, M. S. Molinuevo, D. A. Barrio and L. Bruzzone, "Osteogenic activity of vanadyl (IV)–ascorbate complex: Evaluation of its mechanism of action," *The international journal of biochemistry & cell biology*, vol. 38, no. 7, pp. 1171-1180, 2006.

- [12] A. M. Cortizo, G. Ruderman, F. N. Mazzini and M. S. Molinuevo, "Novel vanadium-loaded ordered collagen scaffold promotes osteochondral differentiation of bone marrow progenitor cells," *International journal of biomaterials*, 2016.
- [13] E. O'Neill, G. Awale, L. Daneshmandi, O. Umerah and K. W. H. Lo, "The roles of ions on bone regeneration," *Drug discovery today*, vol. 23, no. 4, pp. 879-890, 2018.
- [14] C. Vaitis, G. Sourkouni and C. Argirusis, "Metal organic frameworks (MOFs) and ultrasound: a review," *Ultrasonic sonochemistry*, vol. 52, pp. 106-119, 2019.
- [15] L. Guan-Lin and S. G. Kazarian, "Recent advances and applications to cultural heritage using ATR-FTIR spectroscopy and ATR-FTIR spectroscopic imaging," *Analyst*, vol. 147, no. fasc. 9, pp. 1777-97, 2022.
- [16] A. Samui and S. K. Sahu, "Characterizations of MOFs for biomedical application," *Metal-Organic Frameworks for Biomedical Applications*, pp. 277-295, 2020.
- [17] E. Ghorbani-Kalhor, "A metal-organic framework nanocomposite made from functionalized magnetite nanoparticles and HKUST-1 (MOF-199) for preconcentration of Cd (II), Pb (II), and Ni (II)," *Microchimica Acta*, vol. 183, pp. 2639-2647, 2016.
- [18] R. Barddestani, G. S. Patience and S. Kaliaguine, "Experimental methods in chemical engineering: specific surface area and pore size distribution measurements—BET, BJH, and DFT," *The Canadian Journal of Chemical Engineering*, vol. 97, no. 11, pp. 2781-2791, 2019.
- [19] K. Maes, L. I. Martin, S. Khelifi, A. Hoffman, K. Leus, P. Van Der Voort, E. Goovaerts, P. F. Smet, V. Van Speybroeck, F. Callens and H. Vrielinck, "Identification of vanadium dopant sites in the metal–organic framework DUT-5 (Al)," *Physical Chemistry Chemical Physics*, vol. 23, no. 12, pp. 7088-7100, 2021.
- [20] M. Zhang, B. Yang, Z. Yuan, Q. Sheng, C. Jin, J. Qi, M. Yu, Y. Liu and G. Xiong, "Preparation and performance testing of corn starch/pullulan/gallic acid multicomponent composite films for active food packaging," *Food Chemistry*, vol. X, no. 19, p. 10782, 2023.
- [21] Q. Liu, Z.-F. Li, Y. Liu, H. Zhang, Y. Ren, C.-J. Sun, W. Lu, Y. Zhou, L. Stanciu, E. A. Stach and J. Xie, "Graphene-modified nanostructured vanadium pentoxide hybrids with extraordinary electrochemical performance for Li-ion batteries," *Nature communications*, vol. 6, no. 1, p. 6127, 2015.
- [22] W. M. Carvalho Jr, L. Cassayre, D. Quaranta, F. Chauvet, R. El-Hage, T. Tzedakis and B. Biscans, "Stability of highly supersaturated vanadium electrolyte solution and

characterization of precipitated phases for vanadium redox flow battery," *Journal of Energy Chemistry*, vol. 61, pp. 436-445, 2021.

- [23] L. Cooper, T. Hidalgo, M. Gorman, T. Lozano-Fernández,, R. Simón-Vázquez, C. Olivier, N. Guillou, C. Serre, C. Martineau, F. Taulelle, D. Damasceno-Borges, G. Maurin, A. González-Fernández,, P. Horcajada and T. Devic, "A biocompatible porous Mg-gallate metal–organic framework as an antioxidant carrier," *Chemical Communication*, vol. 51, no. 27, pp. 5848-5851, 2015.
- [24] C. Yang, J. Zhang, S. Han, X. Wang, L. Wang, W. Yu and Z. Wang, "Compositional controls on pore-size distribution by nitrogen adsorption technique in the Lower Permian Shanxi Shales, Ordos Basin," *Journal of Natural Gas Science and Engineering*, vol. 34, pp. 1369-1381, 2016.

**CHAPTER V:
ALTERNATIVE SYSTEMS
FOR DRUG DELIVERY**

**RELEASE AND ACTIVITY OF IRON COMPLEXES:
EFFECT OF Fe OXIDATION STATES AND CHELATING
AGENTS ON IRON BIO-ACCESSIBILITY FROM
DIFFERENT SUPPLEMENTS**

PART 1: INTRODUCTION

Iron deficiency anemia (IDA) is a pathological state characterized by reduced oxygen delivery that provokes generalized weakness and, consequently, low productivity [1-2]. The most diffused treatment to reduce iron deficiency is oral iron supplementation. Nevertheless, the absorption of iron in subjects is very low, ranging from 5% to 28% [2-4] and the unabsorbed percentage is responsible for the most common observed side effects, i.e. gastrointestinal alterations [2]. In the last years, US Food and Drug Administration (FDA) approved formulations containing different iron-complex forms such as ferric citrate (Auryxia), ferric maltol (Accrufer), and derisomaltose (Monoferric) [2; 5-7]. However, an adequate therapy of IDA is still a challenge. Iron is mostly found as ferrous Fe (II) and ferric Fe (III) ions. Since intestinal mucosa can absorb only Fe (II) ions, the oxidized form Fe (III) needs to be reduced before being internalized [8]. Different chelating or encapsulating agents for both ferrous and ferric ions in the form of nano or micro-carriers [8-11] have been developed to reduce the negative effects caused by oral iron assumption while increasing the low bioavailability of the metal ion. Research is focusing on characterizing the active form of the iron complex rather than the complete formulation of commercial products, which contain large quantities of excipients that can significantly alter the bioavailability of metal ion. Seven commercial products containing different chelating agents (i.e. lipidic Fe(III)-pyrophosphate, Fe(III)-pyrophosphate, lipidic Fe(II)-sulphate, Fe(III)-saccharate and Fe(III)-EDTA) were analyzed. The effect of different complex forms on the iron release and bioavailability was studied directly analyzing the final commercial products. Formulations were characterized by means of infrared and thermal analyses to evaluate the presence of interactions among the different components able to significantly affect iron bio-accessibility. The effect of iron oxidation state, complexing agent, and particle dimension on the iron bioavailability were also analyzed using the Caco-2 Cell monolayer model.

PART 2: MATERIALS AND METHODS

2.1 MATERIALS

All reagents and solvents were purchased from Sigma-Aldrich (Milan, Italy). Commercial products containing ferric or ferrous ions in different complexed forms were chosen among iron supplements that differed only in terms of complex-iron and formulation (i.e. capsule or tablet) but that contained superimposable excipients and other active substances, i.e. folic acid, and ascorbic acid in comparable amount. All commercial products were purchased by a pharmacy apart from sample MB (Emosid® commercialized also as Didone®) that was provided by Medibase s.r.l.

2.2 INFRARED ANALYSIS

FTIR spectra of samples were recorded in the range $4000 - 750 \text{ cm}^{-1}$ with a resolution of 2 cm^{-1} using a NICOLET iS50 FT-IR (Thermo, USA). OMNIC correction ATR software was used for baseline and spectra correction [12].

2.3 DIFFERENTIAL SCANNING CALORIMETRY (DSC)

DSC thermographs were recorded using Q1000 calorimeter (TA instruments). 5 mg of each sample ($n = 3$) were sealed in an anodized aluminum hermetic pan and heated from $30 \text{ }^{\circ}\text{C}$ to $300 \text{ }^{\circ}\text{C}$, with a heating rate of $10^{\circ}\text{C}/\text{min}$, under nitrogen ($50 \text{ mL}/\text{min}$.) [13].

2.4 THERMOGRAVIMETRIC ANALYSIS (TGA)

Thermogravimetric analysis was conducted with SDT-Q600 (TA Instruments, USA), following the procedure reported in [13]. Briefly, 20-25 mg of each sample ($n=3$) were put in a platinum crucible and heated from 30°C to 650°C , with a heating ramp of $10^{\circ}\text{C}/\text{min}$, under nitrogen flow.

2.5 DYNAMIC LIGHT SCATTERING (DLS) MEASUREMENTS

The granulate formulations inside the capsule, that were based on heterogeneous delivery systems (i.e. for example liposomes or similar vehicles), were put in 10 mL of ultrapure water (UPW). The samples (n=3) were then kept under agitation for 2 hours. The average size approximated to the hydrodynamic radius and the particles size distribution were evaluated by DLS measurements at 37°C. Samples were analyzed also after 7 days to evaluate the stability of the suspended particles [14].

2.6 IRON BIOAVAILABILITY

2.6.1 IRON SOLUBILITY

The formulations under examination were incubated at pH 2 at 37°C for 2 h. At the end of the 2 h pancreatin and bile were added bringing the pH to values close to 7 to simulate the intestinal phase. The formulations were kept under these conditions for 3h. Subsequently, the samples were centrifuged to separate the supernatant for the quantification of iron by spectrophotometric assay [15].

2.6.2 IRON DIALYSABILITY

Formulations were immersed in UPW solution at pH 2.8 (acidified by 6 M HCl) in the presence of pepsin and kept under stirring at 37 °C for 2 h. After 2 hours, it was added to all the samples a cylindrical tube closed at one end with dialysis membrane (cut-off 10 kDa). 0.15 M PIPES buffer pH 6.3 (PIPES (piperazine-N,N -bis[2-ethanesulfonic acid] disodium salt) was added in the cylindrical tube and all the formulations kept at 37°C for additional 30 minutes. Subsequently, the mixture of pancreatin and bile salts, consisting in 0.2 g porcine pancreatin and 1.2 g bile extract suspended in 100 mL of 0.1 M NaHCO₃, was added, and incubated for another 2 hours. Finally, the dialysates were centrifuged (10000 g for 20 minutes). Iron concentration was measured spectrophotometrically [16-17].

2.6.3 GASTROINTESTINAL METHOD

Gastrointestinal method was derived by Minekus et al. [18]. Briefly, one dose of each formulation was immersed in simulated salivary fluid (SSF) at 37°C. After adding CaCl₂·2 H₂O in an amount sufficient to obtain a total concentration of 0.75 mM in SSF, the mixture was brought to 37°C and stirred at 50 rpm for 2 minutes to imitate the agitation in the oral cavity, then the pH was adjusted to 3, using 0.1 M HCl and the concentration of CaCl₂·2H₂O decreased to 0.075 mM. This mixture was incubated at 37 °C for 120 minutes under shaking at 50 rpm to simulate stomach conditions. To mimic the small intestinal stage, total concentration of 0.6 mM CaCl₂·2H₂O was realized and bile salt was added, to obtain a final concentration of 10 µM. Then, the pH was adjusted to 7 by adding 0.1 M NaOH. Pancreatic enzyme was added to obtain 2000 U mL⁻¹ of lipase activity and the mixture maintained for 120 minutes. The supernatants were used for the determination of iron spectrophotometrically [18].

2.7 IRON BIOACCESSABILITY

The human cell line Caco-2 was cultured as reported by Rodriguez-Ramiro et al. [19]. Cells were seeded at a density of 10⁵ cells/well in 12-well plates and used in the iron uptake experiments after 14 days post seeding. A 1.5 mL aliquot of the dialysate was added to each well and after 24 h-incubation, cells were harvested for analysis. The supernatants were analyzed before and after the contact with cells to quantify iron consumption.

2.8 STATISTICAL ANALYSIS

All samples were in triplicate. Data were reported as average values ± standard deviations (SD). Results were subjected to ANOVA test. For all the statistical treatments, the level of significance was set at $p \leq 0.05$ [20].

PART 3: RESULTS AND DISCUSSIONS

3.1 FORMULATIONS

The composition of the different analyzed formulations is reported in Table 17.

Table 17: Composition of analyzed formulations.

Sample	Iron-complex	Formulation
CS	Lipidic Pyrophosphate-Fe(III)	Capsule
SF	Lipidic Pyrophosphate-Fe(III)	Capsule
TF	Pyrophosphate-Fe(III)	Tablet
MB	Lipidic Sulphate-Fe(II)	Capsule
IF	Lipidic Sulphate-Fe(II)	Capsule
EM	Saccharate-Fe(III)	Capsule
FF	EDTA-Fe(III)	Tablet

3.2 INFRARED ANALYSIS

Infrared and thermal (TGA-DSC) analyses were performed to assess the presence of interactions among the components in each investigated formulation. FTIR is widely used for conformational analysis and structural characterization of metal complexes, since the formation of ion-complexes induces shifts of absorbance bands of involved functional groups. Infrared spectra of all the formulations were recorded and depicted in Figure 42.

Despite the presence of significant amounts of similar excipients, spectra of different samples containing identical iron-complexes can be grouped being characterized by the presence of typical bands of the counterpart of iron ions. Indeed, formulations MB and IF (lipidic -FeSO₄ complexes) showed superimposable spectra, as well as the series CS, SF, and TF showed very similar spectra being based on lipidic-pyrophosphate iron complexes. IF and MB spectra showed the typical ferrous sulphate bands centered at 1642 cm⁻¹ and 1098 cm⁻¹ due to asymmetric and symmetric O=S-O stretching. IR spectra of CS, SF, and TF showed the bands assigned to the symmetric and asymmetric P-O-P vibrations at about 748 cm⁻¹ and 947 cm⁻¹ respectively, and the bands corresponding to the P-O stretching that fall in the 1000–1200 cm⁻¹ range [21-22]. Sample EM showed the saccharide typical bands in the region 1100-1000 cm⁻¹ [12] whereas sample FF showed the typical bands of

EDTA-iron complex as reported by Wagner & Baran in their characterization of EDTA-Fe (III) complex by means of IR and Raman spectroscopy, i.e. the band at 1654 cm^{-1} related to carboxylate (COO^-) stretching [23] and the band at 1175 cm^{-1} due to (CNC) stretching [10]. Typical bands of folic acid, i.e., band at 3414 cm^{-1} corresponding to the OH stretching, band at 1542 cm^{-1} due to NH bending, and band in the range of 1400 and 1444 cm^{-1} corresponding to phenol and pterin ring [24], were evident in all the samples spectra together with the doubled band at $2900\text{-}2800\text{ cm}^{-1}$ related to the asymmetric and symmetric stretching of CH_2 moieties [12]. All spectra showed the two bands of vitamin C centered at 1764 cm^{-1} and 1675 cm^{-1} related to the stretching vibration of five -membered lactone ring and the large band at $3300\text{-}3500\text{ cm}^{-1}$ due to stretching of OH bonds [25].

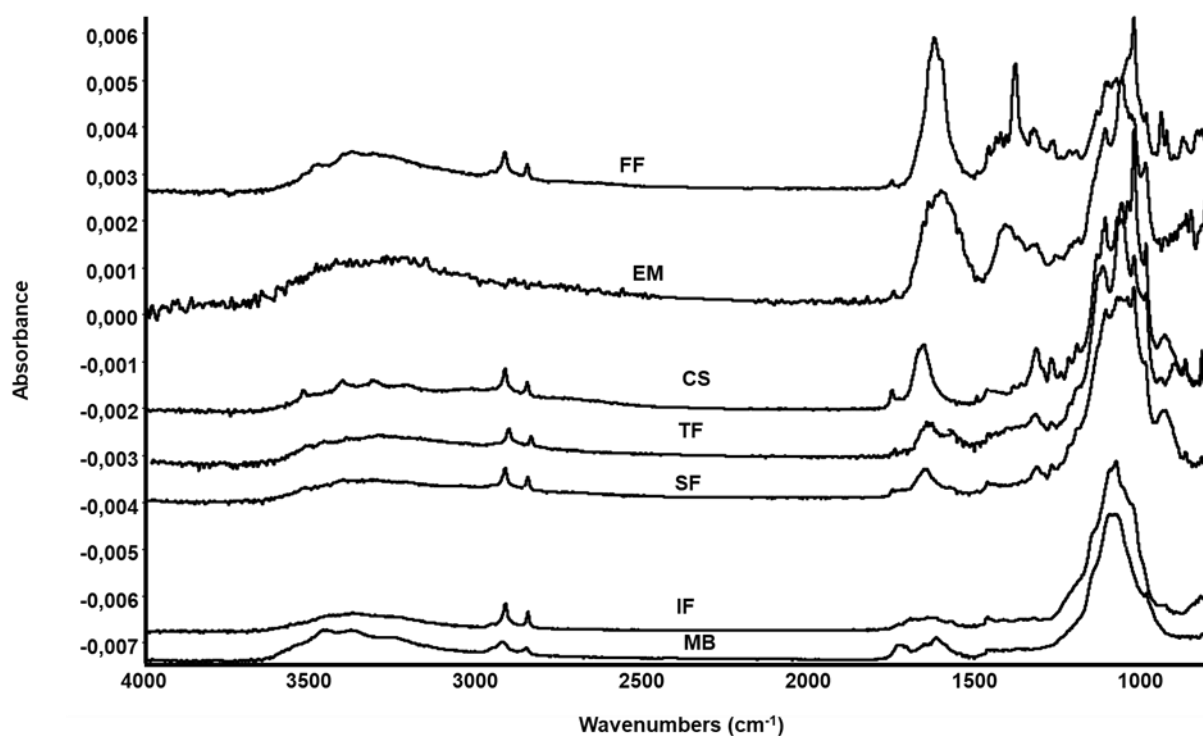


Figure 42: FTIR spectra of complete formulations. Capsule formulations were tested opening the capsule and analyzing the preparation without any treatment. Tablet formulations were finely pulverized.

Interestingly, in formulations based on different complexes of ferric ions no shift of the bands related to vitamin C was observed. Contrarily, in MB and IF formulations (ferrous ions) a small shift of both bands was recorded, thus suggesting the interaction between ferrous ions and ascorbic acid. These strong interactions are important since vitamin C can prevent the oxidation of Fe (II) ions maintaining them in soluble form, and thus favoring their absorption [25]. Similar evidence was also

found by Nimbka et al. and Bartewaska [1; 25]. To confirm this observation thermal analyses (DSC and TGA) were performed.

3.3 DIFFERENTIAL SCANNING CALORIMETRY (DSC)

The DSC analysis was conducted on the dry state formulations: Figure 43 summarizes the DSC thermographs of all the investigated formulations.

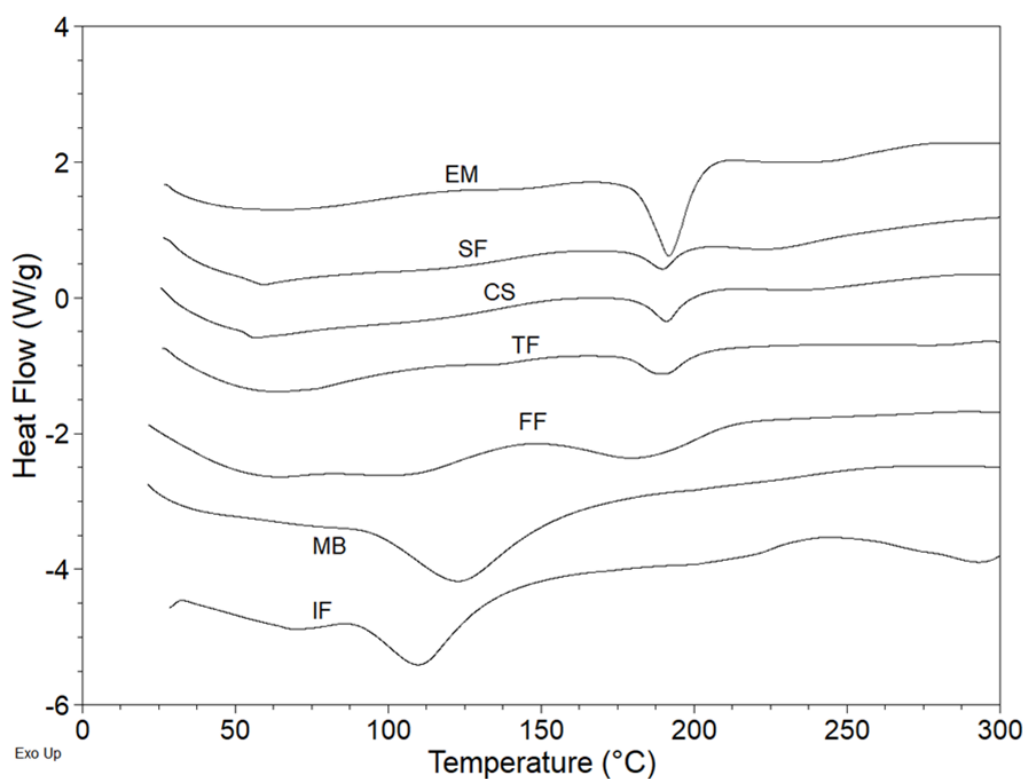


Figure 43: DSC profiles of selected formulations.

DSC thermographs highlighted significant differences among formulations. Formulations CS, SF, TF, EM, and FF showed superimposable thermographs with a single endothermic phenomenon centered at 190°C-200 °C, due to the decomposition of ascorbic acid [26]. Contrarily, formulations IF and MB showed the endothermic phenomenon at a significantly lower temperature, (i.e. 120°C-130°C) that is related to ascorbate form when bound to metal ions as also observed by Raghavendra in their study on lithium l-ascorbate [27]. The DSC data confirms the FT-IR evidence.

3.4 THERMOGRAVIMETRIC ANALYSIS (TGA)

To further analyze the stability and interaction strength of the different compositions, TGA was performed. Indeed, TGA can help to point out how the composition can affect the stability of the system at dry state. To gain a comparable information R, i.e. the ratio between the weight loss in the 400-600°C range (structured component) and the weight loss in the 200-400°C range (labile component) was calculated, Table 18.

Table 18: Weight loss percentage as a function of temperature. R: ratio between weight loss in 400-650°C and 200-400°C.

Sample	Weight Loss (%)			R
	30-200°C	200-400°C	400-600°C	
CS	11±1 ^a	49±1 ^a	8±1 ^a	0.17 ^a
SF	11±1 ^a	44±2 ^b	8±1 ^a	0.18 ^a
TF	10±1 ^a	54±1 ^c	9±1 ^a	0.16 ^a
FF	13±1 ^{a,b}	47±3 ^{a,b}	20±2 ^b	0.42 ^c
EM	13±1 ^{a,b}	39±2 ^d	10±1 ^a	0.26 ^d
MB	15±1 ^b	34±1 ^e	18±3 ^b	0.53 ^e
IF	14±1 ^b	44±2 ^{a,b}	15±2 ^b	0.34 ^f

Different letters in the same column indicate significant differences ($p < 0.05$; ANOVA one-way test).

As observed in DSC analysis, differences among formulations can be observed in both the first (30-200°C) and third (400-650°C) ranges of weight loss. Samples CS, SF and TF showed a lower weight loss in 400-650°C range, which is generally related to structured components, thus suggesting a lower degree of interactions among the formulation components. The three formulations containing pyrophosphate complex showed a superimposable stability as highlighted by a comparable R value. The highest stability can be found for sample MB and FF formulations.

3.5 DYNAMIC LIGHT SCATTERING (DLS) MEASUREMENTS

Mean dimension and polydispersity index of formulations commercialized as capsules (i.e., CS, SF, IF and MB) were evaluated after 2 h and 7 days in fluid to evaluate the formulation colloidal stability. Table 19 summarizes the results of size analysis. Size distributions graphs after 2 hours are depicted in Figure 44.

Table 19: Particle size of selected formulations after 2 hours and 7 days.

Sample	2h		7 days	
	Z-average (nm)	PDI	Z-average (nm)	PDI
CS	115±4	0.29±0.01	87±4	0.38±0.01
SF	126±3	0.30±0.01	136±4	0.34±0.05
MB	184±6	0.25±0.01	214±9	0.25±0.01
IF	11±0	0.32±0.03	-	-

Selected formulations showed different behaviors. Formulations CS and SF (lipidic pyrophosphate-Fe (III)) showed similar particle size with a superimposable polydispersity index after 2h.

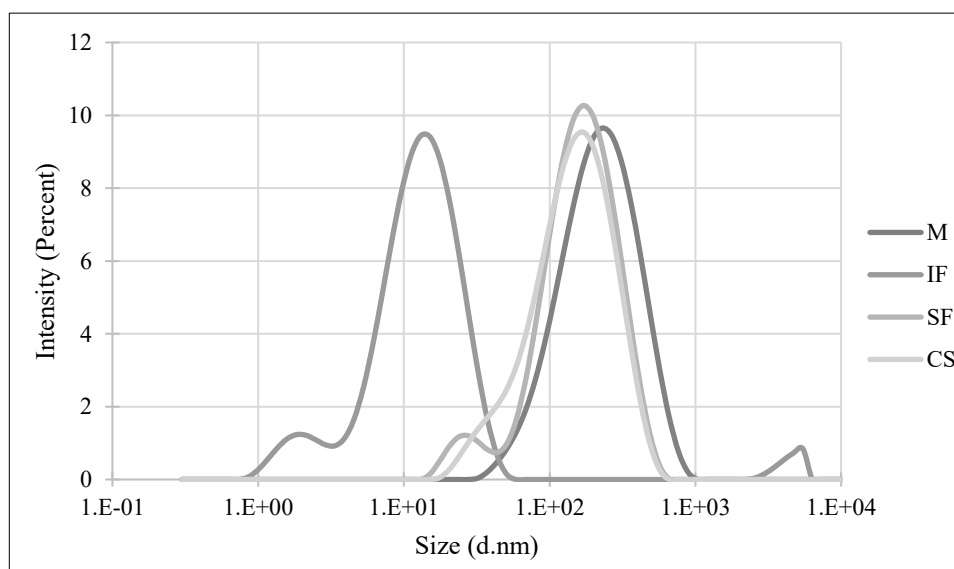


Figure 44: Particles' size distribution performed by DLS analysis.

After 7 days the two formulations showed opposite behavior, a significant decrease of the mean particle size with a significant increase of PDI was observed for formulation CS whereas for SF we found an increase of both the particle size and the PDI. Formulations based on lipidic ferrous sulphate, i.e. MB and IF showed completely different characteristics after 2 hours. IF showed the smallest particles and after 7 days the system was demonstrated to be unstable: a complete precipitation was observed. Formulation MB was, instead, characterized by the largest particle size, but showed the lowest PDI that was not subjected to changes after 7 days, thus underlying its good colloidal stability.

3.6 IRON AVAILABILITY

Three different methods have been exploited to quantify iron availability from commercial products. The first and simplest tested method was the solubility test that simulates gastric and intestinal environment controlling both pH and digestive enzymes concentration. The dialysability method differs from the previous one mainly on the use of a dialysis membrane able to simulate epithelial tissue. Finally, the last tested method was the gastrointestinal method that is designed to simulate the entire human digestive tract. As shown by data summarized in Table 20, solubility test permits to quantify the higher amount of iron. No significant difference was found between dialysability and gastrointestinal test. No significant differences have been obtained changing the used method, even if a significantly higher amount of iron was detected using both the dialysability and the gastrointestinal methods. Although *in-vitro* results cannot be used as the real *in-vivo* adsorption values, however significant correlations can be found. For example, Aragón et al. [26] compared the validity of an iron dialysability method with *in-vivo* data to assess the iron bioavailability from staple biofortified food crops. The *in-vitro* dialysability results showed a similar trend to the *in-vivo* results and were highly and statistically correlated. The study also found that the results from the *in-vitro* method yielded more statistically significant differences between treatments than the *in-vivo*. This can be explained by reduced variability in the data compared to *in-vivo*. An additional benefit is that there are no differences in baseline iron status such as can be seen in human studies which results in high variability in iron bioavailability as compared to *in-vitro* methods as observed in different studies [26-28]. This demonstrates that the *in-vitro* models provide better control over conditions of the experiments which may lead to precise and reproducible results. The *in-vitro* test is also simple, rapid, and low cost and many samples can be evaluated at one time.

The percentages of iron ions available using the three different methods are listed in Table 20.

Table 20: Percentage of released iron ions using the three reported methods (starting amount 30 mg of iron)

Sample	Solubility	Dialysability	GI
CS	20±1%	9±1%	12±1%
SF	25±1%	19±1%	28±1%
TF	15±1%	8±1%	18±1%
FF	32±1%	28±1%	28±1%
MB	41±1%	41±1%	38±1%
IF	37±1%	36±1%	34±1%
EM	12±1%	7.0±1%	12±1%

Argyri et al. [27-28] obtained a correlation model between the iron absorption values of 494 individuals and the values of the dialysis tests. The same study was also conducted by others [27-28] highlighting an excellent correlation between the *in-vivo* results and the *in-vitro* dialysability method. Using the models proposed in the literature, the bioavailability values of iron from the analyzed formulations were obtained, Figure 45.

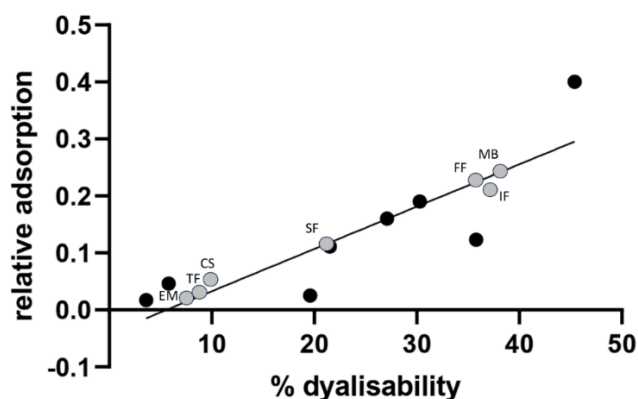


Figure 45: Correlation between the % of iron dialysability and the corresponding “in vivo relative adsorption values obtained by [28].

Basing on the used models, all formulations can be grouped into different blocks depending on the oxidation state of iron ions. All formulations containing ferrous ions seem to be more easily released and consequently absorbed as compared to those containing ferric ions. This can be related, as highlighted by infrared and thermal analyses, to the higher stability of ascorbate Fe (II).

3.7 IRON BIO-ACCESSIBILITY: CACO-2 CELLS

The formulations under study were compared for their ability to promote iron uptake by Caco-2 cells, which are known to resemble the enterocytes lining the small intestine and, therefore, can be used as a biologic model mimicking the intestinal barrier [17]. There are no significant differences in terms of cellular response, i.e. the iron supplied is completely absorbed. Therefore, based on the different release profile from the analyzed formulations the higher amount of iron absorbed by the cells, considering 30 mg of iron contained in each formulation, occurs for the MB formulation that guarantees an absorption of approximately 50% of the iron. This percentage is reduced to 35% for IF, 30% for the SF, and less than 20% for the other formulations, Figure 46.

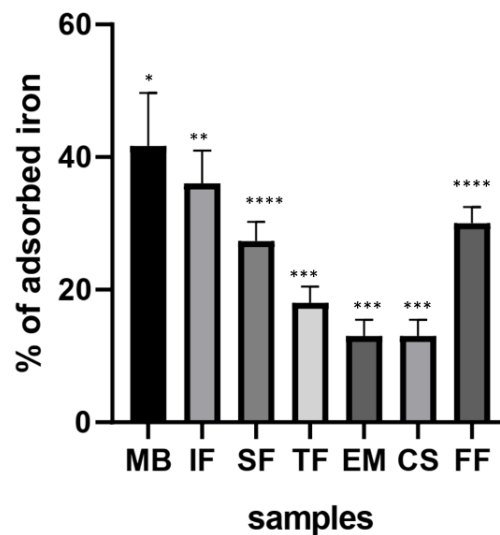


Figure 46: Percentage of iron absorption using Caco2 Cells model. Asterisks indicated a significant difference.

PART 4: CONCLUSIONS

Different formulations containing iron complexes were evaluated.

Infrared and thermal analyses highlighted that ferrous ions complexes (MB and IF) were able to strictly interact with ascorbic acid thus forming stable soluble systems that represent a protection system for ferrous ions.

DLS analysis pointed out that MB formulation showed the highest colloidal stability as highlighted by the identical PDI value after 2 hours and 7 days.

Applying the literature proposed models, a significant difference can be observed in terms of bio-accessibility with lipidic sulphate ferrous MB showing the highest availability. This difference can be related to the higher stability of Fe (II) complex that permits, once in contact with gastrointestinal environment, to not be easily released and not be subjected to the physiological oxidation process to ferric ions that, once free in solution, are insoluble. This high colloidal stability is reflected in an enhanced bioavailability of MB, as compared to the other investigated formulations, as highlighted by the *in-vitro* tests used to quantify the iron release.

BIBLIOGRAPHY

- [1] S. Nimbkar, M. M. Leena, J.A. Moses, C. Anandharamakrishnan. Development of iron-vitamin multilayer encapsulates using 3 fluid nozzle spray drying. *Food Chem.* 406 (2023) 135035.
- [2] K. Singh, D. S. Chopra, D. Singh, N. Singh. Nano-formulations in treatment of iron deficiency anaemia: An overview. *Clin. Nutr. ESPEN* 52 (2022) 12-19.
- [3] Y.Y. Zhang, R. Stockmann, K. Ng, J. A. Broadbent, S. Stockwell, H. Suleria, N.E. K. Shaik, R. R. Unnithan, S. Ajlouni. Characterization of Fe(III)-binding peptides from pea protein hydrolysates targeting enhanced iron bioavailability *Food Chem.* 405 (2023) 134887.
- [4] Fabiano, E. Brilli, S. Fogli, D. Beconcini, S. Carpi, G. Tarantino, Y. Zambito. Sucrosomial® iron absorption studied by in vitro and ex-vivo models. *Eur. J. Pharm. Sci.* 111 (2018) 425–431.
- [5] V. Markova, R. Hansen, L.L. Thomsen, A. Pinborg, T. Moos, C. Holm. Intravenous iron isomaltoside versus oral iron supplementation for treatment of iron deficiency in pregnancy: protocol for a randomized, comparative, open-label trial. *Trials* 21 (2020) 742.
- [6] J.E. Onken, D.B. Bregman, R.A. Harrington, D. Morris, P. Acs, B. Akright B, C. Barish, B.S. Bhaskar, G.N. Smith-Nguyen, A. Butcher, T. A. Koch, L.T. Goodnough. A multicenter, randomized, active-controlled study to investigate the efficacy and safety of intravenous ferric carboxymaltose in patients with iron deficiency anaemia. *Transfusion* 54 (2014) 306-315.
- [7] R.F. Pollock, P. Biggar. Indirect methods of comparison of the safety of ferric derisomaltose, iron sucrose and ferric carboxymaltose in the treatment of iron deficiency anaemia. *Expet. Rev. Hematol.* 13 (2020) 187-195.
- [8] K. Shubham, T. Anukiruthika, S. Dutta, A.V. Kashyap, J. A. Moses, C. Anandharamakrishnan. Iron deficiency anemia: A comprehensive review on iron absorption, bioavailability and emerging food fortification approaches. *Trends Food Sci. Technol.* 99 (2020) 58–75.
- [9] B. Gaigher, E. do Nascimento da Silva, V. Lacerda Sanches, R. F. Milani, F. Galland, S. Cadore, M. Grancieri, M.T.B. Pacheco. Formulations with microencapsulated Fe-peptides

- improve in vitro bioaccessibility and bioavailability. *Current Research in Food Science* 5 (2022) 687–697.
- [10] C. Wagner, E.J. Baran Vibrational spectra of two Fe(III)/EDTA complexes useful for iron supplementation. *Spectrochim. Acta A Mol. Biomol.* 75 (2010) 807–810
- [11] C. Tan, A.C. Karaca, E. Assadpour, S.M. Jafar. Influence of different nano/micro-carriers on the bioavailability of iron: Focus on in vitro–in vivo studies. *Adv. Colloid Interface Sci.* 318 (2023) 102949.
- [12] G. Leone, S. Pepi, M. Consumi, S. Lamponi, M. Fragai, M. Martinucci, V. Baldoneschi, O. Francesconi, C. Nativi, A. Magnani. Sodium hyaluronate-g-2-((N-(6-aminohexyl)-4-methoxyphenyl)sulfonamido)-N-hydroxyacetamide with enhanced affinity towards MMP12 catalytic domain to be used as visco-supplement with increased degradation resistance. *Carbohydr. Polym.* 271 (2021) 118452.
- [13] G. Leone, M.D. Volpato, N. Nelli, S. Lamponi, E. Boanini, A. Bigi, A. Magnani. Continuous multilayered composite hydrogel as osteochondral substitute. *J Biomed Mater Res Part A* 103A (2015) 2521–2530.
- [14] L. Talarico, M. Consumi, G. Leone, G. Tamasi, A. Magnani, Solid Lipid Nanoparticles Produced via a Coacervation Method as Promising Carriers for Controlled Release of Quercetin. *Molecules* 26 (2021) 2694.
- [15] N. Sulaiman, D.I. Givens, S. Anitha. A Narrative Review: In-vitro Methods for Assessing Bio-Accessibility/Bioavailability of Iron in Plant-Based Foods. *Front. Sustain. Food Syst.* 5 (2021) 727533.
- [16] K. Argyri, A. Birba , D.D. Miller , M. Komaitis , M. Kapsokefalou. Predicting relative concentrations of bioavailable iron in foods using in vitro digestion: New developments. *Food Chemistry* 113 (2009) 602 – 607.
- [17] K. Argyri, E. Theophanidi, A. Kapna, C. Staikidou, G. Pounis, M. Komaitis, C. Georgiou, M. Kapsokefalou. Iron or zinc dialyzability obtained from a modified in vitro digestion procedure compare well with iron or zinc absorption from meals. *Food Chemistry* 127 (2011) 716–721.
- [18] M. Minekus, M. Alminger, P. Alvito, S. Ballance, T. Bohn, C. Bourlieu, , F. Carrière, R. Boutrou, M. Corredig, D. Dupont,§ C. Dufour, L. Egger, M. Golding, S. Karakaya, B. Kirkhus, S. Le Feunteun, U. Lesmes, A. Macierzanka, A. Mackie, S. Marze, D. J. McClements, O.

- Ménard, I. Recio, C.N. Santos, R.P. Singh, G.E. Vegarud, M.S.J. Wickham, W. Weitschies, A. Brodkorb. A standardised static in vitro digestion method suitable for food-an international consensus. *Food Funct* 5 (2014) 1113–1124
- [19] Rodriguez-Ramiro, C. Dell'Aquila, J. L. Ward, A. L. Neal, S.F.A Bruggraber, P. R. Shewry, S. Fairweather-Tait. Estimation of the iron bioavailability in green vegetables using an in vitro digestion/Caco-2 cell model. *Food Chem.* 301 (2019) 125292.
- [20] G. Leone, M. Consumi, C. Franzi, G. Tamasi, S. Lamponi, A. Donati, A. Magnani, C. Rossi, C. Bonechi. Development of liposomal formulations to potentiate natural lovastatin inhibitory activity towards 3-hydroxy-3-methyl-glutaryl coenzyme A (HMG-CoA) reductase. *J. Drug Deliv. Sci. Technol.* 43 (2018) 107–112.
- [21] J. Zheng, X. Ou, B. Zhang, C. Shen, J. Zhang, L. Ming, Y. Han. Effects of Ni²⁺ doping on the performances of lithium iron pyrophosphate cathode material. *J. Power Sources* 268 (2014) 96–105.
- [22] G. Leone, S. Pepi, M. Consumi, F. F. Mahdizadeh, S. Lamponi, A. Magnani. Phosphorylated xanthan gum-Ag(I) complex as antibacterial viscosity enhancer for eye drops formulation. *Carbohydr. Polym.* 267 (2021) 118196.
- [23] M. Consumi, G. Leone, S. Pepi, A. Pardini, S. Lamponi, C. Bonechi, G. Tamasi, C. Rossi, A. Magnani. Calcium ions hyaluronan/gellan gum protective shell for delivery of oleuropein in the knee, *Int. J. Polym. Mater. Polym. Biomater.*, 71 (2022), 414-424.
- [24] E. Assadpour, S.M. Jafari, Y. Maghsoudlou, Evaluation of folic acid release from spray dried powder particles of pectin-whey protein nano-capsules. *Int. J. Biol. Macromol.* 95 (2017) 238–247.
- [25] M.A. Bryszewska Comparison Study of Iron Bioaccessibility from Dietary Supplements and Microencapsulated Preparations. *Nutrients* 11 (2019) 273
- [26] J. Pantwalawalkar, H. More, D. Bhang, U. Patil, N. Jadhav. Novel curcumin ascorbic acid cocrystal for improved solubility *J. Drug Deliv. Sci. Technol.* 61 (2021) 102233.
- [27] K. Raghavendra Rao, H.L. Bhat, E. Suja. Studies on lithium l-ascorbate dihydrate: An interesting chiral nonlinear optical crystal. *Mater. Chem. Phys.* 137 (2013) 756-763.

[28] I.J. Aragón, D. Ortiz, H. Pachón. Comparison between in vitro and in vivo methods to screen iron bioavailability. *CYTA J Food* 10 (2012) 103-111.

CONCLUSIONS

POLYMERIC AND METAL-ORGANIC FRAMEWORKS FOR DRUG DELIVERY SYSTEMS

In this work different frameworks for the release of active molecules and extracts were explored. Polymeric drug delivery systems based on polyelectrolyte complexes, polysaccharide blends and synthetic polymeric theta-gels were synthesized and characterized as vehicles for bioactive substances.

Xanthan gum and chitosan based delivery systems were prepared and tested as vehicles to deliver vegetable extracts based on red rice and Annurca apple analyzing their effects on the antioxidant power, cholesterol synthesis and bioavailability, and lipoprotein oxidation. The combination of phytochemical nutraceuticals with lipid lowering activity were demonstrated to be a valid alternative to the use of high doses of active molecules (monacolina K, lovastatine, etc.) to reduce cholesterol levels.

A Hyaluronan – gellan gum-based system was tested for the delivery of olive leaves extract in the osteoarthritic knee. The GG-HA blend allows the fast release of the bioactive matrix based on oleuropein extract, thus providing a system able to guarantee at the same time an adequate viscosupplementation and anti-inflammatory action thanks to the presence of oleuropein.

For the same bioactive substance, a different vehicle was prepared starting from two of the most used biocompatible synthetic polymers, PVA and PEG. PVA in the form a theta-gel can be prepared in a basic environment, without any influence on the properties of the gels. Different molecular weights for both polymers were tested. Contrarily to what found for hyaluronan - gellan gum system, the obtained PVA-PEG matrices guaranteed a slow release of oleuropein. The slow release of the oleuropein-based extract may suggest a use of these matrices for the prolonged deliverance therapies for active extracts.

A metal-organic framework based on vanadium and gallic acid was synthesized and characterized. The synthetic parameters as active time and amplitude of sonication were tested and varied to optimize the MOF structure and properties in terms of particle size, system colloidal stability, surface

charge, specific surface area and porosity to develop suitable drug delivery systems for active molecules and natural extracts.

Commercial products for oral iron supplementation containing different iron (II or III) chelating agents were studied, focusing on the active iron complex, and evaluating the effect of iron oxidation state, complexing agent, and particle dimensions on the iron bioavailability. The study allowed to discriminate the formulation (MB) with the highest colloidal stability, which was reflected in an enhanced iron bioavailability, as compared to the others, as highlighted by the *in vitro* tests used to quantify the iron release.